

im²

Instituto Universitario
de Matemática Multidisciplinar

MODELLING FOR ENGINEERING & HUMAN BEHAVIOUR 2020

July 8-10, 2020

Edited by

R. Company, J.C. Cortés,
L. Jódar and E. López-Navarro



UNIVERSITAT
POLITÈCNICA
DE VALÈNCIA

CIUDAD POLITÈCNICA
DE LA INNOVACIÓN



Modelling for Engineering & Human Behaviour 2020

València, 8 – 10 July 2020

This book includes the extended abstracts of papers presented at XXII Edition of the Mathematical Modelling Conference Series at the Institute for Multidisciplinary Mathematics “Mathematical Modelling in Engineering & Human Behaviour”.

I.S.B.N.: 978-84-09-25132-2

Version: 3-12-2020

Report any problems with this document to ellona1@upvnet.upv.es.

Edited by: R. Company, J. C. Cortés, L. Jódar and E. López-Navarro.

Credits: The cover has been designed using images from [kjpargeter/freepik](https://www.kjpargeter.com/).

This book has been supported by the European Union through the Operational Program of the [European Regional Development Fund (ERDF) / European Social Fund (ESF)] of the Valencian Community 2014-2020. [Record: GJIDI/2018/A/010].

im²

Instituto Universitario
de Matemática Multidisciplinar



Fons Europeu de
Desenvolupament Regional

Una manera de fer Europa

Contents

Dopamine imbalance: A systemic approach to diseases and treatments , by Salvador Amigó.....	1
New solution for automatic and real time detection of railroad switch failures and diagnosis , by Jorge del Pozo, Laura Andrés, Rafael Femenía and Laura Rubio.....	8
An integrated model to optimize Berth Allocation Problem and Yard Planner , by C. Burgos, J.C. Cortés, D. Martínez-Rodríguez, J. Villanueva-Oller and R.J. Villanueva.....	12
Dynamical analysis of a new three-step class of iterative methods for solving nonlinear systems , by Raudys R. Capdevila, Alicia Cordero and Juan R. Torregrosa.....	19
Integrating the human factor in FMECA-based risk evaluation through Bayesian networks , by S. Carpitella, J. Izquierdo, M. Plajner and J. Vomlel.....	24
Stable positive Monte Carlo finite difference techniques for random parabolic partial differential equations , by M.-C. Casabán, R. Company and L. Jódar.....	30
Invariant energy in short-term personality dynamics , by Antonio Caselles, Salvador Amigó and Joan C. Micó.....	36
Suitable approximations for the self-accelerating parameters in iterative methods with memory , by F. I. Chicharro, N. Garrido, A. Cordero and J.R. Torregrosa.....	42
Predictive maintenance system for a dam based on real-time monitoring and diagnosis , by Ernesto Colomer, Carlos Canales, Jesús Terradez and Salvador Mateo.....	48
Approximating the matrix hyperbolic tangent , by Emilio Defez, José Miguel Alonso, Javier Ibáñez, Pedro Alonso-Jordá and Jorge Sastre.....	52
Efficient finite element modelling of sound propagation in after-treatment devices with arbitrary cross section , by F.D. Denia, E.M. Sánchez-Orgaz, B. Ferrándiz, J. Martínez-Casas and L. Baeza.....	59
Iterative algorithms for computing generalized inverses , by A. Cordero, N. Garrido, P. Soto-Quiros and J.R. Torregrosa.....	66
Communities' detection in weakly connected directed graphs , by J. M. Montañana, A. Hervás and P. P. Soriano.....	72
Comparison in the use of ANSYS and SAP2000 in the modelling and structural calculation of bridges , by Miriam Labrado, Ernesto Colomer, Adrián Zornoza and Álvaro Potti.....	78

Analysing nonlinear oscillators subject to Gaussian inputs via the random perturbation technique , by J.-C. Cortés, E. López-Navarro, J.-V. Romero and M.-D. Roselló. .	82
A note on the use the semifocal anomaly as temporal variable in the two body problem , by José Antonio López Ortí, Francisco José Marco Castillo and María José Martínez Usó.	87
Epidemiological modelling of COVID-19 in Granada, Spain: Analysis of future scenarios , by José-Manuel Garrido, David Martínez-Rodríguez, Fernando Rodríguez-Serrano, Raul S-Julián and Rafael-J. Villanueva.	91
Probabilistic calibration of a model of herpes simplex type 2 with a prefixed error in the uncertainty of the data , by Juan-Carlos Cortés, Pablo Martínez-Rodríguez, Jose-A. Morano, José-Vicente Romero, María-Dolores Roselló and Rafael-J. Villanueva.	96
A proposal for quantum short time personality dynamics , by Joan C. Micó, Salvador Amigó and Antonio Caselles.	102
Energy footprint reduction of Chile’s social interest homes: an integer linear programming approach , by Felipe Monsalve and David Soler.	109
Statistical solution of a second-order chemical reaction , by J.-C. Cortés, A. Navarro-Quiles, J.-V. Romero and M.-D. Roselló.	115
On comparing Spotify Top 200 lists , by F. Pedroche and J. A. Conejero.	121
New autonomous system for slope stability control in linear infrastructure , by Álvaro Potti, Gonzalo Munielo, Julián Santos and Jordi Marco.	125
Application of a twin model for monitoring and predictive diagnosis of Pirihueico Bridge , by Marcelo Márquez, Francisca Espinoza, Sandra Achurra, Julia Real, Ernesto Colomer and Miriam Labrado.	129
N-soft set based multi-agent decisions: A <i>decide-then-merge</i> strategy , by J.C.R. Alcantud, G. Santos-García and M. Akram.	133
Deep Learning AI-based solution for vineyard real-time health monitoring , by Ana Sancho, Eliseo Gómez, Albert Pérez and Julián Santos.	138
New system for the automatic counting of vehicles in roundabouts and intersections , by Teresa Real, Rubén Sancho, Guillém Alandí and Fernando López.	142
A System Dynamics model to predict the impact of COVID-19 in Spain , by M.T. Sanz, A. Caselles, J. C. Micó and C. Soler.	146
An epidemic grid model to address the spread of Covid-19. The case of Valencian Community (Spain) , by M.T Signes Pont, J.J. Cortés Plana, H. Mora Mora and C. Bordehore Fontanet.	152
The Relativistic Harmonic Oscillator in a Uniform Gravitational Field , by Michael M. Tung.	157
A disruptive technology that enables low cost real-time monitoring of road pavement condition by any ordinary vehicle circulating on the road, and automatically designs plans for predictive maintenance , by Francisco José Veá, Adrián Zornoza, Juan Ramón Sánchez and Ismael Muñoz.	163

Dopamine imbalance: A systemic approach to diseases and treatments

Salvador Amigó¹

Departament de Personalitat, Avaluació i Tractaments Psicològics,
Universitat de València (Spain).

1 Introduction

Psycho-Neuro-Endocrine-Immunology is a scientific research field with an emphasis on multidisciplinary studies aiming at integrating different disciplines: Psychology, Psychiatry, Neurobiology, Endocrinology, Immunology and Neurology, and the relationships of this cross-talk with physical and psychological health and diseases.

Dopamine is a neurotransmitter and several studies support the notion that dopamine is a coregulatory of the endocrine and immune systems. It has been associated with many health problems like drug addiction, cardiovascular diseases, Parkinson disease, chronic fatigue syndrome, cancer, etc.

The Systems Theory Approach represents the best scientific option to understand the origin of diseases and possible treatments derived from the dopamine imbalance and its influence on all the systems that make up our body. And this is the objective of this speech.

2 Chronic low-grade inflammation and dopaminergic system

Chronic low-grade inflammation contributes to the progression of many disorders and conditions, which includes chronic stress, metabolic disorders (e.g., obesity, metabolic syndrome), dysbiosis, and medical illnesses (e.g., cardio-vascular disease, diabetes, cancer, chronic infectious diseases, and autoimmune and inflammatory disorders) [1].

The metabolic demands of chronic low-grade inflammation (energy costs can increase the overall daily energy expenditure by as much as 30%) induce a reduction of striatal dopamine (DA). This is due to the impact of inflammatory cytokines on mesolimbic DA signaling [1]. These authors explain: “Inflammatory signaling molecules play a critical role in communicating information relevant to shifts in immunometabolism that impact available energy resources in the body, a prerequisite for the mesolimbic DA system to generate accurate estimates of expected value of reward and guide effort allocation and energy expenditure. This function may

¹e-mail: salvador.amigo@uv.es

have originated during evolution as a means of suppressing exploratory behavior and shifting energy resources to the immune system for fighting infection and healing wounds in an ancestral environment rife with pathogens and predators” (p.1).

Regarding the symptoms of anhedonia from multiple diseases, increased inflammation as indexed by C-reactive protein (CRP) produces decreased connectivity between the ventral striatum and mPFC, inducing dejection.

3 Dopamine reduces inflammation

DA and its downstream signaling has an antiinflammatory function [2]. These authors verified that astrocytic DRD2 (dopamine D2 receptor) activation suppresses neuroinflammation in the central nervous system, and it provides a new strategy for targeting the astrocyte-mediated innate immune response in the central nervous system during ageing and disease.

On the other hand, dopamine (DA) inhibits NLRP3 inflammasome activation via dopamine D1 receptor (DRD1) [3]. Moreover, activation of dopamine D2 receptors simultaneously ameliorates various metabolic features of obese women [4]. The metabolic syndrome comprises a cluster of metabolic anomalies including insulin resistance, abdominal obesity, dyslipidemia, and hypertension. These authors proved that short-term bromocriptine (a D2R agonist) treatment facilitates glucose metabolism, lowers systolic blood pressure, and stimulates resting energy expenditure in obese humans.

4 Inflammation resistance, metabolism and dopamine

Inflammation is a mechanism for energy balance in the body. Inflammation resistance will lead to obesity [5]. These authors explain this mechanism: “Abundant literature on obesity suggests that chronic inflammation is a consequence of energy accumulation in the body. The emerging evidence strongly supports that the inflammatory response induces energy expenditure in a feedback manner to fight against energy surplus in obesity. If this feedback system is deficient (Inflammation Resistance), energy expenditure will be reduced and energy accumulation will lead to obesity. In this perspective, we propose that an increase in inflammation in obesity promotes energy expenditure with a goal to get rid of energy surplus” (p.1).

That means inflammation can be beneficial to the organism, and inflammation resistance can lead to chronic low-grade inflammation and related diseases. For example, physical exercise contributes to reducing obesity, but inflammation response occurs during physical exercise, which increase energy expenditure and suppresses food intake. Physical exercise may break the inflammation resistance to promote energy expenditure. If the body lacks response to the pro-inflammatory cytokines (Inflammation resistance), the energy metabolism will be impaired leading to an increased risk for obesity [6].

Why does this happen? The acute inflammation that exercise induces in an isolated session causes a homeostatic response and a subsequent physiological adaptation, eventually causing a reduction in inflammation and exercising a response anti-inflammatory on the long run [7, 8].

Physical exercise produces short-term stress response. That enhances innate/primary, adaptive/secondary, vaccine-induced, and anti-tumor immune responses, and post-surgical recovery. Therefore, short-term stress psychology/physiology could be harnessed to enhance immunoprotection, as well as mental and physical performance. On the other hand, chronic stress has

long-been known to play a role in the etiology of numerous diseases [9].

Acute or short-term increases in systemic inflammation lead to an increase in DA, while chronic inflammation has the opposite effect [10] that is way DA can reduce systemic inflammation.

5 Methylphenidate and inflammation

Methylphenidate (MPD) is a dopaminergic agonist. MPD at a low dose might exert its therapeutic action by inhibiting DAT (dopamine active transporter) and increasing the tonic (basal) level of extracellular dopamine.

DA elevation induced by MPD was significantly greater when subjects were pre-treated with LPS (immune activator lipopolysaccharide) compared to PBO (placebo) [10]. LPS-induced activation causes acute systemic inflammation and depression-like behavior, but in this experiment, they did not observe fatigue when LPS was co-administered with MPD.

Regarding to physical exercise and food intake, the combination of aerobic exercise and methylphenidate may have a positive effect on fatigue, cognitive function, and functional ability in patients with melanoma receiving $IFN - \alpha$ [11], and MPD reduced overall energy intake with a selective reduction in dietary fat, which is consistent with a reward deficiency model of obesity whereby low brain dopamine predicts overeating and obesity, and administering agents that increase dopamine results in reduced feeding behavior [12].

MPD improved all symptoms (with effects on proinflammatory cytokines) of the posttraumatic stress disorder (PTSD) symptomatology in a rat model. Moreover, the combination of MPD with Desipramine produced the most dramatic beneficial effects [13]. In a sample from children with ADHD, MPD normalized immunological parameters [14]. Also, in an experiment with healthy volunteers, MPD robustly induced an epinephrine-dominant stress response, and the acute epinephrine-induced stress response was characterized by rapid accumulation of mature and functional NK cells in the peripheral circulation [15]. The authors conclude: “This is in line with studies using other acute stressors and supports the role of the acute stress response in rapidly mobilizing the innate immune system to counteract incoming threats” (p.1).

6 Methylphenidate and cancer

Cancer is an inflammatory disease. The inflammatory response found in many cancers is one of chronic inflammation, resulting in an environment rich in innate immune cells, which secrete substances that promote angiogenesis and cell proliferation [16].

Dopaminergic agonists can inhibit lung cancer progression by reducing angiogenesis and tumor [17], or increases the efficacy of anticancer drugs in breast and colon cancer [18], and the activation of short-term stress physiology increased chemokine expression and T cell trafficking and enhanced Type 1 cytokine-driven cell-mediated immunity that is crucial for resistance to squamous cell carcinoma [19].

On the other hand, MPD appears safe when used in the treatment of depression and fatigue in advanced cancer, and reducing depression and fatigue [20] and improves cognition, mood, and function of brain tumor patients [21]. Fatigue is strongly correlated with depression in cancer patients and both are driven by activation of the pro-inflammatory cytokine network linking inflammation and cancer-related fatigue and depression [22].

Could MPD also have an anticancer effect?

We can propose at least two routes to explain the possible antitumor effects of MPD. MPD is capable of reducing significantly the levels of phosphorylation of proteins JNK1/2 (c-Jun amino-terminal kinases 1 and 2) and increasing ERK1/2 (extracellular signal-regulated kinases 1 and 2) [23]. On the other hand, low-dose MPD increases the levels of proteins linked to cell proliferation in the hippocampus, including brain-derived neurotrophic factor (BDNF) increased in mice [24]. Some studies propose the BDNF/TrkB signaling as an anti-tumor target [25].

7 Mathematical model of methylphenidate single dose effects: a perspective of the future

Our research group, with Joan Carles Micó, Antonio Caselles and I, have been working on mathematical modeling of MPD effects, and the reproduction of those effects using a psychological procedure, the Self-Regulation Therapy [26].

For the mathematical analysis, the response model was applied as an integro-differential equation, whose usefulness has been shown to model the dynamic effect of a stimulant drug [27, 28]. The model is as follows:

$$\left. \begin{aligned} \frac{dm(t)}{dt} &= -\alpha \cdot m(t) \\ m(0) &= M \\ \frac{ds(t)}{dt} &= \alpha \cdot m(t) - \beta \cdot \int_0^t e^{-\frac{x-t}{\tau}} \cdot s(x) \cdot y(x) dx \\ s(0) &= 0 \\ \frac{dy(t)}{dt} &= a(b - y(t)) + p \cdot s(t) \cdot y(t) \\ y(0) &= y_0 \end{aligned} \right\} \quad (1)$$

Note that (1) is a coupled a system of two differential equations and one integro-differential equation. The $m(t)$ variable is evolution of the stimulus before entering in the metabolizing organism system, being M the stimulus initial amount and α is the stimulus assimilation rate. The $s(t)$ variable represents the stimulus, being β is the stimulus metabolizing rate. The $y(t)$ variable represents the General Factor of Personality (GFP) dynamics; and b and y_0 are respectively its tonic level and its initial value.

Its dynamics is a balance of three terms, which provide the time derivative of the GFP: the homeostatic control ($a(b - y(t))$), i.e., the cause of the fast recovering of the tonic level b , the excitation effect ($p \cdot s(t) \cdot y(t)$), which tends to increase the GFP, and the inhibitor effect ($\beta \cdot \int_0^t e^{-\frac{x-t}{\tau}} \cdot s(x) \cdot y(x) dx$), which tends to decrease the GFP and is the cause of a continuously delayed recovering. Parameters a , p , q and τ are named respectively the homeostatic control power, the excitation effect power, the inhibitor effect power and the inhibitor effect delay.

And we have been able to mathematically check and model the effects on mood produced by the MPD, increasing happiness and reducing depression [29][29]. Positive affect has been associated with changes in the number of immune system cells, and also with the function of the system (greater NK cell cytotoxicity and helper T cells, and increases in secretory IgA (S-IgA) responses to antigen challenge) [30], and study and model the effects of MPD on biological markers, such as glutamate or regulatory genes [31–33].

With all that has been stated so far, there is a splendid expectation for the future regarding the medical application of MPD and other dopamine agonists in the treatment of multiple diseases, including cancer.

References

- [1] Treadway, M.T., J.A. Cooper, and A.H. Miller, Can't or Won't? Immunometabolic Constraints on Dopaminergic Drive. *Trends Cogn Sci*, 2019. 23(5): 435-448.
- [2] Shao, W., Zhang, S.Z., Tang, M., Zhang, X.H., Zhou, Z., Yin, Y.Q., Zhou, Q.B., Huang, Y.Y., Liu, Y.J., Wawrousek, E., et al. (2013). Suppression of neuroinflammation by astrocytic dopamine D2 receptors via α B-crystallin. *Nature* 494, 90–94.
- [3] Yan Y, Jiang W, Liu L, et al. Dopamine controls systemic inflammation through inhibition of NLRP3 inflammasome. *Cell*. 2015;160(1-2): 62-73. doi:10.1016/j.cell.2014.11.047.
- [4] Kok P, et al. Activation of dopamine D2 receptors simultaneously ameliorates various metabolic features of obese women. *Am J Physiol. Endocrinol Metab*. 2006;291: E1038-E1043.
- [5] SYe J, Keller JN. Regulation of energy metabolism by inflammation: a feedback response in obesity and calorie restriction. *Aging (Albany NY)*. 2010;2(6): 361-368. doi:10.18632/aging.100155.
- [6] Wang H, Ye J. Regulation of energy balance by inflammation: common theme in physiology and pathology. *Rev Endocr Metab Disord*. 2015;16(1): 47-54. doi:10.1007/s11154-014-9306-8.
- [7] Beiter, T., Hoene, M., Prenzler, F., Mooren, F. C., Steinacker, J. M., Weigert, C., et al. (2015). Exercise, skeletal muscle and inflammation: ARE-binding proteins as key regulators in inflammatory and adaptive networks. *Exercise immunology review*, 21: 42-57.
- [8] Phillips, M. D., Patrizi, R. M., Cheek, D. J., Wooten, J. S., Barbee, J. J., & Mitchell, J. B. (2012). Resistance training reduces subclinical inflammation in obese, postmenopausal women. *Medicine and science in sports and exercise*, 44(11), 2099-110.
- [9] DhabharFS. The short-term stress response – mother nature’s mechanism for enhancing protection and performance under conditions of threat, challenge, and pportunity. *Frontiers in Neuroendocrinology* 2018 49 175–192. (<https://doi.org/10.1016/j.yfrne.2018.03.004>).
- [10] Petrulli JR, Kalish B, Nabulsi NB, Huang Y, Hannestad J, Morris ED. Systemic inflammation enhances stimulant-induced striatal dopamine elevation. *Transl Psychiatry*. 2017;7(3):e1076. Published 2017 Mar 28. doi:10.1038/tp.2017.18.
- [11] Schwartz AL, Thompson JA, Masood N. Interferon-induced fatigue in patients with melanoma: a pilot study of exercise and methylphenidate. *Oncol Nurs Forum*. 2002;29(7): E85-E90. doi:10.1188/02.ONF.E85-E90.
- [12] Goldfield GS, Lorello C, Doucet E. Methylphenidate reduces energy intake and dietary fat intake in adults: a mechanism of reduced reinforcing value of food? *The American Journal of Clinical Nutrition*. 2007 Aug;86(2): 308-315. doi: 10.1093/ajcn/86.2.308.

- [13] Aga-Mizrachi S, Cymerblit-Sabba A, Gurman O, Balan A, Shwam G, Deshe R et al (2014). Methylphenidate and desipramine combined treatment improves PTSD symptomatology in a rat model. *Transl Psychiatry* 4: e447.
- [14] Oades, R. D., Myint, A. M., Dauvermann, M. R., Schimmelmann, B. G., and Schwarz, M. J. (2010b). Attention-deficit hyperactivity disorder (ADHD) and glial integrity: an exploration of associations of cytokines and kynurenine metabolites with symptoms and attention. *Behav. Brain Funct.* 6:32. doi: 10.1186/1744-9081-6-32
- [15] Bigler MB, Egli SB, Hysek CM, et al. Stress-Induced In Vivo Recruitment of Human Cytotoxic Natural Killer Cells Favors Subsets with Distinct Receptor Profiles and Associates with Increased Epinephrine Levels. *PLoS One.* 2015;10(12): e0145635. Published 2015 Dec 23. doi:10.1371/journal.pone.0145635.
- [16] Disis ML. Immune regulation of cancer. *J Clin Oncol.* 2010;28(29): 4531-4538. doi:10.1200/JCO.2009.27.2146.
- [17] L. H. Hoepfner, Y. Wang, A. Sharma et al., “Dopamine D2 receptor agonists inhibit lung cancer progression by reducing angiogenesis and tumor infiltrating myeloid derived suppressor cells,” *Molecular Oncology*, 9(1): 270-281, 2015.
- [18] Asada M, Ebihara S, Numachi Y, Okazaki T, Yamanda S, et al. Reduced tumor growth in a mouse model of schizophrenia, lacking the dopamine transporter. *Int J Cancer.* 2008;123: 511–518.
- [19] Dhabhar, F. S., Saul, A. N., Daugherty, C., Holmes, T. H., Bouley, D. M., & Oberyszyn, T. M. (2010). Short-term stress enhances cellular immunity and increases early resistance to squamous cell carcinoma. *Brain, Behavior, and Immunity*, 24(1): 127-137.
- [20] Lasheen, W., Walsh, D., Mahmoud, F., Davis, M. P., Rivera, N., & Khoshknabi, D. S. (2010). Methylphenidate side effects in advanced cancer: a retrospective analysis. *The American journal of hospice & palliative care*, 27(1): 16-23. <https://doi.org/10.1177/1049909109345145>.
- [21] Meyers CA, Weitzner MA, Valentine AD, Levin VA. Methylphenidate therapy improves cognition, mood, and function of brain tumor patients. *J Clin Oncol.* 1998;16(7): 2522-2527. doi:10.1200/JCO.1998.16.7.2522.
- [22] Bower JE, Lamkin DM. Inflammation and cancer-related fatigue: mechanisms, contributing factors, and treatment implications. *Brain Behav Immun.* 2013;30 (Suppl):S48–57.
- [23] Comim CM, Pereira JG, Ribeiro SJ, Quevedo J, Boeck CR. Methylphenidate treatment affects mitogen-activated protein kinase activation in the striatum of young rats. *Acta Neuropsychiatr.* 2013;25(4): 235-239. doi:10.1111/acn.12015.
- [24] Oakes, H.V., DeVee, C.E., Farmer, B. et al. Neurogenesis within the hippocampus after chronic methylphenidate exposure. *J Neural Transm* 126, 201–209 (2019). <https://doi.org/10.1007/s00702-018-1949-2>.

- [25] Roesler R, de Farias CB, Abujamra AL, Brunetto AL, Schwartzmann G. BDNF/TrkB signaling as an anti-tumor target. *Expert Rev Anticancer Ther.* 2011;11(10): 1473-1475. doi:10.1586/era.11.150.
- [26] Amigó, S., Caselles, A. and Micó, J.C. Methylphenidate and the Self-Regulation Therapy increase happiness and reduce depression: a dynamical mathematical model. *Modelling for Engineering & Human Behaviour 2018*, 6-9. Valencia (Spain).
- [27] Amigó, S., Caselles, A. and Micó, J.C. (2008). A dynamic extraversion model: the brain's response to a single dose of a stimulant drug. *British Journal of Mathematical and Statistical Psychology*, 61: 211–231. doi:10.1348/000711007X185514.
- [28] Caselles, A., Micó, C., and Amigó, S. (2011). Dynamics of the General Factor of Personality in response to single dose of caffeine. *The Spanish Journal of Psychology*, 14: 675–692. <http://dx.doi.org/10.5209/rev.2011.v14.n2.16>.
- [29] Amigó, S., Caselles, A. and Micó, J.C. Methylphenidate and the Self-Regulation Therapy increase happiness and reduce depression: a dynamical mathematical model. *Modelling for Engineering & Human Behaviour 2018*, 6-9. Valencia (Spain).
- [30] Dockray S, Steptoe A. Positive affect and psychobiological processes. *Neurosci Biobehav Rev.* 2010;35(1): 69-75. doi:10.1016/j.neubiorev.2010.01.006.
- [31] Amigó, S., Caselles, A., Micó, J.C. and García, J.M. (2009). Dynamics of the unique trait of personality: blood's glutamate in response to methylphenidate and conditioning. *Revista Internacional de Sistemas*, 16: 35-40.
- [32] Amigó, S., Caselles, A. and Micó, J. C. (2013). Self-regulation therapy to reproduce drug effects: A suggestion technique to change personality and DRD3 gene expression. *The International Journal of Clinical and Experimental Hypnosis*, 61: 282–304.
- [33] Micó, J.C., Amigó, S. and Caselles, A. (2012). Changing the General Factor of Personality and the c-fos expression with methylphenidate and Self-Regulation Therapy. *The Spanish Journal of Psychology*, 15: 850-867.

New solution for automatic and real time detection of railroad switch failures and diagnosis

Jorge del Pozo^{b1}, Laura Andrés^{b2}, Rafael Femenía^{b3} and Laura Rubio^{b4}

(b) Universitat Politècnica de Catalunya,
(†) Institute of Multidisciplinary Mathematics,
Universitat Politècnica de València.

1 Introduction

Nowadays, the use of railways is being increasingly promoted in Europe and the world. However, its constant evolution towards higher loads, frequencies and speeds can cause affections in the railway infrastructure, generating problems in its elements and track devices, as is the case of the railroad switch (critical track devices to ensure circulation).

The high dynamic forces and the frequent changeover operations carried out on railway switch, make them into elements with a considerably shorter useful life (3 to 5 times) than the rest of the track superstructure and therefore very prone to failure [1].

These failures can have very serious consequences on railway operations, and even lead to derailments (12 % of derailments in Spain are a direct consequence of the railroad switch [2]). Therefore, the maintenance and control of railway switching systems is essential.

Currently, periodic visual inspection of these elements is the most commonly used technique for maintenance, although its effectiveness is low since in the period between two visual inspections the failure of the railroad switch can occur.

For this reason, the objective is the development of a system capable of detecting, diagnosing and predicting defects in railway switch, based on the real-time monitoring of the current curve of the motor of the railroad switch.

2 Methodology

As mentioned above, a system capable of performing predictive maintenance on a railroad switch, in order to detect and diagnose, prematurely, the appearance of different pathologies was developed. Therefore, this section tries to explain the methodology used by the system.

¹e-mail: jorgedelpozo@gmail.com

²e-mail: lauanlo@etsii.upv.es

³e-mail: rafequi@cam.upv.es

⁴e-mail: lauruga1@cam.upv.es

- i.* **Data logging.** This phase is carried out by means of a system of wireless nodes, which includes a current transducer, capable of recording the current curve of the railway switch control system in each of its operations
- ii.* **Data processing.** This phase includes the algorithm necessary for the processing of the data. Two algorithms are used for this:

- **Detection algorithm:** capable of detecting the presence of an anomaly in the operation of the railroad switch, comparing the current consumption curve with a reference curve, taken from the railway switchgear in good condition.

As inputs for this algorithm it is necessary to have the reference curve with its thresholds and the signal monitored in real time by the current sensor. Initially, it was necessary to adapt the experimental signal to the input data of the algorithm (noise removal, compensation of phase shifts between the recorded signal and the reference signal, etc.) From the analysis and processing of these data, the algorithm can provide information on the state of the railroad switch (switch in good condition or switch in bad condition) and the similarity index between both curves. 1 shows a diagram of the process followed:

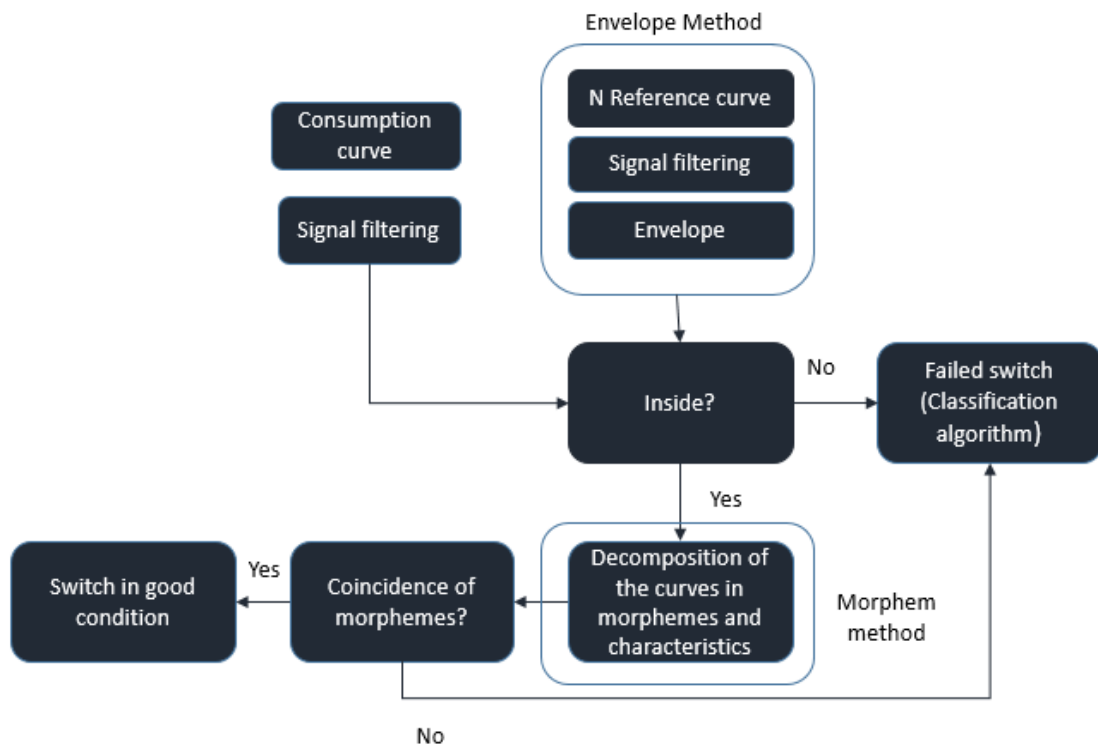


Figure 1: Diagram of detection algorithm. Source: Own self-made

- **Classification algorithm:** once a defect has been detected, the second algorithm developed is responsible for diagnosing the type of failure.

In order to achieve the purpose of this algorithm, it was necessary to introduce as input the current curve measured by the sensor and catalogued “in bad condition” using the previous algorithm. The implemented mathematical model was in charge

of analysing the curve to provide as output a vector with the different probabilities of the existence of one type of defect or another in the curve, identifying in this way the anomaly present in the analysed railroad switch.

To do this, a classification method is proposed to make an intelligent diagnosis of the defect in the railway switchgear using an SVM (support vector machine) methodology, which is based on the theory of statistical learning and the principle of minimum structural risk, applied to small problems.

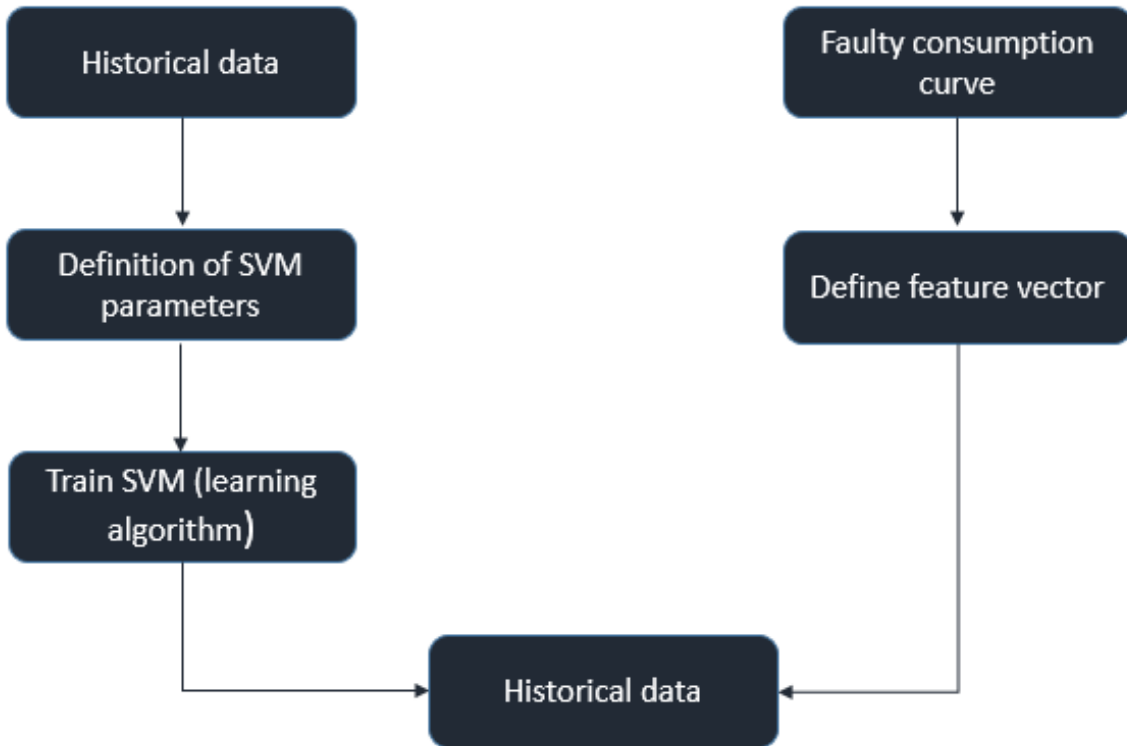


Figure 2: Diagram of classification algorithm. Source: self-made

3 Results and discussion

To verify the correct operation of the system, it was necessary to obtain several records of a railroad switch in good condition in order to obtain the reference curve, as well as different records of the monitoring carried out by the current sensor, in order to make the pertinent comparison between the two and determine the state of the railroad switch.

These data from good railroad switch were used to validate the obtaining of the reference curve and its respective thresholds. Subsequently, it was necessary to take records with the current sensor and use results from scientific studies and current curve simulations to compare these curves with the reference curve obtained from the data provided. With the results of the tests, the system was readjusted and the operation of the system was validated.

Once this point was reached, it was possible to carry out tests in a real environment, where very promising results were obtained from the use of the system, with a very low error rate.

4 Conclusions and future work

The conclusions that can be obtained from the development presented, with a view to directing future work, are the following:

- The system makes it possible to detect and diagnose different types of pathologies on railway switch, based on continuous and real-time monitoring.
- The system allows the implantation of a predictive philosophy to carry out the maintenance of the railway switch, which can mean potential savings in maintenance tasks.
- Economic, simple and easy system to install on the switch rail.

References

- [1] V. C. F. B. S. & S. M. Atamuradov, “Failure diagnostics for railway point machines using expert systems”, 2009.
- [2] García, F.P. “Desarrollo de nuevos algoritmos aplicados al mantenimiento predictivo óptimo centrado en la fiabilidad y la monitorización remota basada en la condición (RCM2)”. Ed. Universidad de Castilla-La Mancha. 2005.

An integrated model to optimize Berth Allocation Problem and Yard Planner

C. Burgos ^{b1}, J. C. Cortés ^b D. Martínez-Rodríguez ^b J. Villanueva-Oller [#] and R. J. Villanueva ^b

(b) Instituto Universitario de Matemática Multidisciplinar.
Universitat Politècnica de Valencia

(#) Escuela Técnica Superior de Ingeniería Informática.
Universidad Rey Juan Carlos, Madrid.

1 Introduction

International trade is considered as the exchange of capital, goods, and services across international borders or territories. It represents a significant share of the gross domestic product of the countries. As a consequence, maritime transport, which is closely related with the international trade, is increasingly in demand. The shipping lines and terminal ports need to improve their operational strategies to fulfill this requirement.

The main objective of VALKNUT project is to model the two main problems that terminal ports are involved on a daily basis. The goal of this contribution is to present these problems and their solutions.

The former problem is named *Berth Allocation Problem (BAP)*. Its main objective is twofold. Firstly, to determine the best berth position to dock the vessel and secondly assigning the appropriate Quay Cranes (QC) to operate it (unload and load). The purpose is to minimize the vessel operating time and the use of resources of the terminal. The later problem, named *Yard Planner*, is about how to organize the yard to optimize the routes of the yard trucks. They are the responsible for loading and unloading the containers in the vessels. The mathematical models of both problems are defined in [1].

Despite both problems are closely related, first, we will study them separately. Then, we will proceed to merge both procedures.

BAP and Yard Planner have been modeled using linear programming. Linear programming is a method used to obtain the best solution of a model whose requirements are represented by linear relationships, named conditions. To obtain the best solution among the candidates, these solutions are evaluated by a specific function, named fitness function, which is the one we have to minimize or maximize.

¹e-mail: clabursi@posgrado.upv.es

2 Modelling Berth Allocation Problem

As it have been pointed out in the Introduction section, the two main objectives of BAP are to organize the arrived vessels in the suitable berth position and to establish the appropriate QC to operate the vessel. This requires to take into account several aspects. The vessel should be berth near to the assigned unload zone in the yard. Also, the vessel should verify the agreement between navy and terminal, SLA, which determines the maximum time the vessel needs to be unload. If the terminal can not afford to verify the SLA, it must pay an economic penalization for the delay. The established berth position can not disturb the proper operation of the other vessels, since they also must to verify their corresponding SLA.

This Section is devoted to describe the model of BAP, [1]. Let us consider that we want to dock the n vessels that arrive at the time interval $[0, H]$. First of all, we assume that the berth is defined by a dock line of length L and it is divided into sectors of length S , see Figure 1. Also, to determine the best QCs, we will consider that they are divided by groups and each one determines different times and different resources to operate the vessel.

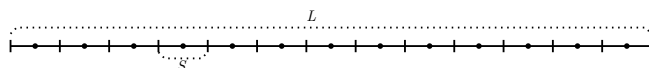


Figure 1: Representation of the berth layout considered in this modelling.

Once the berth is defined the following information for each vessel, b_i $1 \leq i \leq n$ is required:

- Length of vessel.
- Theoretical arrival time.
- Theoretical departure time.
- Minimum time the vessel can arrive and their penalization.
- Maximum time the vessel can departure and their penalization.
- QC groups available to operate b_i and its corresponding time of operation. Note that not all the QC groups can operate all the vessels.

With these information, and minimizing on one hand, the penalization given by the non-verification of the SLA and, on the other hand, the resources of the terminal, the model give us for each vessel the suitable group of QC to operate the vessel, the best berth position the vessel has to be docked and the time the vessel begins and finish to operate.

However, in order to obtain meaningful solutions, some restrictions, described in [1], have to be imposed in the model. The most important are detailed as follows:

- Only one quay profile assigned to each vessel.
- The amount of quay cranes operating at the same time not exceed the total amount of cranes.
- Each vessel begins to operate at one time instant.

- There are not conflict of space and time of two vessels.
- All the vessels moor within the length of the wharf.

In Figure 2, a possible planning of BAP is illustrated. The squares represent the vessels. The Y axis the berthing line, and the X axis the time, being H the planning horizon and E the time the last vessel needs to be operated.

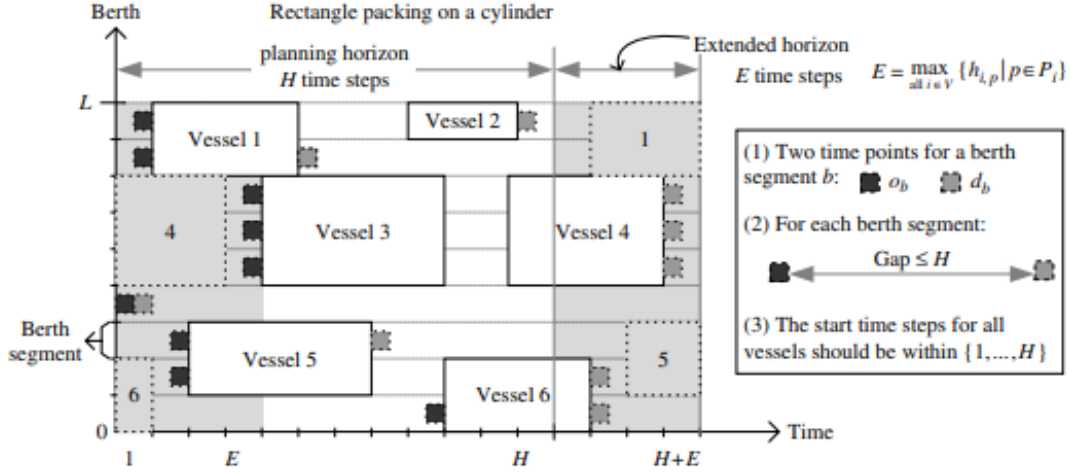


Figure 2: Arbitrary planning for BAP.

2.1 Numerical example

This subsection is devoted to illustrate the above model with a numerical example. Let us consider we want to plan 3 vessels that arrive at the time interval $[0, 10]$. The length of the berth is 150 m and it is divided into three segments of length 50 m . Table 1 collects the available information for each vessel.

	b_1	b_2	b_3
Length	70	90	90
Theoretical arrival time	5	5	3
Feasible arrival time	4	4	3
Penalization arrival time	1.2	1.1	1.15
Theoretical departure time	7	7	9
Feasible departure time	8	8	10
Penalization departure time	1.5	1.7	1.6
Quay crane profiles / unload time	2/1,1/2	2/1,1/2	3/1, 2/2, 1/3

Table 1: Available information for each vessel.

Executing BAP model, the best planning is detailed in Table 2. As it can be seen, the obtained results are in accordance with the physical limitations of the terminal and there are not overlapping between the berth position and times of different vessels.

	b_1	b_2	b_3
Berth position	85	45	85
Time the vessel begins to operate	7	5	3
Time the vessel ends to operate	8	7	4
Selected QC profile / unload time	2/1	1/2	1/3

Table 2: Solution of BAP in the context of Example 2.1

3 Modelling Yard Planner

This section is devoted to describe the modelling of Yard Planner. Its main objective is to establish the best zone of the yard the vessel may unload and load their containers in order to minimize the routes of the yard trucks.

First of all, let us define the topology of the yard. It is divided into blocks and each one is also divided into subblocks. The blocks are separated between them by a passing lane. The passing lane has one direction, thus, the trajectories from the vessels to the yard subblocks in loading and in unloading direction are different. Two subblocks are neighbours if they are positioned one in front of each other. In the modelling process, two neighbours subblocks can not be operated at the same time. Figure 3 illustrates an arbitrary topology of the yard. As we can see, K_1 and K_{21} are neighbours subblocks.

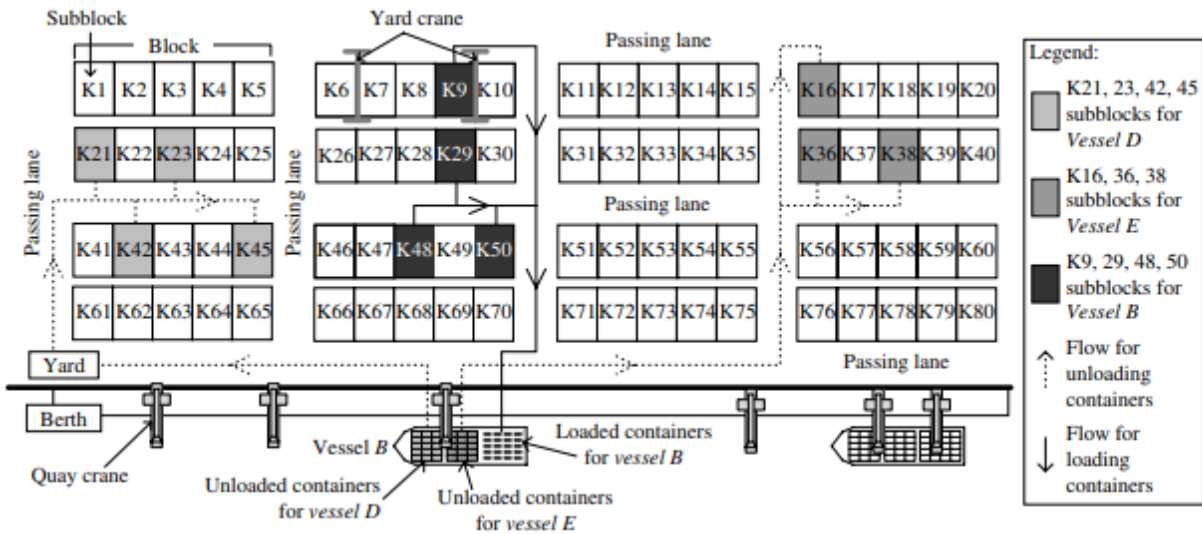


Figure 3: Arbitrary topology for a terminal yard.

To execute this model, we need the following information for each vessel b_i $1 \leq i \leq n$ obtained by BAP.

- Vessel berth position.
- Time the vessel begins to operate.

Also, it is necessary the following information for the terminal yard:

UD	S_1	S_2	S_3	S_4	S_5	S_6	S_7	S_8	S_9	S_{10}
b_1	100	120	140	160	180	100	120	140	160	180
b_2	150	170	190	210	230	150	170	190	210	230
b_3	200	220	240	260	280	200	220	240	260	280

 Table 3: Unload distances in m for vessels described in Table 1.

LD	S_1	S_2	S_3	S_4	S_5	S_6	S_7	S_8	S_9	S_{10}
b_1	280	260	240	220	200	280	260	240	220	200
b_2	230	210	190	170	150	230	210	190	170	150
b_3	180	160	140	120	100	180	160	140	120	100

 Table 4: Load distances in m for vessels described in Table 1.

- Yard organization, blocks and subblocks.
- Subblocks neighbours from others.
- Amount of subblocks each vessel needs.
- UD: Distance of each vessel to each subblock in uploading direction.
- LD: Distance of each vessel to each subblock in loading direction.

With these inputs and minimizing the routes of yard trucks, the model is able to establish the suitable subblocks for each vessel. However, restrictions in the model formulation must be imposed to obtain realistic solutions. The most important are:

- Each subblock is reserved for one vessel.
- There is a fixed quantity of subblocks for each vessel.
- Two neighbour subblocks can not be operate at the same time.
- For each block there is only one subblock operating at the same time.

3.1 Numerical example

The main objective of this subsection is to illustrate with a numerical example the model described in this Section. Let us consider we want to assign the best subblocks for the three vessels studied in Example 2.1. Each vessel needs two subblocks to unload the containers. The yard is composed by two blocks and each one is divided into five subblocks. The topology of the yard is illustrated in Figure 4, we can observe that the neighbour subblocks are S_1 and S_6 , S_2 and S_7 , S_3 and S_8 , S_4 and S_9 and S_5 and S_{10} . The distance of the vessels to each subblock in unload and load direction are collected in Tables 3 and 4, respectively. Executing the Yard Planner model, the best established subblocks for b_1 are subblocks S_2 and S_6 , for b_2 subblocks S_1 and S_7 and for b_3 , subblocks S_3 and S_{10} . In Figure 5 we can see a coloured representation of this solution.

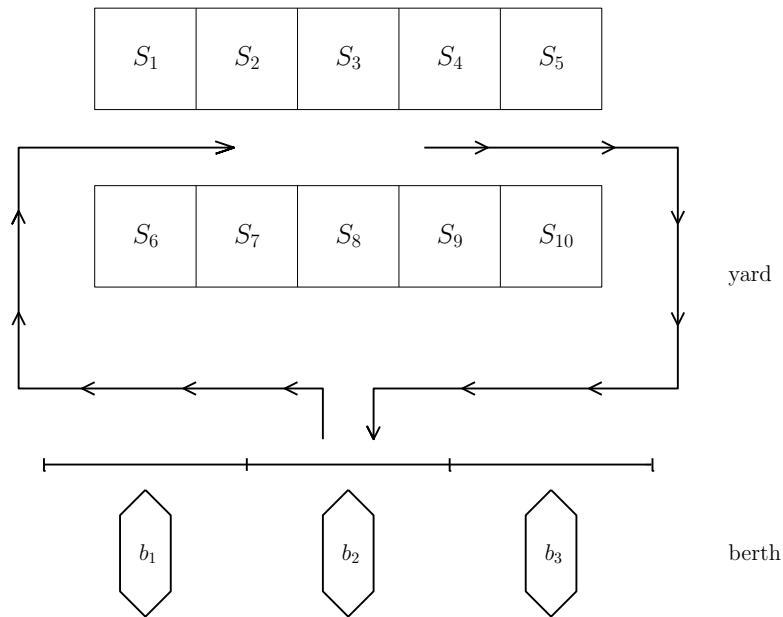


Figure 4: Topology for the yard in the context of Example 3.1.

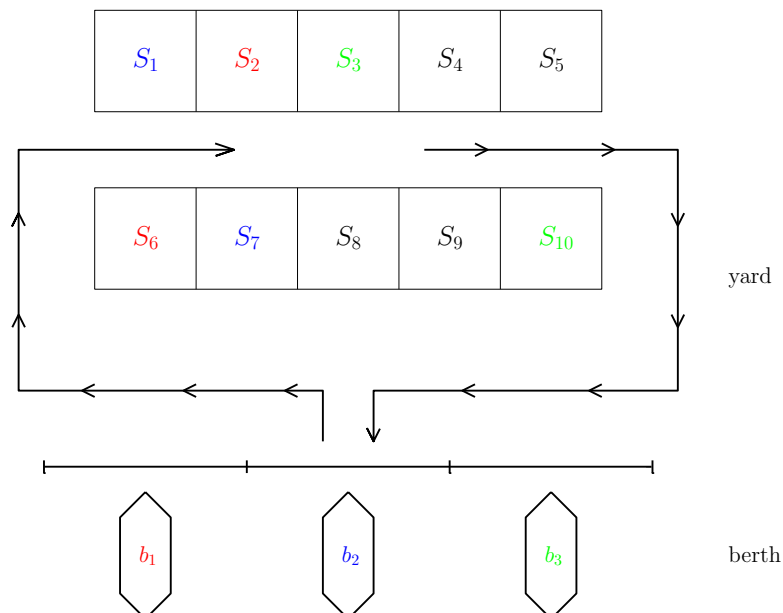


Figure 5: Solutions of the Yard Planner in the context of Example 3.1. S_3 and S_{10} (red) correspond to b_1 , S_1 and S_7 (blue) to b_2 and S_3 and S_{10} (green) to b_3 .

4 Combination of both models

In this contribution, both problems have modelled independently. However, they are closely related. On the one hand, to find the best vessel berthing position, it is required to specify the assigned subblocks to unload the vessel. On the other hand, to find the suitable subblock of the yard, it is important to know the berthing position for the vessel. To deal with this dependence, in [1] the authors solve first the *BAP* assuming arbitrary subblocks of the yard assigned to the vessel. Then, with the information obtained in the first problem, *Yard Planner* is solved. In this second problem, a set of subblocks are assigned from each vessel. This information is used to solve BAP again. Iterating these steps, we can establish the best dock to berth the vessel and the best zone of the yard to unload the containers.

Acknowledgements

This work has been partially supported by the Ministerio de Economía y Competitividad grant MTM2017-89664-P and by the Ministerio de Ciencia, Innovación y Universidades (Retos Colaboración 2017) grant RTC-2017-6566-4, “VALKNUT”.



References

- [1] Zhen, L., Chew, E. P., and Lee, L. H. (2011). An integrated model for berth template and yard template planning in transshipment hubs. *Transportation Science*, 45(4), 483-504.

Dynamical analysis of a new three-step class of iterative methods for solving nonlinear systems

Raudys R. Capdevila^{b1}, Alicia Cordero^b and Juan R. Torregrosa^b

(b) Instituto de Matemática Multidisciplinar, Universitat Politècnica de València,
Camino de Vera s/n, 46022 València, Spain.

1 Introduction

The main problem is to find the solution of the nonlinear equations system $F(x) = 0$, with n unknowns and n equations, where $F : D \subset \mathbb{R}^n \rightarrow \mathbb{R}^n$ is a sufficiently Fréchet differentiable multivariate function. The solution of this task can be obtained as fixed-point of some function $G : \mathbb{R}^n \rightarrow \mathbb{R}^n$ by means of the fixed-point iteration method with the general form

$$x^{(k+1)} = G(x^{(k)}), \quad k = 0, 1, \dots,$$

being $x^{(0)}$ the initial estimation.

The classical Newton's method [1] reaching the second order convergence is the most popular, although in mathematical literature we can find other methods with higher order and addressing different techniques like: Adomian decomposition [2], multi-point methods free from second derivative [3] and weight function techniques [4]. Once a class of methods has been designed, it is necessary to carry out a multidimensional real dynamical study (see [5]) in order to obtain the most suitable parameters for setting stable schemes. In this work we present a real multidimensional dynamical analysis of one iterative family of three steps, derived from a class of sixth convergence order. This class is based on weight functions techniques and was presented by the authors in [6].

1.1 The iterative family and basical definitions

Being F a real Fréchet differentiable enough function and $H : \mathbb{R}^{n \times n} \rightarrow \mathbb{R}^{n \times n}$ a matrix weight function with a variable $t^{(k)} = I - [F'(x^{(k)})]^{-1}[x^{(k)}, y^{(k)}; F]$, the following class of iterative schemes was designed in [6]

$$\begin{aligned} y^{(k)} &= x^{(k)} - [F'(x^{(k)})]^{-1}F(x^{(k)}), \\ z^{(k)} &= y^{(k)} - H(t^{(k)})[F'(x^{(k)})]^{-1}F(y^{(k)}), \\ x^{(k+1)} &= z^{(k)} - H(t^{(k)})[F'(x^{(k)})]^{-1}F(z^{(k)}), \quad k \geq 0. \end{aligned} \tag{1}$$

¹e-mail: raucapbr@doctor.upv.es

Let $X = \mathbb{R}^{n \times n}$ denote the Banach space of real square matrices of size $n \times n$, function $H : X \rightarrow X$ can be defined such that the Fréchet derivative satisfies

$$(a) \quad H'(u)(v) = H_1uv, \text{ where } H' : X \rightarrow \mathcal{L}(X) \text{ and } H_1 \in \mathbb{R},$$

$$(b) \quad H''(u, v)(v) = H_2uvw, \text{ where } H'' : X \times X \rightarrow \mathcal{L}(X) \text{ and } H_2 \in \mathbb{R}.$$

Is necessary remark that, when k tends to infinity, then variable $t^{(k)}$ tends to the identity matrix I . So, there exist real H_1, H_2 such that H can be expanded around I as

$$H(t^{(k)}) = H(I) + H_1(t^{(k)} - I) + \frac{1}{2}H_2(t^{(k)} - I)^2 + O((t^{(k)} - I)^3).$$

The convergence analysis made in [6] is summarized in the following result.

Theorem 1 *Let $F : D \subseteq \mathbb{R}^n \rightarrow \mathbb{R}^n$ be a sufficiently Fréchet differentiable function in an open neighborhood D of $\xi \in \mathbb{R}$ such that $F(\xi) = 0$, and $H : \mathbb{R}^{n \times n} \rightarrow \mathbb{R}^{n \times n}$ a sufficiently differentiable matrix function. Assume that $F'(x)$ is non singular at ξ and $x^{(0)}$ is an initial value close enough to ξ , then the sequence $\{x^{(k)}\}_{k \geq 0}$ obtained from expression (9) converges to ξ with order 6 if $H_0 = I, H_1 = 2$ and $|H_2| < \infty$, where $H_0 = H(0)$ and I is the identity matrix, being its error equation*

$$e^{(k+1)} = \frac{1}{4}[(H_2^2 - 22H_2 + 120)C_2^5 + (-24 + 2H_2)C_2^2C_3C_2 + (-20 + 2H_2)C_3C_2^3 + 4C_3^2C_2]e^{(k)6} + O(e^{(k)7}), \text{ where } C_q = \frac{1}{q!}[F'(\xi)]^{-1}F^{(q)}(\xi), q = 2, 3, \dots$$

The weight function is chosen as $Y(t) = I + 2t + \frac{1}{2}\alpha t^2$ where $\alpha \in \mathbb{R}$. This function satisfies hypothesis of the Theorem 1 conditions and by substitution in (1), a new one-parameter family is then obtained which will be called as PSH_6 .

$$\begin{aligned} y^{(k)} &= x^{(k)} - [F'(x^{(k)})]^{-1}F(x^{(k)}), \\ z^{(k)} &= y^{(k)} - \left[I + 2t^{(k)} + \frac{1}{2}\alpha t^{(k)2} \right] [F'(x^{(k)})]^{-1}F(y^{(k)}), \\ x^{(k+1)} &= z^{(k)} - \left[I + 2t^{(k)} + \frac{1}{2}\alpha t^{(k)2} \right] [F'(x^{(k)})]^{-1}F(z^{(k)}), \quad k \geq 0. \end{aligned} \quad (2)$$

By denoting G like a vectorial fixed-point function associated to the some iterative method and acting on a general function $F : D \subseteq \mathbb{R}^n \rightarrow \mathbb{R}^n$, we define the orbit of $x^{(0)}$ like a set of the successive images by G of the latter: $\{x^{(0)}, G(x^{(0)}), \dots, G^m(x^{(0)})\}$. The dynamical behavior of a point $x \in \mathbb{R}^n$ can be classified examining its asymptotic performance, thus the point x^* such that $G(x^*) = x^*$ is denominated a fixed point of G . In the same way, a periodic point x of period $k \geq 1$ is one that $G^k(x) = x$ and $G^{k-p}(x) \neq x$, for $p < k$. Some results about stability of fixed points are summarized in the theorem ([7], page 558).

Theorem 2 *Let $G : \mathbb{R}^n \rightarrow \mathbb{R}^n$ be \mathcal{C}^2 . Assume x^* is a period- k point. Let $\lambda_1, \lambda_2, \dots, \lambda_n$ be the eigenvalues of $G'(x^*)$.*

a) *If all the eigenvalues λ_j satisfy $|\lambda_j| < 1$, then x^* is attracting.*

b) *If one eigenvalue λ_{j_0} holds $|\lambda_{j_0}| > 1$, then x^* is unstable, that is, repelling or saddle.*

c) If all the eigenvalues λ_j satisfy $|\lambda_j| > 1$, then x^* is repelling.

The fixed point whose all eigenvalues have $|\lambda_j| \neq 1$ are called hyperbolic, it is a saddle hyperbolic point if some eigenvalues have $|\lambda_{j0}| > 1$ and the rest have $|\lambda_{j0}| < 1$. If the fixed point is not a root of $F : D \subseteq \mathbb{R}^n \rightarrow \mathbb{R}^n$ then is called a strange fixed point and its stability is classified according to the Theorem 2.

Additionally, if x^* is an attracting fixed point of the rational function G , we can define its basin of attraction $\mathcal{A}(x^*)$ like the set of pre-images of any order such that

$$\mathcal{A}(x^*) = \{x^0 \in \mathbb{R}^n : G^m(x^0) \rightarrow x^*, m \rightarrow \infty\}.$$

2 Results and discussion

In this section we realize the dynamical study of the family PSH_6 acting on the function $p(x) = \{x_1^2 - 1, x_2^2 - 1\}$ applying the previous concepts and a set of real multidimensional discrete dynamical tools.

2.1 Stability analysis of the iterative family acting on $p(x)$

By applying the iterative expression of PSH_6 on the polynomial system $p(x) = 0$, we obtain its rational multidimensional operator associated $U = \{u_1(x, \alpha), u_2(x, \alpha)\}$, whose the j th coordinate is

$$u_j(x, \alpha) = \frac{1}{256x_j^7} \left(\alpha (-1 + x_j^2)^4 - 16 (x_j^2 - 5x_j^4 + 15x_j^6 + 5x_j^8) + 4x_j^2 (\alpha(-1 + x_j^2) + 16x_j^2(-1 + 3x_j^2)) \right. \\ \left. (-1 + (1/65536x_j^{14}) (\alpha(-1 + x_j^2)^4 - 16(x_j^2 - 5x_j^4 + 15x_j^6 + 5x_j^8))^2) \right), \quad j = 1, 2. \quad (3)$$

By analyzing expression $u_j(x, \alpha) = x_j$, it is possible to formulate the following results about the stability of fixed points related to the iterative family (2).

Theorem 3 *The rational function $U(x, \alpha)$ associated to the family of iterative methods (2) has the superattracting fixed points $(1, 1), (1, -1), (-1, 1), (-1, -1)$ roots of the polynomial $p(x)$, and the real strange fixed points due to the pairs (l_i, l_j) for $i, j \leq 18$, whose entries are the roots of polynomial*

$$l(x, \alpha) = (-\alpha^3 + (\alpha^3 - 112\alpha^2 + 15104\alpha + 3190784) x^{18} + (9\alpha^3 + 32\alpha^2 + 80128\alpha - 2146304) x^{16} \\ + 4(9\alpha^3 + 520\alpha^2 + 43712\alpha + 437248) x^{14} + 4(21\alpha^3 + 1512\alpha^2 + 50240\alpha - 237568) x^{12} \\ + 2(63\alpha^3 + 4000\alpha^2 + 64640\alpha + 149504) x^{10} + 2(63\alpha^3 + 2864\alpha^2 + 22912\alpha - 24576) x^8 \\ + 4(21\alpha^3 + 568\alpha^2 + 2112\alpha + 1024) x^6 + 12\alpha(3\alpha^2 + 40\alpha - 64) x^4 + 3\alpha^2(3\alpha + 16)x^2),$$

and the real strange fixed points composed by the roots of polynomials $p(x)$ and $l(x)$, depending on α :

- i) If $\alpha \in (-\infty, -93.210875) \cup (0, 327.44373142)$ then, the set of all strange fixed points \mathcal{A} is composed by four repulsive and eight saddle points.
- ii) If $\alpha \in (327.44373142, 369.97117)$ then, there are twelve attracting strange fixed points, sixteen repulsive strange fixed points and forty saddle fixed points.
- iii) If $\alpha \in (\alpha^*, \infty)$ then, there are twenty repulsive strange fixed points and twenty four saddle fixed points.

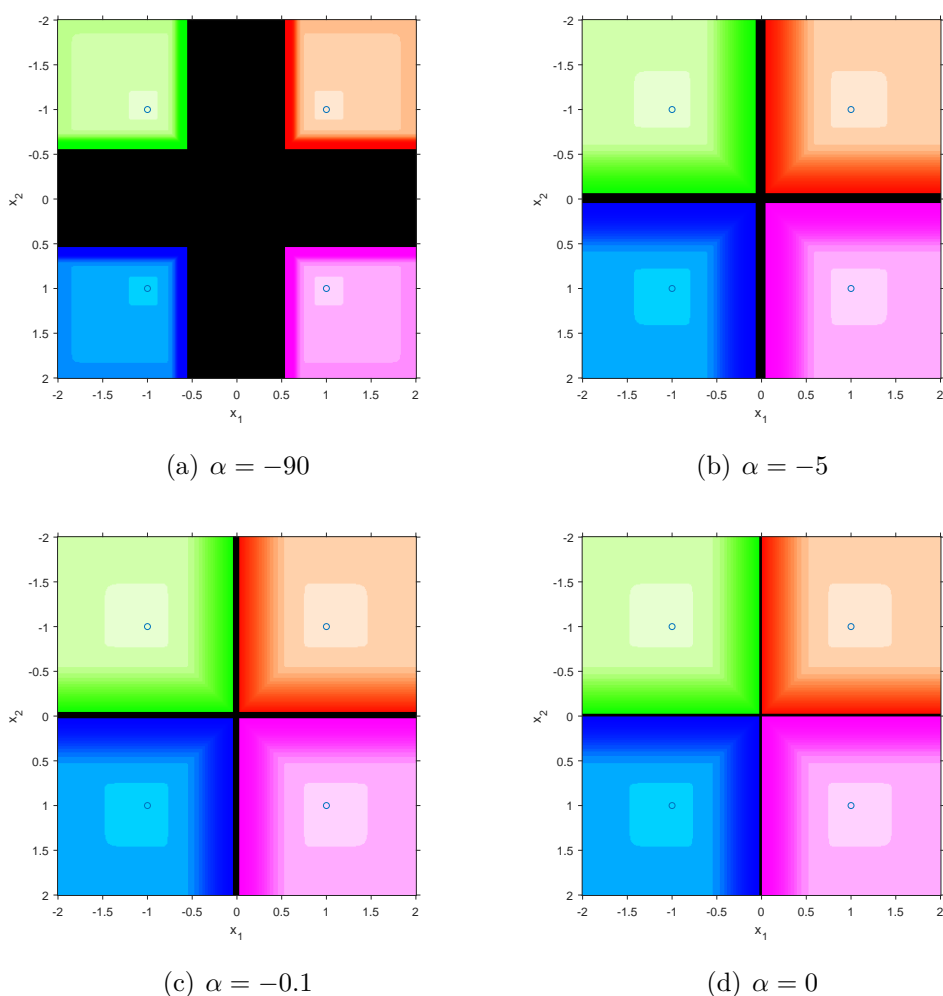


Figure 1: Stable dynamical planes in the safety domain $\alpha \in [-93.210875, 0]$

Given the results of Theorems 3 we state the domain of $\alpha \in [-93.210875, 0]$ where not exist neither real strange fixed points, hence stable dynamical behavior can be found. In Figure 1 some dynamical planes are showed related with the later domain. We have built a mesh with step equal to 0.01, every initial estimation is iterated 100 times as long as there is no convergence to one of the roots of $p(x)$ with an error equal to 10^{-3} .

The color of the points in mesh are painted depending of the roots (represented with circles) to which their converge and color is brighter when lesser are the iterations. If all the iterations are completed and no convergence to any roots is reached, then the point is painted in black.

We can see in Figure 1 the basins of attraction of every roots and how the black areas of no convergence are narrower as the α parameter increases.

3 Conclusions and future work

In this work with the use of real multidimensional tools, a first glance of the real stability of the elements of family PSH_6 of iterative methods has been studied for quadratic polynomial systems.

As future work we propose the study of the existence and behavior of critical points as well as that of periodic or strange attractors.

Acknowledgements

This research was partially supported by PGC2018-095896-B-C22 (MCIU/AEI/FEDER, UE).

References

- [1] Ortega, J. M., W. C. Rheinholdt, Iterative solution of nonlinear equations in several variables, Academic Press, New York, 1970.
- [2] Babolian, E., Biazar, J., Vahidi, A. R., Solution of a system of nonlinear equations by Adomian decomposition method *Applied Mathematics and Computation*, Volume(150): 847–854, 2004
- [3] Hernández, M. A., Second-derivative-free variant of the Chebyshev method for nonlinear equations *Journal of Optimization Theory and Applications* , Volume(104): 501–515, 2000
- [4] Sharma, J. R., Guha, R. K., Sharma, R., An efficient fourth-order weighted-Newton method for systems of nonlinear equations *Numerical Algorithms* , Volume(62): 307–323, 2013
- [5] Cordero, A., Soleymani, F., Torregrosa, J. R., Dynamical analysis of iterative methods for nonlinear systems or how to deal with the dimension ? *Applied Mathematics and Computation* , Volume(244): 398–412, 2014
- [6] Capdevila, R., Cordero, A., Torregrosa, J. R., A new three-step class of iterative methods for solving nonlinear systems *Mathematics*, 2019, 7, 1221 doi:10.3390/math/121221: 1-14, 2019
- [7] Robinson, R. C., An Introduction to Dynamical Systems, Continuous and Discrete, Providence, Americal Mathematical Society, RI, USA, 2012.

Integrating the human factor in FMECA-based risk evaluation through Bayesian networks

S. Carpitella ^{b1}, J. Izquierdo[‡], M. Plajner^b and J. Vomlel^b

(b) Department of Decision-Making Theory, Institute of Information Theory and Automation (UTIA) - Czech Academy of Sciences, Pod Vodárenskou věží 4, CZ 18208 Prague 8, Czech Republic,

(‡) Fluing-Institute for Multidisciplinary Mathematics (IMM),
Universitat Politècnica de València, Cno. de Vera s/n, 46022 Valencia, Spain.

1 Introduction and objectives

Risk management processes play a fundamental part in any business context and rely on accurate conduction of the risk assessment stage. Risks are commonly evaluated according to the preliminary definition of suitable parameters mainly aimed at highlighting their severity and the frequency of occurrence. However, it may be interesting to integrate the human factor as a parameter of evaluation, being human activity directly related with many risks of diverse nature. This contribution develops the traditional Failure Modes, Effects and Criticality Analysis (FMECA) [1] for quantitative risk analysis from a Bayesian Network (BN)-based perspective, which reveals to be useful to make more accurate predictions about parameters' values. The main purpose consists in providing a framework for analysing causal relationships for risk evaluation and deriving probabilistic inference among significant risk factors. These parameters are represented by linguistic variables and include the human factor as a key element of analysis.

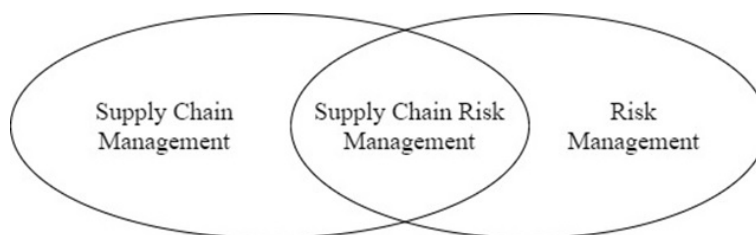


Figure 1: Supply chain risk management definition inspired in [13].

To substantiate this idea, we present and solve a real-world use case on a fundamental business topic, namely supply chain risk management (SCRM), which originates from the intersection between the processes of risk management and supply chain management [13], as exemplified in Figure 1. This choice is further motivated by the fact that FMECA has been recently extended to supply chain risk evaluation [14], currently being a lively topic of research.

¹e-mail: carpitella@utia.cas.cz

2 The proposed approach

Traditional approaches for risk evaluation and management performed by FMECA represent helpful tools to globally enhance systems and processes conditions [2]. However, such approaches require previous clarification of several assumptions/simplifications [3]. FMECA is a systematic procedure to identify and analyse all the failure modes potentially involving systems or their main components, through the definition of the related causes and effects. In particular, the method aims to prioritise the failure modes under analysis by calculating the index called Risk Priority Number (*RPN*) for each of them. The *RPN* is traditionally derived from the multiplication of three main factors, namely severity (*S*), occurrence (*O*) and detection (*D*), generally ranged within discrete intervals. Severity *S* measures the impact of a given failure mode with respect to the global performance; occurrence *O* estimates the frequency of a failure mode within a given time horizon; detection *D* expresses the probability of correct failure identification. The three risk factors are commonly assessed in a qualitative and subjective way, what may lead to imprecise results with the consequent adoption of ineffective decisions in terms of preventive and/or mitigation actions. This assumption represents one of the reasons why the traditional *RPN* has been widely criticized in the literature. The *RPN* formula appears far too simplistic [4,5], since it does not consider the different importance of the three aforementioned parameters [6,7], i.e. different weights in evaluating risks. Other studies underline as the non-continuous distribution of the values of the *RPN* makes imprecise the assessment of differences between two consecutive values assumed by the index [4,8]. Apart from other various drawbacks, one has to observe as FMECA does not consider the simultaneous occurrence of multiple failure scenarios.

A BN-based approach can provide a wider range of benefits in risk analysis, in terms of modelling complex systems, making accurate predictions about parameters' values, and computing with precision the occurrence probability of failure events [9]. A BN is a compact and modular distribution of random variables. A BN is an acyclic graph in which variables are placed at the nodes, and the arcs are loaded with probabilities [10,11]. A BN is a twofold object: it has a qualitative aspect, i.e. the graph showing the mainly cause-effect relationships, and the quantitative distribution of probabilities [12]. In a BN, evidence information propagates and updates our belief (*a priori* probability) on non-observed variables to get new (*a posteriori*) knowledge. This is an objective of inference, including diagnosis, prediction, inter-causal relationships, etc. Conditional probabilities (and the structure itself) can be learnt from data. In this sense, BNs constitute optimal decision-making tools, which also enable simulation to observe outcomes derived from a range of actions. BNs rely on identifying relations of conditional independence; determining conditional probability tables and joint probability distributions, and performing inference: calculating *a posteriori* probabilities, \mathbf{P} , for variables of interest, \mathbf{X} , given observed values of some variables or evidence, \mathbf{e} , still considering hidden variables, \mathbf{Y} :

$$\mathbf{P}(\mathbf{X}|\mathbf{e}) = \alpha \mathbf{P}(\mathbf{X}, \mathbf{e}) = \alpha \sum_{\mathbf{y}} \mathbf{P}(\mathbf{X}, \mathbf{e}, \mathbf{y}).$$

Here α is a normalizing factor, and $\mathbf{P}(\mathbf{X}|\mathbf{e})$ expresses the (vector) probability of variables in vector \mathbf{X} , given the (vector) evidence \mathbf{e} .

We finally propose to consider new aspects with respect to those traditionally used for the *RPN* calculation. Specifically, the role played by human resources will be integrated within the risk function calculation, something that existing approaches scarcely take into

account. Our objective is to integrate the human factor in FMECA-based risk assessment, taking advantage of BNs' ability for inference, which incorporates uncertainty, thus enabling to obtain valuable information for risk assessment to help decision-making processes in planning, operating, maintenance etc. in industry, and other fields.

Risks are herein quantitatively assessed on the basis of evaluations attributed to severity and occurrence probability, two of the three parameters considered by the traditional FMECA approach. Instead of considering the probability of detection as a third risk parameter, we introduce a new factor for risk evaluation as a novelty within the framework of traditional FMECA. This factor is linked to the concept of human error probability. By synthesising the degree of human experience, professional training, skills, and work-related stress when leading a given task, this factor considers the presence of human resources in charge of specific activities.

All the three considered risk parameters, namely severity (S), occurrence (O) and human factor (H), will be evaluated by means of a five-point scale. The higher/lower the evaluation of these parameters, the higher/lower the contribution to the risk function.

3 Real-world application

We consider a problem of SCRM involving the warehouse design and management for a real manufacturing company located in the south of Italy. The decision-making problem consists in optimising new procedures of warehouse operations as well as best practices to cope with the safety updates established by the COVID-19 protocol [15], and to pursue process automation and operational efficiency.

Ten major supply chain risks (SCRs) potentially impacting the warehouse reorganisation problem have been identified and various brainstorming sessions have been led to carry on the assessment process. To this end, a decision-making group made of twenty stakeholders was involved. Decision-makers were grouped into five main categories based on their roles: manager, responsible, worker (warehouse), worker (production), worker (external area). To exemplify the procedure of input data collection, Table 1 shows the evaluations provided by the responsible of the safety and security system, one of the experts belonging to the "responsible" category.

Table 1: SCRs and factors evaluations from the responsible of the safety and security system

ID	SCR	S	O	H	Score
SCR ₁	Safety	5	3	2	3
SCR ₂	Damages	2	2	2	2
SCR ₃	Communication	4	3	1	2
SCR ₄	Transportation	3	2	2	2
SCR ₅	Commerce	2	3	2	2
SCR ₆	Performance	4	2	1	2
SCR ₇	Disruptions	5	2	1	2
SCR ₈	Delivery	3	2	2	2
SCR ₉	Environment	4	4	3	4
SCR ₁₀	Strategy	3	3	2	3

Integer geometric mean values of the evaluations for the three risk parameter have been computed as a score (global risk value) associated to each SCR for the given decision-maker.

We aim to exploit the ability of BNs to model variables and their interconnected structure by identifying relations of conditional independence, and determining their conditional probability table as well as their joint probability distribution in order to eventually develop a Bayesian network integrating the human factor in FMECA-based risk assessment. Figure 2 and Figure 3, respectively, show the final network of relations, and the incorporation of evidence into the BN. Results have been obtained by iterating the BIC algorithm through the Hugin software for BN learning. One can note, both SCRs and decision-makers' roles are considered as variables in the network.

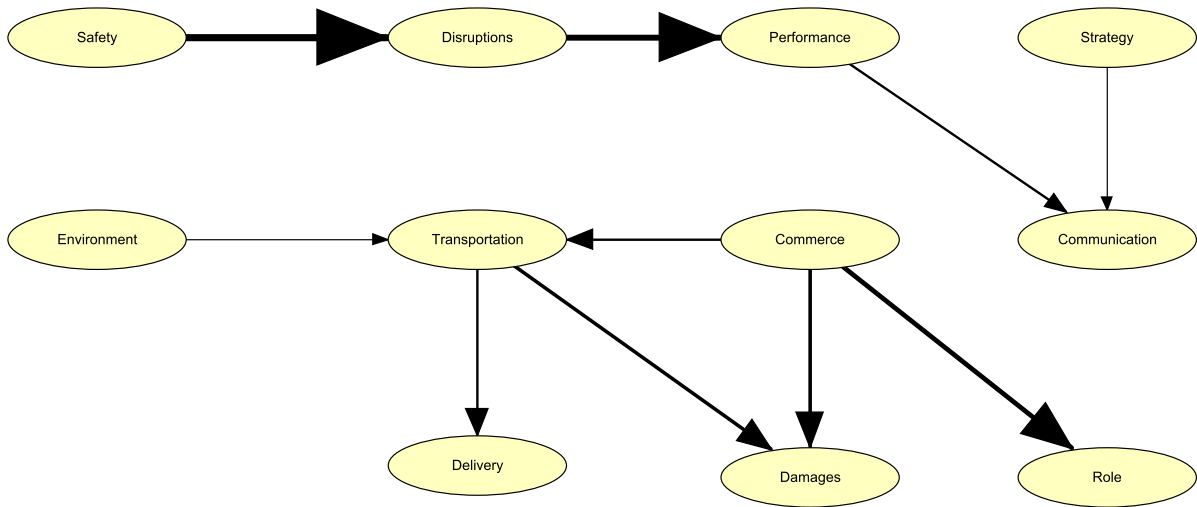


Figure 2: Network of relationships

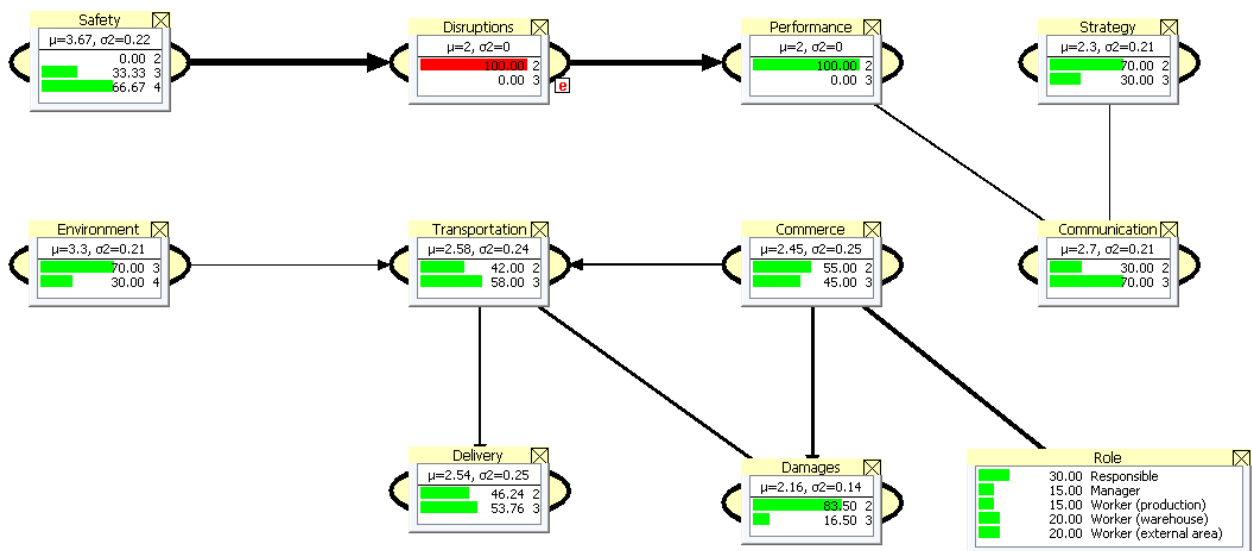


Figure 3: Entering evidence into the BN

4 Discussion of results

We can derive various considerations by observing results reported in the final network. First of all, we point out the existence of two main groups of SCRs in terms of dependence as well as the presence of stronger mutual relations, highlighted by the thickness of the arrows.

Immediate practical implications are described as follows. Safety and disruptions risks are highly related but inversely whereas significant relations between other risks (such as for instance between disruptions and performance or among transportation, commerce and damages) are directly proportional. This result is justified by the fact that, the occurrence of a disruption implies the temporary breakdown of operational activities, what minimises risks for human safety. Safety risks are instead higher in absence of disruptions, that is when loading and unloading operations are carried out in continuum.

Another important result refers to the relation of dependence between the variable "role" and commercial risks. Differently from other types of risks, for which evaluation is more objective and independent on the role of the decision-maker who is expressing opinions, commercial risks are role-sensible; in other terms, differently perceived by managers, responsible human resources and workers. This consideration leads to the fact that decision-makers belonging to different categories will attribute significantly different evaluations to the parameters related to commercial risks and/or unpredictable price raises. Managers typically associate them with higher values; responsible subjects, medium values; and workers, lower values.

Lastly, we can observe as environment risks contemplating the high degree of uncertainty enterprises are experiencing during the COVID-19 era are mainly related with transportation difficulties, which are, in their turn, connected with such fundamental logistic aspects as commercial problems, packaging damages and inefficient delivery.

5 Conclusions and future work

This contribution is focused on the importance of leading an accurate risk assessment in order to proceed towards an effective risk management. The traditional FMECA analysis has been presented as the most common way for risk evaluation purposes on the basis of the *RPN* index for each identified risk. The possibility of integrating the human factor under a BN-based perspective has been discussed and a use case on SCRM has been solved by showing the presence of significant dependence among the considered variables.

Future developments of the present work of research regard the possibility of considering diverse scenarios of risk evaluation. For example, several decision-makers of different enterprises may be involved to generalise the process of supply chain risk evaluation for a given industrial sector of activity. Moreover, different weights may be attributed to the considered risk factors by integrating a multi-criteria decision-making approach. Also, networks resulting from different algorithms may be compared.

References

- [1] I. E. Commission, Analysis Techniques for System Reliability: Procedure for Failure Mode and Effects Analysis (FMEA). International Electrotechnical Commission, 2006.

-
- [2] Curkovic, S., Scannell, T., Wagner, B. Using FMEA for supply chain risk management *Modern management science & Engineering*, 1(2):251–265, 2013.
- [3] Flage, R., Askeland, T. Assumptions in quantitative risk assessments: when explicit and when tacit? *Reliability Engineering & System Safety*, 106799, 2020.
- [4] Liu, H.-C., Liu, L., Liu, N., Mao, L.-X. Risk evaluation in failure mode and effects analysis with extended VIKOR method under fuzzy environment *Expert Systems with Applications*, 39(17):12926–12934, 2012.
- [5] Liu, Y., Fan, Z.-P., Yuan, Y., Li, H. A FTA-based method for risk decision-making in emergency response *Computers & Operations Research*, 42:49–57, 2014.
- [6] Zhang, Z., Chu, X. Risk prioritization in failure mode and effects analysis under uncertainty *Expert Systems with Applications*, 38(1): 206–214, 2011.
- [7] H.-C. Liu, FMEA using uncertainty theories and MCDM methods, in *FMEA using uncertainty theories and MCDM methods*, 13–27, Springer, 2016.
- [8] Chang, D.-S., Sun, K.-L. P. Applying DEA to enhance assessment capability of FMEA *International Journal of Quality & Reliability Management*, 2009.
- [9] Zoullouti, B., Amghar, M., Nawal, S. Using Bayesian networks for risk assessment in healthcare system, in *Bayesian Networks-Advances and Novel Applications*, IntechOpen, 2019.
- [10] Neapolitan, R.E. Learning Bayesian networks. Prentice Hall, 2004.
- [11] Korb, K.B., Nicholson, A.E. Bayesian artificial intelligence. Chapman & Hall/CRC, 2004.
- [12] Weber, P., Medina-Oliva, G., Simon, C., Iung, B. Overview on Bayesian networks applications for dependability, risk analysis and maintenance areas *Engineering Applications of Artificial Intelligence, Special Section: Dependable System Modelling and Analysis*, 25:671–682, 2012.
- [13] Blos, M.F., Quaddus, M., Wee, H., Watanabe, K. Supply chain risk management (SCRM): a case study on the automotive and electronic industries in Brazil *Supply Chain Management: An International Journal*, 2009.
- [14] Mzougui, I., Carpitella, S., Certa, A., El Felsoufi, Z., Izquierdo, J. Assessing supply chain risks in the automotive industry through a modified MCDM-based FMECA *Processes*, 8(5), 579:1–22, 2020.
- [15] INAIL. Documento tecnico sulla possibile rimodulazione delle misure di contenimento del contagio da SARS-CoV-2 nei luoghi di lavoro e strategie di prevenzione. <https://www.inail.it/cs/internet/comunicazione/pubblicazioni/catalogo-generale/pubbl-rimodulazione-contenimento-covid19-sicurezza-lavoro.html>, 2020.

Stable positive Monte Carlo finite difference techniques for random parabolic partial differential equations

M.-C. Casabán^{b1}, R. Company^b and L. Jódar^b

(b) Instituto Universitario de Matemática Multidisciplinar,
Universitat Politècnica de València, Camino de Vera s/n, 46022 València, Spain.

1 Introduction

Integral Transform technique is a powerful method for solving random partial differential equations (RPDEs) in unbounded domains [1], but an alternative is needed in the case of bounded domains. In the deterministic case, the finite difference methods are the most used because they are easy to implement and efficient enough. But these methods extended to the random scenario have the drawback coming from the complexity of the computation of the statistical moments (the expectation and the standard deviation) arising from the operational random calculus throughout the iterative levels of the discretization steps and the necessity to store the information of all the previous levels of the iteration process [2, 3].

In this work we study the following RPDE of parabolic type often encountered in heat and mass transfer theory in heterogeneous media

$$\frac{\partial u(x, t)}{\partial t} = \frac{\partial}{\partial x} \left[p(x) \frac{\partial u(x, t)}{\partial x} \right] - q(x) u(x, t), \quad 0 < x < 1, \quad t > 0, \quad (1)$$

$$u(0, t) = g_1(t), \quad t > 0, \quad (2)$$

$$u(1, t) = g_2(t), \quad t > 0, \quad (3)$$

$$u(x, 0) = f(x), \quad 0 \leq x \leq 1. \quad (4)$$

In this model (1)–(4) we will assume, without loss of generality, that involved s.p.'s: $p(x)$ and $q(x)$ in the coefficients, $f(x)$ in the initial condition and $g_i(t)$, $i = 1, 2$, in the boundary conditions, have one degree of randomness (finite degree of randomness [4]), i.e. they have the form

$$\left. \begin{array}{l} h(s) = F(s, A), \\ A \text{ a r.v.}, F \text{ a differentiable real function of the variable } s. \end{array} \right\} \quad (5)$$

Then the s.p. $h(s)$ has sample differentiable trajectories, i.e. for a fixed event $\omega \in \Omega$, (Ω sample space) the real function $h(s, \omega) = F(s, A(\omega))$ is a differentiable function of the real

¹e-mail: macabar@imm.upv.es

variable s . In addition we assume that all the input data $p(x)$, $q(x)$, $f(x)$ and $g_i(t)$, $i = 1, 2$ are mean square continuous s.p.'s in variables x and t , respectively, $p(x)$ is also a mean square differentiable s.p. and the sample realizations of the random inputs $p(x)$, $q(x)$, $g_i(t)$, $i = 1, 2$ and $f(x)$ satisfy the following conditions:

$$0 < a_1 \leq p(x, \omega) \leq a_2 < +\infty, \quad x \in [0, 1], \text{ for almost every (a.e.) } \omega \in \Omega, \quad (6)$$

$$\frac{|p'(x, \omega)|}{p(x, \omega)} \leq b < +\infty, \quad x \in [0, 1], \text{ for a.e. } \omega \in \Omega, \quad (7)$$

$$q_{\min} \leq q(x, \omega) \leq q_{\max}, \quad x \in [0, 1], \text{ for a.e. } \omega \in \Omega, \quad (8)$$

$$g_i(t, \omega) \geq 0, \quad i = 1, 2, \quad t > 0, \text{ for a.e. } \omega \in \Omega, \quad (9)$$

$$0 \leq f(x, \omega) \leq f_{\max}, \quad x \in [0, 1], \text{ for a.e. } \omega \in \Omega, \quad (10)$$

where $p'(x)$ denotes the mean square derivative of $p(x)$.

2 Random finite difference scheme, numerical strategy and simulations

We develop a **stable** and **consistent** numerical random finite difference scheme preserving **positivity** of the solution stochastic process together with Monte Carlo technique that provides a useful tool to obtain accurate values of the expectation and the standard deviation of the approximating process even for large values of the time variable.

2.1 Random finite difference scheme

Let us consider the uniform partition of the spatial interval $[0, 1]$, of the form $x_i = ih$, $0 \leq i \leq M$, with $Mh = 1$. For a fixed time horizon, T , we consider $N + 1$ time levels $t^n = nk$, $0 \leq n \leq N$ with $Nk = T$. The numerical approximation of the solution s.p. of the random problem (1)–(4) is denoted by u_i^n , i.e. $u_i^n \approx u(x_i, t^n)$, $0 \leq i \leq M$, $0 \leq n \leq N$. Now, by using a forward first-order approximation of the time partial derivative and centred second-order approximations for the spatial partial derivatives in (1) one gets the following random numerical scheme for the spatial internal mesh points

$$\frac{u_i^{n+1} - u_i^n}{k} = p_i \frac{u_{i-1}^n - 2u_i^n + u_{i+1}^n}{h^2} + p'_i \frac{u_{i+1}^n - u_{i-1}^n}{2h} - q_i u_i^n, \quad 1 \leq i \leq M-1, \quad 0 \leq n \leq N-1, \quad (11)$$

where $p_i = p(x_i)$, $p'_i = p'(x_i)$ and $q_i = q(x_i)$. The resulting random discretized problem (1)–(4) can be rewritten in the following form

$$\left. \begin{aligned} u_i^{n+1} &= \frac{k}{h^2} \left(p_i - \frac{h}{2} p'_i \right) u_{i-1}^n + \left(1 - k q_i - \frac{2k}{h^2} p_i \right) u_i^n + \frac{k}{h^2} \left(p_i + \frac{h}{2} p'_i \right) u_{i+1}^n, \\ &1 \leq i \leq M-1, \quad 1 \leq n \leq N-1, \\ u_0^n &= g_1^n, \quad u_M^n = g_2^n, \quad 1 \leq n \leq N, \\ u_i^0 &= f_i, \quad 0 \leq i \leq M, \end{aligned} \right\} (12)$$

where $g_1^n = g_1(t^n)$, $g_2^n = g_2(t^n)$, and $f_i = f(x_i)$. We introduce the following definitions.

Definition 1 A random numerical scheme is said to be $\|\cdot\|_p$ -stable in the fixed station sense in the domain $[0, 1] \times [0, T]$, if for every partition with $k = \Delta t$, $h = \Delta x$ such that $Nk = T$ and $Mh = 1$,

$$\|u_i^n\|_p \leq C, \quad 0 \leq i \leq M, \quad 0 \leq n \leq N, \quad (13)$$

where C is independent of the step-sizes h , k and the time level n .

Definition 2 Let us consider a random finite difference scheme $F(u_i^n) = 0$ for a RPDE $\mathcal{L}(u) = 0$ and let the local truncation error $T_i^n(U(\omega))$ for a fixed event $\omega \in \Omega$ be defined by

$$T_i^n(U(\omega)) = F(U_i^n(\omega)) - \mathcal{L}(U_i^n(\omega)),$$

where $U_i^n(\omega)$ denotes the theoretical solution of $\mathcal{L}(u)(\omega) = 0$ evaluated at (x_i, t^n) . We call $T_i^n(U)$ by

$$\|T_i^n(U)\|_p = (\mathbb{E} [|T_i^n(U)|^p])^{1/p} = \left(\int_{\Omega} |T_i^n(U(\omega))|^p f_{T_i^n(U)}(\omega) d\omega \right)^{1/p}.$$

With previous notation, the random finite difference scheme $F(u_i^n) = 0$ is said to be $\|\cdot\|_p$ -consistent with the RPDE $\mathcal{L}(u) = 0$ if

$$\|T_i^n(U)\|_p \rightarrow 0 \quad \text{as } h = \Delta x \rightarrow 0, \quad k = \Delta t \rightarrow 0.$$

Theorem 1 With the previous notation under conditions

$$h \leq \frac{2}{b}, \quad k \leq \frac{h^2}{2a_2}, \quad (\text{If } q_{max} < 0), \quad k \leq \frac{h^2}{2a_2 + h^2 q_{max}}, \quad (\text{If } q_{max} \geq 0), \quad (14)$$

on the discretized step-sizes $h = \Delta x$ and $k = \Delta t$, the random numerical solution s.p. $\{u_i^n\}$ of the random finite difference scheme (12) for the random partial differential model (1)–(10) is positive for $0 \leq i \leq M$ at each time-level $0 \leq n \leq N$ with $T = kN$. Furthermore the random finite difference scheme (12) is $\|\cdot\|_p$ -stable in the fixed station sense taking the value

$$C = \alpha(T) G(T),$$

where

$$\begin{aligned} G(T) &= \max_{0 \leq t \leq T} \{g_{1,max}(T), g_{2,max}(T), f_{max}\} \\ g_{i,max}(T) &= \max_{0 \leq t \leq T} \{g_i(t, \omega), \text{ for a.e. } \omega \in \Omega\}, \quad i = 1, 2. \end{aligned} \quad (15)$$

and

$$\alpha(T) = \begin{cases} 1 & \text{if } q_{min} \geq 0, \\ e^{T|q_{min}|} & \text{if } q_{min} < 0. \end{cases} \quad (16)$$

2.2 Numerical strategy and simulations

From a computational point of view, the handling of the random scheme (12) in a direct way makes unavailable the computation of approximations beyond a few first temporal levels. This is because, throughout the iterative temporal levels, $n = 1, \dots, N$, it is necessary to store the symbolic expressions of all the previous levels of the iteration process collecting big and complex random expressions with which the expectation and the standard deviation must be computed. Furthermore, although the random expressions can be stored it does not guarantee that the two first statistical moments could be computed in a numerical way. For this reason we propose to use the random numerical scheme (12) together with the Monte Carlo technique avoiding the described computational drawbacks. The procedure is as follows: to take a number K of realizations of the random data involved in the random PDE (1)–(4) according to their probability distributions; to compute the numerical solution, $u_i^n(\omega_j)$, $j = 1, \dots, K$, of the sampling deterministic difference schemes of (12); to obtain the mean and the standard deviation of these K numerical solutions evaluated in the mesh points $i = 1, \dots, M - 1$, at the last time-level N , denoted respectively by

$$\mathbb{E}_{\text{MC}}^K[u_i^N] = \mu(u_i^N(\omega_1), u_i^N(\omega_2), \dots, u_i^N(\omega_K)). \quad (17)$$

$$\sqrt{\text{Var}_{\text{MC}}^K[u_i^N]} = \sigma(u_i^N(\omega_1), u_i^N(\omega_2), \dots, u_i^N(\omega_K)). \quad (18)$$

Example 1 We consider the problem (1)–(4) with the random data

$$p(x) = a e^{-x}, \quad q(x) = -c, \quad g_1(t) = e^{ct} \left(\frac{1}{2} + at \right), \quad g_2(t) = e^{ct} \left(\frac{e^2}{2} + aet \right), \quad f(x) = \frac{e^{2x}}{2}, \quad (19)$$

where the r.v. a follows a Gaussian distribution of mean $\mu = 0.5$ and standard deviation $\sigma = 0.1$ truncated on the interval $[0.4, 0.6]$, and the r.v. $c > 0$ has a beta distribution of parameters $(2; 4)$ truncated on the interval $[0.45; 0.55]$. We will assume that a and c are independent r.v.'s. Note all random input data $p(x)$, $q(x)$, $g_1(t)$, $g_2(t)$ and $f(x)$ are m.s. continuous and $p(x)$ is m.s. differentiable too. In addition, conditions (6)–(10) are satisfied with

$$a_1 = 0.4 e^{-1}, \quad a_2 = 0.6 e^0, \quad -0.55 \leq q(x, \omega) \leq -0.45, \quad \omega \in \Omega, \quad 0 \leq f(x, \omega) \leq 3.69453.$$

From [5, Sec. 3.8.5.] the exact solution of problem (1)–(4), (19) when both parameters a and c are deterministic, is given by

$$u(x, t) = e^{ct} \left(ae^{xt} + \frac{e^{2x}}{2} \right). \quad (20)$$

In our context, both a and c are r.v.'s, and expression (20) must be interpreted as a s.p. Then, using the independence between r.v.'s a and c , the expectation and the standard deviation of s.p. (20) can be computed. Numerical convergence of the expectation and the standard deviation of the approximate solution s.p. using Monte Carlo (MC) technique is illustrated in the following way. With a fixed time $T = 1$, we have chosen both the spatial and temporal step-sizes $h = 0.0125$ and $k = 0.0001$, respectively, according to the stability conditions (14) and we have varied the number of realizations, K , of the r.v.'s a and c involved in the random problem (1)–(4), (19). Then, at the temporal level $N = 10000$ where the time $T = Nk = 1$ is achieved, we have

computed the expectation (mean), $\mathbb{E}_{MC}^K[u_i^N]$ (17), and the standard deviation, $\sqrt{\text{Var}_{MC}^K[u_i^N]}$ (18), of the K -deterministic solutions, u_i^N , obtained to solve the K -deterministic difference schemes from (12). Table 1 collects the RMSEs (Root Mean Square Errors) computed using the following expressions

$$\text{RMSE} \left[\mathbb{E}_{MC}^K[u_i^N] \right] = \sqrt{\frac{1}{M-1} \sum_{i=1}^{M-1} (\mathbb{E}[u(x_i, t^N)] - \mathbb{E}_{MC}^K[u_i^N])^2}, \quad (21)$$

$$\text{RMSE} \left[\sqrt{\text{Var}_{MC}^K[u_i^N]} \right] = \sqrt{\frac{1}{M-1} \sum_{i=1}^{M-1} \left(\sqrt{\text{Var}[u(x_i, t^N)]} - \sqrt{\text{Var}_{MC}^K[u_i^N]} \right)^2}, \quad (22)$$

where $\mathbb{E}[u(x_i, t^N)]$ and $\sqrt{\text{Var}[u(x_i, t^N)]}$ denote the expectation and standard deviation of the exact solution s.p. (20), respectively. It is observed the good behaviour of both approximations

K	RMSE $\left[\mathbb{E}_{MC}^K[u_i^N] \right]$	RMSE $\left[\sqrt{\text{Var}_{MC}^K[u_i^N]} \right]$	CPU, s	$\mathbb{E}_{MC}^K / \sqrt{\text{Var}_{MC}^K}$
50	1.45604e - 02	1.32856e - 02	630.516	
200	1.11710e - 02	1.84435e - 03	982.375	
800	1.08512e - 02	1.06139e - 03	2052.330	
3200	4.20138e - 03	6.01374e - 03	6209.480	
12800	2.07183e - 04	1.69504e - 03	22600.100	

Table 1: RMSEs and CPU time (in seconds) spent to compute the approximations to the expectation (mean), \mathbb{E}_{MC}^K , and the standard deviation, $\sqrt{\text{Var}_{MC}^K}$ in the level time $N = 10000$, for $K \in \{50, 200, 800, 3200, 12800\}$ MC realizations, on the spatial domain $[0+h, 1-h]$, $x_i = ih$, $1 \leq i \leq 79$, $h = 0.0125$.

the expectation and the standard deviation as the number K of simulations increases. That is, the accuracy of the approximations to both statistical moments increases when the number of MC simulations is growing. In this sense, Figure 1 and Figure 2 reflects the improvement of the approximations considering the study of the relative errors. Computations have been carried out by Mathematica[®] software version 12.0.0.0, for Windows 10Pro (64-bit) AMD Ryzen Threadripper 2990WX, 3.00 GHz 32 kernels.

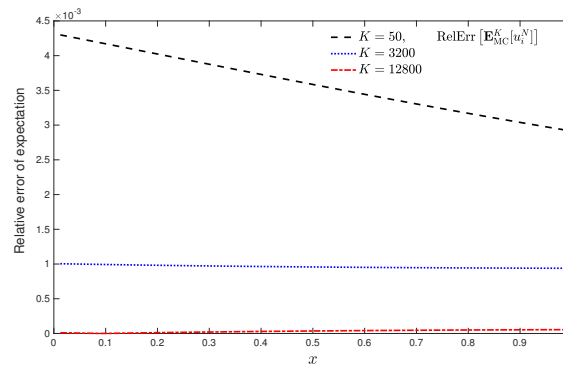


Figure 1: Relative errors of the approximations to the expectation (mean), $\mathbb{E}_{MC}^K[u_i^N]$.

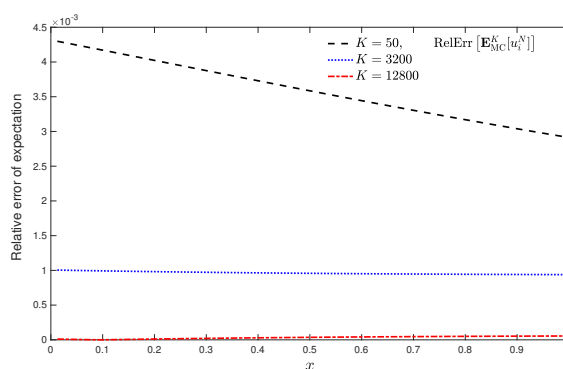


Figure 2: Relative errors of the approximations to the standard deviation, $\sqrt{\text{Var}_{\text{MC}}^K[u_i^N]}$.

3 Conclusions and future work

The random scheme (12) developed is consistent, conditionally stable and positive. This random scheme combined with the MC method solves the computational problem of methods random iterations as it avoids collapsing in the calculation of symbolic expressions to few temporary steps. In this way, it is possible the computation of the mean and the standard deviation. The convergence strategy used is to choose the discretization step-size h and k , verifying the stability conditions, and increase the number of MC realizations until that the errors no longer change substantially. This method can even be applied to non-linear or two-dimensional problems.

Acknowledgements

This work has been supported by the Spanish Ministerio de Economía, Industria y Competitividad (MINECO), the Agencia Estatal de Investigación (AEI) and Fondo Europeo de Desarrollo Regional (FEDER UE) grant MTM2017-89664-P.

References

- [1] Casabán, M.-C., Company, R., Jódar L., Numerical Integral Transform Methods for Random Hyperbolic Models with a Finite Degree of Randomness *Mathematics*, 7(9):1-21, 2019.
- [2] M.A. Sohaly, Random difference scheme for diffusion advection model, *Advances in Difference Equations*, 54, 2019.
- [3] Casabán, M.-C., Company, R., Jódar L., Numerical solutions of random mean square Fisher-KPP models with advection, *Mathematical Methods in Applied Sciences*, 43:8015-8031, 2020.
- [4] Soong, T.T., Random Differential Equations in Science and Engineering. New York, Academic Press, 1973.
- [5] Polyanin A.D., Nazaikinskii V.E., Handbook of Linear Partial Differential Equations for Engineers and Scientists, Boca Raton, USA, Taylor & Francis Group, 2016.

Invariant energy in short-term personality dynamics

Antonio Caselles ^{‡1}, Salvador Amigó [#], and Joan C. Micó [‡],

(‡) IASCYS member, Departament de Matemàtica Aplicada,
Universitat de València, (retired),

(#) Departament de Personalitat, Avaluació i Tractaments Psicològics,
Universitat de València,

(‡) Institut Universitari de Matemàtica Multidisciplinar,
Universitat Politècnica de València.

1 Introduction

This work presents a way to find a time-invariant energy associated to the short-term personality dynamics as a consequence of an arbitrary stimulus. First of all, the short-term personality dynamics is presented as a second order differential equation [1], derived from the original first order integro-differential equation [2] called as the response model. In the following, the referred second order formulation can be presented from the perspective of the classical mechanics, through the Lagrangian and the Hamiltonian functions [1]. However, although the Hamiltonian is a true energy (a sum of kinetic and potential energies), it depends explicitly on time. Consequently it is not an invariant energy [3]. Besides, both the second order differential equation and the Hamiltonian are mathematically similar (in Physics) to the mathematical approach to a particle with variable mass subjected to a retrieving force with a time-dependent retrieving constant. This problem is known in the specialized literature as the harmonic oscillator with time-dependent mass and frequency. Fortunately, this problem can be transformed into a formulation that provides the well-known Ermakov-Lewis invariant [4], which can be reinterpreted as an energy invariant [5]. Thus, starting from our second order differential equation that describes the short-time personality dynamics, and following one of the methods presented in [4], an Ermakov-Lewis invariant is found, which can be interpreted as a personality energy-invariant.

2 The response model and its Lagrangian-Hamiltonian approach

The response model [2] is given by the following integro-differential equation:

$$\left. \begin{aligned} \frac{dq(t)}{dt} &= a \cdot (b - q(t)) + \delta \cdot s(t) \cdot q(t) - \sigma \cdot \int_{t_0}^t e^{\frac{x-t}{\tau}} \cdot s(x) \cdot q(x) dx \\ q(t_0) &= q_0 \end{aligned} \right\} \quad (1)$$

¹e-mail: antonio.caselles@uv.es

The function $s(t)$ represents an arbitrary stimulus and $q(t)$ the General Factor of Personality (GFP). For more details about the meaning of Eq. (1) as well as its parts and parameters see [2]. Taking the time derivative in Eq. (1) and making the subsequent substitutions, the second order differential equation, and its initial conditions arise:

$$\left. \begin{aligned} \ddot{q}(t) + \gamma(t) \cdot \dot{q}(t) + v(t) \cdot q(t) &= \frac{a \cdot b}{\tau} \\ q(t_0) &= q_0 \\ \dot{q}(t_0) &= a \cdot (b - q_0) + \delta \cdot s_0 \cdot q_0 \end{aligned} \right\} \quad (2)$$

In Eq. (2):

$$v(t) = \left(\frac{a}{\tau} + \sigma \cdot s(t) - \frac{\delta}{\tau} \cdot s(t) - \delta \cdot \dot{s}(t) \right) \quad (3)$$

$$\gamma(t) = \frac{d}{dt} \left(\ln \left(u(t) \right) \right) = \frac{\dot{u}(t)}{u(t)} \quad (4)$$

$$u(t) = u_0 e^{(a + \frac{1}{\tau})(t - t_0) - \delta \int_{t_0}^t s(x) dx} \quad (5)$$

Eq. (2) is an equivalent version of Eq. (1), and u_0 is an undetermined constant by the moment. In addition, s_0 is the stimulus' value in the initial time $t = t_0$. Note that this version is equivalent to that of a harmonic oscillator with time-dependent mass $u(t)$ and time-dependent frequency $v(t)$ subjected to a constant force $a \cdot \frac{b}{t}$. The difference with respect to the physical problem is that, here, the frequency $v(t)$ can take an arbitrary sign during its evolution, while in physics it is always positive (due to it, $v(t)$ always appears as $\omega^2(t)$). Eq. (2) is the version of the response model to be used from now onward. The Lagrangian, (L), the momentum (p) and the Hamiltonian (H) corresponding to Eq. (2) are [1]:

$$L(t, q, \dot{q}) = \frac{1}{2} u(t) \cdot \dot{q}^2 - \frac{1}{2} u(t) \cdot v(t) \cdot q^2 + \frac{a \cdot b}{\tau} u(t) \cdot q \quad (6)$$

$$p = \frac{\partial L}{\partial \dot{q}} = u(t) \cdot \dot{q} \quad (7)$$

$$H(t, p, q) = \frac{\partial L}{\partial \dot{q}} \dot{q} - L(t, q, \dot{q}) = \frac{1}{2} \frac{p^2}{u(t)} + \frac{1}{2} u(t) \cdot v(t) \cdot q^2 - \frac{a \cdot b}{\tau} u(t) \cdot q \quad (8)$$

Note that Eq. (8) represents actually energy in its physical sense because it can be rewritten as:

$$H(t, q, p) = T(t, p) + V(t, q) \quad (9)$$

where $T(t, p) = \frac{1}{2} \frac{p^2}{u(t)}$ is the kinetic energy and $V(t, q) = \frac{1}{2} u(t) \cdot v(t) \cdot q^2 - \frac{a \cdot b}{\tau} u(t) \cdot q$ is the potential energy. However, it is not an invariant energy due to it is explicitly time-dependent. Would it be possible to get an invariant energy with the suitable changes? This is the goal of the following section.

3 Getting the invariant energy

In [4], Ray and Reid provide several methods to get invariants related to Eqs. (2) and (8); these are known as Ermakov-Lewis invariants (note that a collection of invariants can be got). Here we follow what we think is the most intuitive Ray and Reid's, which works directly on Eq. (2) [4]. First of all, the change $Q(t) = \sqrt{u(t)} \cdot q(t)$ provides the equation:

$$\ddot{Q}(t) + \Omega(t) \cdot Q(t) = \frac{a \cdot b}{\tau} \sqrt{u(t)} \quad (10)$$

where:

$$\Omega(t) = v(t) - \left(\frac{1}{2} \frac{\dot{u}(t)}{u(t)} - \frac{1}{2} \frac{\dot{u}^2(t)}{u^2(t)} \right) \quad (11)$$

That is, the mentioned change reduces Eq. (2) to Eq. (10), which is the equation of a harmonic oscillator with frequency $\Omega(t)$ subjected to a retrieving force $\frac{a \cdot b}{\tau} \sqrt{u(t)}$. Two new consecutive changes are needed now: the first on Eq. (10), on the dependent variable $x(t) = \frac{Q(t)}{C(t)} + A(t)$, and the second on the independent variable $T = \int_{t_0}^t \frac{dr}{C^2(r)}$, where $C(t)$ and $A(t)$ are undetermined auxiliary functions by the moment. These changes provide:

$$\begin{aligned} & \ddot{x}(T) + C^3(t) \left(\ddot{C}(t) + \Omega(t) \cdot C(t) \right) \cdot x(T) + \\ & + C^3(t) \left(-\ddot{C}(t) \cdot A(t) - 2\dot{C}(t) \cdot \dot{A}(t) - C(t) \cdot \ddot{A}(t) - \Omega(t) \cdot C(t) \cdot A(t) - \frac{a \cdot b}{\tau} \sqrt{u(t)} \right) = 0 \end{aligned} \quad (12)$$

where $\ddot{x}(T) = \frac{d^2 x(T)}{dT^2}$. In order that Eq. (12) becomes an equation with constant parameters, we force the following to hold:

$$\ddot{C}(t) + \Omega(t) \cdot C(t) = \frac{k}{C^3(t)} \quad (13)$$

$$\ddot{A}(t) + 2 \frac{\dot{C}(t)}{C(t)} \dot{A}(t) + k \frac{A(t)}{C^4(t)} + \frac{a \cdot b}{\tau} \frac{\sqrt{u(t)}}{C(t)} \quad (14)$$

where k is an undetermined constant. Then Eq. (12) becomes:

$$\ddot{x}(T) + k \cdot x(T) = 0 \quad (15)$$

The Lagrangian, momentum and Hamiltonian corresponding to Eq. (15) are:

$$L_x(t, x, \dot{x}) = \frac{1}{2} \quad (16)$$

$$p_x = \frac{\partial L}{\partial \dot{x}} = \dot{x} \quad (17)$$

$$H_x(t, x, p_x) = \frac{\partial L}{\partial x} \dot{x} - L_x(t, x, \dot{x}) = \frac{p_x^2}{2} + \frac{k}{2} x^2 \quad (18)$$

Note that the Hamiltonian H_x is explicitly time-independent, therefore it is invariant. In fact, by undoing the changes proposed before, we obtain the corresponding Ermakov-Lewis

invariant [4] that, such as Padmanabhan emphasises in [5], it has been demonstrated that is an invariant energy:

$$E = \frac{1}{2} \left(\sqrt{u(t)} \cdot C(t) \cdot \dot{q} + C^2(t) \cdot \dot{A}(t) + \left(\frac{1}{2} C(t) \frac{\dot{u}(t)}{\sqrt{u(t)}} - \sqrt{u(t)} \cdot \dot{C}(t) \right) q \right)^2 + \frac{k}{2} \left(\frac{\sqrt{u(t)}}{C(t)} q + A(t) \right)^2 \quad (19)$$

Note that in the invariant energy E given by Eq. (19), $C(t)$ and $A(t)$ must hold Eqs. (13) and (14). In addition, Eq. (15) can be solved analytically in function of $A(t)$ and $C(t)$ auxiliary variables by undoing the changes proposed before, and consequently:

$$\begin{aligned} q(t) &= \frac{C(t)}{\sqrt{u(t)}} \left(-A(t) + k_1 \int_{t_0}^t \frac{dr}{C^2(r)} + k_2 \right) \quad \text{if } k = 0 \\ q(t) &= \frac{C(t)}{\sqrt{u(t)}} \left(-A(t) + k_1 \cdot \exp \left(\sqrt{k} \int_{t_0}^t \frac{dr}{C^2(r)} + k_2 \cdot \exp \left(-\sqrt{k} \int_{t_0}^t \frac{dr}{C^2(r)} \right) \right) \right) \quad \text{if } k > 0 \\ q(t) &= \frac{C(t)}{\sqrt{u(t)}} \left(-A(t) + k_1 \cdot \sin \left(\sqrt{-k} \int_{t_0}^t \frac{dr}{C^2(r)} + k_2 \cdot \cos \left(\sqrt{-k} \int_{t_0}^t \frac{dr}{C^2(r)} \right) \right) \right) \quad \text{if } k < 0 \end{aligned} \quad (20)$$

4 Application case: a dose of methylphenidate

The application case consists in one subject that consumed 10 mg of methylphenidate, and its GFP was measured every 7.5 minutes during 180 minutes (3 hours), with the 5 adjectives scale, GFP-FAS [6], in the interval $[0, 50]$. The initial condition was also measured before consumption, with value q_0 , which is considered as initial condition for Eq. (20). The stimulus equation is given by:

$$s(t) = s_0 e^{-\beta \cdot t} + \begin{cases} \frac{\alpha \cdot M}{\beta - \alpha} (e^{-\alpha \cdot t} - e^{-\beta \cdot t}) : \alpha \neq \beta \\ \alpha \cdot M \cdot t \cdot e^{-\alpha \cdot t} : \alpha = \beta \end{cases} \quad (21)$$

Note that taking into account Eq. (21), calculating Eqs. (3), (5) and (11) (necessary to compute Eqs. (19) and (20) through Eqs. (13) and (14)), become very complex, due to the nonlinear character of Eqs. (13) and (14). Thus, the version that considers $k = 0$ in both Eqs. (19) and (20) is chosen for simplicity. In addition, the invariant energy, Eq. (19), for $k = 0$ can be split into three terms:

$$\begin{aligned} E &= T_e + V_e + R_e = \frac{1}{2} \left(\sqrt{u(t)} \cdot C(t) \dot{q} + C^2(t) \cdot \dot{A}(t) \right)^2 + \\ &+ \frac{1}{2} \left(\left(\frac{1}{2} C(t) \frac{\dot{u}(t)}{\sqrt{u(t)}} - \sqrt{u(t)} \cdot \dot{C}(t) \right) q \right)^2 + \\ &+ \left(\sqrt{u(t)} \cdot C(t) \cdot \dot{q} + C^2(t) \cdot \dot{A}(t) \right) \left(\left(\frac{1}{2} C(t) \frac{\dot{u}(t)}{\sqrt{u(t)}} - \sqrt{u(t)} \cdot \dot{C}(t) \right) q \right) \end{aligned} \quad (22)$$

where T_e is a kinetic energy, V_e a potential energy and R_e a lost energy. This splitting is based on the fact that $A(t)$ has the same dimensions as q , $C(t)$ is non dimensional, and that $A(t)$

and q variables and its derivatives play these roles in the different kinds of energies observed in similar problems in Physics. Once the initial values of $A(t)$, $A_0 = q_0$, $\dot{A}_0 = \dot{q}_0$, have been determined and taking $k_1 = 1$ and $k_2 = 1$, the initial values of $C(t)$ become $C_0 = -1.053$, $\dot{C}_0 = -0.066$. In addition, due to the term $(a + \frac{1}{\tau})(t - t_0)$, in the $u(t)$ function of Eq. (5), can be divergent, depending on the a or τ values, the constant u_0 is taken as $u_0 = e^{-(a + \frac{1}{\tau})(T - t_0)}$, where T is the border time of the experiment (180 min.). Then the calibration of Eq. (20) can be seen in Fig. 1. while the three energies split in Eq. (22) can be seen in Fig. 2 and the total energy E in Fig. 3. Observe the invariance of this last energy.

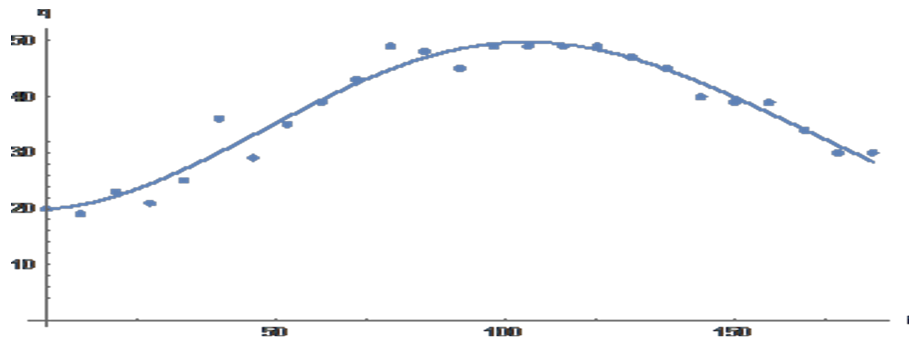


Figure 1: Experimental values (dots) and the theoretical values (curve) of the GFP (q) versus time.

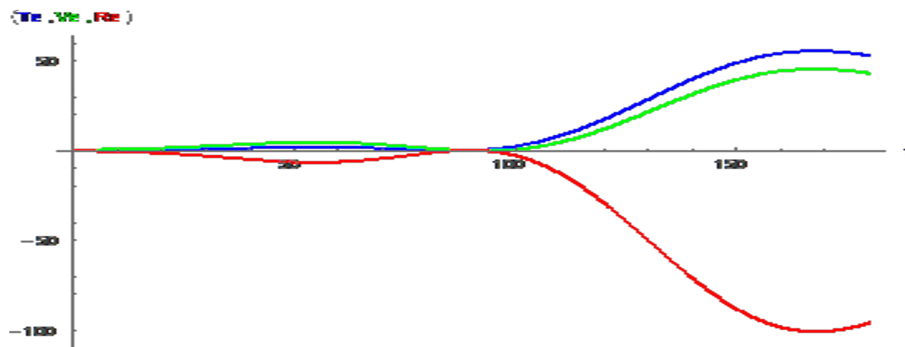


Figure 2: Kinetic energy T_e (upper curve), potential energy V_e (intermediate curve) and lost energy R_e (lower curve) versus time.

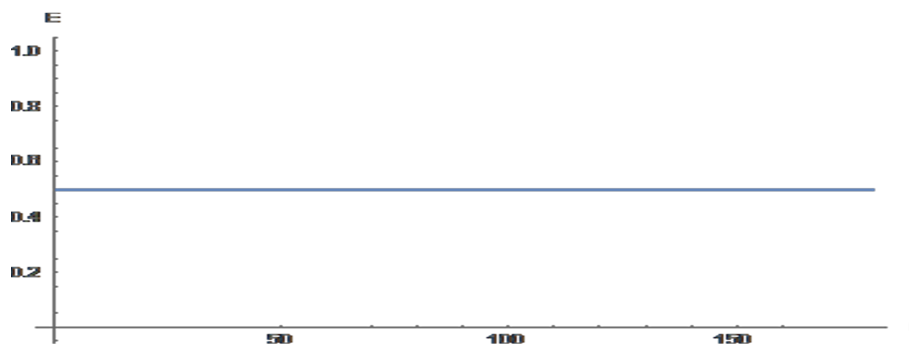


Figure 3: Invariant energy E versus time.

5 Conclusions and future work

We want to emphasize that an invariant energy has been found in the context of the short-term personality dynamics. However, it has been found at the price to compute the dynamics of the auxiliary variables $A(t)$ and $C(t)$ through the nonlinear Eqs. (13) and (14). Even in the case here considered, $k = 0$, the calculation complexity is present. However, this case provides the splitting of the invariant energy into three interesting terms: kinetic, potential and lost energies. Nevertheless, we are conscious that this theoretical progress in personality theory must find its own applications. Firstly, consider that having an invariant in the context of any theory is highly important because it permits to characterize or classify non-well identified problems in its corresponding theory, for instance, the classification of orbits in the two-bodies problem. Thus, a future work should be to try to classify personality typologies by the found invariant energy, for instance, those related to health, even, to try to change a disordered personality by another stable one through planned stimuli, such as the self-regulation therapies suggest [7]. On the other hand, When the short-term personality dynamics, given by Eq. (1), tries to be applied to two or more consecutive stimuli, the model calibrations become useless due to the arising of habituation phenomena. However, due to the invariant energy is always conserved, the habituation phenomena could be predicted and thus, this invariant could be used to predict the long-term personality dynamics, i.e., when two or more consecutive stimuli influence on an individual [8].

References

- [1] Micó, J.C. Amigó, S. Caselles, A. Hamiltonian approach to human personality dynamics: an experiment with methylphenidate. *Proceedings of the Modelling for Engineering and Human Behaviour*, 209-212, Universitat Politècnica de València, 2018.
- [2] Micó, J.C. Amigó, S. Caselles, A. Advances in the General Factor of Personality Dynamics. *Revista Internacional de Sistemas*, 22: 34-38, 2018.
- [3] Landau, L. D., Lifshitz, E. M. *Mecánica (Vol. 1 del Curso de Física Teórica)*. Barcelona, Ed. Reverté, 2002.
- [4] Ray, J. R., Reid, J. L. Invariants for forced time-dependent oscillators and generalizations. *Physical Review A*, 26: 1042-1047, 1982.
- [5] Padmanabhan, T. Demystifying the constancy of the Ermakov-Lewis invariant for a time dependent oscillator. *arXiv-1712.07328v1 [physics.class-ph]*, 1-5, 2017.
- [6] Amigó, S., Micó, J. C., Caselles, A. Five adjectives to explain the whole personality: a brief scale of personality. *Revista Internacional de Sistemas*, 16: 41-43, 2009.
- [7] Amigó, S., Caselles, A., Micó, J. C. The self-regulation therapy to reproduce drug effects: a suggestion technique to change personality and the DRD3 gene expression. *International Journal of Clinical and Experimental Hypnosis*, 61: 282-304, 2013.
- [8] Caselles, A., Micó, J. C. Amigó, S. Cocaine addiction and personality: A mathematical model. *British Journal of Mathematical and Statistical Psychology*, 63: 449-480, 2010.

Suitable approximations for the self-accelerating parameters in iterative methods with memory

F. I. Chicharro ^{b1}, N. Garrido ^b, A. Cordero [‡] and J.R. Torregrosa [‡]

(b) Escuela Superior de Ingeniería y Tecnología, Universidad Internacional de La Rioja
Av. La Paz 137, 26006-Logroño, Spain,

(‡) Instituto de Matemática Multidisciplinar, Universitat Politècnica de València,
Camí de Vera s/n, 46022-València, Spain.

1 Introduction

Solving the nonlinear equation $f(x) = 0$, $f : D \subseteq \mathbb{R} \rightarrow \mathbb{R}$ is a common problem in several areas of Science and Engineering. Since exact solutions of the nonlinear equation are hardly available, scientists best rely on numerical solutions, such as those given by iterative methods.

Iterative procedures for finding the root α of f can be classified according to different criteria: the presence or absence of derivatives in the iterative expression, single- or multiple-root finding methods, or the number of previous iterations to obtain the current one, among others. For instance, we can find iterative methods without memory for finding single roots with derivatives [1] and derivative-free [2], or multiple-root finding with derivatives [3] and derivative-free [4]. In the methods with memory counterpart for single roots, we can also find [5] with derivatives, or [6] without derivatives.

Focusing on the last type of schemes, they are known as iterative methods with memory. These methods can be expressed by

$$x_{k+1} = M(x_k, x_{k-1}, \dots, x_{k-p}),$$

where M describes the iterative method. Therefore, p previous values of the sequence are necessary to obtain the following one. The major advantage of this sort of methods is to enhance the order of convergence of the original method without introducing new evaluations of the function f [7].

One technique to obtain iterative schemes with memory starts with an iterative method without memory that includes a parameter. Depending on the error equation of the method, the parameter can be replaced by an expression that includes the previous iterations. A basic example of this technique can be found at [8]. Starting from Traub's method [9], the parameter δ is included in the denominator of the first step. Its order of convergence is

$$e_{k+1} = 2c_2(c_2 + \delta)e_k^3 + \mathcal{O}(e_k^4),$$

¹e-mail: francisco.chicharro@unir.net

where $e_k = x_k - \alpha$ and $c_j = \frac{f^{(j)}(\alpha)}{j!f'(\alpha)}$, $j \geq 2$. Replacing δ by a suitable approximation that includes the previous iterates, the method becomes into an iterative procedure with memory.

The strategy to obtain these expressions is essential. In this work we propose suitable approximations that are present in the literature for different iterative methods with memory. On the one hand, the polynomials approximation, such as Newton's interpolation polynomial. On the other hand, the non-polynomials approximation, such as Padé's approximants. Finally, we discuss on the most suitable choice in terms of convergence and stability.

2 Inclusion of memory

Generally, the error equation is of the form

$$e_{k+1} = K(k_0 + k_1\delta + k_2c_j)e_k^p + \mathcal{O}(e_k^{p+1}),$$

where K , k_0 , k_1 and k_2 are constants. In order to cancel the error of order p , the parameter must satisfy

$$\delta = -\frac{k_0 + k_2c_j}{k_1},$$

but c_j includes $f^{(j)}(\alpha)$ and α is unknown. Therefore, an approximation of $f^{(j)}(\alpha)$ is performed. There are two main trends in this situation: Newton's interpolation polynomial and Padé's approximants.

2.1 Newton's interpolation polynomial

Newton's interpolation polynomial has been applied in [10]. In this case, the iterative expression is

$$\begin{aligned} y_k &= x_k - \frac{f(x_k)}{f[x_k, w_k]}, \\ x_{k+1} &= y_k - \left(1 + \frac{f(y_k)}{f(x_k)} + \lambda \frac{f^2(y_k)}{f^2(x_k)}\right) \frac{f(y_k)}{f[y_k, w_k]}, \quad k = 1, 2, \dots, \end{aligned} \quad (1)$$

where $w_k = x_k + \delta f(x_k)$, being δ and λ free parameters. The error equation of (1) is

$$e_{k+1} = -K \frac{C_2}{2} (1 + \delta f'(\alpha))^2 e_k^4 + \mathcal{O}(e_k^5).$$

Therefore, for increasing the order of convergence, we need to approximate $\delta \approx -\frac{1}{f'(\alpha)}$. Using Newton's polynomial of first degree $N(t) = f(x_k) + f[x_k, x_{k-1}](t - x_k)$, we have

$$f'(\alpha) \approx N'(x_k) = f[x_k, x_{k-1}],$$

and the R -order of the method [11] is 4.45.

2.2 Padé's approximant

Padé's approximant has been applied in [12]. The starting iterative expression is

$$\begin{aligned} y_k &= x_k - \frac{f(x_k)}{f'(x_k) + \delta f(x_k)}, \\ x_{k+1} &= y_k - \frac{1 + \beta u_k + u_k^2}{1 + (\beta - 2)u_k + P_2(\beta)u_k^2} \frac{f(y_k)}{f'(x_k) + 2\delta f(x_k)}, \quad k = 1, 2, \dots, \end{aligned} \quad (2)$$

where $u_k = f(y_k)/f(x_k)$, $P_2(\beta) = 0.17\beta^2 - 0.8075\beta + 2.9166$, and both δ and λ are free parameters. The error equation of (2) is

$$e_{k+1} = K(\delta + c_2)e_k^4 + \mathcal{O}(e_k^5).$$

Again, for increasing the order of convergence, $\delta \approx c_2 = -\frac{f''(\alpha)}{2f'(\alpha)}$. Using Padé's approximant

$$m(t) = \frac{a_1 + a_2(t - x_k)}{1 + a_3(t - x_k)},$$

and constraining

$$\begin{cases} m(x_k) = f(x_k), \\ m(x_{k-1}) = f(x_{k-1}), \\ m'(x_k) = f'(x_k), \end{cases}$$

the approximation can be performed as

$$\delta \approx -\frac{f''(\alpha)}{2f'(\alpha)} = \frac{f(x_k) - f(x_{k-1}) + f'(x_k)(x_{k-1} - x_k)}{(f(x_k) - f(x_{k-1}))(x_k - x_{k-1})}.$$

In this case, the R -order is 4.24.

3 Effects on dynamical behavior

The dynamical behavior of the iterative methods highlights the stability of the methods in the sense of the amount of initial estimations that converge to the desired root. Many papers collect the basics of the dynamical analysis [13, 14] in general, and [15, 16] in the particular case of iterative methods with memory.

For the sake of comparison, we are showing different dynamical planes of the original methods and after the inclusion of memory. The dynamical planes have been generated following the guidelines of [17]. The specific values are

- 200 points of grid in the square $\Re\{z\} \in [-5, 5]$, $\Im\{z\} \in [-5, 5]$ for the method without memory, and $x_k \in [-5, 5]$, $x_{k-1} \in [-5, 5]$.
- 50 maximum of iterations.
- The method interprets convergence when the difference between the iterate and α is lower than 10^{-6} .
- The nonlinear function is $f(z) = z^2 - 1$, $z \in \hat{\mathbb{C}}$, for the methods without memory, and $f(x) = x^2 - 1$, $x \in \mathbb{R}$, for methods with memory.
- The {blue, orange, black} colors represent the convergence to $\{-1, 1, \text{other}\}$.

Figure 1 represents the dynamical planes of (1) without memory, using $\delta = \frac{1}{10}$ and $\lambda \in \{-550, -\frac{9}{2}, 10\}$, while Figure 2 is the version of (1) with memory, for the same set of values of λ .

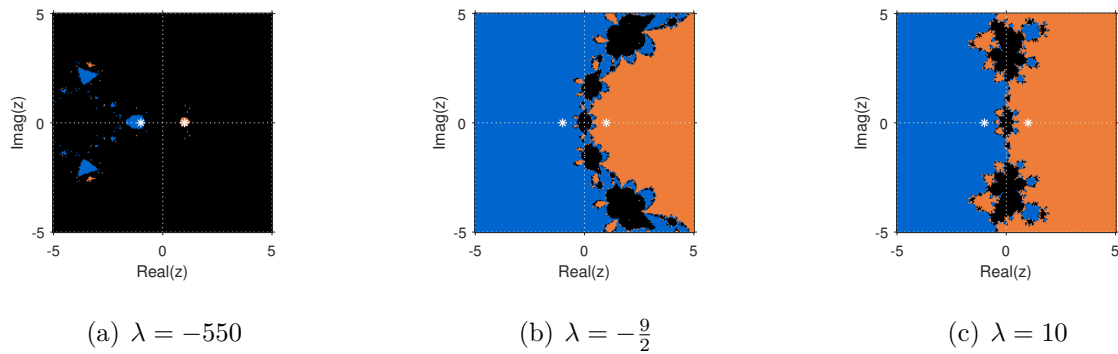


Figure 1: Dynamical planes of method (1) without memory, $\delta = \frac{1}{10}$.

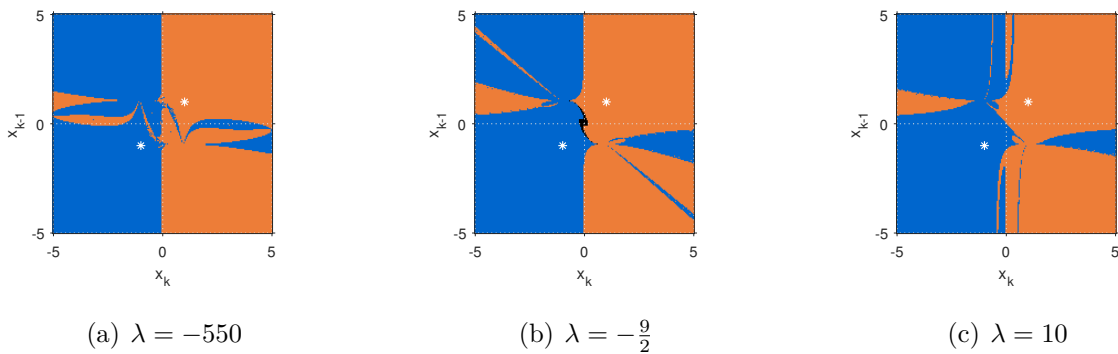


Figure 2: Dynamical planes of method (1) with memory.

There is presence of black regions in Figure 1, that show the convergence to a point that does not match with the roots. With the inclusion of memory, we can see in Figure 2 that regions in black are trifling, and almost every initial guess converges to the roots of the polynomial.

Figure 3 represents the dynamical planes of (2) without memory, using $\delta = \frac{1}{10}$ and $\lambda \in \{4, \frac{32}{5}, 67\}$, while Figure 4 is the version of (2) with memory, for the same set of values of λ .

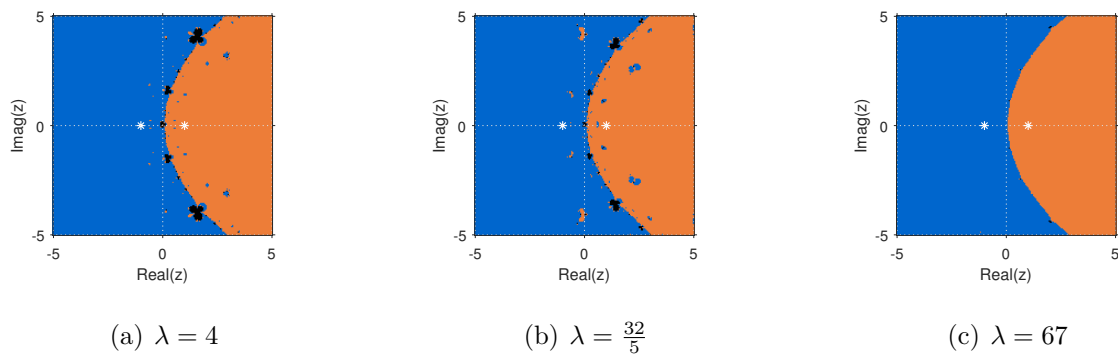


Figure 3: Dynamical planes of method (2) without memory, $\delta = \frac{1}{10}$.

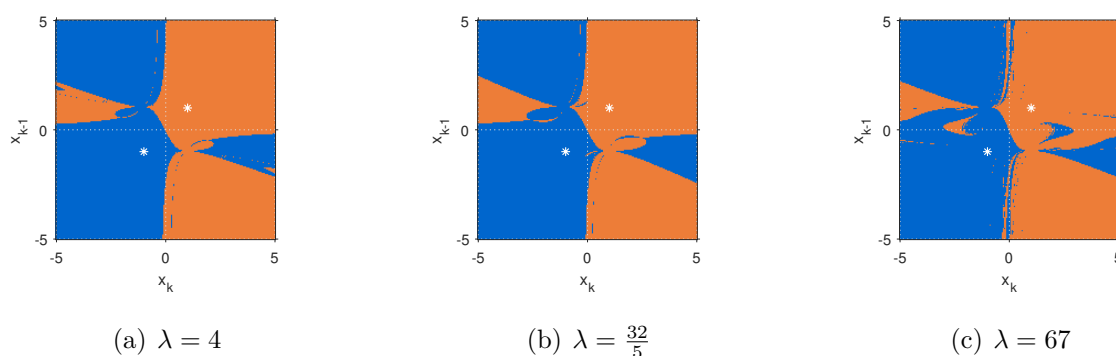


Figure 4: Dynamical planes of method (2) with memory.

In Figure 3 we can observe that the higher value of λ , the wider stability. The inclusion of memory removes the presence of black regions, as Figure 4 evidences.

4 Conclusions

The inclusion of memory in iterative methods enhances the order of convergence of the original method with no additional cost in function evaluations. Two techniques have presented: Newton's interpolation polynomial and Padé's approximant. In the first case, the original method has significant basins of attraction that do not own to the roots. The inclusion of memory has softened these basins, and almost every initial iterate converges to the expected solution. In the second case, a similar behavior can be observed.

Acknowledgements

This research was supported by PGC2018-095896-B-C22 (MCIU/AEI/FEDER, UE).

References

- [1] Amorós, C., Argyros, I.K., González, R., Magreñán, Á.A., Orcos, L., Sarría, Í., Study of a high order family: local convergence and dynamics, *Mathematics* 7(225), 2019.
- [2] Chicharro, F.I., Cordero, A., Torregrosa, J.R., Dynamics and fractal dimension of Steffensen-type methods, *Algorithms* 8(2):271–279, 2015.
- [3] Akram, S., Zafar, F., Yasmin, N., An optimal eighth-order family of iterative methods for multiple roots, *Mathematics* 7(672), 2019.
- [4] Yun, B.I., A derivative free iterative method for finding multiple roots of nonlinear equations, *Applied Mathematics Letters* 22(12): 1859–1863, 2009.
- [5] Lee, M.Y., Kim, Y.I., Magreñán, Á.A., On the dynamics of tri-parametric family of optimal fourth-order multiple-zero finders with a weight function of the principal m th root of a function-to-function ratio, *Applied Mathematics and Computation* 315: 564–590, 2017.

- [6] Džunić, J., Petković, M.S., On generalized biparametric multipoint root finding methods with memory, *Journal of Computational and Applied Mathematics*, 255: 362–375, 2014.
- [7] Petković, M.S., Neta, B., Petković, L.D., Džunić, J., Multipoint Methods for Solving Nonlinear Equations. Amsterdam, Academic Press, 2013.
- [8] Chicharro, F.I., Cordero, A., Garrido, N., Torregrosa, J.R., Impact on stability by the use of memory in Traub-type schemes, *Mathematics* 8(274), 2020.
- [9] Traub, J.F., Iterative Methods for the Solution of Equations. New York, Prentice-Hall, 1964.
- [10] Chicharro, F.I., Cordero, A., Torregrosa, J.R., Dynamics of iterative families with memory based on weight functions procedure, *Journal of Computational and Applied Mathematics* 354:286–298, 2019.
- [11] Ortega, J.M., Rheinboldt, W.G., Iterative Solutions of Nonlinear Equations in Several Variables. New York, Academic Press, 1970.
- [12] Chicharro, F.I., Cordero, A., Garrido, N., Torregrosa, J.R., On the choice of the best members of the Kim family and the improvement of its convergence, *Mathematical Methods in the Applied Sciences* 43(14):8051–8066, 2020.
- [13] Blanchard, P., The dynamics of Newton's method, *Proceedings of the Symposia in Applied Mathematics* 49:139–154, 1994.
- [14] Revaney, R.L., An Introduction to Chaotic Dynamical Systems. Colorado, Addison-Wesley, 1989.
- [15] Campos, B., Cordero, A., Torregrosa, J.R., Vindel, P., A multidimensional dynamical approach to iterative methods with memory, *Applied Mathematics and Computation* 271:701–715, 2015.
- [16] Campos, B., Cordero, A., Torregrosa, J.R., Vindel, P., Stability of King's family of iterative methods with memory, *Journal of Computational and Applied Mathematics* 318:504–514, 2017.
- [17] Chicharro, F.I., Cordero, A., Torregrosa, J.R., Drawing dynamical and parameters planes of iterative families and methods, *The Scientific World Journal* ID 780153, 2013.

Predictive maintenance system for a dam based on real-time monitoring and diagnosis

Ernesto Colomer^{b1}, Carlos Canales^{b2}, Jesús Terradez^{b3} and Salvador Mateo^{b4}

(b) Institute of Multidisciplinary Mathematics,
Universitat Politècnica de València.

1 Introduction

In this paper, we describe the development of a novel predictive maintenance system valid for any type of dam (considering the wide variety that exists around the world) that, at low cost, continuously allows to monitor key parameters registered in situ and in real time (leaks, vibrations and seats). Unlike other solutions, the system has deep mathematical support to analyze and process the registered data, being able to carry out continuous and predictive diagnoses of the state of the infrastructure. With this, it offers a powerful tool for predictive maintenance, something that enables potential savings in dam maintenance tasks.

Thus, this paper highlights four objectives that have been overcome in the development of the system: 1) develop a water balance methodology with the support of image treatment to locate and quantify leaks, 2) develop a model of elements finite that represents the tensile-deformational state of the dam, 3) obtain the seats through the mathematical treatment of the images collected by a high-resolution camera, and 4) train and develop a Neural Network that offers a predictive character to the solution, offering the evolution of the main structural parameters of the dam.

2 Method

This section describes the methodology used to develop the system.

First, it was necessary to develop hardware for the data acquisition required by the system. The hardware was made up of two fundamental units: Measurement Unit and Gateway Unit. Regarding the Measurement Unit, it was responsible for collecting the necessary data for the correct operation of the software: leaks, vibrations and seats. As for the equipment necessary to measure leaks, it measures the variation of the reservoir volume and the flow of the incoming tributaries from a series of time-lapse cameras, as well as a meteorological station and a series

¹e-mail: ercoro1@cam.upv.es

²e-mail: carcagu1@ade.upv.es

³e-mail: jesterna@cam.upv.es

⁴e-mail: salmavil@upvnet.upv.es

of piezoresistive piezometers. For the measurement of vibrations, inertial sensors located at different points of the face of the dam were used. Finally, regarding the measurement of the seats, a high resolution 4K camera was used. Regarding the Gateway Unit, it acted as an access point to receive all the information that the Measurement Unit collects, in addition to having a microprocessor where all the data processing algorithm was inserted (software).

Once hardware sensors were validated, software with all the algorithms necessary to apply predictive maintenance techniques to the dam was developed. This was achieved through the use and training of an advanced Neural Network, for which previously it was necessary to develop three algorithms with the purpose of obtaining all the input values from the correct treatment of the data previously collected by the hardware. The development of these four algorithms (three previous algorithms and the neural network) is explained as follows:

1. Algorithm for the quantification and identification of leaks: an algorithm for the treatment of time-lapse camera images [1] was developed to detect the variation in volume of the dammed water and the incoming flow. This variation was obtained by means of photogrammetry corrected with a new digital treatment that achieves a good geometric coincidence of each one of the photographs, using a method of control points with transformation functions. Likewise, it was completed with an algorithm that solves the proposed water balance equation, using the piezoresistive piezometer readings as a support measure. The water balance is the difference between the flow that enters the system through tributaries and precipitation, and the one that leaves it by evaporation, spillways and leaks [2]. Thus, from the continuous modelling of this balance, it was possible to obtain the leaks that are occurring in the dam environment. In addition, to solve the equation, a Digital Terrain Model (DTM) was necessary to define the geometry of the reservoir basin and determine the storage volume and the surface of the sheet of water in an initial state. Considering also the previous placement of piezometers, the location where the leaks are occurring can be delimited.
2. Algorithm for the treatment of vibrations: it allowed establishing stress-strain relationships, using a finite element model (FEM) of the dam and its surroundings [3], to offer a diagnosis of the dam's structural state in real time. This tensile-deformational model captures the dynamic-structural response of the dam to different stresses. From the values that the FEM calculates in real time, continuous verifications could be made about the stability of the dam, evaluating, among other things, the stability against sliding and overturning. In addition, in the case of dams of loose materials, the last limit equilibrium method was applied to determine the liquefaction risk in the presence of seismic stresses (even of small magnitude). The model was designed in three stages: first, a pre-process that represents the geometry and initial conditions, second, a calculation that applies the non-linear equations, and lastly, a post-process that provides the results. of stresses and deformations at the points of interest of the dam.
3. Algorithm for seat measurement: an image treatment algorithm was applied capable of successively comparing the images collected by the 4K high-resolution camera, from a reference mark located at the crowning point of the dam. The technique [4], which has millimetre precision, considers the position of the marks between one photo and another afterwards, eliminating glare, and establishing a base layer and a detail layer.

4. Algorithm that allows to know the evolution of parameters that define the structural health status of the dam, using a predictive model based on an optimized neural network, that depends on a previous complex network [5]. The network took as an input the parameters obtained in terms of leaks, vibrations and seats, establishing possible connections between pairs of parameters through the comparison of all the data contained in each of the series. The set of connections between the parameters was compiled in a square matrix, where each of the values ranges from 0 (null connection) to 1 (full connection), depending on the intensity of the connection. For the training of the neural network, the numerical model of the dam discussed above was used. In this way, a large number of scenarios were generated to represent the greatest number of possible situations at different levels of failure, from small seats and leaks, to their full-level collapse, analyzing the values of leaks vibrations or seats that were obtained for each generated situation. In this way, it offered a prediction of the evolution of the characteristic structural parameters of the dam.

With hardware and software developed, it was necessary to enable a wireless communication between different devices and the Gateway Unit. Then, information could be sent to the cloud, here the results could be shown.

3 Results and discussion

For the validation of the system, two test groups were designed, a first group in charge of verifying the behaviour at a laboratory level, and a second group where the system is already assembled and installed in a dam.

In relation to the first group of tests, the hardware was verified, both the time-lapse camera and the 4K photographic camera, which recorded images in the field, for which its resolution, its capture angle, its battery consumption and data storage were positively evaluated. Piezoresistive piezometers and inertial sensors were tested with stimulation of known efforts in the laboratory, and the meteorological station contrasted their records with the measurements obtained by one belonging to the Agencia Estatal de Meteorología (AEMET). The communication was validated simulating real distances and interferences that occur in a dam in question.

The software was tested by introducing random inputs to the algorithms and corroborating the results. In the case of the leaks obtaining algorithms, a simulation was applied in a tank system for calibration. To check the operation of the settlement obtaining algorithms, images of elements whose settlement is controlled and known were introduced, and it was verified that the results obtained coincided. The tests related to the FEM and the neural network were made according to the measurements obtained as explained above, verifying that the high degree of accuracy of predictions.

Once the system was validated at the laboratory, the entire system was installed in a dam, placing in it hardware and communication elements that contain the solution. Thus, the recording and processing of the data began. Generally, the checks carried out were associated with verifying the overall functionality of the system.

With the devices installed, tests were made for the tightness, breakout force or autonomy of the batteries. All of them were satisfactory. Likewise, the accuracy and speed in sending information to the Gateway, and from the Gateway to the cloud, were also verified, demonstrating automation in the sample results. In addition, the high precision with which the results were

offered, the mode of instrumentation or the need for pre-development auscultations, among others, were fully defined.

4 Conclusions and future work

The conclusions that can be obtained from the development presented, with a view to directing future work, are the following:

- The system allows the implantation of a predictive philosophy to carry out the maintenance of the dam, which can mean potential savings in maintenance tasks.
- The system has simple and low-cost hardware that allows the variables related to leaks, vibrations and seats to be monitored simultaneously, thanks to an advanced mathematical contribution in the treatment of the data.
- The model obtains risks and attributes that other systems do not offer, such as liquefaction risk and the ability to locate leaks.
- The solution is valid to be applied in any type of dam.

References

- [1] Gleason C.J. et.al. “Technical note: semiautomated effective width extraction from time-lapse RGB imagery of a remote, braided Greenlandic river”. (2015).
- [2] J.I.López Moreno. “Estimación de pérdidas de agua por evaporación en embalse del Pirineo”. *Cuadernos de investigación geográfica / Geographical Research Letters*, ISSN 0211-6820, N^o 34, (2008).
- [3] Roberto Aguiar et.al. “Análisis de presas de gravedad con hormigón rodillado. Aplicación al proyecto jubones”. (2011).
- [4] Brownjohn, JMW; Xu, Y; Hester, D; et al. “Evaluating a video gauge for deformation measurements of two UK long span bridges”. (2016).
- [5] Santillán D., et. al. “Predicción de lecturas de aforos de filtraciones de presas bóveda mediante redes neuronales artificiales”. (2014).

Approximating the matrix hyperbolic tangent

Emilio Defez^{b1}, José Miguel Alonso^b, Javier Ibáñez^b, Pedro Alonso-Jordá[#] and Jorge Sastre[†]

(b) Instituto de Matemática Multidisciplinar,
Universitat Politècnica de València,

Camino de Vera s/n, 46022, Valencia, Spain,

(b) Instituto de Instrumentación para Imagen Molecular,
Universitat Politècnica de València,

Camino de Vera s/n, 46022, Valencia, Spain,

(#) Grupo Interdisciplinar de Computación y Comunicaciones,
Universitat Politècnica de València,

Camino de Vera s/n, 46022, Valencia, Spain,

(†) Instituto de Telecomunicación y Aplicaciones Multimedia,
Universitat Politècnica de València,

Camino de Vera s/n, 46022, Valencia, Spain.

1 Introduction. On hyperbolic matrix functions

Our objective is to find approximations of the hyperbolic tangent matrix function $\tanh(A)$, $A \in \mathbb{C}^{n \times n}$, defined as:

$$\tanh(A) = \sinh(A) (\cosh(A))^{-1} = (\cosh(A))^{-1} \sinh(A), \quad (1)$$

where

$$\cosh(A) = \frac{1}{2} (e^A + e^{-A}), \quad \sinh(A) = \frac{1}{2} (e^A - e^{-A}) \quad (2)$$

are defined in terms of the exponential matrix e^A . The hyperbolic tangent matrix function is used to give an analytical solution of the radiative transfer equation [1], in the study of calor transference [2, 3], in the study of symplectic systems [4, 5] or in graph theory [6].

In this work, we are going to focus on the study of two methods to compute the hyperbolic tangent matrix function $\tanh(A)$.

Method based on the exponential matrix. This method is based on the definition (2) and formula (1), from which the following matrix rational expression is immediately deduced:

$$\tanh(A) = (e^{2A} - I) (e^{2A} + I)^{-1} = (e^{2A} + I)^{-1} (e^{2A} - I), \quad (3)$$

where I denotes the identity matrix with the same dimension as A . Expression (3) reduces the approximation of the hyperbolic tangent matrix function to the approximation of the exponential matrix e^{2A} . There are profuse and well known literature about the approximation of this

¹e-mail: edefez@imm.upv.es

matrix function. In general, the most competitive methods used in practice are those based on polynomial approximations and on Padé rational approximations, where the first methods are generally more accurate and with less computational cost. There are different polynomial approximations of the exponential matrix based on distinct classes of matrix polynomials such as Taylor, see reference [7] for example, or Hermite, see reference [8]. Recently, a method based on Bernoulli matrix polynomials has been proposed in [9].

All these methods use the scaling and squaring technique. This technique is based on identity $e^A = \left(e^{2^{-s}A}\right)^{2^s}$ that satisfies the matrix exponential. In the scaling phase, an integer scaling factor s is taking and the approximation of $e^{2^{-s}A}$ is made using any of the proposed methods so that the required precision is obtained with the lowest possible computational cost. In the squaring phase, we obtain e^A by s repeated squaring.

Method based on the Taylor expansion. The other possibility for computing the matrix hyperbolic tangent function is to use the Taylor series of this function

$$\tanh(z) = \sum_{n \geq 1} \frac{2^{2n}(2^{2n} - 1)\mathcal{B}_{2n}z^{2n-1}}{(2n)!}, |z| < \frac{\pi}{2}, \quad (4)$$

where \mathcal{B}_{2n} are the Bernoulli's numbers. An algorithm have been developed based on a scaling and recovering technique based on the matrix formula

$$\tanh(2A) = 2 \left(I + \tanh^2(A)\right)^{-1} \tanh(A), \quad (5)$$

in accordance with the scalar formula

$$\tanh(2z) = \frac{2 \tanh(z)}{1 + \tanh^2(z)}.$$

Throughout this paper, we denote by $\sigma(A)$ the set of the eigenvalues of matrix $A \in \mathbb{C}^{n \times n}$. The matrix I_n (or I) denotes the matrix identity of order n . For a matrix $A \in \mathbb{C}^{n \times n}$, we design by $\rho(A)$ its spectral radius, defined as

$$\rho(A) = \max \{|\lambda|; \lambda \in \sigma(A)\}.$$

With $\lceil x \rceil$ we denote rounds to the nearest integer greater than or equal to x and $\lfloor x \rfloor$ rounds to the nearest integer less than or equal to x . The matrix norm $\|\cdot\|$ stands for any subordinate matrix norm; in particular $\|\cdot\|_1$ is the 1-norm.

This work is organized as follows. Section 2 presents a scaling and recovering Taylor algorithm. Section 3 shows numerical results and finally Section 4 gives some conclusions.

2 Taylor algorithm for computing the matrix hyperbolic tangent

Let

$$f(z) = \sum_{k \geq 1} \frac{2^{2k} (2^{2k} - 1) \mathcal{B}_{2k} z^{2k-1}}{(2k)!}$$

be the Taylor series expansion of the hyperbolic tangent function, with radius of convergence $r = \pi/2$. The matrix hyperbolic tangent can be defined for all $A \in \mathbb{C}^{n \times n}$ by the series

$$f(A) = \sum_{k \geq 1} \frac{2^{2k} (2^{2k} - 1) \mathcal{B}_{2k} A^{2k-1}}{(2k)!}, \rho(A) < \pi/2 \quad (6)$$

where \mathcal{B}_{2n} are the Bernoulli's numbers, defined by recursive expression

$$\mathcal{B}_0 = 1, \quad \mathcal{B}_k = - \sum_{i=0}^{k-1} \binom{k}{i} \frac{\mathcal{B}_i}{k+1-i}, k \geq 1. \quad (7)$$

To simplify the notation, we denote with

$$\tanh(A) = \sum_{k \geq 0} q_{2k+1} A^{2k+1}$$

the series expansions (6) and with

$$T_{2m+1}(A) = \sum_{k=0}^m q_{2k+1} A^{2k+1} = A \sum_{k=0}^m p_k B^k = AP_m(B) \quad (8)$$

the Taylor approximation of order $2m + 1$ of $\tanh(A)$, where $B = A^2$.

In the Paterson-Stockmeyer method, see [10], an integer m_k is chosen from the set

$$\mathbb{M} = \{2, 4, 6, 9, 12, 16, 20, 25, 30, \dots\},$$

and the powers B^i , $2 \leq i \leq q$, are calculated, where $q = \lceil \sqrt{m_k} \rceil$ or $q = \lfloor \sqrt{m_k} \rfloor$, such that

$$\begin{aligned} P_{m_k}(B) = & \quad (9) \\ & ((p_{m_k} B^q + p_{m_k-1} B^{q-1} + p_{m_k-2} B^{q-2} + \dots + p_{m_k-q+1} B + p_{m_k-q} I) B^q \\ & + p_{m_k-q-1} B^{q-1} + p_{m_k-q-2} B^{q-2} + \dots + p_{m_k-2q+1} B + p_{m_k-2q} I) B^q \\ & + p_{m_k-2q-1} B^{q-1} + p_{m_k-2q-2} B^{q-2} + \dots + p_{m_k-3q+1} B + p_{m_k-3q} I) B^q \\ & \dots \\ & + p_{q-1} B^{q-1} + p_{q-2} B^{q-2} + \dots + p_1 B + p_0 I. \end{aligned}$$

can be computed with the necessary accuracy and with minimal computational cost.

The computations of m and s are based on the relative backward error of approximating $\tanh(A)$ by means Taylor approximation (8). This error is defined as the matrix ΔA such that $\tanh(A + \Delta A) = AP_m(B)$. Using symbolic calculation, it can be verified that the backward error can be expressed as

$$\Delta A = A \sum_{k \geq m+1} c_k^{(m)} B^k.$$

Hence, the relative backward error can be bound as follows:

$$E_b(A) = \frac{\left\| A \sum_{k \geq m+1} c_k^{(m)} B^k \right\|}{\|A\|} \leq \left\| \sum_{k \geq m+1} c_k^{(m)} B^k \right\| \leq \sum_{k \geq m+1} c_k^{(m)} \beta_m^k \equiv h_m(\beta_m), \quad (10)$$

Table 1: Values of Θ_{m_k} , $1 \leq k \leq 7$.

$m_1 = 2$	$1.2718118261000 \times 10^{-5}$
$m_2 = 4$	$1.6575933006240 \times 10^{-3}$
$m_3 = 6$	$1.3352140114028 \times 10^{-2}$
$m_4 = 9$	$6.3719251200942 \times 10^{-2}$
$m_5 = 12$	$1.4760680276850 \times 10^{-1}$
$m_6 = 16$	$2.8505734287018 \times 10^{-1}$
$m_7 = 20$	$4.2841083927297 \times 10^{-1}$

where $\beta_m = \max \{ \|B^k\|^{1/k} : k \geq m+1, c_{m+1}^{(m)} \neq 0 \}$. Let Θ_m be

$$\Theta_m = \max \left\{ \theta \geq 0 : \sum_{k \geq m+1} |c_k^{(m)}| \theta^k \leq u \right\}, \quad (11)$$

where u is the unit roundoff in IEEE double precision arithmetic ($u = 2^{-53}$). The values Θ_m can be calculated with the required precision by using symbolic computations. Algorithm 1 computes the order $m_k \in \mathbb{M}$, $k_0 \leq k \leq M$, where m_{k_0} and m_M are the minimum and maximum order, respectively, of Taylor approximation, and the scaling factor s . For a matrix $A \in \mathbb{C}^{n \times n}$, the values Θ_{m_k} are given in Table 1. To simplify notation, we denote $\beta_k \equiv \beta_{m_k}$ and $\Theta_k \equiv \Theta_{m_k}$, $k_0 \leq k \leq M$. The scaled factor $s \geq 0$ is computed as

$$s = \max \left(0, \left\lceil \frac{1}{2} \log_2 \frac{\beta_k}{\Theta_k} \right\rceil \right). \quad (12)$$

With those values of m_k and s we obtain:

$$E_b(2^{-s}A) \leq h_{m_k}(4^{-s}\beta_k) < h_{m_k}(\Theta_k) < u,$$

i.e., the relative backward error of $T_{2m_k+1}(2^{-s}A)$ is lower than the unit roundoff u .

A MATLAB implementation, named *tanh_tayps*, has been developed to compute $\tanh(A)$ by the Taylor approximation (8) of the scaled matrix $2^{-s}A$, using the Paterson-Stockmeyer method for computing (8) and the Expression (5) for recovering $\tanh(A)$.

3 Numerical experiments

The following algorithms have been compare to evaluate the performance and accuracy of the two methods in charge of approximating the hyperbolic tangent matrix function.

- **tanh_exptayns**: MATLAB implementation based on Expression (3), using MATLAB function `exptaynsv3` for computing e^{2A} , see [11]. Maximum Taylor polynomial order allowed for the matrix exponential computation was $m = 30$.
- **tanh_tayps**: MATLAB implementation of Algorithm 1. A minimum order $m_{k_0} = 2$ and a maximum order $m_M = 16$ have been used, which correspond to Taylor polynomials with orders between 5 and 33.

Three tests, each of them composed of one of the following sets of matrices, were performed:

	TEST a)	TEST b)	TEST c)
$Er(tanh_tayps) < Er(tanh_exptayns)$	100	100	94, 83
$Er(tanh_tayps) > Er(tanh_exptayns)$	0	0	5, 17
$Er(tanh_tayps) = Er(tanh_exptayns)$	0	0	0
$P(tanh_tayps)$	1886	1600	938
$P(tanh_exptayns)$	1303	1200	677

Table 2: Relative error (Er) and number of matrix products (P) comparison between *tanh_exptayns* and *tanh_tayps* for the three tests.

a) **Diagonalizable complex matrices:** 100 diagonalizable complex matrices of size 128×128 .

These matrices are obtained as the result of $A = V \cdot D \cdot V^{-1}$, where D is a diagonal matrix (with real and complex eigenvalues) and V is an orthogonal matrix being $V = H/\sqrt{n}$, where H is a Hadamard matrix and n its number of rows or columns. As 1-norm, we have that $2.56 \leq \|A\|_1 \leq 256$. The matrix hyperbolic tangent was calculated “*exactly*” as $\tanh(A) = V \cdot \tanh(D) \cdot V^T$ thanks to the `vpa` MATLAB function.

b) **Non-diagonalizable complex matrices:** 100 non-diagonalizable complex matrices of size

128×128 . These matrices are computed as $A = V \cdot J \cdot V^{-1}$, where J is a Jordan matrix with complex eigenvalues whose modules are less than 5 and the algebraic multiplicity is randomly generated between 1 and 4. V is an orthogonal random matrix with elements in the interval $[-0.5, 0.5]$. As 1-norm, we have obtained that $45.13 \leq \|A\|_1 \leq 51.18$. The “*exact*” matrix cosine was computed as $\tanh(A) = V \cdot \tanh(J) \cdot V^{-1}$, by means of `vpa` function.

c) **Matrices from the Matrix Computation Toolbox (MCT) [12] and from the Eigtool**

MATLAB Package (EMP) [13]: 55 matrices of size 128×128 . These matrices have been chosen because they have highly different and significant characteristics from each other. We decided to scale these matrices so that they have 1-norm not exceeding 512. For that matrices, we have obtained $1 \leq \|A\|_1 \leq 489.3$. The “*exact*” matrix hyperbolic tangent has been calculated by using two methods:

- Find a matrix V and a diagonal matrix D so that $A = VDV^{-1}$ by using the `eig` MATLAB function. In this case $F_1 = V \tanh(D)V^{-1}$.
- Compute the Taylor approximation of the hyperbolic tangent function (F_2), with different polynomial orders (m) and the scaling parameters (s). The procedure is finished when the obtained result is the same for distinct values of m and s .

The “*exact*” matrix hyperbolic tangent is considered only if

$$\frac{\|F_1 - F_2\|}{\|F_1\|} < u.$$

The percentage of cases in which the relative error (Er) of *tanh_tayps* code is greater, lower or equal than *tanh_exptayns* is given in Table 2, together with the number of products (P) involved.

4 Conclusions

As deduced from the results given in Table 2, in the vast majority of cases, algorithm *tanh_tayps* is more accurate than *tanh_exptayns* although with a little more computational cost. This supports the recommendation made in [14] to use Taylor's development against other alternatives, whenever possible.

Acknowledgements

This work has been partially supported by Spanish *Ministerio de Economía y Competitividad* and European Regional Development Fund (ERDF) grants TIN2017-89314-P and by the *Programa de Apoyo a la Investigación y Desarrollo 2018* of the Universitat Politècnica de València (PAID-06-18) grants SP20180016.

References

- [1] Garij V. Efimov, Wilhelm Von Waldenfels, Rainer Wehrse, Analytical solution of the non-discretized radiative transfer equation for a slab of finite optical depth *Journal of Quantitative Spectroscopy and Radiative Transfer*, 53(1): 59–74, 1995.
- [2] Antti Lehtinen, Analytical treatment of heat sinks cooled by forced convection (PhD thesis). Tampere University of Technology, Finland, 2005.
- [3] Kaj Lampio, Optimization of fin arrays cooled by forced or natural convection (PhD thesis). Tampere University of Technology, Finland, 2018.
- [4] R. Hilscher, P. Zemánek, Trigonometric and hyperbolic systems on time scales *Dynamic Systems and Applications*, 18(3): 162–184, 2009.
- [5] P. Zemánek, New Results in Theory of Symplectic Systems on Time Scales (PhD thesis). Masarykova Univerzita, Czech Republic, 2011.
- [6] Ernesto Estrada, Grant Silver, Accounting for the role of long walks on networks via a new matrix function *Journal of Mathematical Analysis and Applications*, 449(2): 1581–1600, 2017.
- [7] J. Sastre, J. Ibáñez, E. Defez, P. Ruiz, New scaling-squaring Taylor algorithms for computing the matrix exponential *SIAM Journal on Scientific Computing*, 37(1): A439–A455, 2015.
- [8] J. Sastre, J. Ibáñez, E. Defez, P. Ruiz, Efficient orthogonal matrix polynomial based method for computing matrix exponential *Applied Mathematics and Computation*, 217(14): 6451–6463, 2011.
- [9] E. Defez, J. Ibáñez, P. Alonso-Jordá, José M. Alonso, J. Peinado, On Bernoulli matrix polynomials and matrix exponential approximation *Journal of Computational and Applied Mathematics*, <https://doi.org/10.1016/j.cam.2020.113207>.

- [10] Michael S. Paterson, Larry J. Stockmeyer, On the number of nonscalar multiplications necessary to evaluate polynomials *SIAM Journal on Computing*, 2(1): 60–66, 1973.
- [11] P. Ruiz, J. Sastre, J. Ibáñez, E. Defez, High performance computing of the matrix exponential *Journal of Computational and Applied Mathematics*, 291: 370–379, 2016.
- [12] N. J. Higham, The matrix computation toolbox, <http://www.ma.man.ac.uk/higham/mctoolbox>. 2002.
- [13] T.G. Wright, Eigtool, version 2.1. <http://www.comlab.ox.ac.uk/pseudospectra/eigtool>. 2009
- [14] James Corwell, William Dale Blair, Industry Tip: Quick and Easy Matrix Exponentials *IEEE Aerospace and Electronic Systems Magazine*, 35(5): 49–52, 2020.

Efficient finite element modelling of sound propagation in after-treatment devices with arbitrary cross section

F.D. Denia ^{b1}, E.M. Sánchez-Orgaz ^b, B. Ferrándiz ^b, J. Martínez-Casas ^b and L. Baeza ^b

(b) Centro de Investigación en Ingeniería Mecánica, Universitat Politècnica de València, Camino de Vera s/n, 46022 Valencia, Spain

(b) Instituto Univ. de Seguridad Industrial, Radiofísica y Medioambiental, Universitat Politècnica de València Camino de Vera s/n, 46022 Valencia, Spain

1 Introduction

The acoustic modelling of exhaust after-treatment devices, such as catalytic converters (CC) and diesel particulate filters (DPF) [1–3], usually requires the use of multidimensional numerical techniques to assess the influence of higher order modes on the sound attenuation performance [4]. Three-dimensional (3D) wave propagation can be considered through the finite element method (FEM). With a view to improving the computational expenditure of full 3D FEM, an efficient modelling technique is presented in this work to speed up transmission loss (TL) calculations in after-treatment devices with arbitrary cross section incorporating monoliths. The efficient modelling approach is based on the mode matching method [5–7], combining: (1) transversal pressure modes computed through a 2D FEM approach for devices with arbitrary but axially uniform cross section [8–10]; (2) compatibility conditions of the acoustic fields at the device geometric discontinuities. For the acoustic modelling of monoliths, these are replaced by four pole transfer matrices relating the acoustic fields at both sides of the monolithic region [1, 3, 4, 11–14]. Mode matching TL results are compared with full 3D FE simulations and experimental measurements for some selected configurations, showing a good agreement (results are not shown here for the sake of brevity). For a given accuracy, the computational efficiency of the mode matching technique proposed in this work improves that of full 3D FE calculations. TL improvements are achieved by suitable locations of a DPF inlet/outlet ducts. Next, a Genetic Algorithm (GA)-based optimization approach is used in order to improve the attenuation performance of the after-treatment device by varying the geometry as well as the monolith properties [15]. Results show that the optimized configuration outperforms the initial design at target frequencies [16].

Figure 1 shows the main features of the acoustic problem under consideration. Taking as reference the work presented in an earlier study [4], now the cross section of each duct/chamber is arbitrary, although axially uniform. Therefore, the transversal pressure modes are no longer available from an analytical point of view, being computed numerically in the current investigation. As indicated in the previous paragraph, a 2D FE-based numerical approach is considered

¹e-mail: fdenia@mcm.upv.es

to solve the transversal eigenvalue problem with a view to improving the computational expenditure.

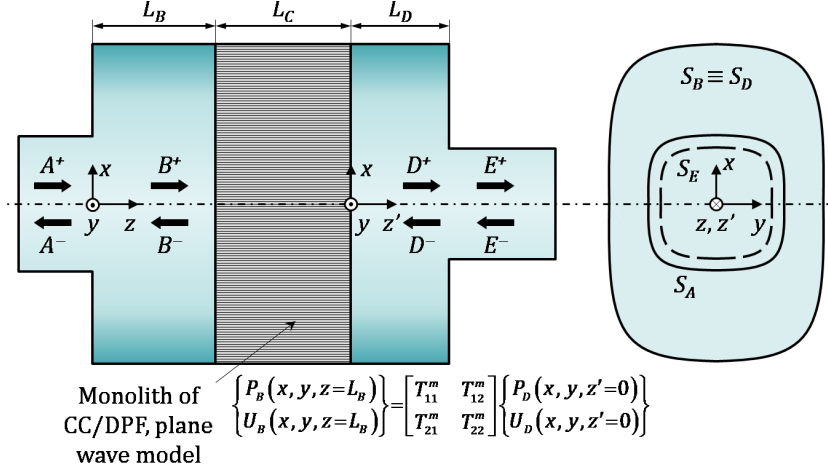


Figure 1: Exhaust after-treatment device scheme (CC/DPF) including different regions with arbitrary cross section involved in the acoustic propagation. The monolith is replaced by a transfer matrix and therefore only 1D sound propagation takes place in the capillary ducts.

In the mode matching method, the compatibility conditions of the acoustic fields (pressure and axial velocity) are expressed as weighted integrals, the weighting functions being a suitable selection of transversal pressure modes. To illustrate the approach, the pressure and velocity continuity at the inlet expansion yield

$$\int_{S_A} P_A(x, y, z=0) \psi_{A,s}(x, y) dS = \int_{S_A} P_B(x, y, z=0) \psi_{A,s}(x, y) dS, \quad (1)$$

$$\int_{S_A} U_A(x, y, z=0) \psi_{B,s}(x, y) dS = \int_{S_B} U_B(x, y, z=0) \psi_{B,s}(x, y) dS. \quad (2)$$

Expressing the acoustic fields as series expansions and taking into account the orthogonality properties of the pressure modes, the following algebraic relations are obtained:

$$(A_s^+ + A_s^-) \int_{S_A} \psi_{A,s}^2(x, y) dS = \sum_{n=1}^{N_m} (B_n^+ + B_n^-) \int_{S_A} \psi_{B,n}(x, y) \psi_{A,s}(x, y) dS, \quad (3)$$

$$\sum_{n=1}^{N_a} k_{A,n} (A_n^+ - A_n^-) \int_{S_A} \psi_{A,n}(x, y) \psi_{B,s}(x, y) dS = k_{B,s} (B_s^+ - B_s^-) \int_{S_A} \psi_{B,s}^2(x, y) dS. \quad (4)$$

Similar expressions to Eqs. (1)-(4) are obtained for the outlet contraction. Regarding the monolith, the combination of orthogonality and the plane wave transfer matrix provide

$$B_s^+ e^{-jk_{B,s}L_B} + B_s^- e^{jk_{B,s}L_B} = T_{11}^m (D_s^+ + D_s^-) + T_{12}^m (k_{D,s}/(\rho_0\omega)) (D_s^+ - D_s^-), \quad (5)$$

$$k_{B,s}/(\rho_0\omega) (B_s^+ e^{-jk_{B,s}L_B} - B_s^- e^{jk_{B,s}L_B}) = T_{21}^m (D_s^+ + D_s^-) + T_{22}^m (k_{D,s}/(\rho_0\omega)) (D_s^+ - D_s^-). \quad (6)$$

Note that, as indicated in [4], neither integrations nor modal summations appear in Eqs. (5) and (6). In addition, these equations do not depend on the geometry of the transversal cross section (provided that this is axially uniform) and relate directly wave amplitudes with

equal modal number [4].

2 Results and discussion

For illustration purposes, the approach described in the previous section is used to compute the TL-based acoustic attenuation for two DPF configurations with rectangular and triangular cross section, respectively (further details of the filter properties can be found in [2]). Rounded corners are included in both cases. Figure 2 shows information related to a number of transversal higher order modes considered in the numerical mode-matching approach.

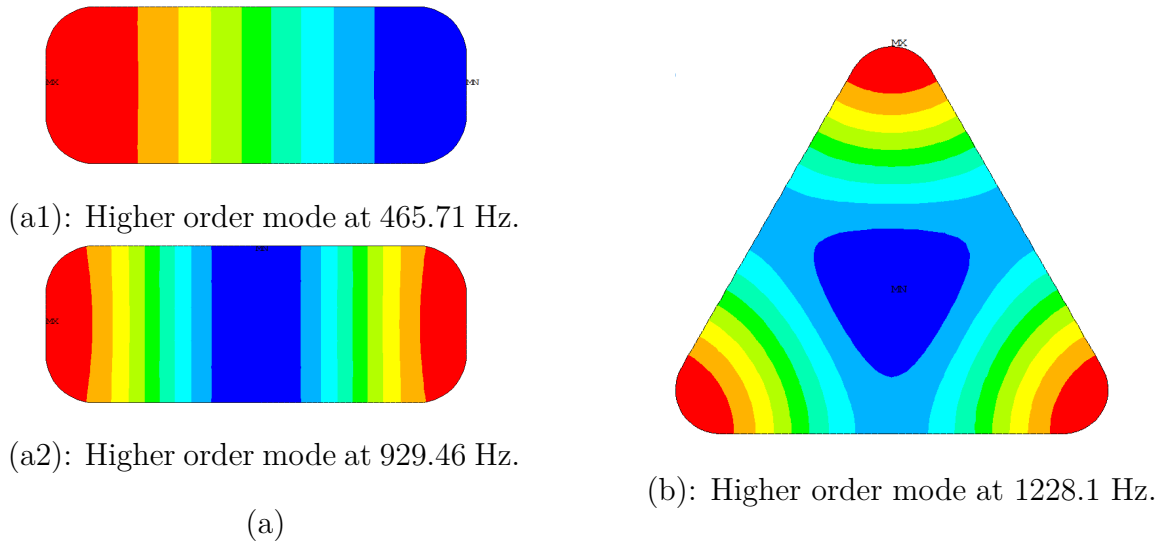


Figure 2: Example of pressure higher order modes: (a) rounded rectangular cross section; (b) rounded triangular cross section. Green regions correspond to nodal lines (zero pressure).

As a result, the acoustic performance of the DPF is first improved following the procedure described in the literature [5], where the inlet duct is centred and the outlet is located on the nodal line of the first relevant higher order mode (see transversal modes in Fig. 2) to avoid its propagation and the corresponding detrimental effect on the TL. In the case of a circular cross section with radius R , the radial coordinate of the nodal line is $0.6276R$ [5]; for the particular rectangular cross section considered in the current investigation, the nodal line is located at a lateral distance of 0.0913 m from the centre (see mode at 929.46 Hz in Fig. 2(a)); finally, for the triangular geometry the vertical distance of the nodal line from the bottom is 0.1824 m (see mode at 1228.1 Hz in Fig. 2(b)). The beneficial impact of these duct locations on the DPF acoustic attenuation is shown in Figure 3. To outperform the initial design TL at target frequencies, a GA-based optimization approach can also be used.

With this purpose, the corresponding scheme is set up using *Matlab R2018a*, in order to perform an acoustic optimization of an after-treatment device, by obtaining the optimal chamber dimensions and monolith properties with a view to maximizing its acoustic attenuation at the frequency range [20, 3200] Hz. A catalytic converter [1, 11–13] with cylindrical chamber is presented hereinafter as a case study, in order to show the validity of the proposed method. The modelling technique based on numerical mode matching, described in Section 1, is again

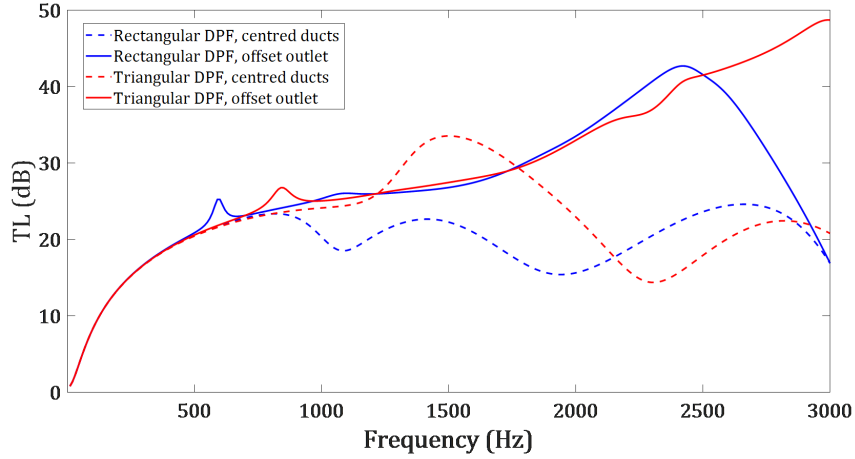


Figure 3: TL versus frequency for after-treatment devices (DPF) with rectangular and triangular cross sections. Example of attenuation improvement through outlet duct offset location.

used in order to speed up the calculation of the objective function f_0 relative to each individual during the GA optimization. f_0 is defined following [16] in order to maximize the mean TL at the target frequency range, while reducing its standard deviation to avoid steep behaviour.

Table 1 shows the range $[x_i^{min}, x_i^{max}]$ of each variable x_i involved in the GA-based optimization: lengths of the corresponding sections of the chamber L_B , L_C and L_D (see Figure 1); certain parameters of the monolith, such as resistivity R and porosity ϕ [1, 11–13]; and the position of the inlet and outlet ducts with respect to the centre of the chamber circular section: x_{in} , y_{in} , x_{out} and y_{out} .

On the other hand, attenuation increases with chamber radius R_C , and therefore this is subject to dimensional constraints. In this study, $R_C = 0.1275$ m, and so are the radii of the inlet and outlet ducts, $R_{in} = R_{out} = 0.0258$ m. Finally, the capillaries of the monolith can have a circular \bigcirc , square \square or triangular \triangle cross-section.

x_i	x_i^{min}	x_i^{max}	x_i^{opt}	x_i^1	x_i^2
L_B [m]	0.05	0.15	0.0535	0.0535	0.0535
L_C [m]	0.1	0.3	0.3	0.3	0.3
L_D [m]	0.05	0.15	0.0674	0.0674	0.0674
R [rayl/m]	500	1000	1000	1000	1000
ϕ	0.7	0.9	0.9	0.9	0.9
x_{in} [m]	-0.1	0.1	-0.0778	0	0
y_{in} [m]	-0.1	0.1	0.0111	0	0
x_{out} [m]	-0.1	0.1	0.0026	-0.0778	0
y_{out} [m]	-0.1	0.1	-0.008	0.0111	0
Capillary type			\triangle	\triangle	\triangle

Table 1: Range of each variable x_i .

Case \mathbf{x}^{opt} in Table 1 shows that resistivity and monolith length values converged to the maximum values, as expected. Figure 4 shows the TL calculations for \mathbf{x}^{opt} , showing that

attenuation is maximized by offsetting the inlet duct at approximately the nodal line of the first relevant higher order mode (as described in Section 1). As expected, additional analyses show that similar attenuation is obtained by decentring the outlet duct instead of the inlet duct (case \mathbf{x}^1), while attenuation worsens when centering both ducts (case \mathbf{x}^2).

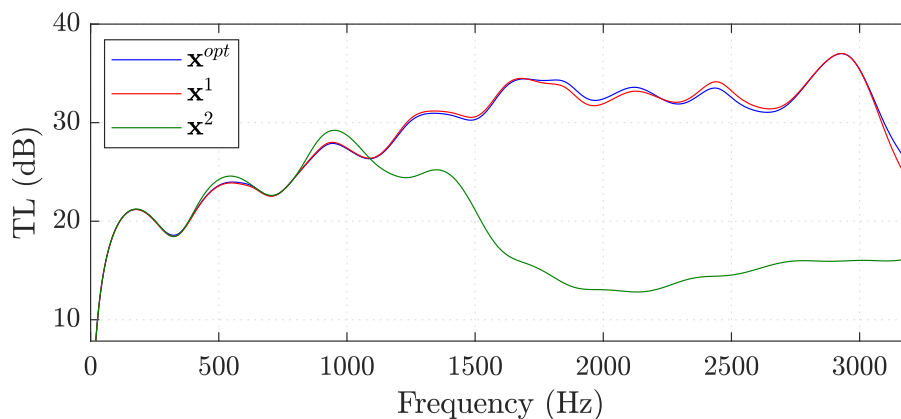


Figure 4: TL for circular cross-section CC with different inlet/outletduct configurations.

3 Conclusions and future work

An efficient modelling technique based on numerical mode matching has been presented in this work to speed up acoustic TL calculations in exhaust after-treatment devices (CC and DPF) with arbitrary cross section incorporating monoliths. The technique has been successfully combined with a GA-based optimization algorithm to obtain the optimal values of a number of design parameters (properties of the capillary ducts, type of monolith, chamber and monolith lengths, location of the inlet/outlet ducts on the chamber cross section, etc.). In future works, the effect of soot, mean flow and temperature gradients will also be studied.

Acknowledgements

The authors gratefully acknowledge the financial support of Ministerio de Ciencia, Innovación y Universidades–Agencia Estatal de Investigación through project TRA2017-84701-R and Generalitat Valenciana through project PROMETEO/2016/007.

References

- [1] Selamet, A., Easwaran, V., Novak, J.M., Kach, R.A., Wave attenuation in catalytic converters: reactive versus dissipative effects. *Journal of the Acoustical Society of America*, 103: 935–943, 1998.
- [2] Allam, S., Ábom, M., Sound propagation in an array of narrow porous channels with application to diesel particulate filters. *Journal of Sound and Vibration*, 291: 882–901, 2006.

-
- [3] Jiang, C., Wu, T.W., Xu, M.B., Cheng, C.Y.R., BEM modeling of mufflers with diesel particulate filters and catalytic converters. *Noise Control Engineering Journal*, 58: 243–250, 2010.
- [4] Denia, F. D., Martínez-Casas, J., Carballeira, J., Nadal, E., Fuenmayor, F. J., Computational performance of analytical methods for the acoustic modelling of automotive exhaust devices incorporating monoliths. *Journal of Computational and Applied Mathematics*, 33: 995–1006, 2018.
- [5] Selamet, A., Ji, Z.L., Radavich, P.M., Acoustic attenuation performance of circular expansion chambers with offset inlet/outlet: II. Comparison with experimental and computational studies. *Journal of Sound and Vibration*, 213: 619–641, 1998.
- [6] Kirby, R., Denia, F.D., Analytic mode matching for a circular dissipative silencer containing mean flow and a perforated pipe. *Journal of the Acoustical Society of America*, 122: 3471–3482, 2007.
- [7] Denia, F.D., Selamet, A., Fuenmayor, F.J., Kirby, R., Acoustic attenuation performance of perforated dissipative mufflers with empty inlet/outlet extensions. *Journal of Sound and Vibration*, 302: 1000–1017, 2007.
- [8] Kirby, R., A comparison between analytic and numerical methods for modelling automotive dissipative silencers with mean Flow. *Journal of Sound and Vibration*, 325: 565–582, 2009.
- [9] Fang, Z., Ji, Z.L., Numerical mode matching approach for acoustic attenuation predictions of double-chamber perforated tube dissipative silencers with mean Flow. *Journal of Computational Acoustics*, 22: article number 1450004, 2014.
- [10] Sánchez-Orgaz, E.M., Denia, F.D., Baeza, L., Kirby, R., Numerical mode matching for sound propagation in silencers with granular material. *Journal of Computational and Applied Mathematics*, 35: 233–246, 2019.
- [11] Denia, F.D., Antebas, A.G., Kirby, R., Fuenmayor, F.J., Multidimensional acoustic modelling of catalytic converters. *16th International Congress on Sound and Vibration*, Kraków, Poland, 2009.
- [12] Denia, F.D., Baeza, L., Kirby, R., Selamet, A., A multidimensional analytical study of sound attenuation in catalytic converters. *39th International Congress and Exposition on Noise Control Engineering (Inter-noise)*, Lisbon, Portugal, 2010.
- [13] Denia, F.D., Martínez-Casas, J., Baeza, L., Fuenmayor, F.J., Acoustic modelling of exhaust devices with nonconforming finite element meshes and transfer matrices. *Applied Acoustics*, 73: 713–722, 2012.
- [14] Sánchez-Orgaz, E.M., Denia, F.D., Martínez-Casas, J., Baeza, L., Efficient approaches for the acoustic modelling of automotive exhaust devices. Application to configurations incorporating granular materials and monoliths. *24th International Congress on Sound and Vibration*, London, UK, 2017.
- [15] Fonseca de Lima, K., Lenzi, A., Barbieri, R., The study of reactive silencers by shape and parametric optimization techniques. *Applied Acoustics*, 72: 142–150, 2011.

- [16] Ferrándiz, B., Denia, F.D., Martínez-Casas, J., Nadal, E., Ródenas, J.J., Topology and shape optimization of dissipative and hybrid mufflers. *Structural and Multidisciplinary Optimization*, 62: 269–284, 2020.

Iterative algorithms for computing generalized inverses

A. Cordero ^b, N. Garrido ^{b1}, P. Soto-Quiros [‡] and J.R. Torregrosa ^b

(b) Instituto de Matemáticas Multidisciplinar, Universitat Politècnica de València,
Camino de Vera, s/n, 46022, Valencia, España

(‡) Escuela de Matemática, Instituto Tecnológico de Costa Rica,
Cartago, 30101, Costa Rica

1 Introduction

Recently, many iterative methods without memory have been published for approximating the inverse or some generalized inverse of a complex matrix A of arbitrary order (see, for example [1–4] and the references therein). This topic has a significant role to play in many areas in Applied Sciences and Engineering, such as multivariate analysis, image and signal processing, approximation theory, cryptography, etc. (see [5]).

The discretization process of boundary problems or partial differential equations by means of divided difference technique or finite elements yields to an important number of linear systems to be solved. This statement is applicable both in equations with integer derivatives and in the case of fractional derivatives (see, for example [6, 7]). In these linear problems usually the matrix of coefficients is too big or ill-conditioned to be solved analytically. So, iterative methods can play a key role.

The main purpose of this chapter is to design a secant-type iterative scheme with memory, free for inverse operators and efficient under the point of view of cpu-time, for estimating the inverse of a non-singular complex matrix. We also argue the generalization of the proposed scheme for approximating the Moore-Penrose inverse of complex rectangular matrices. As far as we know, this is the first time that this kind of methods with memory are applied to estimate generalized inverses. This might be the first step to develop higher-order methods with memory in the future. This kind of schemes have proven to be very stable for scalar equations; we expect a similar performance in the case of matrix equations.

Let us consider a non-singular complex matrix A of size $n \times n$. The extension of the iterative methods for the real equation $g(x) = ax - 1 = 0$ to obtain the inverse of A , that is the zero of the matrix function $G(X) = X^{-1} - A$, give us the called Schulz-type schemes.

The most known of these schemes to estimate A^{-1} is Newton-Schulz method [8], whose iterative expression is

$$X_{k+1} = X_k(2I - AX_k), \quad k = 0, 1, \dots, \quad (1)$$

¹e-mail: neugarsa@upvnet.upv.es

where I denotes the identity matrix of size n . Schulz in [9] demonstrated that the eigenvalues of matrix $I - AX_0$ must be less than 1 to assure the convergence of scheme (1). Taking into account that the residuals $E_k = I - AX_k$ in each iteration of (1) satisfy $\|E_{k+1}\| \leq \|E_k\|^2$, Newton-Schulz method has quadratic convergence. In general, it is known that this scheme converges to A^{-1} with $X_0 = \alpha A^*$ or $X_0 = \alpha A$, where $0 < \alpha < 2/\rho(A^*A)$, $\rho(\cdot)$ denotes the spectral radius and A^* the conjugate transpose of A . Such schemes are also used for sensitivity analysis when accurate approximate inverses are needed for both square and rectangular matrices.

In this paper, we construct an iterative method with memory (that is, $k + 1$ iterate is obtained not only from the iterate k but also from other previous iterates) for computing the inverse of a nonsingular matrix. In the iterative expression of the designed method does not appear inverse operators. We establish the order of convergence of the proposed scheme and we extend it for approximating the Moore-Penrose inverse of rectangular matrices. For analyzing the order of convergence of an iterative method with memory, we use the concept of *R-order* introduced in [10] by Ortega and Rheinboldt.

From here, the work is organized as follows. In the next section, we describe how a secant-type method, free of inverse operators, is constructed for estimating the inverse of a nonsingular complex matrix, proving its order of convergence. In Section 3 we study the generalization of the proposed methods for computing the Moore-Penrose inverse of a rectangular complex matrix. Section 4 is devoted to the numerical test for analyzing the performance of the proposed schemes and to confirm the theoretical results. With a section of conclusions the paper is finished.

2 A secant-type method for matrix inversion

Let us recall that for an scalar nonlinear equation $g(x) = 0$, the secant method is an iterative scheme with memory such that

$$x_{k+1} = x_k - \frac{g(x_k)}{\alpha_k},$$

with α_k satisfying $g(x_k) - g(x_{k-1}) = \alpha_k(x_k - x_{k-1})$, $k \geq 0$, given x_0 and x_{-1} as initial approximations.

For a nonlinear matrix equation $G(X) = 0$, where $G : \mathbb{C}^{n \times n} \rightarrow \mathbb{C}^{n \times n}$, the secant method can be described as

$$X_{k+1} = X_k - A_k^{-1}G(X_k), \quad k \geq 0,$$

where X_0 and X_{-1} are initial estimations and being A_k a suitable linear operator satisfying

$$A_{k+1}(X_{k+1} - X_k) = G(X_{k+1}) - G(X_k) \Leftrightarrow A_{k+1}S_k = Y_k,$$

where $S_k = X_{k+1} - X_k$ and $Y_k = G(X_{k+1}) - G(X_k)$. So, it is necessary to solve, at each iteration, the linear system $A_{k+1}S_k = Y_k$. It is proven in [11] that, with this formulation, secant method converges to the solution of $G(X) = 0$.

Let us consider an $n \times n$ nonsingular complex matrix A . We want to construct iterative schemes for computing the inverse A^{-1} of A , that is, iterative methods for solving the matrix equation

$$G(X) = X^{-1} - A = 0. \tag{2}$$

The secant method was adapted by Monsalve et al. in [11] to estimate the solution of (2), that is the inverse of A , when the matrix is diagonalizable. The secant method applied to

$G(X) = X^{-1} - A$ (see [11]) gives us:

$$\begin{aligned} X_{k+1} &= X_k - S_{k-1} [G(X_k) - G(X_{k-1})]^{-1} G(X_k) \\ &= X_k - (X_k - X_{k-1}) [X_k^{-1} - X_{k-1}^{-1}]^{-1} (X_k^{-1} - A). \end{aligned} \quad (3)$$

Now, we extend the result presented in [11] to any nonsingular matrix, no necessarily diagonalizable. We propose the secant-type method:

$$X_{k+1} = X_{k-1} + X_k - X_{k-1} A X_k, \quad k = 0, 1, 2, \dots \quad (4)$$

being X_0 and X_{-1} initial approximations given.

The analysis of the convergence of iterative method with memory (4) is presented in the following result.

Theorem 1 *Let $A \in \mathbb{C}^{n \times n}$ be a nonsingular matrix, with singular value decomposition $U^* A V = \Sigma$. Let X_0 and X_{-1} be such that $V^* X_{-1} U$ and $V^* X_0 U$ are diagonal matrices. Then, sequence $\{X_k\}$, obtained by (4), converges to A^{-1} with super-linear convergence.*

3 A secant-type method for approximating the Moore-Penrose inverse

Now, we would like to extend the proposed iterative scheme for computing the Moore-Penrose inverse [5] of a $m \times n$ complex matrix A , denoted by A^\dagger . It is the unique $n \times m$ matrix X satisfying the equations

$$A X A = A, \quad X A X = X, \quad (A X)^* = A X, \quad (X A)^* = X A.$$

If $\text{rank}(A) = r \leq \min\{m, n\}$, by using the singular value decomposition of A , we obtain

$$A = U \begin{bmatrix} \Sigma & 0 \\ 0 & 0 \end{bmatrix} V^*,$$

being $\Sigma = \text{diag}(\sigma_1, \sigma_2, \dots, \sigma_r)$, $\sigma_1 \geq \sigma_2, \dots, \geq \sigma_r > 0$, U and V are unitary matrices with $U \in \mathbb{C}^{m \times m}$ and $V \in \mathbb{C}^{n \times n}$. It is also known that

$$A^\dagger = V^* \begin{bmatrix} \Sigma^{-1} & 0 \\ 0 & 0 \end{bmatrix} U,$$

where $\Sigma^{-1} = \text{diag}(1/\sigma_1, 1/\sigma_2, \dots, 1/\sigma_r)$.

The convergence of method (4) for Moore-Penrose inverse is established in the following result.

Theorem 2 *Let $A \in \mathbb{C}^{m \times n}$ be a matrix with $\text{rank}(A) = r$, with singular value decomposition*

$$U^* A V = \begin{pmatrix} \Sigma & 0 \\ 0 & 0 \end{pmatrix}.$$

Let X_{-1} and X_0 be initial estimations such that

$$V^* X_{-1} U = \begin{pmatrix} \Sigma_{-1} & 0 \\ 0 & 0 \end{pmatrix} \quad \text{and} \quad V^* X_0 U = \begin{pmatrix} \Sigma_0 & 0 \\ 0 & 0 \end{pmatrix},$$

being Σ_{-1} and Σ_0 diagonal matrices of size $r \times r$. Then, sequence $\{X_k\}$, obtained by (4), converges to A^\dagger with super-linear order of convergence.

Method	m	n	Iter	$\ X_{k+1} - X_k\ _2$	ACOC
Newton-Schulz	20	10	14	$9.7e - 12$	2.0005
Secant	20	10	13	$9.9e - 10$	1.6199
Newton-Schulz	300	400	21	$2.03e - 11$	2.0007
Secant	300	400	27	$1.4e - 7$	1.6267
Newton-Schulz	500	600	23	$3.8e - 9$	2.0028
Secant	500	600	31	$5.2e - 10$	1.6197
Newton-Schulz	1000	900	25	$4.5e - 8$	2.0055
Secant	1000	900	36	$2.5e - 9$	1.6205

Table 1: Results for approximating the Moore-Penrose inverse of a rectangular random matrix

4 Numerical experiments

In this section, we will check the behavior for the calculation of the inverse and the Moore-Penrose inverse of different test matrices A , using the secant method, which we compared with the Newton-Schulz scheme (1). Numerical computations have been carried out in Matlab R2018b with a processor Intel(R) Xeon(R) CPU E5-2420 v2 at 2.20GHz. As stopping criterion we have used $\|X_{k+1} - X_k\|_2 < 10^{-6}$ or $\|F(X_{k+1})\|_2 < 10^{-6}$.

In order to numerically check the theoretical results, Jay introduced in [13] the order of approximate computational convergence (COC), defined as

$$\text{order} \approx \text{COC} = \frac{\ln(\|F(X_{k+1})\|_2 / \|F(X_k)\|_2)}{\ln(\|F(X_k)\|_2 / \|F(X_{k-1})\|_2)}.$$

In a similar way, the authors presented in [14] another numerical approximation of the theoretical order, denoted by ACOC, and defined as

$$\text{order} \approx \text{ACOC} = \frac{\ln(\|X_{k+1} - X_k\|_2 / \|X_k - X_{k-1}\|_2)}{\ln(\|X_k - X_{k-1}\|_2 / \|X_{k-1} - X_{k-2}\|_2)}.$$

We use indistinctly any of these computational order estimates, to show the accuracy of these approximations on the proposed method. In case of vector COC (or ACOC) is not stable, we write '-' in the corresponding table.

Example 1 *In this example, matrix A is a $m \times n$ random matrix for different values of m and n . The initial estimation used for the Newton-Schulz scheme is $X_0 = A^T / \|A\|^2$ and for the secant method $X_{-1} = \frac{A^T}{\|A\|^2}$ and $X_0 = 0.5 \frac{A^T}{\|A\|^2}$.*

Table 1 shows the results obtained by Newton-Schulz and secant-type method for the different random matrices, the number of iterations, the residuals and the value of ACOC. The results are in concordance with the order of convergence of each scheme, in spite of being non-square matrices. Both methods give us an approximation of the Moore-Penrose inverse of A .

Example 2 *In this example we are going to test Newton-Schulz and secant methods on several known square matrices of size $n \times n$, constructed by using different Matlab functions. Specifically, the test matrices are:*

- a) $A = \text{gallery}('ris', n)$. Hankel matrix of size $n \times n$

Method	Matrix	n	Iter	$\ X_{k+1} - X_k\ _2$	$\ F(X_{k+1})\ $	COC
Newton-Schulz	Lehmer	10	18	$3.5e - 7$	$6.3e - 15$	-
Secant	Lehmer	10	20	$3.9e - 9$	$1.7e - 11$	1.6164
Newton-Schulz	Hankel	100	8	$1.1e - 5$	$1.2e - 11$	1.9993
Secant	Hankel	100	11	$1.9e - 12$	$4.4e - 13$	1.6180
Newton-Schulz	Toeplitz	300	9	$1.7e - 9$	$2.5e - 15$	1.9975
Secant	Toeplitz	300	11	$6.3e - 11$	$6.4e - 11$	1.6182
Newton-Schulz	Leslie	400	22	$4.3e - 5$	$2.3e - 13$	1.9995
Secant	Leslie	400	33	$4.2e - 12$	$1.0e - 14$	1.6177

Table 2: Results for approximating the inverse of classical square matrices

- b) $A = \text{gallery}('grcar', n)$. Toeplitz matrix of size $n \times n$
- c) $A = \text{gallery}('lehmer', n)$. Symmetric and positive definite matrix of size $n \times n$, $a_{i,j} = i/j, \forall i, j$
- d) $A = \text{gallery}('leslie', n)$. Leslie matrix of size $n \times n$. This type of matrices appears in problems of population models
- e) $A = \text{gallery}('invo', n)$. Matrix ill-conditioned of size $n \times n$, such that $A^2 = I$.

By using the stopping criterion

$$\|X_{k+1} - X_k\|_2 < 10^{-10} \quad \text{or} \quad \|F(X_{k+1})\|_2 < 10^{-10}$$

and the initial matrix $X_{-1} = \frac{A^T}{\|A\|^2}$ and $X_0 = 0.5 \frac{A^T}{\|A\|^2}$, we obtain the numerical results that appear in Table 2. In this cases, as in the previous ones, the proposed method shows good performance in terms of stability, precision and number of iterations needed. We must take into account that both schemes have different orders of convergence, which is displayed in Table 2.

5 Conclusions

An iterative method with memory for approximating the inverse of nonsingular square complex matrices and the Moore-Penrose inverse of rectangular complex matrices is presented. As far as we know, it is the first time that a scheme with memory is employed to approximate the solution of nonlinear matrix equations. The proposed scheme is free of inverse operators and its iterative expression is simple, therefore, it is computationally efficient. From particular initial approximations, the convergence is guaranteed for all matrices, without conditions. Numerical tests allow us to analyze the performance of the proposed scheme and confirm the theoretical results.

Acknowledgements

This research was supported in part by PGC2018-095896-B-C22 (MCIU/AEI/FEDER, UE) and in part by VIE from *Instituto Tecnológico de Costa Rica* (Research #1440037).

References

- [1] Li H.B.; Huang T.Z.; Zhang Y.; Liu X.P.; Gu T.X. Chebyshev-type methods and preconditioning techniques, *Appl. Math. Comput.* **2011**, 218, 260–270.
- [2] Soleymani, F.; Stanimirović, P.S. A higher order iterative method for computing the Drazin inverse, *Scientific World Journal* **2013**, 2013, Article ID 708647.
- [3] Toutounian, F.; Soleymani, F. An iterative method for computing the approximate inverse of a square matrix and the Moore-Penrose inverse of a nonsquare matrix, *Appl. Math. Comput.* **2015**, 224, 671–680.
- [4] Soleymani, F.; Salmani, H.; Rasouli, M. Finding the Moore-Penrose inverse by a new matrix iteration, *Appl. Math. Comput.* **2015**, 47, 33–48.
- [5] Ben-Israel A., Greville T.N.E. *Generalized inverses*, Second ed., Springer: New York, NY, 2003.
- [6] Gu, X.; Huang, T.; Ji C.; Carpentieri, B.; Alikhanov, A.A. Fast iterative method with a second-order implicit difference scheme for time-space fractional convection-diffusion equation, *J. Sci. Comput.* **2017**, 72(3), 957–985.
- [7] Li, M.; Gu, X; Huang, C.; Fei, M.; Zhang, G. A fast linearized conservative finite element method for the strongly coupled nonlinear fractional Schrödinger equations, *J. Comput. Phys.* **2018**, 358, 256–282.
- [8] N. J. HIGHAM, *Functions of matrices: Theory and Computation*. SIAM, Philadelphia, 2008.
- [9] Schulz, G. Iterative Berechnung der reziproken matrix, *Z. Angew. Math. Mech.* **1933**, 13, 57–59.
- [10] Ortega, J.M.; Rheinbolt, W.C. *Iterative Solutions of Nonlinear Equations in Several Variables*, Academic Press, Inc. 1970.
- [11] Monsalve, M.; Raydan M. A secant method for nonlinear matrix problem, *Lecture Notes in Electrical Engineering*, **2011**, 80, 387–402.
- [12] Wang, G.; Wei, Y.; Qiao, S. *Generalized inverses*; Science Press: New York, NY, USA, 2004.
- [13] Jay, L. A note of Q-order of convergence, *BIT*, **2001**, 41, 422–429.
- [14] Cordero, A; Torregrosa, J.R. Variants of Newton’s method using fifth-order quadrature formulas, *Appl. Math. Comput.* **2007**, 190, 686–698.

Communities' detection in weakly connected directed graphs

J. M. Montañana^{b1}, A. Hervás^{‡2}, and P. P. Soriano^{#3}

(b) High Performance Computing Center Stuttgart (HLRS),
University of Stuttgart, Nobelstraße 19, 70569 Stuttgart, Germany,

(‡) Instituto Universitario de Matemática Multidisciplinar,
Universitat Politècnica de València,

Camino de Vera, s/n 46022 Valencia, Spain,

(#) SEPyC, Universitat Politècnica de València,
Camino de Vera, s/n 46022 Valencia, Spain.

Three years ago we have presented an algorithm for detection of directional communities in a directed graph [1], oriented to the process of access to the SUPE [2, 3]. Two years ago, we have presented an algorithm for the generation of directed graphs with dispersed nodes and weighted edges. Neural networks, social networks, the contagion of diseases, bibliographies, the student access to the SUPE, the public transport networks on trains and bus lines; or the trophic chains [7–9], there are problems whose modeling leads to weakly connected directed graph or, in the worst case, directed and disconnected graph. In this paper, we will analyze the behavior of the algorithms proposed in [10] using generator benchmarks for weakly connected directed graphs [11].

1 Introduction

Many complex systems can be modeled by graphs and networks, [2, 3, 7–9] so that the elements are represented by vertices and the relations between elements by edges. These edges can be directed if the relationships are one-way, or non-directed if they are both ways. Additionally, these edges can be assigned a numerical value that we will call the weight or capacity of the edge. The number of edges that the graph has represents another factor to take into account, as it indicates whether the network is dispersed or highly connected. The study of those subgraphs whose vertices have relatively many connections themselves with respect to the graph structure, the so-called communities, is also interesting. In some problems, the study of communities allows quantitative and qualitative approaches and obtaining some knowledge about the structure of the graph [1, 4–6, 12].

¹montanana@hls.de

²ahervas@mat.upv.es

³psoriano@upvnet.upv.es

There is an extensive literature in the study of communities, mostly focused on non-directed graphs, [4,8,9,12] in our case we focus our work on the study of communities in directed graphs, weakly connected, with weights on the edges. These weights can be homogeneous, well balanced, or poorly conditioned. [1,3,10,11]. A wide range of interesting problems is offered to us if we want to accept the challenge.

2 Method

The existing algorithms are not capable of correctly detecting the communities in these types of graphs when there are many edges connecting some communities with other ones. For this reason, we seek to propose a method that allows removing those edges.

The method we propose has two phases. The first one targets to detect community centers. In a second phase, we prune the weak and less important edges responsible for the incorrect community detection by the existing detection algorithms.

The method proposed in [12] considers the centers of the communities to those vertices that maximize the product of the local density and geometric distance between the other community centers. In particular, they define it as the difference between the distance and a value of threshold d_c , like the following equation. Although, it is unclear who those authors find the optimal value for d_c , because in their paper they state that their evaluated cases are insensitive to that parameter d_c .

$$\rho_i = \sum \chi(d_{ij} - d_c) \text{ where } \chi(d_{ij} - d_c) = 1 \text{ when } d_{ij} - d_c < 0, \text{ and } \chi(d_{ij} - d_c) = 0 \text{ otherwise. (1)}$$

However, this proposal does not work in the weakly connected directed graphs that are the subject of our studies.

Therefore, we consider defining another distance function. We replace the geometric distance term by the distances weighted. We define it as the minimum of the sum of the inverse of the weights of the possible paths that joins two vertices i and j :

$$d_{ij} = \frac{1}{w_{ix}} + \frac{1}{w_{xy}} + \dots + \frac{1}{w_{zj}} \quad (2)$$

In the **first phase**, we obtain a set of *potential community centers*. These are those vertices with a smaller average distance with the rest of the vertices in the graph than the vertices in their environment.

In the **second phase** of the method consists of a *pruning process* of the lower weight edges. The process consists of cutting a single edge on each minimum distance path between two potential community centers only if that edge has a weight smaller than certain **pruning percentage** of the average weight of the edges on that path. This process has to be applied first to the closer pairs of potential centers, and later the more distant ones. In this way, it will be eliminated the edges that have relatively less influence on their area, although they have greater weight than edges in other areas of the graph.

3 Results and discussion

In order to evaluate the algorithm, we use a generator of weakly connected directed graphs [11], on which we apply our proposal.

We evaluated different sizes of weakly connected directed graphs generated with different seeds. The graphs had been generated with the open-source tool available at [13]. The experiments consisted of generating synthetic graphs with additional edges between the communities. We apply the Girvan Newman [14] before and after pruning edges.

The next figures show the communities detected on graphs of different sizes. Figures 1 and 2 show 8 communities graphs, and the Figures 3 and 4 show 20 and 50 communities graphs.

The results show in all cases that the expected communities be detected correctly. The verification of the correctness of the detection can be done because the synthetic generator provides the graphs and their expected communities with the list of which vertices belong to each community.

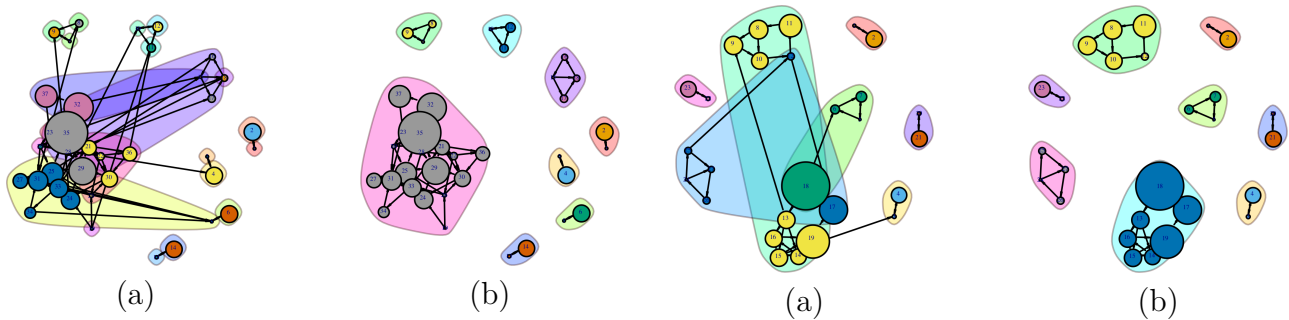


Figure 1: (a) Graph with 20% additional edges between communities, (b) graph where were detected 8 communities after pruning edges.

Figure 2: (a) Graph with 20% additional edges between communities, (b) graph where were detected 8 communities after pruning edges.

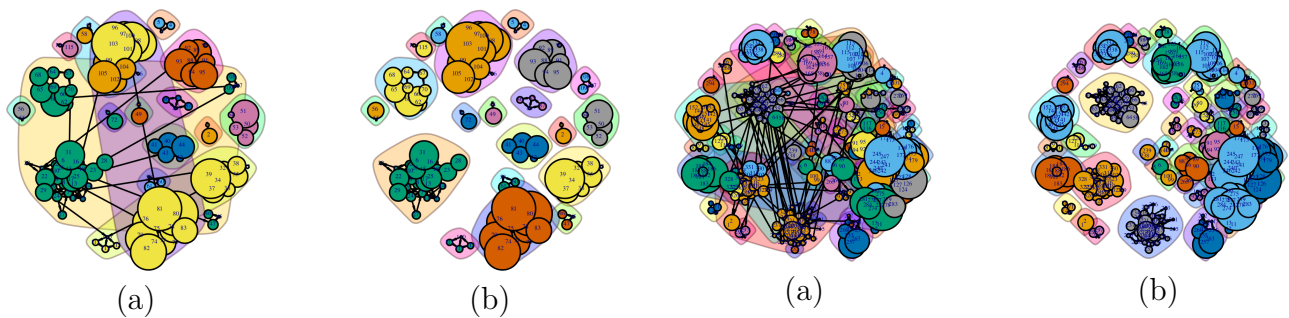


Figure 3: (a) Graph with 20% additional edges between communities, (b) graph where were detected 20 communities after pruning edges.

Figure 4: (a) Graph with 20% additional edges between communities, (b) graph where were detected 50 communities after pruning edges.

Our next step was to run a test with synthetic graphs. For this, we consider weakly connected directed graphs with twenty communities, which were generated with a free open source synthetic generator [11]. Figure 5 shows the distribution of edges by weight on one of the evaluated graphs with 20 initial communities. It is important to mention that the weight of 65% of the paths is lower or equal to 10 units.

The evaluation of the proposed algorithm consists of increasing a 10% of the edges in the graph with edges all with the same weight connecting randomly selected vertices. The weight of the noise edges on the evaluations ranges from 0.01 to 10 units. The reason is that most of

the existing edges in the graphs are in this interval, and the pruning algorithm will not be able to prune edges with weight too much high than the average weight. We will refer to the added edges as noise.

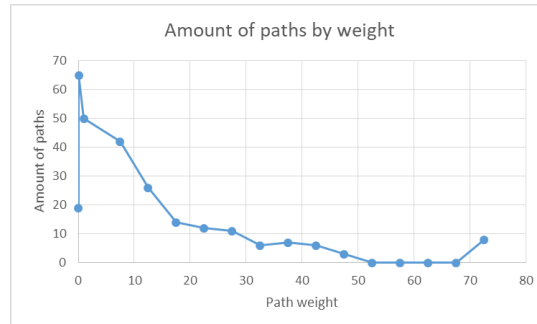


Figure 5: Distribution of edges by weight.

For the graphs thus obtained we apply the pruning algorithm, with a percentage pruning coefficient ranging between 0% and 10%. Some selected results can be seen in Tables 1.a, 1.b and 1.c.

Table 1 shows the number of disjoint communities after applying the proposed algorithm for different weights of the noise edges and the pruning percentage. Values equal to 20, highlighted with green font, are the optimum cases when all the noise edges between the initial communities are pruned. Values below 20 indicate that it was not removed all the added noise edges between communities, depending on the case, there may be a community detection algorithm that detects the correct communities. If the values exceed 20, highlighted in red, it means that the pruning level was excessively high, since we have fractured the graph obtaining more communities than actually exist.

Among the 200 synthetic evaluated cases, the most common results are similar to the ones shown in Tables 1.a and 1.b. These results show that increasing the weight of the noise requires increasing the pruning percentage to achieve similar results. However, there is a percentage level from which valid edges get pruned and initial communities to get broken. That case is shown in Table 1.b, where shows that the pruning algorithm should not be used for a higher pruning percentage than 5% when the noise weight is higher than 0.5.

Other less frequent cases, less than 5% of the cases, shown results similar to the Table 1.c. In those cases, the algorithm was only able to remove the noise between communities when the weight was small compared with the weight of the edges in the graph. This happens when the algorithm doesn't prune edges because is not able to differentiate between the valid and the noise edges.

From our experience, we recommend using the proposed algorithm to help the existing community detection algorithms, and not use it for the detection of communities. We also recommend not to use a higher pruning percentage than 5% when the noise weight be unknown, which is a frequent case when processing data from real scenarios.

		Pruning percentage																								
		none	1%	2%	3%	4%	5%	6%	7%	8%	9%	10%														
Weight of noise edges	10.0	6	6	6	6	7	7	7	7	7	7	7	Weight of noise edges	10.0	7	8	8	9	9	9	10	10	10	12	12	
	5.0	6	6	6	6	6	7	8	8	8	8	8		5.0	7	8	9	9	8	9	10	10	11	12	12	
	1.0	6	6	6	6	13	17	17	15	16	18	19		1.0	7	8	8	12	15	17	18	20	21	21	11	
	0.9	6	6	6	6	14	17	17	16	16	19	19		0.9	7	8	8	11	16	17	18	21	21	21	11	
	0.8	6	6	6	6	17	18	16	16	16	19	19		0.8	7	8	8	12	15	18	21	21	21	21	11	
	0.7	6	6	6	6	17	18	18	18	15	19	19		0.7	7	8	8	15	17	18	21	21	21	21	11	
	0.6	6	6	6	7	18	18	17	15	15	19	19		0.6	7	8	8	15	17	19	21	21	21	21	11	
	0.5	6	6	13	18	18	18	16	17	16	19	19		0.5	7	8	7	11	20	20	20	20	20	20	11	
	0.4	6	6	15	15	18	16	16	17	16	19	19		0.4	7	8	7	13	16	20	20	20	20	20	12	
	0.3	6	6	15	15	13	16	16	19	16	19	19		0.3	7	9	7	11	17	20	20	20	20	20	20	
	0.2	6	11	15	13	13	16	16	20	16	19	19		0.2	7	9	20	17	20	20	20	20	20	20	17	
	0.1	6	15	13	13	20	20	20	20	20	20	20		0.1	7	20	20	15	20	20	20	20	20	17	20	20
	0.01	6	20	20	20	20	20	20	20	20	20	20		0.01	7	20	19	19	19	19	19	19	19	19	19	
	none	20	20	20	20	20	20	20	20	20	20	20		none	20	20	20	20	20	20	20	20	20	20	20	

(a)

(b)

		Pruning percentage																					
		none	1%	2%	3%	4%	5%	6%	7%	8%	9%	10%											
Weight of noise edges	10.0	6	6	6	7	7	7	7	7	7	7	Weight of noise edges	10.0	6	6	6	7	7	7	7	7	7	7
	5.0	6	6	6	7	7	7	7	7	7	7		5.0	6	6	6	7	7	7	7	7	7	7
	1.0	6	6	6	7	7	7	7	7	7	7		1.0	6	6	6	7	7	7	7	7	7	7
	0.9	6	6	6	7	7	7	7	7	7	7		0.9	6	6	6	7	7	7	7	7	7	7
	0.8	6	6	6	7	7	7	7	7	7	7		0.8	6	6	6	7	7	7	7	7	7	7
	0.7	6	6	6	7	7	7	7	7	7	7		0.7	6	6	6	7	7	7	7	7	7	7
	0.6	6	6	6	7	7	7	7	7	7	7		0.6	6	6	6	7	7	7	7	7	7	7
	0.5	6	6	6	7	7	7	7	7	7	7		0.5	6	6	6	7	7	7	7	7	7	7
	0.4	6	6	6	7	7	7	7	7	7	7		0.4	6	6	6	7	7	7	7	7	7	7
	0.3	6	6	6	7	7	7	7	7	7	7		0.3	6	6	6	7	7	7	7	7	7	7
	0.2	6	6	6	11	11	20	20	20	20	20		0.2	6	6	6	11	11	20	20	20	20	20
	0.1	6	6	18	20	20	20	20	20	20	20		0.1	6	6	18	20	20	20	20	20	20	20
	0.01	6	20	20	20	20	20	20	20	20	20		0.01	6	20	20	20	20	20	20	20	20	20
	none	20	20	20	20	20	20	20	20	20	20		none	20	20	20	20	20	20	20	20	20	20

(c)

Table 1: Number of disjoint communities after applying the proposed algorithm for different weights of the noise edges and the pruning percentage. Each table corresponds to a different synthetic case generated with a different seed. (a) a scenario where increasing the pruning coefficient increases the number of disjoint communities. (b) a scenario where the pruning edges with a coefficient higher than 5% broke communities that should not be broken. (c) not significant amount of edges can be pruned and communities remain connected.

4 Conclusions and future work

In this paper, we have proposed a novel edge pruning method for the improve the communities' detection in weakly connected directed graphs. Our results showed that the Girvan-Newmann algorithm to obtain a correct detection of communities after applying the pruning method in the evaluated cases but not before that.

We believe that the proposal in this paper is a valuable contribution for the researchers in the area, and can be used in combination with any other existing algorithm.

As future work, we plan to run a more extensive evaluation and process the obtained graphs with different community detection algorithms.

References

- [1] Hervás A., Soriano P.P., Capilla R., and Peinado J. An algorithm to obtain directional communities in a directed graph. in Proceedings of the Mathematical Modelling in Engi-

neering & Human Behaviour 2016. 18th Edition of the Mathematical Modelling Conference Series at the Institute for Multidisciplinary Mathematics pp 347-352, 2016

- [2] Hervás, A.; Jiménez-García, A. ; Soriano Jiménez, P.P. ; Capilla, R.; Peinado Pinilla, J.; Guardia J.; Perón M. Applying a graph model for the Spanish Public University System. Mathematical Modelling in Engineering & Human Behaviour 2015. 17th Ed. of the Mathematical Modelling Conference Series at the Institute for Multidisciplinary Mathematics
- [3] Hervás A, et al. (2017) Applying a graph model for the Spanish public university system in Modeling Human Behavior: Individuals and Organizations. (Nova Science Publishers, Inc.), pp. 9–24.
- [4] Lancichinetti A, Fortunato S (2009) Community detection algorithms: A comparative analysis. Phys. Rev. E 80(5)
- [5] Lancichinetti A, Fortunato S (2009) Benchmarks for testing community detection algorithms on directed and weighted graphs with overlapping communities. Phys. Rev. E 80(1)
- [6] Lancichinetti A, Fortunato S, Radicchi F (2008) Benchmark graphs for testing community detection algorithms. Phys. Rev. E 78(4)
- [7] Feng S, Hu B, Nie C, Shen X (2016) Empirical study on a directed and weighted bus transport network in China. Physica A: Statistical Mechanics and its Applications 441(C):85–92.
- [8] Sienkiewicz J, Hołyst JA (2005) Statistical analysis of 22 public transport networks in Poland. Phys. Rev. E 72(4)
- [9] Xu X, Hu J, Liu F, Liu L (2007) Scaling and correlations in three bus-transport networks of China. Physica A: Statistical Mechanics and its Applications 374(1):441–448.
- [10] Hervás, A., Soriano-Jiménez, P. P., Jiménez, A., Peinado, J., Capilla, R., and Montañana, J. M. A Case Study Of Directional Communities In A Directed Graph: The Accessing Procedure To The Spanish Public University System. Modeling Human Behavior, 9.
- [11] Montañana, J. M., Hervás, A., and Soriano, P. P. (2019). A Proposal for a Benchmark Generator of Weakly Connected Directed Graphs. Open Journal of Modelling and Simulation, 8(1), 18-34.
- [12] Tao You, Ben-Chang Shia, Zhong-Yuan Zhang. Community Detection in Complex Networks Using Density-based Clustering Algorithm.
- [13] Montañana, J. M., Hervás, A., Soriano-Jiménez, P.P. Project *Graph-Generators*, Available at <https://github.com/jmmontanana/Graph-Generators/tree/master/Weakly-Connected-Directed-Graphs>
- [14] Girvan, M. and Newman, M. E., Community structure in social and biological networks, Proc. of the National Academy of Sciences, 2002, vol 99, 12, pages 7821-7826

Comparison in the use of ANSYS and SAP2000 in the modelling and structural calculation of bridges

Miriam Labrado^{b1}, Ernesto Colomer^{b2}, Adrián Zornoza^{b3} and Álvaro Potti^{b4}

(b) Institute of Multidisciplinary Mathematics,
Universitat Politècnica de València.

1 Introduction

Nowadays, the field of civil engineering, and more specifically that associated with structural calculation, is undergoing a phase of continuous evolution, in which more and more structures are subjected to greater demands of use. In this sense, one of the structural typologies that has been most affected by this trend refers to bridge structures, resulting in a structural complexity that has resulted in the need to improve calculation methods to guarantee safety and production costs. Therefore, new tools and/or technologies are required to carry out the calculation and design of these structures. It is in this point, where the mathematical finite element models of structural elements are acquiring great value. Such models, can be defined as a mathematical method in which a continuous medium is discretized (subdivided) into elements that maintain the properties of the originator. These elements are described by differential equations and solved by mathematical models in order to obtain the specific results [1].

In practice, in most cases these models that represent the structural mechanical behavior with great precision, are of considerable magnitude, and can be provided with thousands of elements, configuring an immense mathematical framework, whose execution requires an infinity of operations. It is then when computer tools become useful, being able to operate automatically and with a very significant speed.

In this sense, there are several commercial programs for the automatic calculation of structures, which base their operation on the Finite Element Method. Therefore, when a structural analysis is to be carried out, the question arises as to which software tool is best to use.

¹e-mail: milabpa@upv.es

²e-mail: ercoro1@cam.upv.es

³e-mail: adzorar@cam.upv.es

⁴e-mail: alpotgui@cam.upv.es

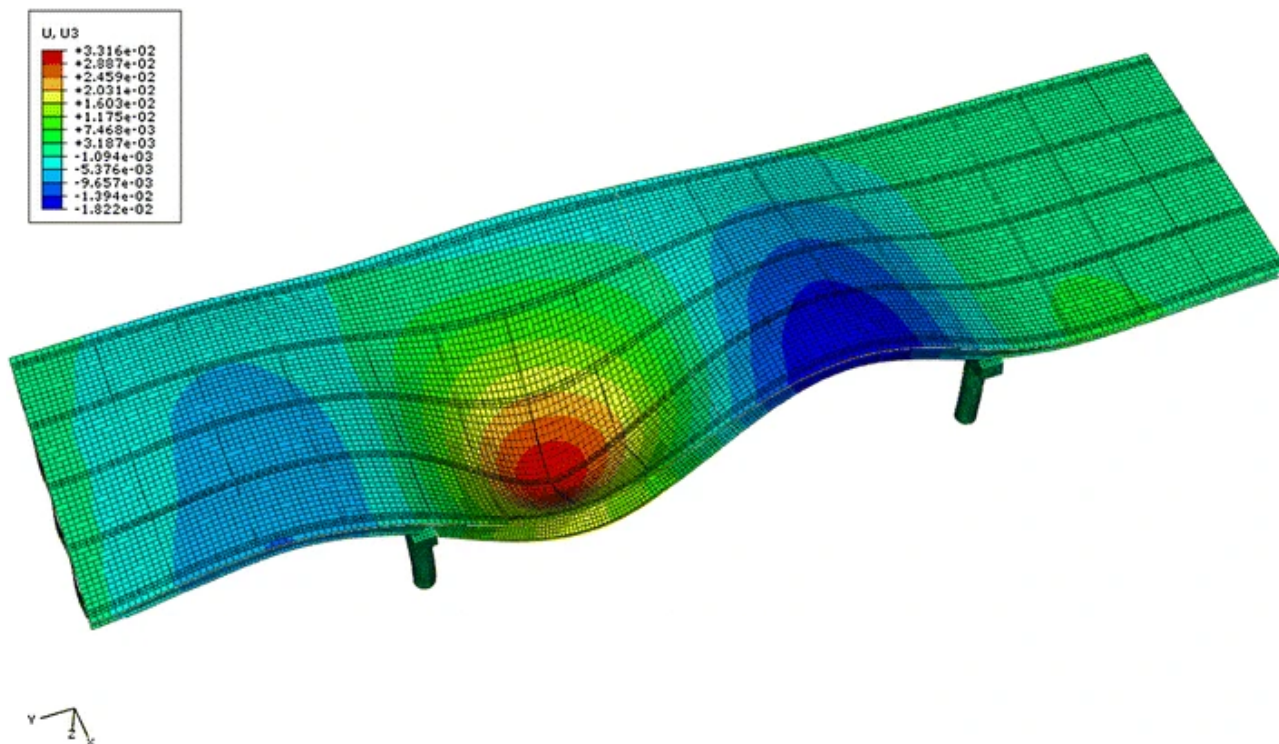


Figure 1: 3D image example of a finite element model of a bridge. Dynamic deformation response under traffic loads effects. Source [2]

In this case, according to Julián Carrillo et. Al [3], two of the most widely used programs for structural calculation worldwide are ANSYS and SAP2000, from which numerous structural analyses have been carried out in the academic, research and professional fields.

Therefore, the aim of this work is to carry out a comparative study between the two structural calculation programs, ANSYS and SAP 2000, to provide users with a decision tool, from which, depending on the type of work to be done, they can optimally choose the program that best suits their needs of use. To this end, first of all, the basic principles of the operation of both software will be explained. Secondly, once this point is reached, the main differences between the two types of software are detected and compared. Finally, in the third part of the study, based on the simulation and modelling of two simple bridge structures, numerically analyse the differences detected.

2 Methodology

As mentioned above, a comparative study was carried out between two of the main structural analysis software that base their use on finite element models. Therefore, this section tries to explain the methodology used.

In the first part of the study, an in-depth analysis was made of the functioning and the way of proceeding, when performing structural calculations, of both programs: ANSYS and SAP2000. For this purpose, the existing scientific literature on the subject and the user manuals of the aforementioned software were reviewed. This part was considered essential, since on

the one hand it allowed the correct understanding of the operation of the programs, and on the other hand it was used as a basis for the comparative study.

In the second part of the study, based on the conclusions obtained in the first part, the following critical factors were considered in order to be compared in the specific case of the structural calculation of bridges: 1) Method of development and creation of the model, 2) definition of materials 3) simulation of dynamic and static analysis.

These parameters were selected, on the one hand, for being fundamental when carrying out a structural analysis of bridges, and on the other hand, for presenting significant differences in the procedure used to carry them out between the two software. Therefore, they represent critical variables when selecting the software according to the case study.

Finally, in the third part of the study, two simple and characteristic bridge structures were modelled, such as a continuous beam bridge and an arch bridge. From these models, different simulations were carried out, based on dynamic and static analyses, which allowed us to conclude the weight or influence of each of the characteristics mentioned above (section 2 of the study) on the final results obtained.

3 Results and discussion

As mentioned above, once the main differentials between the two types of software that affect the structural calculation of bridges have been defined, different simulations, based on dynamic and static models, were carried out on two bridge structures: continuous beam bridge and arch bridge.

Therefore, the stresses and displacements produced in both types of bridges were studied as the main output results. It is worth noting the similarity of the results obtained in the analyzes carried out, both static and dynamic.

However, limitations are observed when carrying out more complex structure modelling using SAP2000 software, due to its model development method.

4 Conclusions and future work

Finally, it is highlighted that in this paper a comparative study has been carried out, from a theoretical and a practical point of view, of the use of two of the main software used in the structural calculation and more specifically in the calculation of bridges. The main conclusions reached are:

- The implementation of the use of finite element models allows the modelling of elements that are not conventionally modelled. So the academic, professional and investigative use is justified.

- The parameterization in the creation of the model used in ANSYS, compared to the pre-defined geometries used in SAP2000, make ANSYS a suitable software to model complex structures without limitations.
- The results obtained in the different simulations show similar results in the use of SAP 2000 or ANSYS.

References

- [1] R. S. M. A. W. M. Ê. T. & L. J. J. Lotti, “Aplicabilidade científica do método dos elementos finitos”. *Revista Dental Press de Ortodontia e Ortopedia Facial*, vol. 11(2), pp. 35-43., 2006.
- [2] V. Zanjani Zadeh & A. Patnaik, “Finite element modeling of the dynamic response of a composite reinforced concrete bridge for structural health monitoring”. *International Journal of Advanced Structural Engineering (IJASE)* volume 6, Article number: 2, 2014.
- [3] W. J. C. L. G. G. P. y. D. F. V. Manchego, “Ansys-CivilFEM y SAP 2000”, 2006.

Analysing nonlinear oscillators subject to Gaussian inputs via the random perturbation technique

J.-C. Cortés^{b1}, E. López-Navarro^{b2}, J.-V. Romero^{b3} and M.-D. Rosello^{b4}

(b) Instituto Universitario de Matemática Multidisciplinar,
Universitat Politècnica de València.

1 Introduction

The aim of this paper is to perform a stochastic analysis of nonlinear oscillators subject to stationary Gaussian forcing sources using the random perturbation technique along with the Maximum Entropy Principle. By combining these two stochastic techniques, we construct reliable approximations of the probability density function of the solution, which is a stochastic process.

Specifically, we will deal with a random nonlinear oscillator subject to small perturbations upon both the position, $X(t)$, and velocity, $\dot{X}(t)$, of the form

$$\ddot{X}(t) + 2\zeta\omega_0\dot{X}(t) + \epsilon X^2(t)\dot{X}(t) + \omega_0^2 X(t) = Y(t), \quad (1)$$

where ζ is the damping coefficient, $\omega_0 > 0$ is the frequency, ϵ is a small perturbation ($|\epsilon| \ll 1$) affecting the nonlinear term $X^2(t)\dot{X}(t)$ and the input term $Y(t)$ is a stationary zero-mean Gaussian stochastic process and mean square differentiable.

The key point of the perturbation technique is to consider that the solution $X(t)$ can be developed in the powers of ϵ . Commonly, when this technique is applied only the first order approximation is considered

$$\widehat{X}(t) = X_0(t) + \epsilon X_1(t). \quad (2)$$

Substituting expression (2) into Eq. (1), produces the next sequence of linear differential equations, that can be solved in cascade,

$$\begin{aligned} \ddot{X}_0(t) + 2\zeta\omega_0\dot{X}_0(t) + \omega_0^2 X_0(t) &= Y(t), \\ \ddot{X}_1(t) + 2\zeta\omega_0\dot{X}_1(t) + \omega_0^2 X_1(t) &= -X_0^2(t)\dot{X}_0(t). \end{aligned} \quad (3)$$

We are interested in analysing, from a probabilistic standpoint, the steady-state solution. Taking advantage of the linear theory, the system (3) can be solved using the convolution inte-

¹e-mail: jccortes@imm.upv.es

²e-mail: ellona1@upvnet.upv.es

³e-mail: jvromero@imm.upv.es

⁴e-mail: drosello@imm.upv.es

gral [1, 2]:

$$X_0(t) = \int_0^\infty h(s)Y(t-s) ds, \quad (4)$$

and

$$X_1(t) = \int_0^\infty h(s) [-X_0^2(t-s)\dot{X}_0(t-s)] ds, \quad (5)$$

where

$$h(t) = (\omega_0^2 - \zeta^2\omega_0^2)^{-\frac{1}{2}} e^{-\zeta\omega_0 t} \sin \left[(\omega_0^2 - \zeta^2\omega_0^2)^{\frac{1}{2}} t \right]$$

is the impulse response function for the underdamped case $\zeta^2 < 1$.

From the approximate solution given in (2), we can calculate the main statistical functions of $\widehat{X}(t)$, namely, higher moments, $\mathbb{E}\{X^n(t)\}$, the variance, $\mathbb{V}\{X(t)\}$, the covariance, $\mathbb{Cov}\{X(t_1), X(t_2)\}$ and the correlation function $\Gamma_{XX}(\tau)$.

2 Results and discussion

This section is addressed to illustrate, by means of an example, the theoretical results. Let us consider $Y(t) = \xi_1 \cos(t) + \xi_2 \sin(t)$, where $\xi_1, \xi_2 \sim N(0, 1)$ the trigonometric stochastic process as excitation. Notice that $Y(t)$ satisfies the hypotheses specified in the previous section. Also, we take $\xi = 0.05$ and $\omega_0 = 1$. Replacing this data into Eq. (1) reads,

$$\ddot{X}(t) + 0.1\dot{X}(t) + \epsilon X^2(t)\dot{X}(t) + X(t) = \xi_1 \cos(t) + \xi_2 \sin(t), \quad \xi_1, \xi_2 \sim N(0, 1). \quad (6)$$

Now we shall obtain the main statistical functions of $\widehat{X}(t)$. To compute the mean of the approximation, we use the expectation operator in (2). Applying (4) and (5) and using that we can interchange the expectation operator with the mean square integral, we obtain,

$$\mathbb{E}\{\widehat{X}(t)\} = \mathbb{E}\{X_0(t)\} + \epsilon\mathbb{E}\{X_1(t)\} = 0.$$

In addition, we observe that this happens with all moments of odd order. In our case we calculate the first five moments, therefore, $\mathbb{E}\{\widehat{X}^3(t)\} = 0$ and $\mathbb{E}\{\widehat{X}^5(t)\} = 0$. Now, due to the positiveness of the second and fourth order moments we will deduce appropriate bounds for ϵ . First, let us compute $\mathbb{E}\{\widehat{X}^2(t)\}$ up to the first order term of ϵ ,

$$\begin{aligned} \mathbb{E}\{\widehat{X}^2(t)\} &= \mathbb{E}\{X_0^2(t)\} + 2\epsilon\mathbb{E}\{X_0(t)X_1(t)\} \\ &= \int_0^\infty h(s) \int_0^\infty h(s_1)\Gamma_{YY}(s-s_1) ds_1 ds - 2\epsilon \left(\int_0^\infty h(s) \int_0^\infty h(s_1) \int_0^\infty h(s_2) \int_0^\infty h(s_3) \int_0^\infty h(s_4) \right. \\ &\quad \cdot \left. \left(2\Gamma_{YY}(s_1-s-s_2)\Gamma'_{YY}(s_3-s_4) + \Gamma'_{YY}(s_1-s-s_4)\Gamma_{YY}(s_2-s_3) \right) ds_4 ds_3 ds_2 ds_1 ds \right) \\ &= 100 - 200000\epsilon. \end{aligned}$$

In this case, we derive the bound $\epsilon < 0.0005$. Since $\mathbb{E}\{\widehat{X}(t)\} = 0$, we can deduce that the variance is equal to $\mathbb{E}\{\widehat{X}^2(t)\}$. Secondly, from the expression of $\mathbb{E}\{\widehat{X}^4(t)\}$,

$$\mathbb{E}\{\widehat{X}^4(t)\} = \mathbb{E}\{X_0^4(t)\} + 4\epsilon\mathbb{E}\{X_0^3(t)X_1(t)\} = 30000 - \frac{1153800000000}{6409}\epsilon,$$

we can refine the above bound $\epsilon < 0.000166641$.

Now, we focus on the correlation function of the approximation $\widehat{X}(t)$,

$$\begin{aligned} \Gamma_{\widehat{X}\widehat{X}}(\tau) &= \int_0^\infty \int_0^\infty h(s)h(s_1)\Gamma_{YY}(\tau - s_1 + s) ds ds_1 \\ &\quad - \epsilon \int_0^\infty h(s) \int_0^\infty h(s_1) \int_0^\infty h(s_2) \int_0^\infty h(s_3) \int_0^\infty h(s_4) \left\{ 2\Gamma_{YY}(\tau - s - s_2 + s_1)\Gamma'_{YY}(s_3 - s_4) \right. \\ &\quad + \Gamma'_{YY}(\tau - s - s_4 + s_1)\Gamma_{YY}(s_2 - s_3) + \Gamma_{YY}(s_1 - s_2)\Gamma'_{YY}(\tau - s_4 + s + s_3) \\ &\quad \left. + 2\Gamma'_{YY}(s_1 - s_3)\Gamma_{YY}(\tau - s_4 + s + s_2) \right\} ds_4 ds_3 ds_2 ds_1 ds = 100(1 - 2000\epsilon) \cos(\tau). \end{aligned}$$

In this example, the covariance coincide with the correlation function, since $\mathbb{E}\{\widehat{X}(t)\} = 0$,

$$\text{Cov}\{\widehat{X}(t_1), \widehat{X}(t_2)\} = \Gamma_{\widehat{X}\widehat{X}}(\tau) = 100(1 - 2000\epsilon) \cos(\tau), \quad \tau = |t_1 - t_2|.$$

In Fig. 1 we have plotted the approximations of correlation functions for different values of ϵ . It should be noted that when epsilon is larger, the variability decreases.

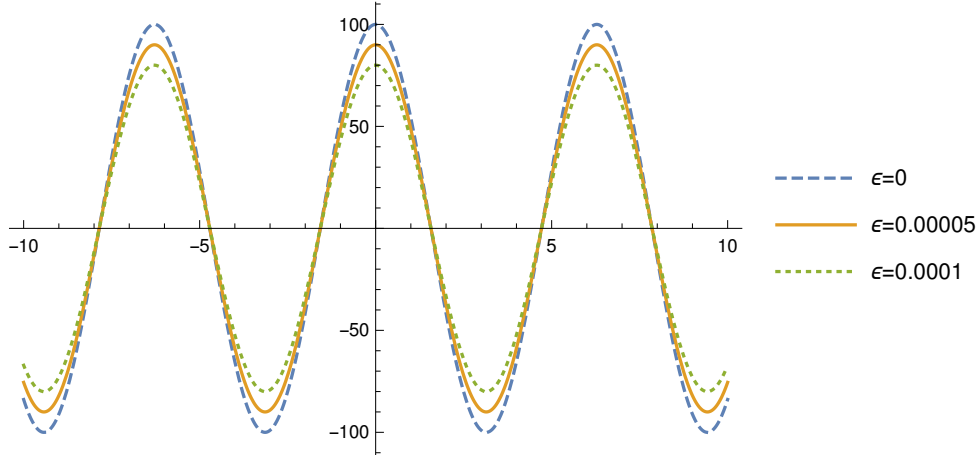


Figure 1: Correlation function $\Gamma_{\widehat{X}\widehat{X}}(\tau)$ of $X(t)$ for different values of ϵ .

Finally, we construct a reliable approximation of the probability density function using the Maximum Entropy Principle,

$$f_{\widehat{X}(t)}(x) = e^{-1-2.243+2.552 \cdot 10^{-8}x-0.004x^2-2.177 \cdot 10^{-9}x^3-3.789 \cdot 10^{-6}x^4+6.754 \cdot 10^{-13}x^5}.$$

In Fig. 2 we show the graphical representation of $f_{\widehat{X}(t)}(x)$.

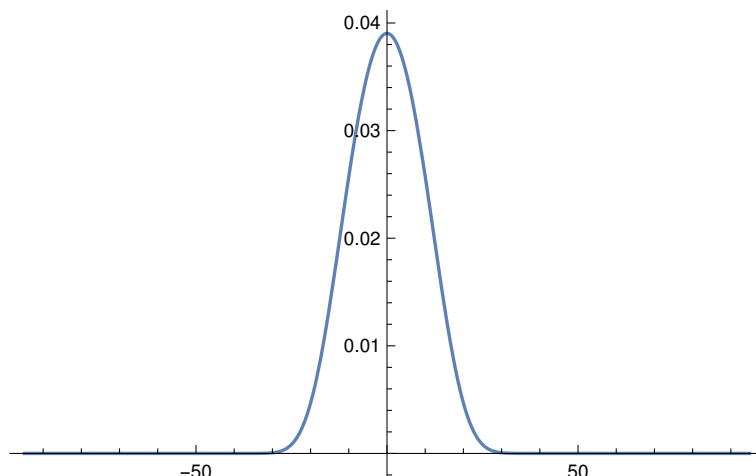


Figure 2: Approximation of PDF, $f_{\hat{X}(t)}(x)$, for $\epsilon = 0.00005$ via the PME.

3 Conclusions

We have studied, from a probabilistic point of view, a random nonlinear oscillator where the term of perturbation affects the crossnonlinear term (position and velocity). Our main contribution has been the approximation of the probability density function taking advantage of the Principle of Maximum Entropy. In this manner, we provide a fuller probabilistic information of the solution.

Acknowledgements

This work has been supported by the Spanish Ministerio de Economía, Industria y Competitividad (MINECO), the Agencia Estatal de Investigación (AEI) and Fondo Europeo de Desarrollo Regional (FEDER UE) grant MTM2017–89664–P. Elena López Navarro has been supported by the European Union through the Operational Program of the [European Regional Development Fund (ERDF)/European Social Fund (ESF)] of the Valencian Community 2014-2020 (GJIDI/2018/A/010).

References

- [1] Crandall, S. H., Perturbation Techniques for Random Vibration of Nonlinear Systems. *The Journal of the Acoustical Society of America*, 35:1700–1705, 1963.
- [2] Soong, T.T., Random Differential Equations in Science and Engineering. New York, Academic Press, 1973.
- [3] El-Tawil, M.A., Al-Jihany, A.S., On the solution of stochastic oscillatory quadratic nonlinear equations using different techniques, a comparison study, *Topol. Methods Nonlinear Anal.* 31(2): 315–330, 2008.

- [4] Cortés, J.-C., Romero, J.-V., Roselló, M.-D., Santamaría, C., Solving random diffusion models with nonlinear perturbations by the Wiener–Hermite expansion method. *Computers & Mathematics with Applications*. 61(8): 1946-1950, 2011.
- [5] Calatayud, J., Cortés, J.-C., Jornet, M., The damped pendulum random differential equation: A comprehensive stochastic analysis via the computation of the probability density function. *Physica A: Statistical Mechanics and its Applications*. 512: 261-279, 2018.

A note on the use the semifocal anomaly as temporal variable in the two body problem

José Antonio López Ortí ^{b1}, Francisco José Marco Castillo ^{b2} and María José Martínez Usó^{#3}

(b) Department of Mathematics. University Jaume I of Castellón,
Av Sos Baynat s/n, Castellón. Spain,

(#)Department of Applied Mathematics. Polytecnic University of Valencia,
Camino Vera s/n. Valencia, Spain.

1 Introduction

One of the most important problems in celestial mechanics is the two-body problem, since this is taken as a basis for both the study of disturbed motion in analytical and numerical methods. It is also taken as a test when evaluating the efficiency of numerical integrators, because it is a problem whose exact solution is well known and so, it is possible to compare its results with those obtained by means of numerical integration. The most interesting case of this problem is when the eccentricity is high, since in this case the motion is much faster in the periapsis region and much slower in the apoapsis region. The use of numerical integrators employing ordinary time as an integration variable presents a serious drawback: if a revolution is divided in equal time steps, we obtain a distribution of orbital positions not convenient for numerical integration, which requires more points in the regions where the motion of the secondary is higher. Analogously, it is also convenient to have a higher concentration of points in the regions with greater curvature. Several possibilities are open in order to solve this problem such as the use of variable steps integrators, the search of a new temporary variable $\Psi \in [0, 2\pi]$ so this could be an admissible change of parameter when the orbit is parameterized with respect to the mean anomaly. This technique is known as analytical regularization of the integration step and is given by means of a relationship in the form $dM = Q(r)d\Psi$ where $Q(r)$ is the so-called partition function. This method achieves good results since it is possible to find an anomaly Ψ so that a distribution of orbital positions more suitable to the dynamics at a constant step is obtained. On the other hand, this technique is compatible with variable step integrators, which allows a higher efficiency.

In the present work we define a new anomaly Ψ , called semifocal anomaly, as the mean between the true anomaly f and the antifocal anomaly f' , defined by Fukushima as the angle between the periapsis and the secondary around the empty focus. In the first place, this paper focuses on the use of this anomaly as temporal variable combined with the numerical integral

¹e-mail: lopez@mat.uji.es

²e-mail: marco@mat.uji.es

³e-mail: mjmartin@mat.upv.es

methods. Secondly, on the study of the analytical theories of perturbed motion in the solar system, such as the planetary theories.

2 Results and discussion

The main goal of this work is the study of new temporal variables in order to improve the analytical and numerical integration methods in celestial mechanics. In this sense, it is necessary to emphasize the pioneering works of Hansen [11], Sundman [12]. More recently, Nacozy [12] define the intermediate anomaly, Janin and Bond [6] the family of generalized anomalies of Sudman, which contains the true, the eccentric and the mean anomalies, Brumberg and Fukushima [3] the elliptic anomaly and Bumberg [2] the regularized length of arc. López [10] define a biparametric family as anomalies which includes all the above mentioned and also the natural family of anomalies [8].

The two body problem is a classic problem in celestial mechanics [1], [5], [13] and its solution in the usual coordinates of the secondary with respect to the primary are (ξ, η) in the orbital plane, which can be obtained as

$$\xi = r \sin f = a(\cos g - e), \eta = r \sin f = a\sqrt{1 - e^2},$$

$$r = \frac{a(1 - e^2)^{3/2}}{1 + e \cos f} = a(1 - e \cos g),$$

where a is the major semiaxis, e the eccentricity and r the vector radius. The eccentric anomaly is connected to the mean anomaly M through the Kepler equation

$$M = g - e \sin g$$

the mean anomaly is defined by $M = n(t - t_0)$ where $n = \sqrt{G(m_1 + m_2)}a^{-3/2}$, m_1 and m_2 the masses of the primary and the secondary respectively, and t_0 the initial epoch of the periapsis.

In this paper, following a similar procedure as in [9] we obtain the most common quantities involved in the two body problem, g , $\sin g$, $\cos g$, r/a related to Ψ through closed equations and we show that this anomaly can be included in the biparametric family and it is symmetrical according to the geometry of the ellipse.

In this work we also obtain the Kepler equation $M = M(\Psi)$, and the series expansions of g , $\sin g$, $\cos g$, r/a , a/r . obtaining the coefficients in closed form by means of recurrence equations. The values of the coefficients can be obtained directly by means of complete elliptic integrals. To use this variable in analytical theories it is necessary the use of the Lagrange Planetary equations [7], [13] and it is requested the inversion of series [4].

It can be shown that this transformation is defined by the relationship:

$$dM = Q(r)d\Psi$$

Where $Q(r)$ is given by $Q(r) = \frac{r^2 r'}{a^3 \sqrt{1 - e^2}}$ being r and $r' = 2a - r$ the radius vectors of the secondary taken from the focus F of the ellipse where the primary and the empty focus of the ellipse are located. We also have

$$\cos g = \frac{\cos \Psi}{\sqrt{1 - e^2 \sin^2 \Psi}}, \quad \sin g = \frac{\sqrt{1 - e^2} \sin \Psi}{\sqrt{1 - e^2 \sin^2 \Psi}}.$$

These relationships allow expressing the coordinates of the secondary in closed form. This anomaly is also related to the true anomaly by means of the simple relationship

$$\sin(f - \Psi) = e \sin \Psi.$$

On the other hand, in numerical integration, local and global errors improve those obtained when using physical time due to a distribution of points on the ellipse more in accordance with the dynamics of the problem, because in case of using physical time as an integration variable, the concentration of points is minimal in the periapsis, that is, the region where the speed is highest and maximum in the apoapsis, where the speed is minimum. This is a key point, because it suffers a huge increment when the eccentricity is high.

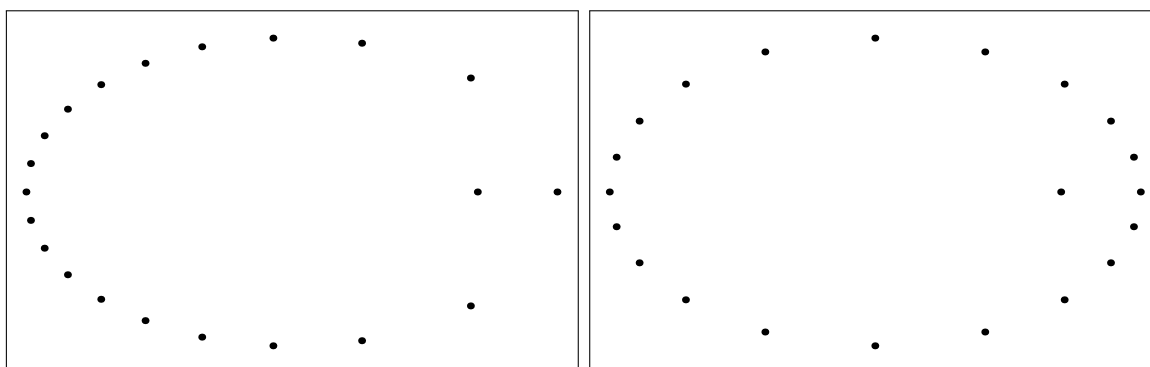


Figure 1: Point distribution points for $e = 0.7$, M left and Ψ right

The figure shows that the point distribution on the ellipse more according with the dynamics than the ordinary time is used, and so the numerical results are improved.

3 Conclusions and future work

The main conclusion of this work can be resumed as:

- The semi-focal anomaly is close to the eccentric anomaly for low values of e . The order of the difference between them in the symmetric family of anomalies is $O(e^2)$.
- The semi-focal anomaly is included in the natural family of anomalies as well as in the biparametric family of anomalies.
- The most common quantities of the two-body problem can be related to the semi-focal anomaly in closed form.
- The semi-focal anomaly is appropriate to develop the most common quantities of the two-body problem. The coefficients of the main developments can be obtained from a recurrence formula.
- The use of semi-focal anomaly improves the results of the numerical integrators in particular for higher values of the eccentricity.

In the future two ways can be explored: firstly the extension of this study to the hyperbolic two body problem, including the attractive and the repulsive branch. Secondly, the semi-focal anomaly can be include in a particular case of the biparametric family when $\alpha - \beta = 1$. This particular case includes in addition to the semifocal anomaly, the most common symmetric anomalies as the eccentric anomaly, the elliptic anomaly an the regularized length of arc. It can also be of interest the study of the optimal in this family for each value of the eccentricity.

Acknowledgements

This work has been partialy suported by grant 16I358.01/1 of University Jaume I of Castellón.

References

- [1] BROWER, D., CLEMENCE, G.M. 1965. *Celestial Mechanics*, Ed Academic Press, New York.
- [2] BRUMBERG, E.V. 1992., Length of arc as independent argument for highly eccentric orbits. *Celestial Mechanics*. **53** 323–328.
- [3] BRUMBERG, E.V., FUFKUSHIMA, T. 1994. Expansions of Elliptic Motion based on Elliptic Functions Theory. ,*Celestial Mechanics*. **60**, 69-89.
- [4] DEPRIT, A.,A Note on Lagrange’s Inversion Formula,*Celestial Mechanics*. **20** (1979) 325–327.
- [5] HAGIHARA, Y. 1970. *Celestial Mechanics*. **vol 2.**, Ed MIT Press, Cambridge MA.
- [6] JANIN, G., BOND, V. R. 1980. The elliptic anomaly, *NASA Technical Memorandum* 58228.
- [7] LEVALLOIS, J.J., KOVALEVSKY, J. 1971. *Géodésie Générale Vol 4*, Ed Eyrolles, Paris.
- [8] LÓPEZ, J. A.; MARCO, F. J., MARTÍNEZ, M. J. 2014. A Study about the Integration of the Elliptical Orbital Motion Based on a Special One-Parametric Family of Anomalies. *Abstract and Appied Analysys. Volume 2014, Article ID 162060*
- [9] J.A. López, V. Agost, M. Barreda. (2017) A new bi-parametric family of temporal transformations to improve the integration algorithms in the study of the orbital motion. *JCAM*. 309, pp 482–492.
- [10] J.A. López, F.J. Marco, M. J. Martínez. (2017). Geometrical definition of a continuous family of time transformations generalizing and including the classic anomalies of the elliptic two-body problem. *JCAM*. 318, pág 479-490.
- [11] NACOZY, P. 1969, Hansen’s Method of Partial Anomalies: an Application. *the Astronomical Journal*. **74** 544–550.
- [12] NACOZY, P. 1977, The intermediate anomaly. *Celestial Mechanics*. **16** 309–313.
- [13] TISSERAND, F. 1896. *Traité de Mécanique Céleste*, Ed Gauthier-Villars, Paris.

Epidemiological modelling of COVID-19 in Granada, Spain: Analysis of future scenarios

José-Manuel Garrido[‡], David Martínez-Rodríguez^{b1},
Fernando Rodríguez-Serrano[‡], Raul S. Julián^b and Rafael-J. Villanueva^b

(‡) Cardiovascular Surgery Service.

Hospital Universitario Virgen de las Nieves, Spain.

(b) Instituto Universitario de Matemática Multidisciplinar,
Universitat Politècnica de València, Spain.

(‡) Department of Anatomy and Human Embryology.
Faculty of Medicine. Universidad de Granada, Spain.

1 Introduction

COVID-19, a disease caused by the novel coronavirus SARS-CoV-2, has become a global pandemic with huge incidence in public health. The first outbreak happened at the end of December in Wuhan, China. Since then, more than two hundred countries have been affected with near four million cases worldwide [2]. The symptoms of the disease cover a broad number of possibilities, from asymptomatic patients to multiple organ failure [1]. The high number of asymptomatic patients, together with the novelty of the disease, have made possible the fast expansion of the virus [3].

In this work, a mathematical model describing the transmission dynamics of COVID-19 is presented. It is based on a modified SEIR model, with the aim at reproducing the evolution of the hospitalization pressure. Also quarantine actions have been taken into account in order to study the effect of the confinement in the spread of the disease.

Regarding to COVID-19, a person may be in different states described below and shown graphically in Figure 1 and described mathematically by the equation system (1).

- **Susceptible (S):** when the person has not the disease and has not passed through it.
- **Lockdown (Q):** when the individual is in lockdown due to public health policies.
- **Latent or exposed (L):** when the person has the disease, but he/she is not capable of infect other people.
- **Infectious (I):** when the person has the disease and he/she can infect other people with SARS-CoV-2.

¹e-mail: damarro3@upv.es

- **Recovered (R):** when the person has passed through the disease and did not need hospital treatment.
- **Hospitalized (H):** when the person is passing the disease and needs hospital treatment.
- **Intensive care unit (U):** when the person is passing the disease and needs intensive care unit (ICU) treatment.
- **Deceased (F):** when the person dies because of SARS-CoV-2.
- **After ICU (HU):** when a person moves from ICU to other non-ICU department inside the hospital once the disease has improved.
- **Discharged (A):** when the person is discharged from hospital.

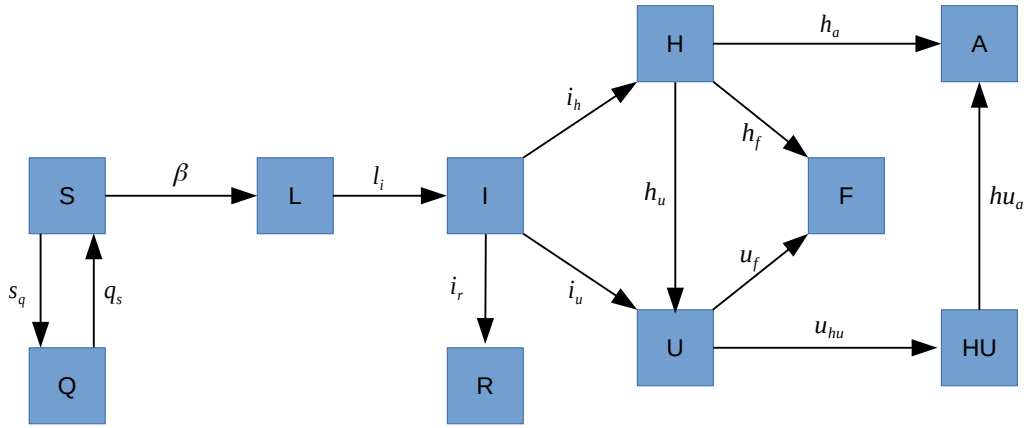


Figure 1: Diagram with the different states considered in the COVID-19 SEIR model. Arrows describe the movement from one state to another.

$$\begin{aligned}
 S(t+1) &= S(t) + q_s(t) - s_q(t) - \beta(t)S(t)\frac{I(t)}{P_T}, \\
 Q(t+1) &= Q(t) + s_q(t) - q_s(t), \\
 L(t+1) &= L(t) + \beta(t)S(t)\frac{I(t)}{P_T} - l_iL(t), \\
 I(t+1) &= I(t) + l_iL(t) - (i_r(t) + i_h(t) + i_u(t))I(t), \\
 H(t+1) &= H(t) + i_h(t)I(t) - (h_u(t) + h_f(t) + h_a(t))H(t), \\
 U(t+1) &= U(t) + i_u(t)I(t) + h_u(t)H(t) - (u_f(t) + u_{hu}(t))U(t), \\
 HU(t+1) &= HU(t) + u_{hu}(t)U(t) - hu_a(t)HU(t), \\
 A(t+1) &= A(t) + h_a(t)H(t) + hu_a(t)HU(t), \\
 F(t+1) &= F(t) + h_f(t)H(t) + u_f(t)U(t), \\
 R(t+1) &= R(t) + i_r(t)I(t).
 \end{aligned} \tag{1}$$

2 Results and discussion

Once the model has been presented, it has been calibrated using NS algorithm [4] with data obtained from the *Hospital Universitario Virgen de las Nieves* in Granada (Spain) [5]. The

province of Granada has 921511 inhabitants, and we consider this value as constant during the simulation time. Our simulations begins on 5 March 2020. The calibrated model and the data used for calibration and validation are shown in Figure 2.

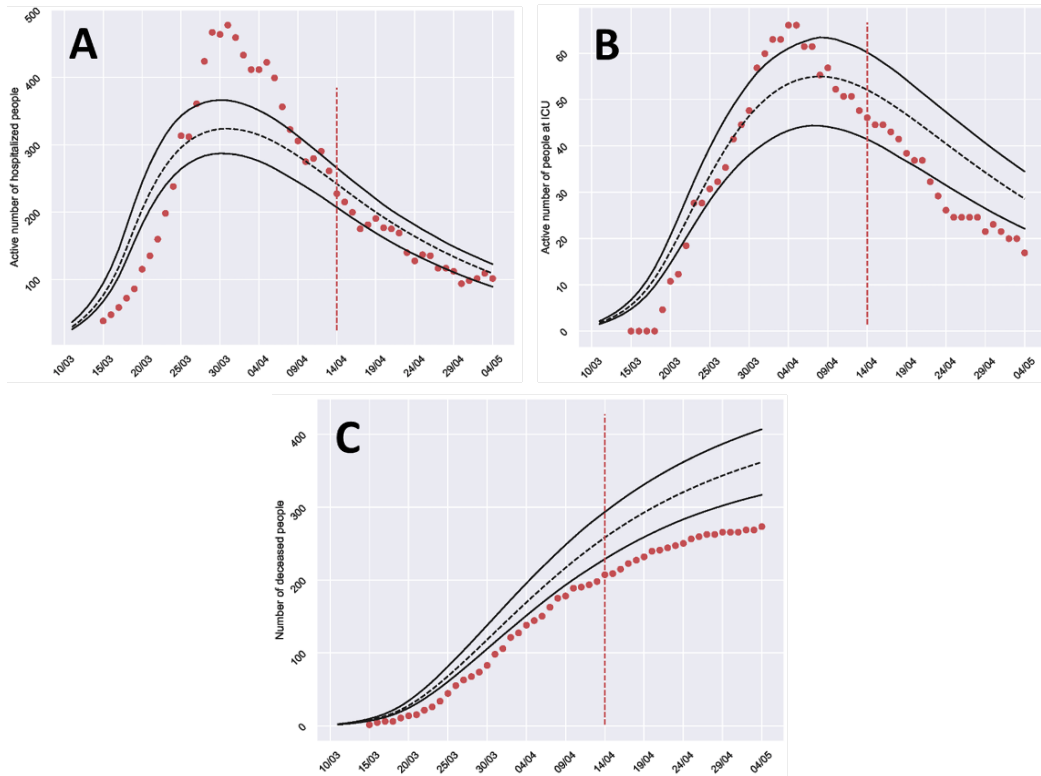


Figure 2: COVID-19 SEIR model calibration and validation for (A) Hospitalizations at ward, (B) Intensive Care Unit and (C) Deceases. The red points on the left of the vertical line of the graphics are used to calibrate the model and the red points on the right of the vertical line of the graphics are used to validate the model.

Assuming that the behaviour of the disease in the future is similar to the behaviour of the disease in the past, some scenarios are simulated in order to study different public health policies that might reduce the infections in future outbreaks of COVID-19. For the simulation, when required, we include that the exit of the quarantine is done gradually during 4 weeks on which every week 25% of people return to normal life.

The β may be modified taking into account: (i) measures avoiding social contacts: home-working, avoiding meetings, safe distancing, room ventilation, limiting the capacity of bars, restaurants, hotels and public places, (ii) measures of protection (facemasks, hand washing), response of the virus to the summer temperatures, the population immunity, etc.

Assuming an optimistic 10% viral β during 14 April – 2 September 2020, by the end of summer the number of cases would be significantly reduced. However, SARS-CoV-2 β could increase in autumn 2020 due to seasonality and other factors (schools reopening, etc.). On this basis, we assessed the analysis considering 100%, 50% or 25% of β from autumn respect to the rate registered before the quarantine.

The evolution of the pandemics depending on the β value are shown in Figure 3.

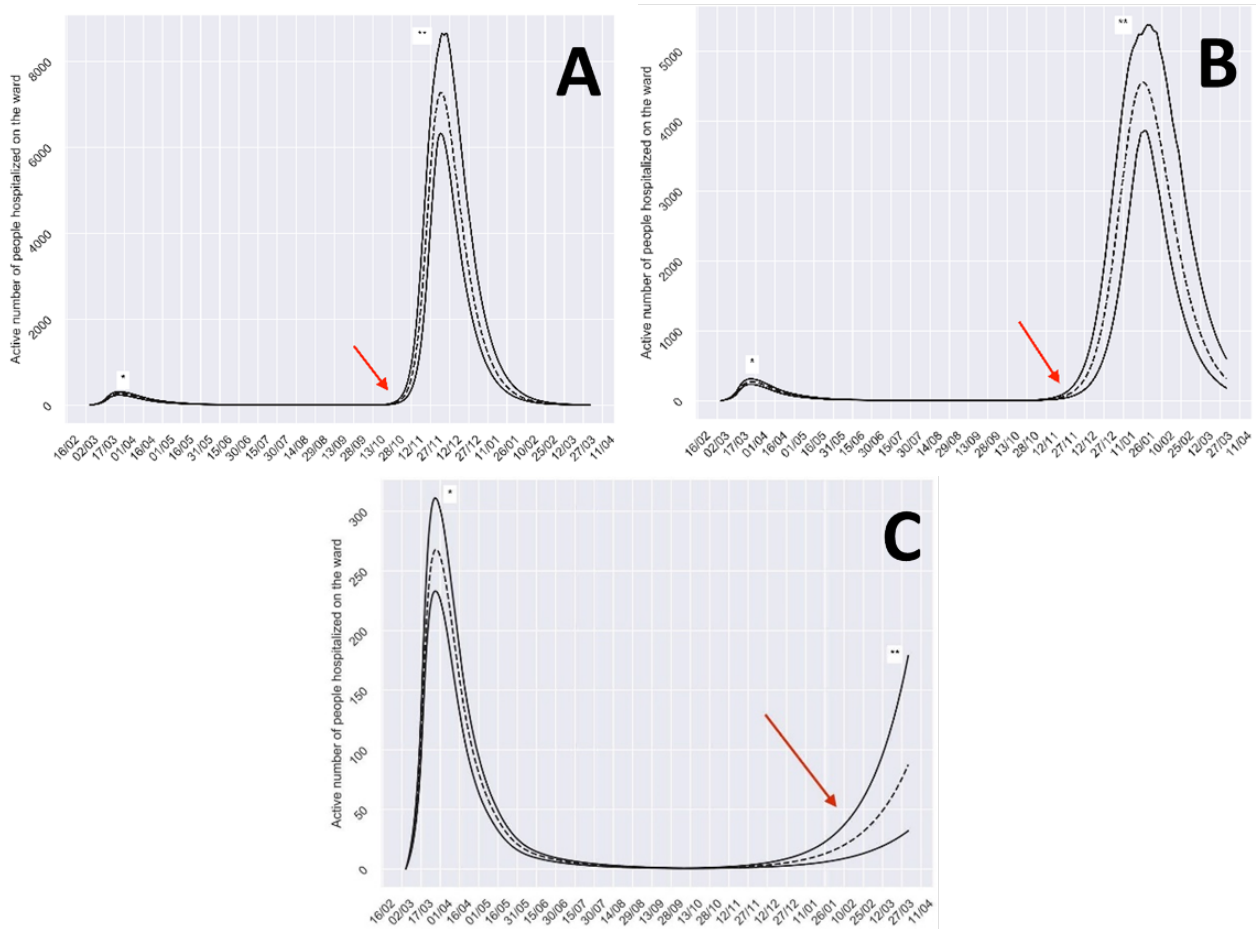


Figure 3: COVID-19 SEIR model evolution depending on the β parameter. (A) Evolution with 100% of initial β , (B) evolution with 50% of initial β and (C) evolution with 25% of initial β . Red arrows are used to point out the moment when more drastic public health measures must be implemented.

3 Conclusions and future work

The modified SEIR model presented can be a useful tool for providing insight into the transmission dynamics of SARS-CoV-2. We simulated mid-term scenarios varying the β after the current quarantine. Those predictions would provide enough time to the health systems to establish appropriate measures. The conclusions of this work suggest that social distancing, together with measures that decrease the contagion will be needed in order to control the pandemics in the next autumn. It will be also important the monitoring of the evolution of the disease in the health system in order to take more aggressive measures if the number of infected people might collapse hospitals again.

Acknowledgements

- the Spanish Ministerio de Economía, Industria y Competitividad (MINECO), the Agencia Estatal de Investigación (AEI) and Fondo Europeo de Desarrollo Regional (FEDER UE)

grant MTM2017-89664-P;

- the European Union through the Operational Program of the [European Regional Development Fund (ERDF) / European Social Fund (ESF)] of the Valencian Community 2014-2020. Files: GJIDI/2018/A/010 and GJIDI/2018/A/009;
- the Ramón Areces Foundation, Madrid, Spain (CIVP18A3920).

References

- [1] Fei Zhou, Ting Yu, Ronghui Du, Guohui Fan, Ying Liu, Zhibo Liu, Jie Xiang, Yeming Wang, Bin Song, Xiaoying Gu, Lulu Guan, Yuan Wei, Hui Li, Xudong Wu, Jiuyang Xu, Shengjin Tu, Yi Zhang, Hua Chen, Bin Cao. Clinical course and risk factors for mortality of adult inpatients with COVID-19 in Wuhan, China: a retrospective cohort study. *The Lancet*, 395:1054–1062, 2020. 10.1016/s0140-6736(20)30566-3
- [2] European Centre for Disease Prevention and Control. <https://www.ecdc.europa.eu/en/geographical-distribution-2019-ncov-cases> (accessed: 8-05-2020)
- [3] Adam J Kucharski, Timothy W Russell, Charlie Diamond, Yang Liu, John Edmunds, Sebastian Funk, Rosalind M Eggo, Fiona Sun, Mark Jit, James D Munday, Nicholas Davies, Amy Gimma, Kevin van Zandvoort, Hamish Gibbs, Joel Hellewell, Christopher I Jarvis, Sam Clifford, Billy J Quilty, Nikos I Bosse, Sam Abbott, Petra Klepac, Stefan Flasche. Early dynamics of transmission and control of COVID-19: a mathematical modelling study. *The Lancet Infectious Diseases*: 20(5):553–558, 2020. 10.1016/s1473-3099(20)30144-4.
- [4] Martínez-Rodríguez, D, Colmenar, JM, Hidalgo, JI, Villanueva Micó, R-J, Salcedo-Sanz, S. *Particle swarm grammatical evolution for energy demand estimation* Energy Sci. Eng. 8:1068–1079, 2020. 10.1002/ese3.568.
- [5] Hospital Universitario Virgen de las Nieves. <https://www.huvn.es> (accessed 8-05-2020)

Probabilistic calibration of a model of herpes simplex type 2 with a prefixed error in the uncertainty of the data

Juan-Carlos Cortés[‡], Pablo Martínez-Rodríguez[‡], Jose-A. Morano[‡], José-Vicente Romero[‡],
María-Dolores Roselló[‡] and Rafael-J. Villanueva^{‡1}

(‡) Instituto Universitario de Matemática Multidisciplinar,
Universitat Politècnica de València, Spain.

1 Introduction

1.1 Importance of herpes simplex virus type 2

Herpes simplex type 2 virus (HSV2) is a sexually transmitted disease. People infected with this virus sporadically suffer hurtful blisters or ulcers at the area of infection along their life, and they significantly increase their likelihood of contracting HIV infection [9]. In addition, pregnant women infected near the time of delivery can transmit the virus to her baby, producing on this baby a high risk for suffering neurological disability or death [1]. This problem is concerning because, in the last times a higher number of women with HSV have been reported [10]. Also, less relevant but more common is the fact that the presence of HSV generates social stigma and a negative psycho-social impact in the infected population. All these factors define HSV infection as an important disease to study in order to develop efficient health care campaigns and to reduce both HSV and HIV new infections.

1.2 Model and method

Model building

Mathematical models provide an useful tool in order to understand the transmission dynamics of a virus infection. The method of this work consists of the development of an epidemic model of the HSV2 in Catalonia (Spain) along 2012-2016. The model is defined by the premise that, as the herpes is a chronic illness, the epidemic model only has two states: susceptible and infected. Also it is defined by the evidence that exist different infection rates between men and women [10]. A compartmental scheme of the proposed model is shown in Figure 1, where k represent the gender of the population.

¹e-mail: rjvillan@imm.upv.es

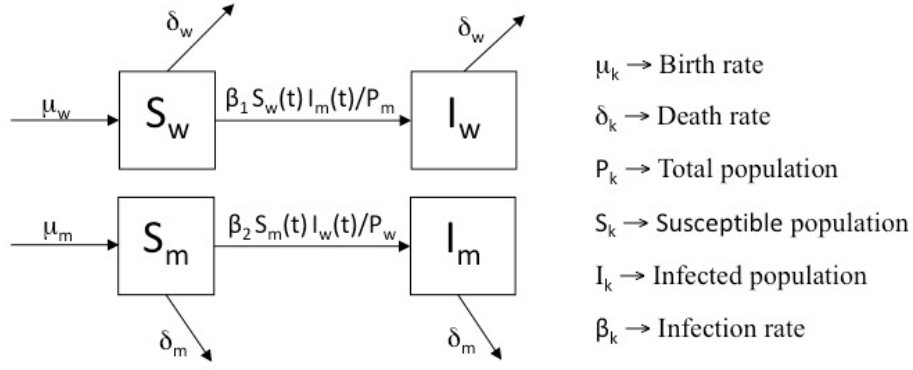


Figure 1: Epidemic model scheme for women ($k=w$) and men($k=m$).

This model is mathematically defined by the system of nonlinear difference equations (1), where Δt is the step time,

$$S_w(t + \Delta t) = S_w(t) + \mu_w P_w \Delta t - \delta_w S_w(t) \Delta t - \beta_1 S_w(t) \frac{I_m(t)}{P_m} \Delta t, \quad (1a)$$

$$I_w(t + \Delta t) = I_w(t) + \beta_1 S_w(t) \frac{I_m(t)}{P_m} \Delta t - \delta_w I_w(t) \Delta t, \quad (1b)$$

$$S_m(t + \Delta t) = S_m(t) + \mu_m P_m \Delta t - \delta_m S_m(t) \Delta t - \beta_2 S_m(t) \frac{I_w(t)}{P_w} \Delta t, \quad (1c)$$

$$I_m(t + \Delta t) = I_m(t) + \beta_2 S_m(t) \frac{I_w(t)}{P_w} \Delta t - \delta_m I_m(t) \Delta t. \quad (1d)$$

Simplified model

In order to get a first approach, the model has been simplified assuming some hypotheses. On the one hand, women and men populations are going to be considered as constant, since this way, the mortality and birth rates do not depend on time. This fact entails the equations $P_w = S_w(t) + I_w(t)$, $P_m = S_m(t) + I_m(t)$, $\mu_w = \delta_w$ and $\mu_m = \delta_m$. The infection rates, from men to women, β_1 , and from women to men, β_2 , also have been considered constant over the time. Finally, we only consider heterosexual relationships because it is a first model approach [10].

Assuming these simplifications, the new model is defined by the system of nonlinear difference equations (2), where $\beta_1, \beta_2, \delta_m$ and δ_w are defined with respect to Δt ,

$$I_w(t + \Delta t) = I_w(t) + \beta_1 (P_w - I_w(t)) \frac{I_m(t)}{P_m} \Delta t - \delta_w I_w(t) \Delta t, \quad (2a)$$

$$I_m(t + \Delta t) = I_m(t) + \beta_2 (P_m - I_m(t)) \frac{I_w(t)}{P_w} \Delta t - \delta_m I_m(t) \Delta t. \quad (2b)$$

Model calibration

Data source and treatment

The data employed in this work corresponds to the reported people who were infected with HSV2 in Catalonia between 2012-2016, which has been retrieved from [2–6]. The initial infected prevalent (existing infected population) has been obtained from [10], assuming that the prevalence rate of Europe in 2012 is similar to Catalonia’s one in 2012.

The available data ($data_k$) represents the reported people and not the total infected populations, therefore, in order to calibrate the model we have included two proportion parameters, $p_m = \frac{R_m}{\Delta I_m}$ and $p_w = \frac{R_w}{\Delta I_w}$, relating the reported cases (R_k) to the new infected individual (ΔI_k). These parameters have been calculated using the known values in year 2012 where R_k has been obtained from [2], and ΔI_k has been obtained from [10], assuming again that the incidence rate in Europe in 2012 is similar to Catalonia’s one. The parameters are shown in Table 1.

	ΔI_k	R_k	p_k
Women(w)	19482.204	136	0.006980
Men(m)	5214.275	101	0.019369

Table 1: Proportion parameters (p_k) of men and women in Catalonia (Spain) in 2012.

The rest of statistical data corresponding to the birth rate, death rate and populations size have been obtained from [7]. As the populations have been considered constant in our model, it has been used the means of the populations size and birth along 2012-2016. This information is shown in the Table 2.

	Population	Births
Men	3658766	37216
Women	3784721	34934

Table 2: Mean of the populations and mean of births in Catalonia (Spain) between 2012-2016.

Calibration of the model using EDA

The parameters calibrated in the model are $\beta_1 = \beta_1 \Delta t$ and $\beta_2 = \beta_2 \Delta t$, where Δt is a monthly period. The model has been calibrated using an algorithm based on Estimated Distribution Algorithms (EDA) [8]. This algorithm consists of the evolution of a computational estimated kernel distribution defined by a set of possible solutions. Along the progress of the process, the not desired solutions are discarded according to their error with respect to the available data (the error of the model has been calculated using the *SMAPE* function (3) since it provides a relative error), and new solutions are generated from the eventual distribution. When the process reaches a prefixed error, the procedure stops. The result obtained via this calibration process is a set of solutions, which defines the uncertainty of the parameters.

$$SMAPE = \frac{100\%}{n} \sum_{t=1}^n \frac{|data_k(t) - R_k(t)|}{|data_k(t)| + |R_k(t)|} \quad (3)$$

In order to calibrate the model it has been worked with a set of 100 solutions and a prefixed objective mean error of 10%. This last value has been selected taking into account the nature of the data and its possible error.

2 Results and discussion

The result of the calibration is the set $\Omega = \{(\beta_1^i, \beta_2^i)\}_{i=1}^{100}$, whose mean error is 7.541% with respect the reported data. The marginal distributions of the parameters of Ω are shown in the Figure 2. Applying a 95% confidence interval to Ω , it has been obtained a model which can capture the uncertainty. In the Figure 3 it can be observed the dynamics of the model calibration with the confidence interval.

The infected ranges follow, in all the cases, an increasing trend along the years. Furthermore it can be appreciated that the infection rates from men to women is higher than the one between women to men.

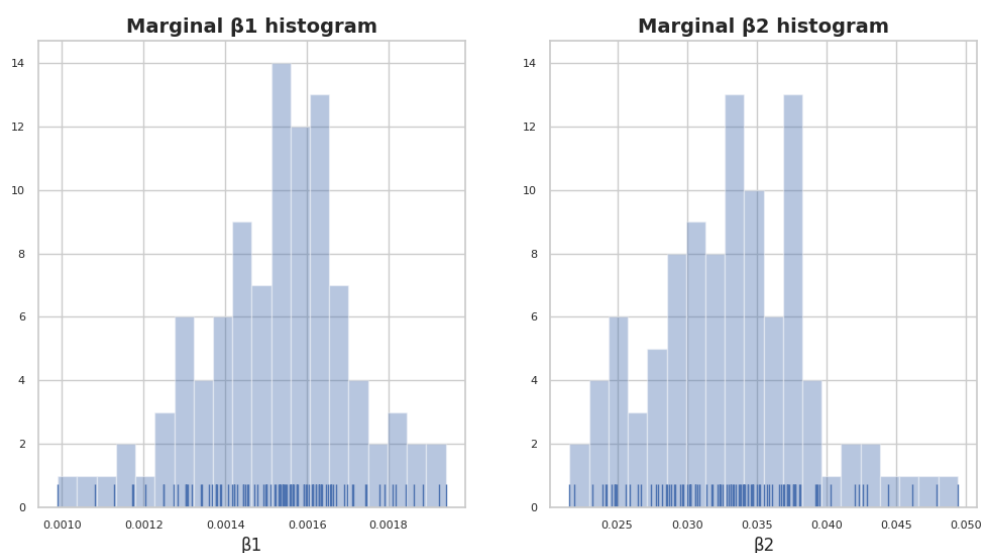


Figure 2: Marginal histograms of the infection rates from men to women (β_1) and women to men (β_2).

3 Conclusion and future work

The methodology applied in this work seems promising. The EDA algorithm has shown to be an useful tool in order to capture the data uncertainty.

The HSV2 model obtained picks correctly up the trend of the available data and explains, in a logic way, the behaviour of the virus infection. However, it will be convenient to track the robustness of the model with future data.

It is important to highlight the fact that the proposed model describes the dynamics of HSV2 infection in the population of Catalonia, and that if the model were to be extrapolated to other populations, it would be necessary to recalibrate the model parameters.

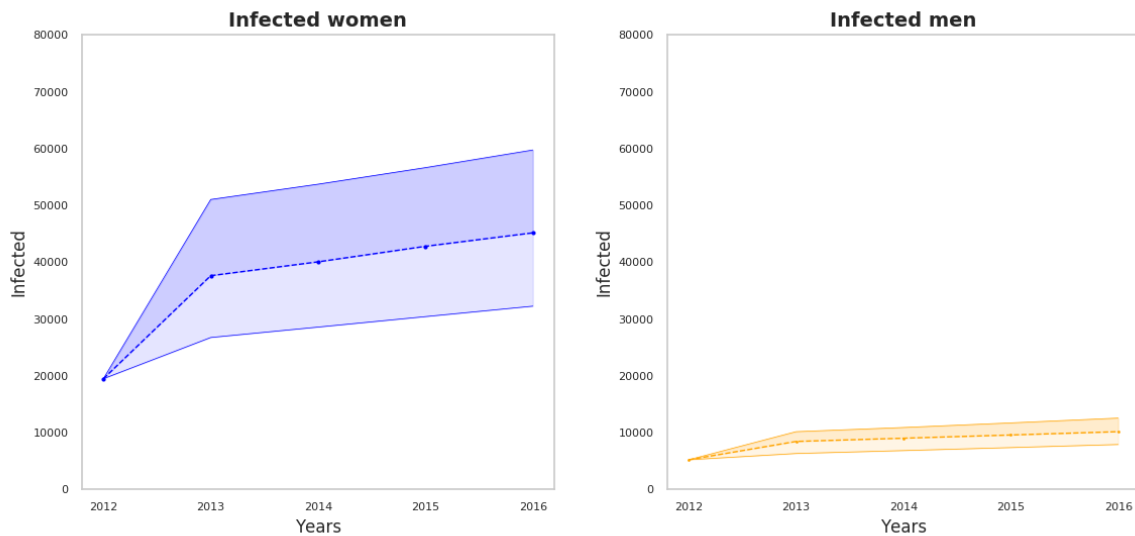


Figure 3: Number of women and men infected with HSV2 between 2012-2016 in Catalonia (Spain). The upper-continuous, middle-dash and lower continuous lines represent, respectively, the 97.5, 50, and 2.5 percentiles (CI 95%).

Acknowledgements

This work has been partially supported by the following research projects:

AICO/2019/215/Generalitat Valenciana grant, the Spanish *Ministerio de Economía, Industria y Competitividad (MINECO)*, the *Agencia Estatal de Investigación (AEI)* and *Fondo Europeo de Desarrollo Regional (FEDER UE) grant MTM2017-89664-P*.

References

- [1] Zane A. Brown, Stacy Selke, Judy Zeh, Jerome Kopelman, Arthur Maslow, Rhoda L. Ashley, D. Heather Watts, Sylvia Berry, Millie Herd, and Lawrence Corey. The acquisition of herpes simplex virus during pregnancy. *New England Journal of Medicine*, 337(8):509–516, August 1997.
- [2] Sistema de Información Microbiológica. Centro Nacional de Epidemiología. Instituto de Salud Carlos III. Annual report of the microbiological information system 2012. Technical report.
- [3] Sistema de Información Microbiológica. Centro Nacional de Epidemiología. Instituto de Salud Carlos III. Annual report of the microbiological information system 2013. Technical report.
- [4] Sistema de Información Microbiológica. Centro Nacional de Epidemiología. Instituto de Salud Carlos III. Annual report of the microbiological information system 2014. Technical report.

- [5] Sistema de Información Microbiológica. Centro Nacional de Epidemiología. Instituto de Salud Carlos III. Annual report of the microbiological information system 2015. Technical report.
- [6] Sistema de Información Microbiológica. Centro Nacional de Epidemiología. Instituto de Salud Carlos III. Annual report of the microbiological information system 2016. Technical report.
- [7] Spanish National Statistical Institute (INE). <https://www.ine.es>.
- [8] Pedro Larrañaga and Jose A. Lozano, editors. *Estimation of Distribution Algorithms*. Springer US, 2002.
- [9] Katharine J Looker, Jocelyn A R Elmes, Sami L Gottlieb, Joshua T Schiffer, Peter Vickerman, Katherine M E Turner, and Marie-Claude Boily. Effect of HSV-2 infection on subsequent HIV acquisition: an updated systematic review and meta-analysis. *The Lancet Infectious Diseases*, 17(12):1303–1316, December 2017.
- [10] Katharine J. Looker, Amalia S. Magaret, Katherine M. E. Turner, Peter Vickerman, Sami L. Gottlieb, and Lori M. Newman. Global estimates of prevalent and incident herpes simplex virus type 2 infections in 2012. *PLoS ONE*, 10(1):e114989, January 2015.

A proposal for quantum short time personality dynamics

Joan C. Micó ^{b1}, Salvador Amigó^{#2}, Antonio Caselles^{‡3}

(b) Institut Universitari de Matemàtica Multidisciplinar,
Universitat Politècnica de València.

(#) Departament de Personalitat, Avaluació i Tractaments Psicològics,
Universitat de València.

(‡) IASCYS member (retired), Departament de Matemàtica Aplicada,
Universitat de València.

1 Introduction

The present work is an attempt to obtain a quantum formulation for the short-term dynamics of personality as a consequence of an arbitrary stimulus. This daring goal lies on the hypotheses that the quantum approach can provide some new richness to the dynamical solutions and individual personality changes observed in behavioural sciences that a classical differential equation approach cannot provide.

First of all, a minimum action principle must be stated to describe this dynamics, i.e., a classical mechanics approach to personality, through the Lagrangian and the Hamiltonian functions [1]. The Hamiltonian permits to state the quantum approach through the corresponding Schrödinger equation.

In addition, these classical and quantum formulations allow postulating a bridge between physics and psychology. In fact, the current problem in physics consists in getting the dynamics (by a set of coupled second order differential equations) from a known Lagrangian. Besides, the inverse Lagrange problem [2] consists in finding the Lagrangian from the known dynamics. In the context of this paper, the inverse Lagrange problem, solved in [3] for the short term dynamics of personality as a consequence of an arbitrary stimulus, is taken: the Lagrangian and the Hamiltonian are presented and, as a consequence, the Schrödinger equation is got by applying the quantization rules on the Hamiltonian.

Personality is here measured by the Five-Adjective Scale of the General Factor of Personality (GFP-FAS) [4], which measures dynamically the General Factor of Personality (GFP), i.e., it is a way to measure the overall human personality [5]. The so-called response model is the mathematical tool used to model the personality dynamics [6]. However, the response model here presented has a slight different mathematical structure, which produces a more realistic dynamics [7]. The response model here presented is an integro-differential equation where the

¹e-mail: jmico@mat.upv.es

²e-mail: Salvador.Amigo@uv.es

³e-mail: Antonio.Caselles@uv.es

stimulus is an arbitrary time function. It is transformed into a second order differential equation for which a Lagrangian and a Hamiltonian are found, solving like this the corresponding inverse Lagrange problem.

Subsequently, the Schrödinger equation is found by applying the known quantization rules, and it is solved as a time-dependent equation, whose exact solution is found by following Ciftja's method in [8]. The corresponding quantum Hamilton equations [9] show its richness in dynamical solutions, in contrast to the classical approach solution.

2 The response model and its Lagrangian-Hamiltonian approach

The response model [7] is given by the integro-differential equation:

$$\dot{q}(t) = a(b - q(t)) + \delta \cdot s(t) \cdot q(t) - \gamma \int_{t_0}^t \exp((x - t)/\tau) \cdot s(x) \cdot q(x) dx \quad (1)$$

$$q(t_0) = q_0 \quad (2)$$

In (1), $q(t)$ represents the GFP dynamics; and b and q_0 are respectively its tonic level and its initial value. Its dynamics is a balance of three terms, which provide the time derivative of the GFP: the homeostatic control ($a(b - q(t))$), i.e., the cause of the fast recovering of the tonic level b , the excitation effect ($\delta \cdot s(t) \cdot q(t)$), which tends to increase the GFP, and the inhibitor effect ($\int_{t_0}^t \exp((x - t)/\tau) \cdot s(x) \cdot q(x) dx$), which tends to decrease the GFP and is the cause of a continuous delayed recovering. Parameters a , δ , γ and τ are named respectively the homeostatic control power, the excitation effect power, the inhibitor effect power and the inhibitor effect delay. In addition, the $s(t)$ time function represents the dynamics of an arbitrary stimulus. For more details about the interpretation of (1) its variables and parameters see [6] and [7]. Note that the tonic level (the b parameter) is the asymptotically stable GFP state that personality would take when the stimulus vanishes. However, in the quantum approach presented below, this parameter is avoided because, from this approach, a family of stable states represents the richness of dynamical states and personality changes found.

Taking the time derivative in (1) and subsequently substituting the integral term in this equation, the second order differential equation and the initial conditions arise:

$$\ddot{q}(t) = (-a - 1/\tau + \delta \cdot s(t)) \dot{q}(t) + (-a/\tau + (\delta/\tau - \gamma)s(t) + \delta \cdot \dot{s}(t)) q(t) + a \cdot b/\tau \quad (3)$$

$$q(t_0) = q_0 \quad (4)$$

$$\dot{q}(t_0) = a(b - q_0) + \delta \cdot s_0 \cdot q_0 \quad (5)$$

Equation (3) is an equivalent version of (1). In it, s_0 is the amount of stimulus in the initial time $t = t_0$. From now onwards (3) is the version of the response model to be used.

The corresponding Lagrangian, (L), momentum (p) and Hamiltonian (H) to (3) are [3]:

$$L(t, q, \dot{q}) = \frac{1}{2}u(t) \cdot \dot{q}^2 - \frac{1}{2}u(t) \cdot v(t) \cdot q^2 + u(t) \frac{a \cdot b}{\tau} \quad (6)$$

$$p = \frac{\partial L}{\partial \dot{q}} = u(t) \cdot \dot{q}(t) \quad (7)$$

$$H(t, q, p) = \frac{\partial L}{\partial \dot{q}} \dot{q} = \frac{1}{2u(t)} p^2 + \frac{1}{2} u(t) \cdot v(t) \cdot q^2 - u(t) \frac{a \cdot b}{\tau} \quad (8)$$

Where in (6), (7) and (8):

$$u(t) = \exp((a + 1/\tau)(t - t_0) - \delta \int_{t_0}^t s(x) dx) \quad (9)$$

$$v(t) = a/\tau + (\gamma - \delta/\tau)s(t - t_0) - \delta \cdot \dot{s}(t - t_0) \quad (10)$$

And the corresponding Hamilton equations are:

$$\dot{q} = \frac{\partial H}{\partial p} = \frac{p}{u(t)} \quad (11)$$

$$\dot{p} = -\frac{\partial H}{\partial q} = -u(t) \cdot v(t) \cdot q + u(t) \cdot a \cdot b/\tau \quad (12)$$

Note that (12) provides only one asymptotic stable state through the term $u(t) \cdot a \cdot b/\tau$.

3 The Schrödinger equation and its exact solution

As above commented, consider that the b parameter is considered as zero from now onwards. Then, to get the quantum formalism, let $\Psi(t, q)$ be the wave function of the Schrödinger equation. To get this equation, the quantization rules are applied to the Hamiltonian given by (8) (with $b = 0$):

$$i\sigma \frac{\partial \Psi(t, q)}{\partial t} = H(t, q, p \rightarrow -i \frac{\partial}{\partial q}) \Psi(t, q) \quad (13)$$

That is:

$$i\sigma \frac{\partial \Psi(t, q)}{\partial t} = -\frac{\sigma^2}{2u(t)} \frac{\partial^2 \Psi(t, q)}{\partial q^2} + \frac{1}{2} u(t) \cdot v(t) \cdot q^2 \cdot \Psi(t, q) \quad (14)$$

In (13) and (14) σ represents the Planck constant. But why not $\sigma = \hbar$, i.e., the true Planck constant? Because the q variable (GFP) is not spatial-type, it is rather an abstract, although measurable, personality variable. If the presented formalism were able to be experimentally contrasted, then the hypothesis about whether the equality $\sigma = \hbar$ holds or not should be clarified.

To solve the time-dependent Schrödinger equation given by (14), the method developed in [8] by Ciftja has been followed. First of all the following change of the wave function is made in (14):

$$\psi(t, q) = \exp(-A(t) \cdot q^2 - B(t)) \phi(t, q) \quad (15)$$

In (15), $A(t)$ and $B(t)$ are undetermined time-functions by the moment. This change provides (16) plus (17) and (18):

$$i\sigma \frac{\partial \phi}{\partial t} = \phi 1(t, q) + \phi 2(t, q) \quad (16)$$

$$\phi 1(t, q) = -\frac{\sigma^2}{2u(t)} \frac{\partial^2 \phi(t, q)}{\partial q^2} (i\sigma \cdot \dot{A}(t) - 2\sigma^2 \frac{A^2(t)}{u(t)} + \frac{1}{2}u(t) \cdot v(t)) \cdot q^2 \cdot \phi(t, q) \quad (17)$$

$$\phi 2(t, q) = (i\sigma \cdot \dot{B}(t) + \sigma^2 \frac{A(t)}{u(t)})\phi(t, q) + 2\sigma^2 \frac{A(t)}{u(t)} q \frac{\partial \phi(t, q)}{\partial q} \quad (18)$$

Now, in (16), the following change of the x independent variable is made:

$$x = \frac{q}{\rho(t)} \quad (19)$$

In (19), $\rho(t)$ is, as well by the moment, an undetermined time-function. This change provides (20) plus (21) and (22):

$$i\sigma \frac{\partial \Gamma(t, x)}{\partial t} = \Gamma 1(t, x) + \Gamma 2(t, x) \quad (20)$$

$$\Gamma 1(t, x) = -\frac{\sigma^2}{2u(t) \cdot \rho^2(t)} \frac{\partial^2 \Gamma(t, x)}{\partial x^2} + (i\sigma \cdot \dot{A}(t) - 2\sigma^2 \frac{A^2(t)}{u(t)} + \frac{1}{2}u(t) \cdot v(t))\rho^2(t) \cdot x^2 \cdot \Gamma(t, x) \quad (21)$$

$$\Gamma 2(t, x) = (i\sigma \cdot \dot{B}(t) + \sigma^2 \frac{A(t)}{u(t)})\Gamma(t, x) + (i\sigma \frac{\dot{\rho}(t)}{\rho(t)} + 2\sigma^2 \frac{A(t)}{u(t)})x \frac{\partial \Gamma(t, x)}{\partial x} \quad (22)$$

In (20): $\Gamma(t, x) = \phi(t, q = \rho(t) \cdot x)$. Now, the following equations are forced to hold in this equation:

$$i\sigma \dot{B}(t) + \sigma^2 \frac{A(t)}{u(t)} = 0 \quad (23)$$

$$i\sigma \frac{\dot{\rho}(t)}{\rho(t)} + 2\sigma^2 \frac{A(t)}{u(t)} = 0 \quad (24)$$

$$(i\sigma \cdot \dot{A}(t) - 2\sigma^2 \frac{A^2(t)}{u(t)} + \frac{1}{2}u(t) \cdot v(t))\rho^2(t) = \frac{\sigma^2}{2u(t) \cdot \rho^2(t)} \quad (25)$$

From (23), (24) and (25), (20) becomes:

$$i\sigma \frac{\partial \Gamma(t, x)}{\partial t} = -\frac{\sigma^2}{2u(t) \cdot \rho^2(t)} \frac{\partial^2 \Gamma(t, x)}{\partial x^2} + \frac{x^2}{2u(t) \cdot \rho^2(t)} \Gamma(t, x) \quad (26)$$

A final change is made in the time independent variable of (26):

$$T = \int_{t_0}^t \frac{dr}{u(r) \cdot \rho^2(r)} \quad (27)$$

That provides:

$$i\sigma \frac{\partial \Omega(T, x)}{\partial T} = -\frac{\sigma^2}{2} \frac{\partial^2 \Omega(T, x)}{\partial x^2} + \frac{x^2}{2} \Omega(T, x) \quad (28)$$

In (28) $\Omega(T, x) = \Gamma(T = \int_{t_0}^t \frac{dr}{u(r) \cdot \rho^2(r)}, x)$. Note that (28) is the Schrödinger equation corresponding to a harmonic oscillator. From the known boundary conditions of stability in (28) as $x \rightarrow \pm\infty$, its energies (eigenvalues) and exact eigenfunctions are [8]:

$$E_n = (n + \frac{1}{2})\sigma; n = 0, 1, 2, \dots \quad (29)$$

$$\Omega_n(T, x) = \exp(-i\frac{E_n}{\sigma})(\frac{1}{\sigma\pi})^{1/4} \frac{2^{-n/2}}{\sqrt{n!}} \exp(-\frac{x^2}{2\sigma}) H_n(\frac{x}{\sqrt{\sigma}}) \quad (30)$$

In (30) H_n are the Hermite polynomials. By unmaking the changes proposed above, the eigenfunctions of the Schrödinger equation (14) are:

$$\Psi_n(t, q) = \frac{1}{\sqrt{2^n n!}} (\frac{1}{\sigma\pi\rho^2(t)})^{1/4} \exp(-i\frac{E_n}{\sigma} \int_{t_0}^t \frac{dr}{u(r)\rho^2(r)} + i\frac{u(t)}{\sigma} \frac{\dot{\rho}(t)}{\rho(t)} q^2) \exp(-\frac{q^2}{2\sigma\rho^2(t)}) H_n(\frac{1}{\sqrt{\sigma}} \frac{q}{\rho(t)}) \quad (31)$$

Note in (31) that it depends only on the undetermined $\rho(t)$ time-function, which implies that it will depend on the $\rho(t)$ solution. In fact, handling appropriately the system provided by (23), (24) and (25), the system can be reduced to one only second order differential equation for $\rho(t)$:

$$\ddot{\rho}(t) + \frac{\dot{u}(t)}{u(t)} \dot{\rho}(t) + v(t) \cdot \rho(t) = \frac{1}{u^2(t) \cdot \rho^3(t)} \quad (32)$$

4 The quantum Hamilton equations

An alternative interpretation of the Quantum Mechanics was proposed by Bohm and Hiley [9], putting the emphasis on the quantum Hamiltonian that can be derived from the exact solution of the Schrödinger equation (31) and (32). This Hamiltonian is obtained by splitting the wave function into the amplitude $\Delta(t, q)$ and the phase $S(t, q)$. The amplitude square provides the probability conservation, while the phase is a correction of the Hamilton-Jacobi equation. It permits to write the quantum Hamiltonian H_q [9]:

$$H_q(t, q, p) = \frac{1}{2u(t)} p^2 + \frac{1}{2} u(t) \cdot v(t) \cdot q^2 - \frac{u(t)}{\sigma^2} \frac{1}{\Delta_n(t, q)} \frac{\partial^2 \Delta_n(t, q)}{\partial q^2} \quad (33)$$

Where, in (33), under the hypothesis that the $\rho(t)$ solution is real in (32):

$$\Delta_n(t, q) = |\Psi_n(t, q)| = \frac{1}{\sqrt{2^n n!}} (\frac{1}{\sigma\pi\rho^2(t)})^{1/4} \exp(-\frac{q^2}{2\sigma\rho^2(t)}) H_n(\frac{1}{\sqrt{\sigma}} \frac{q}{\rho(t)}) \quad (34)$$

Thus, the corresponding quantum Hamilton equations to (33) are:

$$\dot{q} = \frac{\partial H_q}{\partial p} = \frac{p}{u(t)} \quad (35)$$

$$\dot{p} = -\frac{\partial H_q}{\partial p} = -u(t) \cdot v(t) \cdot q + \frac{\sigma^2}{2u(t)} \frac{\partial}{\partial q} \left(\frac{1}{\Delta_n(t, q)} \frac{\partial^2 \Delta_n(t, q)}{\partial q^2} \right) \quad (36)$$

The second order formulation can be recovered from (35) and (36):

$$\ddot{q}(t) + \frac{\dot{u}(t)}{u(t)} \dot{q}(t) + v(t) \cdot q(t) = \frac{\sigma^2}{2u^2(t)} \frac{\partial}{\partial q} \left(\frac{1}{\Delta_n(t, q)} \frac{\partial^2 \Delta_n(t, q)}{\partial q^2} \right) \quad (37)$$

which can be compared with the initial second order formulation of (3) by using the $u(t)$ and $v(t)$ functions:

$$\ddot{q}(t) + \frac{\dot{u}(t)}{u(t)} \dot{q}(t) + v(t) \cdot q(t) = a \cdot b/\tau \quad (38)$$

Note that (37) provides an infinite family of dynamical evolutions and their corresponding asymptotic stable states through the term $\frac{\sigma^2}{2u^2(t)} \frac{\partial}{\partial q} \left(\frac{1}{\Delta_n(t, q)} \frac{\partial^2 \Delta_n(t, q)}{\partial q^2} \right)$, in contrast to the simple asymptotic stable state given by the term $a \cdot b/\tau$ in (38).

5 Conclusions and future work

Note that the richness in dynamical evolutions and their corresponding asymptotic stable states (37), must be investigated in a future time, moreover if it is compared with the simplicity of (38). This investigation could contribute to discover how an individual personality can change, by a bifurcation [9], to another one that could be radically different. In other words, it could provide the answer to the following question: why an individual can develop a disordered personality dynamics after a given stimulus and the same stimulus produces a non-disordered personality dynamics in a different individual?

However, the mathematical work here developed must be specified much more. On a hand, the initial conditions for $\rho(t)$ in (32) that provide real-valued solutions must be found in coherence with the theory units with which the GFP is measured.

On the other hand, note that the general solution of (14) should be expressed as $\Psi(t, q) = \sum_{n=0}^{+\infty} C_n \Psi_n(t, q)$ where C_n are complex numbers. However, the conditions under which the work with the pure states $\Delta_n(t, q) = |\Psi_n(t, q)|$ in (37) is right must be investigated: is a determined stimulus related with an only pure state? Is this approach the right one to describe the arising of the personality bifurcation and the consequent personality change? These questions and other similar must be answered.

Finally, the quantitative and qualitative solutions of (37) must be related with the results of different experimental designs, such as, for instance, the one presented in [3] with methylphenidate, or with other similar stimuli. This should be a definitive point to understand the personality change by the help of the quantum formalism here developed.

References

- [1] L. D. Landau, E. M. Lifshitz, *Mecánica (Vol. 1 del Curso de Física Teórica)*, Barcelona, Ed. Reverté, 2002.
- [2] P. A. M. Dirac, *Lectures on Quantum Dynamics*, New York, Ed. Yeshiva University, 1964.

- [3] J.C. Micó, S. Amigó, A. Caselles, Hamiltonian approach to human personality dynamics: an experiment with methylphenidate, *Modelling for Engineering & Human Behaviour*, 209-212, 2018.
- [4] S. Amigó, J.C. Micó, A. Caselles, Five adjectives to explain the whole personality: a brief scale of personality, *Revista Internacional de Sistemas*, 16: 41-43, 2009.
- [5] S. Amigó, A. Caselles, J.C. Micó, The General Factor of Personality Questionnaire (GFPQ): Only one factor to understand the personality?, *Spanish Journal of Psychology*, 13: 5-17, 2010.
- [6] J.C. Micó, S. Amigó, A. Caselles, From the Big Five to the General Factor of Personality: a Dynamic Approach, *Spanish Journal of Psychology*, 17: 1-18, 2014.
- [7] J.C. Micó, S. Amigó, A. Caselles, Advances in the General Factor of Personality Dynamics, *Revista Internacional de Sistemas*, 22: 34-38, 2018.
- [8] O. Ciftja, A simple derivation of the exact wave function of a harmonic oscillator with time-dependent mass and frequency, *Journal of Physics A: Mathematical and General*, 32: 6385-6389, 1999.
- [9] D. Bohm, B. J. Hiley, *The Undivided Universe (an ontological interpretation of quantum theory)*, London and New York, Ed. Routledge, 1995.

Energy footprint reduction of Chile's social interest homes: an integer linear programming approach

Felipe Monsalve ^{b1} and David Soler[‡]

(b) Escuela Técnica Superior de Ingeniería de Edificación,
Universitat Politècnica de València, Camí de Vera s/n 46022, València, España,

(‡) Instituto Universitario de Matemática Multidisciplinar,
Universitat Politècnica de València, Camí de Vera s/n 46022, València, España.

1 Introduction

In the last few years the energy efficiency concept is becoming increasingly relevant, both on energy production and on public opinion, being year 2018 an inflection point at international level due to ecologist movements across different countries [1]. Although developed economies have had the biggest part of pressure, reappraising productive process becomes essential for developing countries, whose productive sectors may be affected if its energy efficiency is not improved [2]. Building sector is not independent of this tendency. In Europe, the building sector is responsible of about 40% of the total energy consumed and the 45% of the CO2 emissions [3].

According to the International Energy Agency (IEA), energy efficiency is the management and restriction of energy consumption growing [4]. The energy footprint (ot embodied energy) is the total amount of consumed energy above all stages of a product's life cycle, from its raw material extraction to recycle or process waste [5].

With respect to buildings, energy efficiency is strongly attached to their envelope, which separates and controls thermal energy transmission between outside and inside the building. The building's envelope thermal insulation capability from its environment is measured by the thermal transmittance U ($W \cdot m^{-2} \cdot K^{-1}$), defined by McMullan [6] for a n -layer wall by Eq. 1:

$$U = \frac{1}{\frac{1}{h_{int}} + \sum_{i=1}^n \frac{e_i}{\lambda_i} + \frac{1}{h_{ext}}} \quad (1)$$

In Eq. 1, for each layer i , λ_i represents its thermal conductivity ($W \cdot m^{-1} \cdot K^{-1}$) and e_i its thickness (m), while $1/h_{int}$ and $1/h_{ext}$ ($m^2 \cdot K \cdot W^{-1}$) represent the standard internal and external thermal superficial resistance.

¹e-mail: felipe@monsalve.es

IEA reports that during year 2019, heating represented half of energy consumption of homes [7]. Heating is the main component of buildings' energy footprint in its service life.

In Chile, in 2015, during COP21, the government took the commitment of reducing country's emissions at least a 30% by year 2030 [8]. According to the Comisión Nacional de Energía de Chile, residential sector represents a 22% of country's energy consumption, and 37% of this consumption is located in the central zone among Valparaíso and Metropolitana Regions [9]. Furthermore, building's energy consumed on operation phase represents from 75% to 80% of its energy footprint [10].

80% of Chile's homes belong to single-family home typology [11]. The Cámara Chilena de la Construcción has counted a 425.600 homes deficit in the country, and there are 313.943 existing homes in damage condition which need to be replaced [12]. Size, quality and population density from social houses to middle top class ones have minimum differences [2]. The State of Chile, through Housing and Urban Planning Ministry (MINVU) has developed a subsidiary policy for the missing homes [13].

Chile's residential buildings have a lack of isolating in their envelope. This fact together with the materials used on their construction process deeply increase their energy footprint. By using an Integer Linear Programming (ILP) procedure and considering the MINVU's budget, the aim of this work is to select the optimal combination of materials for the opaque part of the envelope of a house in order to achieve the maximum reduction of its energy footprint, while improving at the same time the home's energy efficiency.

2 ILP problem formulation

The problem of minimizing the total energy footprint associated to the opaque part of the envelope of a house can be formulated as an ILP problem. Considering that the façade walls and the roof have a given surface, it is necessary to know the data for each m^2 surface type. For a better understanding of the formulation, the variables and parameters used are presented:

1. Let S_M be the total opaque part of the façade walls and let S_C be the total opaque surface part of the roof.
2. Let n be the number of the different envelope's layers. Each layer $i \in \{1, \dots, n\}$ can be made of m_i different materials available for this layer, and each material $j \in \{1, \dots, m_i\}$ is available in r_{ij} different commercial thicknesses. We will suppose that the first l layers belong to the façade wall's layers (the first layer is the outside one and the l layer is inside one), the rest of the layers ($n - l$) belong to the roof, in the same order.
3. For each $i \in \{1, \dots, n\}$, $j \in \{1, \dots, m_i\}$ and $k \in \{1, \dots, r_{ij}\}$, the following parameters are considered:
 - (a) Let $k_{i,j,k}$ be the mass in kg of $1m^2$ of layer i , made of material j and in thickness k .
 - (b) Let $E_{i,j,k}$ be the energy footprint in MJ for each kg of material j on layer i with thickness k .

- (c) Let $t_{i,j,k}$ be the thickness in m corresponding to value k of material j on layer i .
- (d) Let $c_{i,j,k}$ be the cost in UF (Unidad de Fomento) of $1m^2$ of material j , with thickness k on layer i . The UF is a non-physical Chilean currency, which is used to adjust commercial, accounting and banking transaction up to inflation variation.
4. The envelope's thickness will be between a minimum value, T_{Mmin} (for the wall) and T_{Cmin} (for the roof), and a maximum value, T_{Mmax} (for the wall) and T_{Cmax} (for the roof).
 5. Let U_{Mmax} be the maximum thermal transmittance in $W \cdot m^{-2} \cdot K^{-1}$ allowed for the façade wall and let U_{Cmax} be the maximum thermal transmittance allowed for the roof. Opaque parts, in both cases.
 6. Let P_{max} be the maximum budget in UF allowed for the construction.
 7. There may be incompatibilities among two consecutive layers.
 8. The ILP $x_{i,j,k}$ variables are binary type. Value 1 means that layer i is made of material j with thickness type k , and 0 otherwise.
 9. If λ_j is the thermal conductivity in $W \times m^{-2} \times K^{-1}$ of material j , from Eq. 1 can be deduced that:

$$\sum_{i=1}^n \sum_{j=1}^{m_i} \sum_{k=1}^{r_{ij}} \frac{t_{i,j,k}}{\lambda_j} \geq \frac{1}{U_{max}} - \frac{1}{h_{int}} - \frac{1}{h_{ext}} \quad (2)$$

The ILP formulation of the problem is given by Eqs. 3 to 11:

$$\text{Minimize } S_M \cdot \sum_{i=1}^n \sum_{j=1}^{m_i} \sum_{k=1}^{r_{ij}} E_{i,j,k} \cdot k_{i,j,k} \cdot x_{i,j,k} + S_C \cdot \sum_{i=l+1}^n \sum_{j=1}^{m_i} \sum_{k=1}^{r_{ij}} E_{i,j,k} \cdot k_{i,j,k} \cdot x_{i,j,k} \quad (3)$$

s.t:

$$\sum_{j=1}^{m_i} \sum_{k=1}^{r_{ij}} x_{i,j,k} = 1 \quad \forall i \in \{1, \dots, n\} \quad (4)$$

$$\sum_{i=1}^n \sum_{j=1}^{m_i} \sum_{k=1}^{r_{ij}} c_{i,j,k} \cdot x_{i,j,k} \leq P_{max} \quad (5)$$

$$T_{Mmin} \leq \sum_{i=1}^l \sum_{j=1}^{m_i} \sum_{k=1}^{r_{ij}} t_{i,j,k} \cdot x_{i,j,k} \leq T_{Mmax} \quad (6)$$

$$T_{Cmin} \leq \sum_{i=l+1}^n \sum_{j=1}^{m_i} \sum_{k=1}^{r_{ij}} t_{i,j,k} \cdot x_{i,j,k} \leq T_{Cmax} \quad (7)$$

$$\sum_{i=1}^l \sum_{j=1}^{m_i} \sum_{k=1}^{r_{ij}} \frac{t_{i,j,k}}{\lambda_j} \geq \frac{1}{U_{Mmax}} - \frac{1}{h_{int}} - \frac{1}{h_{ext}} \quad (8)$$

$$\sum_{i=l+1}^n \sum_{j=1}^{m_i} \sum_{k=1}^{r_{ij}} \frac{t_{i,j,k}}{\lambda_j} \geq \frac{1}{U_{Cmax}} - \frac{1}{h_{int}} - \frac{1}{h_{ext}} \quad (9)$$

$$x_{i,j,k} + x_{(i+1),j',k'} \leq 1 \quad \forall (i, j, k - (i + 1), j', k') - incompatible \quad (10)$$

$$x_{i,j,k} \in \{0, 1\} \quad \forall i \in \{1, \dots, n\}, j \in \{1, \dots, m_i\}, k \in \{1, \dots, r_{ji}\} \quad (11)$$

Where:

1. Eq. 3 represents the objective function, that is, the total energy footprint of the opaque part of the house's envelope.
2. Eq. 4 guarantees that each layer is made only of one material and thickness.
3. Eq. 5 ensures that the maximum budget is not exceeded.
4. Eq. 6 restricts façade wall's thickness.
5. Eq. 7 limits roof's thickness.
6. Eq. 8 ensures façade wall's maximum thermal transmittance allowed is not exceeded.
7. Eq. 9 ensures roof's maximum thermal transmittance allowed is not exceeded.
8. Eq. 10 forbids that material j' with thickness k' appears in layer next to i containing material j with thickness k . That is, at most one of those two materials will appear (see [14] for more details about incompatibility between materials).
9. Eq. 11 defines the problem variables as binaries.

Note that to fit as much as possible real problems, this ILP formulation could contain additional constraints involving other parameters.

3 Case study

We present in this work a case study consisting in a social interest home type, where two sections from the opaque part of the envelope are considered, one from the façade walls and one from the roof.

For these sections, different designs with up to 6 layers will be studied according to solutions and real constructive systems which give interesting proposals to each one of the considered scenarios. The function of each layer, depending on the construction solution, may be (from outside to inside): Layer 1, outside facing or structural element; Layer 2, isolating layer; Layer 3, structural element or isolating; Layer 4, isolating; Layer 5, secondary structural element or isolating; Layer 6, inside facing.

In this case study we consider a house from a social interest executed in Villa Alemana (Región de Valparaíso, Chile) by Quinta Servicios Ltda. which has an façade surface of $77,91m^2$ and a roofing surface of $60,83m^2$.

4 Results

This paper presents the optimal solution of the ILP problem, obtained using Wolfram Mathematica software. The materials considered were: clay bricks, galvanized steel profiles, steel stays, copper impregnated pine wood, plaster panel, fibrocement plates, steel framework, expanded polystyrene, glass wool, roofing zinc plates, tiles, asphaltic felt, concrete, ceramic and painting. All chosen materials are presented on the Chilean market and on the MINVU's official list of prices and materials (Tabla Referencial de Precios Unitarios).

Using *Procasclima 2018 version 1.1* software the following properties of the materials were obtained: thermal conductivity, density and primary energy input. And, from MINVU's list of prices were taken de prices of the materials, which include labour costs and tools needed.

The optimal solution obtained with *Mathematica* to the ILP problem provides a façade made of (from outside to inside) layers: fibrocement plates with asphaltic felt, copper impregnated pine wood as main structure, an air layer, copper impregnated pine wood as second structure and plaster panel as inter cover. For roofing layers, the optimal combination is made of, from outside to inside, are tiles, asphaltic felt, glass wool and galvanized steel for roofing structure (see Figure for details). The main results are given Table 1.

	Proposal	Type House	Diference
Energy Footprint [MJ]	41.320	57.079	-28%
Cost [UF]	76,62	46,47	+65%
Walls thermic resistance [$W/(m^2 \cdot K)$]	4,69	0,60	+682%
Roofing thermic resistance [$W/(m^2 \cdot K)$]	3,98	3,96	+0,50%

Table 1: Results

5 Conclusions

The results show that if the economic effort is increased, the energy footprint of each new social interest house can be reduced an amount of 28%, considering Chile's lack of houses, this could mean saving an order of 6.700 millions of MJ .

The proposal of this work means an increase of 65% payment, but the total amount of this solution represents a 16% of the amount available for this part of the house. Its important to know that if MINVU allows a maximum budget of $1.400UF$ per house, MINVU gives up to $520UF$ pear each house [15]. The reason of not using 100% of maximum budget allowed is because most of the families who apply to these houses cannot pay the difference up to $1.400UF$.

If the social interest houses were constructed using this paper proposal the increment of thermic isolation would mean a huge energy and money saving on Chile's homes for heating in winter and cooling in summer for people and minimize the impact on the environment.

References

- [1] Omedes, E., Salvando el 'Planeta A': Los nuevos movimientos contra el cambio climático. *20 minutos*, 2019.
- [2] Celis Damico, F., García Alvarado, R., Trebilcock Kelly, M., Escorcía Oyola, O., Miotto Bruscato, U. & Díaz, M., Análisis energético de las viviendas del centro-sur de Chile. *Arquitecturarevista*, 8: 62-78, 2012.
- [3] Soler, D., Salandin, A. & Bevivino, M., An integer linear programming approach to check the embodied CO2 emissions of the opaque part of a façade. *Modelling for Engineering & Human Behaviour* 204-210, 2019.
- [4] International Energy Agency, *Energy Efficiency 2019*, 2019.
- [5] Sicignano, E., Di Ruocco, R. & Melella, R., Mitigation Strategies for Reduction of Embodied Energy and Carbon, in the Construction Systems of Contemporary Quality Architecture. *Sustainability*, 11 3806, 2019.
- [6] McMullan, R., Environmental science in building. New York, Palgrave Macmillan, 2012.
- [7] International Energy Agency, *Energy efficiency indicators highlights*, 2019.
- [8] Ministerio del Medio Ambiente de Chile *Ministerio del Medio Ambiente de Chile's Web* <https://mma.gob.cl/lideres-del-mundo-logran-acuerdo-historico-en-la-lucha-contra-el-cambio-climatico>, 2014.
- [9] Comisión Nacional de Energía - Ministerio de Energía de Chile. Anuario estadístico de energía 2018, Santiago de Chile, Ministerio de Energía, 2019.
- [10] Muñoz Sanguinetti, C., Estudio de la energía incorporada y emisiones de gases de efecto invernadero en el ciclo de vida de las viviendas en Chile. Concepción, Universidad del Bío-Bío, 2013.
- [11] Observatorio Urbano - Ministerio de Vivienda y Urbanismo de Chile, Viviendas particulares ocupadas según tipo de vivienda. Santiago de Chile, Ministerio de Vivienda y Urbanismo, 2017.
- [12] Cámara Chilena de la Construcción, Déficit de viviendas en Chile *Déficit Habitacional CCHC — Cámara Chilena de la construcción* Online, <https://www.cchc.cl/2019/deficit-habitacional>, 2019.
- [13] Rivera, Á. Historia de la política habitacional en el área metropolitana de Santiago, *Revista CIS*, 16, 27-44, 2012.
- [14] Soler, D. & Salandin, A., Computing the minimum construction cost of a building's external wall taking into account its energy efficiency. *Journal of Computational and Applied Mathematics*, Volume 338: 199-211, 2018.
- [15] Ministerio de Vivienda y Urbanismo de Chile, D.S. N°1 (V. y U.), de 2011 - ACT.21.06.2017 Reglamento Integrado de Subsidio Habitacional. *Diario Oficial*, 2017.

Statistical solution of a second-order chemical reaction

J.-C. Cortés ^{b1}, A.Navarro-Quiles^{b2}, J.-V. Romero ^{b3}, and M.-D. Roselló ^{b4},

(b) Instituto Universitario de Matemática Multidisciplinar,
Universitat Politècnica de València,
Camino de Vera s/n 46022, València, Spain,
(b) Department of Statistics and Operational Research,
Universitat de València,
Dr Moliner 50, 46100, Burjassot, Spain,

1 Introduction

In Reference [1] different and interesting differential equations with applications are considered. In this contribution, motivated by one of the models described in [1], we focus our analysis in how to model a chemical reaction by a differential equation and how to obtain the main statistical information of the solution stochastic process.

A chemical reaction is a process that leads to the chemical transformation of one set of chemical substances to another. In particular, a second-order chemical reaction is a chemical reaction that depends on the concentrations of one-second order reactant or two first-order reactants. That is, let $[A]$ and $[B]$ be the concentrations of two reactants. Given a constant k , usual examples of second-order chemical reactions are:

- $\nu = k[A]^2$, one reactant is consumed at a rate proportional to the square of the reactant's concentration.
- $\nu = k[A][B]$, both reactants are consumed linearly over time.

Where ν denotes the reaction rate and it measures how fast the reactants are consumed. We focus this study in the second type of chemical reaction established below. We start from two reactants A and B which will be consumed linearly. Let $X(t)$ be the number of grams of chemical C formed after the second-order chemical reaction in a time instant t . Suppose that we have a grams of chemical A and b grams of chemical B and the compound is formed by M and N parts of A and B , respectively. Then, the number of grams of chemicals A and B remaining at time t are:

$$A(t) = a - \frac{M}{M+N}X(t), \quad B(t) = b - \frac{N}{M+N}X(t).$$

¹jccortes@mat.upv.es

²ana.navarro@uv.es

³jvromero@mat.upv.es

⁴drosello@mat.upv.es

Therefore, by the law of mass, the reaction rate is proportional to the product of the amounts of A and B remaining at time t , i.e., $\nu \propto A(t)B(t)$. As the derivative of $X(t)$, $X'(t)$, is the exchange rate of the quantity of chemical C , then

$$X'(t) \propto \left(a - \frac{M}{M+N}X(t)\right) \left(b - \frac{N}{M+N}X(t)\right). \quad (1)$$

Reordering expression (1) and introducing a constant of proportionality $k > 0$, we obtain the following second-order differential equation

$$X'(t) = k(\alpha - X(t))(\beta - X(t)), \quad (2)$$

being $\alpha = a(M+N)/N$ and $\beta = b(M+N)/N$. Clearly $X(0) = 0$, thus the solution of equation (2) with initial condition $X(0) = 0$ is established

$$X(t) = \frac{(1 - e^{(\beta-\alpha)kt}) \alpha \beta}{(\alpha - \beta e^{(\beta-\alpha)kt})}. \quad (3)$$

In practice, parameters α and β are fixed at the beginning of the experiment, therefore they have an associated inherent error. In addition, the constant of proportionality k must be obtained from experimental data, thus it contains a certain measurement error. In order to capture this uncertainty, it is more advisable to consider k , α and β as random variables instead of a deterministic constants. Therefore, the randomized initial value problem is

$$\begin{cases} X'(t, \omega) &= k(\omega)(\alpha(\omega) - X(t, \omega))(\beta(\omega) - X(t, \omega)), \\ X(0) &= 0, \end{cases} \quad (4)$$

where $k(\omega)$, $\alpha(\omega)$ and $\beta(\omega)$ are assumed to be absolutely continuous random variables defined in a common complete probability space $(\Omega, \mathcal{F}, \mathbb{P})$, with a known joint probability density function, $f_0(k, \alpha, \beta)$, defined on a positive region. The solution of (4) can be obtained directly from the deterministic, given in (3), by randomizing all the parameters

$$X(t, \omega) = \frac{(1 - e^{(\beta(\omega)-\alpha(\omega))k(\omega)t}) \alpha(\omega) \beta(\omega)}{(\alpha(\omega) - \beta(\omega) e^{(\beta(\omega)-\alpha(\omega))k(\omega)t})}. \quad (5)$$

Therefore, taking into account the randomness, the solution of the initial value problem (4) is a stochastic process.

2 Computing the first probability density function

In this section, we apply the Random Variable Transformation method (see Reference [2]) to obtain the first probability density function of the solution stochastic process $X(t, \omega)$ defined in (5). Fixing $t > 0$, we apply RVT method with the following choice:

$$\begin{aligned} \mathbf{U}(\omega) &= (k(\omega), \alpha(\omega), \beta(\omega))^\top, & \mathbf{V}(\omega) &= (V_1(\omega), V_2(\omega), V_3(\omega))^\top, \\ \mathbf{g} : \mathbb{R}^3 &\rightarrow \mathbb{R}^3, & \mathbf{g}(k, \alpha, \beta) &= (g_1(k, \alpha, \beta), g_2(k, \alpha, \beta), g_3(k, \alpha, \beta))^\top, \end{aligned}$$

being

$$\begin{aligned} v_1 &= g_1(k, \alpha, \beta) = X(t) = \frac{(1 - e^{(\beta-\alpha)kt}) \alpha \beta}{(\alpha - \beta e^{(\beta-\alpha)kt})}, \\ v_2 &= g_2(k, \alpha, \beta) = \alpha, \\ v_3 &= g_3(k, \alpha, \beta) = \beta. \end{aligned}$$

Isolating k , α and β , the inverse mapping $\mathbf{h} : \mathbb{R}^3 \rightarrow \mathbb{R}^3$ is

$$\begin{aligned} k &= h_1(v_1, v_2, v_3) = \frac{\ln\left(\frac{(v_1-v_2)v_3}{v_2(v_1-v_3)}\right)}{t(v_2 - v_3)}, \\ \alpha &= h_2(v_1, v_2, v_3) = v_2, \\ \beta &= h_3(v_1, v_2, v_3) = v_3. \end{aligned}$$

The Jacobian of the inverse mapping \mathbf{h} is

$$J = \frac{1}{t(v_1 - v_2)(v_1 - v_3)} \neq 0.$$

Thus, the joint PDF of the random vector $\mathbf{V}(\omega)$ is

$$f_{\mathbf{V}}(v_1, v_2, v_3) = f\left(\frac{\ln\left(\frac{(v_1-v_2)v_3}{v_2(v_1-v_3)}\right)}{t(v_2 - v_3)}, v_2, v_3\right) \left| \frac{1}{t(v_1 - v_2)(v_1 - v_3)} \right|.$$

Marginalizing with respect to the random variables $V_2(\omega) = \alpha(\omega)$ and $V_3(\omega) = \beta(\omega)$, and considering $t > 0$ arbitrary, the first probability density function of the solution stochastic process $X(t, \omega)$ is determined

$$\boxed{f_1(x, t) = \iint_{\mathbb{R}^+} f_0\left(\frac{\ln\left(\frac{(x-\alpha)\beta}{\alpha(x-\beta)}\right)}{t(\alpha - \beta)}, \alpha, \beta\right) \left| \frac{1}{t(x - \alpha)(x - \beta)} \right| d\alpha d\beta.} \quad (6)$$

3 Numerical example

In this example, we consider that the random parameters $k(\omega)$, $\alpha(\omega)$ and $\beta(\omega)$ are independent random variables with the following distributions:

- $k(\omega)$ follows a Gamma distribution with parameters 3 and 5, i.e., $k(\omega) \sim \text{Ga}(3; 5)$.
- $\alpha(\omega)$ is a truncated Gaussian distribution with mean 1 and standard deviation 0.01, i.e., $\alpha(\omega) \sim N_T(1, 0.01)$, with $T = (0, \infty)$.
- $\beta(\omega)$ follows an Uniform distribution in the interval $[0.4, 0.5]$, i.e., $\beta(\omega) \sim U([0.4, 0.5])$.

Thus, the joint probability density function can be calculated as the product of the marginals

$$f_0(k, \alpha, \beta) = f_k(k) f_\alpha(\alpha) f_\beta(\beta),$$

being $f_k(k)$, $f_\alpha(\alpha)$ and $f_\beta(\beta)$ the probability density functions of $k(\omega)$, $\alpha(\omega)$ and $\beta(\omega)$, respectively. The choice of that probabilistic distributions has been considered taking into account

the positiveness of the parameters. Furthermore, we know the expression for each probability density function:

$$f_k(k) = \begin{cases} \frac{1}{250} e^{-k/5} k^2 & k > 0, \\ 0 & \text{Otherwise.} \end{cases} \quad f_\alpha(\alpha) = \begin{cases} 39.8942 e^{-5000(1-\alpha)^2} & \alpha > 0, \\ 0 & \text{Otherwise.} \end{cases}$$

$$f_\beta(\beta) = \begin{cases} 10 & 0.4 \leq \beta \leq 0.5, \\ 0 & \text{Otherwise.} \end{cases}$$

In Figure 1 we have plotted the first probability density function of the solution stochastic process given in expression (6) in the time interval $[0, 0.5]$. We observe that when the time increases the number of grams (or quantity) of the chemical C also increases. This augment is more pronounced in the early stages, after that it tends to stabilize (approximately with 4 grams of component C). The behaviour of the first probability density function can be also

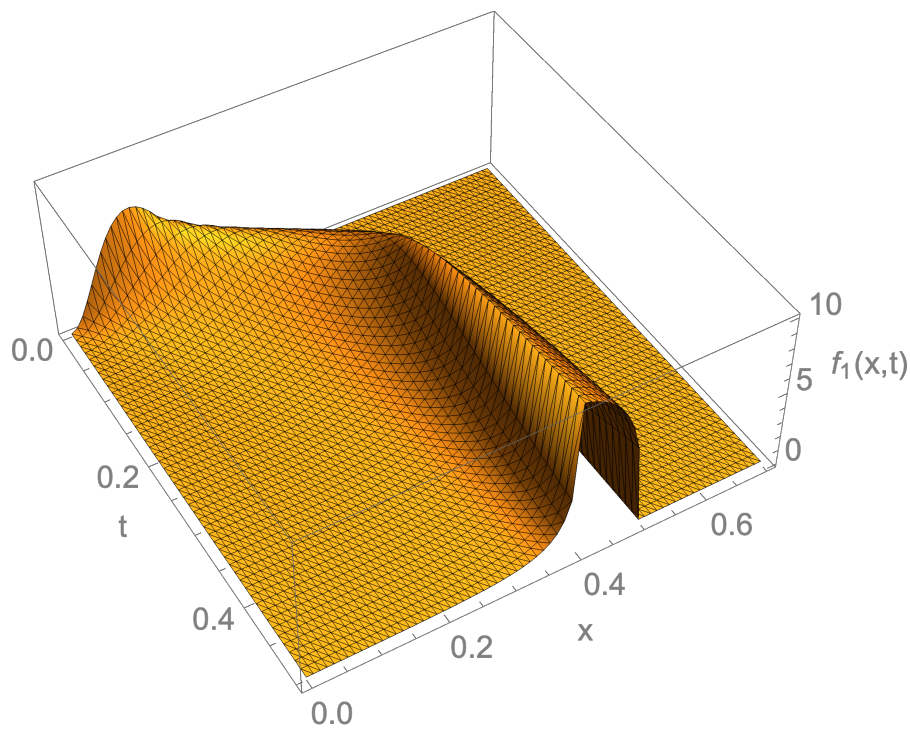


Figure 1: First probability density function, given in (6), of the solution stochastic process, $X(t, \omega)$, in the time interval $[0, 0.5]$.

observed in Figure 2 where the contour plot is represented. We observe also that for larger times the variability tends to vanish. Both graphical representation are in agreement with Figure 3 where the mean and the mean plus/minus a standard deviation is plotted. The mean increase at the first moments and then it stabilizes while the variability also increases but it tends to vanish when the time passes.

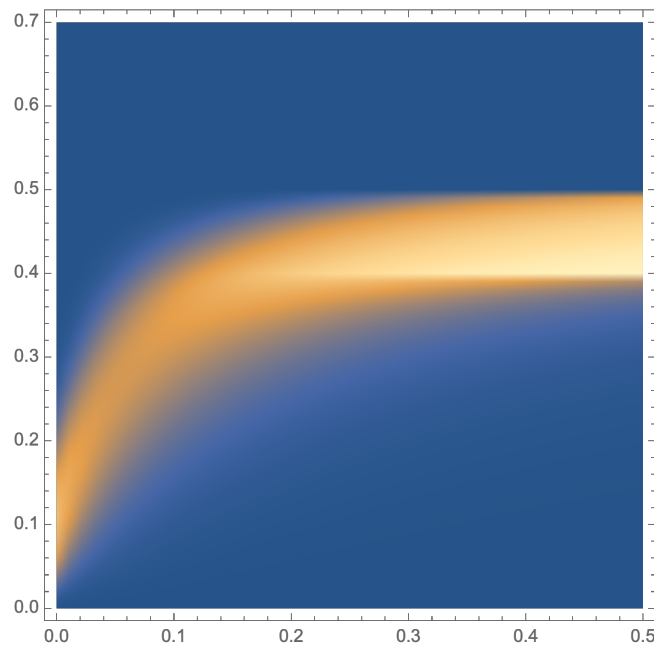


Figure 2: Contour plot of the first probability density function, $f_1(x, t)$, of the solution stochastic process, $X(t, \omega)$, in the time interval $[0, 0.5]$.

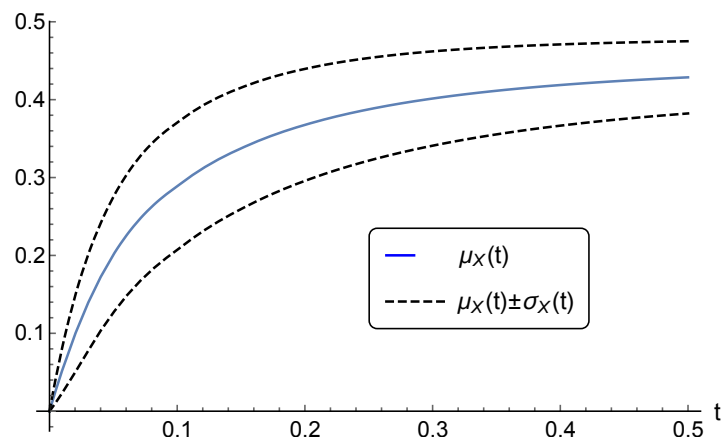


Figure 3: Mean (blue line) and mean plus/minus one standard deviation (black dashed line) of the solution stochastic process, $X(t, \omega)$, in the time interval $[0, 0.5]$.

4 Conclusions

In this work, the first probability density function of a general chemical reaction has been determined. The computation has been carried out by applying the Random Variable Transformation technique. This technique allows us to obtain the joint probability density function of a given random whose comes from mapping another random vector which distribution is assumed known. A numerical example has been performed in order to show the capability of the theoretical result established.

Acknowledgements

This work has been supported by the Spanish Ministerio de Economía, Industria y Competitividad (MINECO), the Agencia Estatal de Investigación (AEI) and Fondo Europeo de Desarrollo Regional (FEDER UE) grant MTM2017-89664-P.

References

- [1] Zill, D. G. and Wright, W. S., Differential Equations with Boundary-Value Problems, México, Cengage Learning, 2013.
- [2] Soong T. T., Random Differential Equations in Science and Engineering, New York, Academic Press, 1973.

On comparing Spotify Top 200 lists

F. Pedroche ^{b1} and J. A. Conejero [‡]

(b) Institut de Matemàtica Multidisciplinària, Universitat Politècnica de València,
Camí de Vera s/n, 46022, València,

(‡) Instituto Universitario de Matemática Pura y Aplicada, Universitat Politècnica de València,
Camí de Vera s/n, 46022, València.

1 Introduction

Spotify is an online service to listen to music on streaming. The users can access this platform by using different devices (desktops, smartphones or tablets) and they can choose between a *Free* service or a *Premium* service. In the last quarter of 2019 Spotify offered a number of (monthly active) users of 271 million, where 124 million were paying subscribers [7]. To a certain extent, Spotify helped the music industry to recover from *music piracy* [8] as long as it operates as a kind of provider of digital music that pays royalties to the owner of the songs (the record label companies such as a Sony, Warner, Universal, etc.) that pays, in turn, the artists or creators. To the end of 2019 there were more than 700 thousand songs (*podcasts*) on the platform [7]. The users can elaborate lists of songs (*playlists*) than can be accessed by anyone (see [1] for an study of the impact of playlists on song success). These playlists can be tagged to inform the mood that they transmit or the proper moment to enjoy them (for example, a user can find the proper pop Latin music to drive to the office). Spotify offers a ranking of the most listened songs on a daily or a weekly basis and it allows to select between the *Top 200* or *Viral 50* rankings [9]. In this paper we offer some insights on how to analyze these rankings by using concepts from the theory of rankings with ties and incomplete rankings [3], [4], [6], [5].

2 Results and discussion

Spotify Top 200 lists can be considered as incomplete rankings due to the fact that there exist some elements (songs or *tracks*) that disappear from ranking to ranking and other elements that are new (new songs that enter into the Top 200 list). One of the standard tools to compare rankings consists of some extensions of the classic Kendall's tau coefficient [2]. In this communication we focus on the measures given in [3] and [6].

We recall, from [6], that letting $V = \{v_1, v_2, \dots, v_n\}$ represent the objects (songs) to be ranked, the incomplete ranking can be represented given by the vector $\mathbf{a} = [a_1, a_2, \dots, a_n]$, where a_i is the position of the element v_i in the ranking. In the case that two elements, v_i and v_j , are tied we have $a_i = a_j$. When an element v_i is not ranked it is denoted as $a_i = \bullet$. The set

¹e-mail:pedroche@imm.upv.es

of ranked elements is denoted as $V_a = \{v_i / a_i \neq \bullet\}$. By using this notation, given two rankings \mathbf{a} and \mathbf{b} , we define the number of common ranked elements as $\bar{n} = |V_a \cap V_b|$.

Example 1 Let $V = \{A, B, C, D, E\}$, and let us consider two rankings \mathbf{a} and \mathbf{b} . Then, $\mathbf{a} = [2, \bullet, 1, \bullet, 1]$ represents the incomplete ranking with ties (C-E, A), where C-E indicates tied elements. Analogously, $\mathbf{b} = [3, 2, \bullet, 4, 1]$ represents the ranking (E, B, A, D). Note that $n = 5$ and $\bar{n} = 2$.

We also recall, from [6], that a matrix A , associated to \mathbf{a} , with elements $a_{ij}, 1 \leq i, j \leq n$ is defined as follows

$$a_{ij} = \begin{cases} 1 & a_i \leq a_j \\ -1 & a_i > a_j \\ 0 & i = j, a_i = \bullet, \text{ or } a_j = \bullet \end{cases}$$

With these ingredients it is possible to define the coefficient

$$\tau_x(\mathbf{a}, \mathbf{b}) = \frac{\sum_{i=1}^n \sum_{j=1}^n a_{ij} b_{ij}}{n(n-1)}$$

and the coefficient called *scaled Kendall tau-extended correlation coefficient* (see [6])

$$\hat{\tau}_x(\mathbf{a}, \mathbf{b}) = \frac{n(n-1)}{\bar{n}(\bar{n}-1)} \tau_x(\mathbf{a}, \mathbf{b})$$

By using the above definitions it is easy to compute the coefficients $\tau_x(\mathbf{a}, \mathbf{b})$ and $\hat{\tau}_x(\mathbf{a}, \mathbf{b})$ for a pair of rankings that represent two Top-200 Spotify lists (see [5]). In the next example we show how we can manage two of these lists.

Example 2 Let us consider just two Spotify Top 200 lists such that 50 new tracks appear on the second ranking (and therefore 50 tracks disappear from the first ranking). All in all we have to take into account $n = 250$ tracks. Let us denote $V = \{1, 2, \dots, 250\}$, and let us denote the rankings by \mathbf{r}_1 and \mathbf{r}_2 , and by \mathbf{a}_1 and \mathbf{a}_2 the corresponding \mathbf{a} . Let us assume that these rankings are the following

\mathbf{r}_1	\mathbf{r}_2	\mathbf{a}_1	\mathbf{a}_2
1	201	1	2
2	1	2	•
⋮	⋮	⋮	⋮
198	249	198	•
199	200	199	•
200	250	200	199
201	2	•	1
⋮	⋮	⋮	⋮
249	198	•	198
250	199	•	200

Note the following: a) \bar{n} is the number of common tracks from $\mathbf{r}_1(1 : 200)$ to $\mathbf{r}_2(1 : 200)$, that is $\bar{n} = 150$ in this example. b) Tracks 2, 198 and 199 are not ranked in $\mathbf{r}_2(1 : 200)$. c) The elements of \mathbf{a}_1 and \mathbf{a}_2 that are not • have values on the set $[1, 200]$.

It is also worthwhile to take a look at the different behaviour than can exhibit the songs that move along a series of weekly Top-200 Spotify lists. In Figure 1 we show the evolution of four tracks during 18 weeks of 2020. Note that track number 1 keeps in the first positions during the whole period, while track 277 enters (and quits) twice, track 59 quits the list very fast, and track 201 enters the list and keeps positions above 100. These plots give an idea of the movements of the lists.

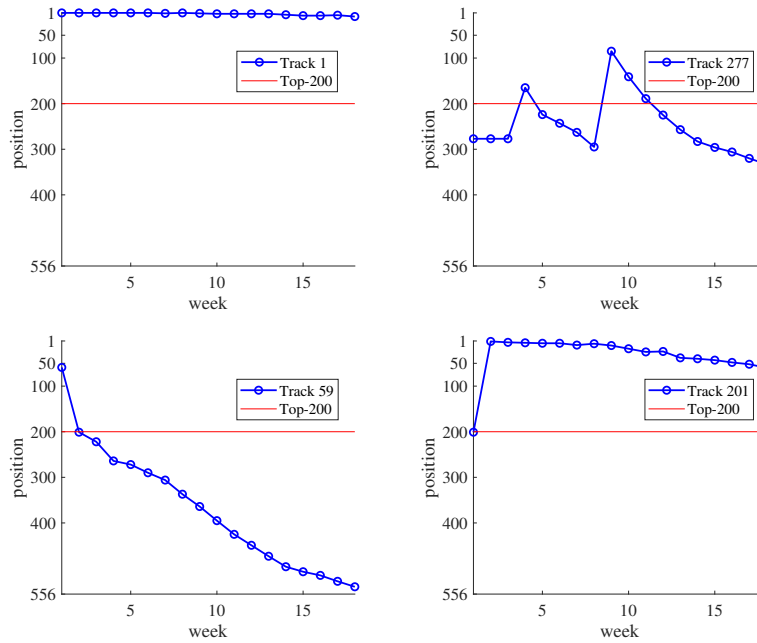


Figure 1: Evolution of some tracks in the weekly global Top 200 lists during a period of 18 weeks

In Figure 2 we show the first positions (up to number 13) of the rankings during 18 weeks of 2020 and we highlight the movements of some songs.

January					February				March					April				
1	1	1	1	1	1	13	1	8	8	8	8	8	8	8	8	8	8	546
2	201	13	13	13	13	1	13	1	13	13	13	13	13	7	514	514	514	8
3	2	219	3	8	8	8	8	13	1	1	1	1	1	71	71	71	71	71
4	13	201	239	3	3	7	324	7	7	7	7	7	7	13	7	7	334	514
5	3	3	201	239	7	3	325	325	325	382	325	71	1	13	334	7	334	
6	8	2	219	201	201	5	7	3	327	325	127	467	334	334	13	1	7	
7	5	8	8	219	239	308	201	335	382	383	5	334	491	1	1	13	93	
8	7	7	2	2	5	2	3	5	3	127	3	127	127	312	312	312	13	
9	4	5	5	5	2	219	5	2	383	3	389	325	325	127	127	127	1	
10	6	4	7	7	219	201	2	324	127	327	382	335	312	325	491	533	547	
11	10	6	4	10	10	10	219	201	5	5	2	5	389	491	325	491	312	
12	9	220	6	4	4	239	10	219	2	2	334	389	290	5	5	419	127	
13	11	10	10	14	6	6	6	10	384	389	383	3	5	273	273	325	142	

Figure 2: Evolution of the first 13 positions of the rankings Top 200 along 18 weeks on 2020. Song 1 corresponds to *Dance Monkey* (Tones and I), Song 13 is *The Box* (Roddy Rich) and song 8 corresponds to *Blinding lights* (The weeknd)

3 Conclusions and future work

In this paper we have seen that a series of Top 200 Spotify lists can be considered as series of incomplete rankings. The shown definitions and measures (see [6] for details) can be applied to pairs of these rankings. Our next objective is to extend the coefficients τ_x and $\hat{\tau}_x$ to be applied to series of more than two rankings, including the case of ties in the rankings. The state of our current research can be found in [5].

References

- [1] Aguiar, L., Waldfogel, J., Platforms, Promotion, and Product Discovery: Evidence from Spotify Playlists, *JRC Digital Economy Working Paper*, No. 2018-04, European Commission, Joint Research Centre (JRC), Seville, 2018.
- [2] Kendall, M.G. A New Measure of Rank Correlation, *Biometrika*, 30(1-2): 81–89, 1938.
- [3] Emond, E.J., Mason, D.W. A New Rank Correlation Coefficient with Application to the Consensus Ranking Problem. *J. Multi-Crit. Decis. Anal.* 2002, 11, 17–28.
- [4] Fagin, R., Kumar, R., Mahdian, M., Sivakumar, D., Vee, E. Comparing Partial Rankings. *SIAM J. Discrete Math.* 20(3), 628–648, 2006.
- [5] Pedroche, F., Conejero, A. J., Corrected Evolutive Kendall's τ coefficients for incomplete rankings with ties. Application to case of Spotify lists. *Mathematics* 8, 1828, 2020.
- [6] Yoo, Y., Escobedo, A.R., Skolfield, J.K. A new correlation coefficient for comparing and aggregating non-strict and incomplete rankings. *Eur. J. Oper. Res.*, 2020, 285(3), 1025-1041.
- [7] *Spotify Reports Fourth Quarter and Full-Year 2019 Earnings*. newsroom.spotify.com. 5 February 2020. Retrieved 13 April 2020.
- [8] <http://www.csun.edu/~ch1842/piracy/history.html>.
- [9] <https://spotifycharts.com/regional>.

New autonomous system for slope stability control in linear infrastructure

Álvaro Potti^{b1}, Gonzalo Munielo^{b2}, Julián Santos^{b3} and Jordi Marco^{b4}

(b) Institute of Multidisciplinary Mathematics,
Universitat Politècnica de València.

1 Introduction

The safety of rail and road lines can be significantly affected when uncontrolled movements on clear slopes adjacent to the track or rockfalls occur due to uncontrolled earth movements caused by adverse environmental conditions, which can cause numerous human and economic losses. The quality of service is also affected because maintenance work requires the temporary interruption of traffic.

According to the General Directorate of Civil Protection and Emergencies, in Spain, due to factors such as rugged terrain, varied geology and climatic conditions, hillside movements are of great importance, causing serious risks especially in urban areas and on roads. This means losses are estimated at 150 million per year, which could be reduced by around 90% [1] if forecasting and mitigation measures are implemented. In countries such as Japan or Italy, estimated losses exceed \$2 billion per year, and \$1.3 billion in the United States. According to UNESCO, between 200 and 300 deaths are directly attributable to landslides worldwide each year, not including those caused by earthquakes [2].

Currently, the diagnosis of the slopes is carried out by means of visual technical inspection of the terrain, analysing the existence of active processes of erosion and/or degradation of the substrate, the presence of wheel tracks on the road and the identification of larger phenomena such as material slides or mass movements. Slopes diagnosed in a "bad condition" or "very bad condition" category are continuously observed, which increases the cost of maintenance. At present, the different equipment used for such inspections are either laser methods or photographic methods. However, both methods have as a common disadvantage the high economic cost due to the use of complementary equipment such as the use of an airplane, helicopter or satellite compared to terrestrial techniques. Also, in the case of laser methods, there are other disadvantages such as longer flight times, the area covered, the large data processing or the precision at very large scales. And in the case of terrestrial photogrammetry, this method is especially applicable in small area landslides.

¹e-mail: alpotgui@cam.upv.es

²e-mail: gonmuiga@etsii.upv.es

³e-mail: jusanve@cam.upv.es

⁴e-mail: jormarte@alumni.uv.es

For this reason, the objective of the article is to develop an autonomous system for controlling the stability of slopes on roads and railways, simple and low cost, capable of providing information on the status of this slope through the flight of a drone and taking images, so that it can act on it before any damage is done to the track, ie allowing predictive action on the slope in question.

2 Method

To achieve this goal, the purposed methodology is divided in four stages. Each of these is described in detail below.

The first stage consists of collecting images of slopes from a drone with a high-resolution digital camera, implementing a flight mission for the drone and analysing the stability of the camera. This analysis is carried out using the ROT rotation method, which allows the comparison of beams that share the same centre of perspective but have different orientation in space.

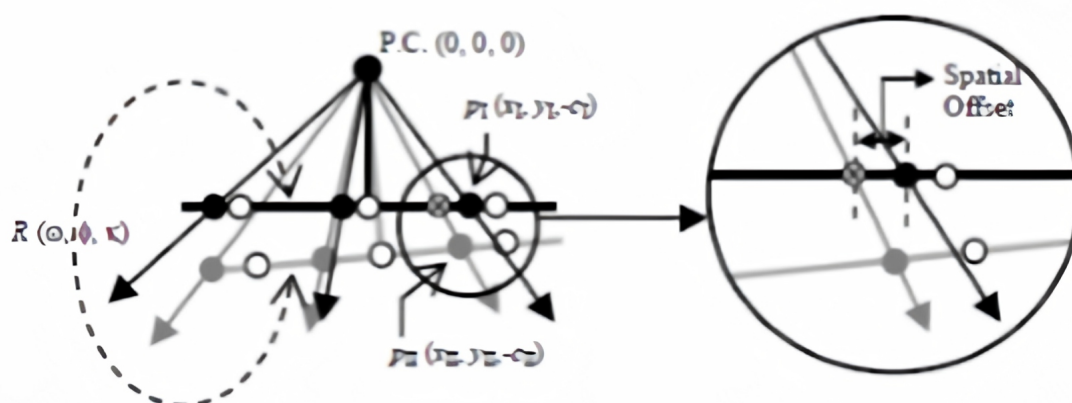


Figure 1: ROT Rotation method

This method checks if there is a set of rotation angles (ω, ϕ, κ) that can be applied to a single beam to produce the other. To evaluate the degree of similarity between the beams reconstructed from different calibrations, the RMSEoffset values (square root error of the average) should not be greater than the size of one pixel (0.00465 mm), which indicates excellent camera stability.

The next stage is aimed at the reconstruction of the 3D surface. To do this, the external image orientation parameters (EOPs) are obtained, using the Structure from Motion (SfM) approach that automates the spatial repositioning of a series of points that coincide between images and the positions of the camera that takes the images with respect to the scene through the SIFT process or scale-invariant feature transform, where common points or characteristics are detected between pairs of images, allowing hundreds of images to be compared in order to extract large quantities of common points or key points.

Once the IOPs of the camera (stability analysis) and the EOPs of the images (SfM approach) have been obtained, the normalization of the image acquired through the epipolar geometry is carried out in order to minimize the search space for the corresponding characteristics of the

superimposed images, since in this way the entire image plane does not have to be covered, but rather can be limited to the epipolar line. To conclude the 3D surface reconstruction, the SGM (Semiglobal Matching) procedure is used to obtain the point cloud in three dimensions.

The third stage is aimed at identifying the slides. The identification is carried out by means of a point cloud based on an examination of the local topographical variability by means of the relation of eigenvalues, the slope and the surface roughness index.

The eigenvalue ratio represents the degree of roughness in three dimensions or the folding edge of the ground surface. The eigenvalue ratio methodology is carried out using Principal Component Analysis (PCA), a technique used to reduce the dimensionality of a data set in determining the geometric properties of the local vicinity of the point image. Eigenvectors represent the orientation of the neighbourhood in 3D space, while eigenvalues define the extent of the area along the directions of their corresponding eigenvectors.

With reference to the slope angle, this is the most important parameter in a slope stability analysis because the slope angle is directly related to the probability of slippage.

The slope angle for each point in an image-based point cloud is estimated using Equation (1), as the eigenvector for each point is calculated based on the PCA analysis in the previous step.

$$|\theta| = \tan^{-1} \frac{\sqrt{N_x^2 + N_y^2}}{N_z} \cdot \frac{180}{\pi} \quad (1)$$

Where θ is the angle of the slope, and N_x , N_y and N_z are the components of the normal vector in the plane.

Finally, surface roughness can be defined as the irregularity of a topographic surface. The developed algorithm uses surface roughness information to detect landslide based on measuring the variability of local topographic surfaces.

The surface roughness index is the standard deviation of the object height (h) using a local window of 0.5 m to calculate the surface roughness (Equation (2)).

$$\gamma = \sqrt{\frac{\sum (h - h')^2}{n - 1}} \quad (2)$$

3 Results and discussion

After the development of the method, flight tests were carried out on several road slopes near the Polytechnic University of Valencia, verifying and validating the operation of the drone for image acquisition.

Once the flight of the drone was validated, different field tests were carried out, which were basically divided into two stages: Firstly, the effectiveness of the mathematical model developed was checked, which included the collection of images, the obtaining of a 3D image based on a point cloud and the identification of landslides. Secondly, the system was tested on several selected road/rail slopes to check that the whole system worked properly under different light and weather conditions.

4 Conclusions and future work

In this article, a non-intrusive method has been defined for monitoring the condition of a slope adjacent to a linear infrastructure. This method is based on the correct planning of the flight of a drone with a high resolution camera together with the development of the algorithm that allows the identification of possible landslides, by means of the relation of eigenvalues (degree of roughness in three dimensions), the slope of the slope and the index of roughness of the surface.

This method confirms that it is possible to detect and extract the geomorphological characteristics of a slope early, thus increasing the efficiency in the location of landslides with respect to other systems along with a much lower cost and, in turn, can be applied to long lengths of road and rail networks.

References

- [1] Instituto Geológico y Minero de España (IGME), 1987.
- [2] Dirección General de Protección y Emergencias. Ministerio del Interior. Recuperado de: <http://www.proteccioncivil.es/web/dgpcye/movimientos-del-terreno>.

Application of a twin model for monitoring and predictive diagnosis of Pirihueico Bridge

Marcelo Márquez^{b1}, Francisca Espinoza^{b2}, Sandra Achurra^{b3}, Julia Real^{b4}, Ernesto Colomer^{b5}
and Miriam Labrado^{b6}

(b) Ministry of Public Works,
Government of Chile,

(†) Institute of Multidisciplinary Mathematics,
Universitat Politècnica de València.

1 Introduction

Bridge collapse in recent years due to lack of maintenance has been increasing. [1]. One of the examples is The Morandi Bridge collapse in Genoa, that killed 41 people in 2018 with serious economic consequences [2]. In addition, common means and methods used for bridge health monitoring do not have the possibility to predict the evolution of the structural state. For this reason, a semi-empirical method based on a twin model and data register in specific points is exposed herein. It achieves to implement a predictive diagnosis of the bridge.

This was applied to Pirihueico Bridge and allows to characterize the response of the structure under operational conditions in real time. This bridge is located at P.K. 114.29 of Route 203, in the commune of Panguipulli in the province of Valdivia (Los Lagos Region, Chile). The environment is characterized by being a forest and tourist area with low population density and an expected low traffic flow, both heavy and light.

2 Method

In this section, it is explained the methodology for the development of the twin model. The steps that have been followed for the modelling are numbered between (*i*) to (*vi*).

First, the visual inspection of Pirihueico Bridge was carried out by the technics staff (*i*). In this visual inspection, the following aspects were determined:

- There was no mismatch or scour in the land near the piles, but there was a special risk of scour in the northwest pile.

¹e-mail: marcelo.marquez@mop.gov.cl

²e-mail: francisca.espinoza@mop.gov.cl

³e-mail: sandra.achurra@mop.gov.cl

⁴e-mail: jureaher@tra.upv.es

⁵e-mail: ercoro1@cam.upv.es

⁶e-mail: milabpa@upv.es

- No fissures were observed in the abutment walls, but there was presence of humidity and efflorescence. No breakage of the lateral or front walls of the abutments was observed.
- There was no cracking in the piles and decks, but there was humidity and efflorescence. No excessive deformation, detachment or breakage of the support devices was observed.
- Moisture was observed in the concrete under damaged expansion joints. Expansion joints damaged due to lack of sealing and insulation were observed.
- No ruts, potholes or holes were observed in the pavement.
- No deterioration was observed in barriers or protections, but a slight oxidation was observed.
- No deterioration was observed in the drainage elements.

Next, the twin model (*ii*) was developed. To represent the structure in the finite element environment, the ANSYS APDL v17.0 software was used. The structure's slab, piles, pile cap and piles were modeled using SOLID-type elements, longitudinal beams and diaphragms using SHELL-type elements and the latticework (Saint Andrew's Crew with horizontal crossbar) using BEAM-type elements. The materials were defined according to a linear elastic constitutive model and their characteristics were as follows:

Material	Characteristic Resistance	Elasticity Modulus	Poisson Coefficient	Density
Concrete	30 MPa	$E = 25000$ MPa	$\mu = 0.2$	$\rho = 2.5$ Ton/ m^3
Steel	370 MPa	$E = 210000$ MPa	$\mu = 0.3$	$\rho = 7.85$ Ton/ m^3

Table 1: Mechanic characteristics of materials. Source: Prepared by the authors.

The interaction of the deck with the abutments was modelled by simulating simple supports at the ends, and the interaction of the structure with the ground was modeled using springs - COMBIN14-type elements. The union between the resistant elements was made by defining finite dimension nodes to make the necessary degrees of freedom.

Regarding the instrumentation carried out on the bridge (*iii*), the parameters to be controlled were first defined: deflections in the middle of a span, inclination in abutments, tilting head of piles, inclination on deck elements, seat in abutments, differential seats in batteries, undercut depth, differential displacements in joints, differential displacements between deck and piles, overvoltage in longitudinal beams, frequencies of the deck and damping coefficient. For that, the following devices were installed on the bridge: inclinometer (x10) in stirrups, pile head and 1/3 of each span, accelerometer (x6) 1/3 of each span, undercut sensor (x4) in pile head, linear displacement sensor (x2) in expansion joints and strain gages (x4) at 1/3 span from pile head.

With the instrumentation and the twin model, it was possible to proceed to the calibration of the model (*iv*). Thus, the dynamic response of the structure was calibrated by comparing and correlating the natural frequencies of the different sections of the structure with the data recorded by the installed inertial sensors. To carry out this calibration, the sections of the superstructure were adjusted, as well as the modulus of elasticity of the materials and the

stiffness of the springs that represent the interaction of the ground with the foundation, until obtaining an accuracy of ± 0.5 Hz between the natural frequency obtained from the registers and the frequency calculated in the model for the vibration mode related to the sensor distribution.

Once the twin model was calibrated, the limits of tolerances (v) in the structural health parameters to be controlled detailed above were established, in accordance with the provisions of the applicable regulations in Chile [3]. These limits focused on: deflections in the center of the span, inclination in abutments, inclination in head of piers, inclination in elements of the deck, seat in abutments, differential seats in piers, depth of scour, differential displacements in joints, overvoltages in longitudinal beams, natural frequencies of the deck and damping coefficients. Therefore, for the monitored structural elements and the parameters mentioned above, three different possible states were defined based on the information obtained:

- EXCESSIVE: It is an indicator of an imminent affection to the global or local integrity.
- ACCEPTABLE: Affecting the use, comfort and/or perception of the structure. It requires the study of its evolution.
- GOOD: No anomalies were detected in the response of the structure.

Finally, the model simulation was carried out to check the structural damage that has occurred in the bridge (vi). For this, the environment in which the structure was located and its background were taken into account, so the effect of different scenarios was simulated according to the following actions:

- Permanent loads: according to [3].
- Live loads: traffic loads according to article 3.7.1.1, 3.7.1.2 y 3.7.1.3. [4] and dynamic effects according to article 3.8 [4].
- Seismic loads: according to section 3.1004 [3].
- Wind loads: according to articles 3.13 – 3.15 [4].

3 Results and discussion

According to the twin model carried out, results were obtained in the different load scenarios, as are presented in this section. These results were obtained for each of the different supporting elements that make up the structure: slab, longitudinal beam, diaphragm, lattice and pile. The evaluation criteria followed are the normative criteria applied by AASHTO for the Allowable Stress Design (ASD) method and the sectional use criterion.

The normative criterion of the AASHTO refers to the admissible voltage or “allowable stress”, tension that the norm allows to increase by a percentage for each load group. The material, reinforced concrete or steel, must not exceed this allowable tension to meet the criteria established by regulations [4].

On the other hand, the sectional use criterion relates the Von Mises stress (σ_{VM}) to which a certain resistant element is subjected to the maximum characteristic stress of the material of the element in question. This criterion therefore refers to the “resistant reserve of the element”.

To obtain an estimate of the degree of solicitation of these elements against the various actions, the sectional use formula was:

$$\text{Sectional use (\%)} = \frac{\sigma_{VM}}{\sigma_c} \cdot 100.$$

Where σ_{max} is maximum tension in each section obtained from the computational model and σ_c is the maximum characteristic tension of the material (concrete resistance or steel elastic limit). A sectional use of 100% indicates that the analyzed section is working at its maximum theoretical tension in elastic regime.

Therefore, the results obtained showed that the most requested element is the longitudinal beams. The maximum solicitation of the longitudinal beam occurred in the span center. This situation is maintained for both permanent and dynamic actions. In addition, it was observed that in admissible scour scenarios, the stresses were slightly increased comparing with the scenarios without scour.

4 Conclusions and future work

This paper develops a twin model of the Pirihueico Bridge, in which different structural parameters were monitored through devices to determine the structural health, allowing to have a predictive diagnosis of the bridge. For that, a series of numerical simulations of the behaviour of the bridge were carried out in different load scenarios.

After the calculation, an adequate general behaviour of the bridge was observed, particularly against statutory traffic overloads, obtaining a more demanding response with respect to dynamic traffic. This requirement on the structural elements was increased to a greater extent in cases in which the seismic loads, both longitudinal and transverse, is concomitant with traffic loads.

Finally, and as expected, it was possible to see how the longitudinal beams are, in all cases, the most requested elements. In this way, it is convenient to give special importance to the inspection and monitoring of its condition, since the formation of plastic ball joints or other types of damage that affect rigidity could lead to a critical situation for stability.

References

- [1] Cook, W. "Bridge Failure Rates, Consequences and Predictive Trends". Utah State University. Logan, USA. (2014).
- [2] Piangiani, G. "Italy Bridge Was Known to Be in Trouble Long Before Collapse". *The New York Times*. Genoa, Italy. (2018).
- [3] "Manual de Carreteras, volumen n°3: Instrucciones y criterios de diseño". Dirección de Viabilidad, Ministerio de Obras Públicas, Gobierno de Chile. (2017).
- [4] "AASHTO, American Association of State Highway and Transportation Officials. Standard Specifications for Highway Bridges". (2002).

N-soft set based multi-agent decisions: A *decide-then-merge* strategy

J.C.R. Alcantud^{b1}, G. Santos-García^{b2} and M. Akram^{#3}

(b) BORDA Research Unit and Multidisciplinary Institute of Enterprise (IME),
University of Salamanca, 37007 Salamanca, Spain,

(b) IME, University of Salamanca,
37007 Salamanca, Spain,

(#)Department of Mathematics, University of the Punjab,
New Campus, Lahore 54590, Pakistan.

1 Introduction

This work is in continuation of the motivating Alcantud et al. [5], which has first established a decision-making methodology when the information is provided in the form of *several* *N*-soft sets [9]. The plan of action in [5] is summarized by the term *merge-then-decide*. Under such strategy, an aggregation operator merges the individual data that are submitted as *N*-soft sets, and then a decision-making algorithm selects the optimal alternative from the aggregate item. Here we show that one may also proceed in a different order. The individual data can produce a list of choices or rankings, and these can afterwards be combined in order to produce a collective choice or ranking.

N-soft sets were introduced by Fatimah et al. [9] in order to improve the performance of soft sets, so that we can formalize the idea of a multinary (rather than simply binary) description of a universe of alternatives in terms of some characteristic attributes. The model has raised considerable attention since its appearance. It has been extended and hybridized with fuzziness [1], bipolarity [11], hesitancy, and other notions of vague knowledge [2, 6, 8]. Strong links with the idea of a rough set have also been brought to light [4]. As an extension of soft topologies [3, 7, 14] by inspiration of the model proposed in [9], *N*-soft topologies are already being developed [13].

Decision mechanisms for *individual* sets of data are available in all these settings. Multi-agent decisions however, have not been considered until Alcantud et al. [5]. We continue this recent line of inspection with a totally renewed approach. We reconsider the case of an analyst facing the choice or the ranking of a list of alternatives that have been characterized by several experts, who submitted their opinions as respective *N*-soft sets. The new proposal suggests that she may first determine an individual ranking for each assessment and then merge these orderings by the recourse to a voting function. Specifically, in this work we use a mechanism

¹e-mail: jcr@usal.es

²e-mail: santos@usal.es

³e-mail: m.akram@pucit.edu.pk

from [9] at the first stage, whereas we use the Borda rule for complete preorders [10] at the second stage.

The strategy is however quite adaptable. Other procedures can be used at the first, the second, or both stages of the *decide-then-merge* strategy.

2 Preliminaries and research target

Henceforth A^k is the Cartesian product of k copies of A , whereas $\mathcal{P}^*(A)$ represents the set of all non-empty subsets of A .

We recall concepts pertaining to two branches of the literature. First, we summarize the model that describes a collection of alternatives by n -ary or evaluations of their relevant characteristics. Secondly, we recall some results about the aggregation of ordinal rankings.

The following common items describe our setting. $O = \{o_1, \dots, o_p\}$ is the list of alternatives that are evaluated by the experts $E = \{x_1, \dots, x_k\}$ who focus on the attributes $T = \{t_1, \dots, t_q\}$. They can rate the alternatives by grades in the ordered scale $G = \{0, 1, 2, \dots, N - 1\}$ where $N \in \{2, 3, \dots\}$. Technically, our input is a finite list of evaluations given by respective N -soft sets [9]. A triple (F, T, N) is an N -soft set on O if F is mapping from T to $2^{O \times G}$, with the property that for each $t \in T$ and $o \in O$ there exists a unique $(o, g_t) \in O \times G$ such that $(o, g_t) \in F(t)$, $g_t \in G$. We have one N -soft set on O put forth by each agent, namely, (F_1, T, N) , \dots , (F_k, T, N) . Thus for any $t_j \in T$, agent a gives exactly one evaluation from G for every $o_i \in O$: the unique r_{ij}^a for which $(o_i, r_{ij}^a) \in F_a(t_j)$. Put shortly, $F_a(t_j)(o_i) = r_{ij}^a \in G$ represents $(o_i, r_{ij}^a) \in F_a(t_j)$. Table 1 summarizes our input.

Table 1: Tabular form of the N -soft sets presented by k experts.

(F_1, T, N)	t_1	t_q		(F_k, T, N)	t_1	t_q
o_1	r_{11}^1	r_{1q}^1	o_1	r_{11}^k	r_{1q}^k
\vdots	\vdots		\vdots		\vdots	\vdots		\vdots
o_p	r_{p1}^1	r_{pq}^1		o_p	r_{p1}^k	r_{pq}^k

Our target is to produce a well grounded ranking of O .

Instead of the *merge-then-decide* strategy in [5] we here present an alternative *decide-then-merge* approach.

3 Results and discussion

We proceed to set forth the two steps that produce a ranking of O from the information provided by the experts. Both have a solid theoretical foundation that we briefly recall.

3.1 Rankings from N -soft set information

In the model under inspection, the natural procedure to rank alternatives uses their extended weighted choice values [9]. This is the direct extension of the standard criterion to decide among alternatives when they are evaluated by soft sets. The analyst selects a weight for each

criterion. Then with the information provided by agent $x \in E$, she ranks o_1, \dots, o_p from largest to smallest extended weighted choice value (EWCV) defined as $\sigma_i^x(w) = \sum_{j=1}^q w_j r_{ij}^x$. In this way the analyst obtains k complete preorders (complete and transitive binary relations), one for each expert x : namely, \succsim^x such that $o_i \succsim^x o_j$ if and only if $\sigma_i^x(w) \geq \sigma_j^x(w)$, for each $x \in E$.

3.2 Aggregation of ordinal information

Once the analyst has prioritized the alternatives according to each individual assessment, she has k individual rankings at her disposal. In order to merge them into a unique collective ranking, we suggest that the Borda rule for complete preorders performs sufficiently well. It is a positional voting rule that is firmly established in social choice. Its application to linear orders is easy to explain, however there are various alternative ways to produce the desired output when ties are allowed. We follow Gärdenfors [10] who uses the following expression: each agent $x \in E$ contributes to the collective assessment of o_i with $B_x(o_i)$ which is the number of alternatives that x thinks are worse than o_i (with respect to \succsim^x), minus the number of alternatives that x prefers to o_i ; then the Borda number of o_i is $B(o_i) = \sum_{x \in E} B_x(o_i)$.

Finally, the analyst recommends any alternative that maximizes B over O . The alternatives are ranked from highest to lowest value of B .

3.3 A synthetic example

Table 2 describes the application of our procedure to a synthetic example. Two experts $\{x, y\}$ rate four alternatives with respect to three attributes $\{a_1, a_2, a_3\}$. The analyst attaches unequal importance to these attributes: the first and second are equally relevant, but the third one is twice as important as any of them. So the weights are $w_1 = w_2 = \frac{1}{4}$ and $w_3 = \frac{1}{2}$ thus $w = (\frac{1}{4}, \frac{1}{4}, \frac{1}{2})$.

Table 2: Tabular form of 4-soft sets presented by the experts $\{x, y\}$, and elements for the selection of alternatives.

Expert x	a_1	a_2	a_3	Expert y	a_1	a_2	a_3
o_1	2	0	2	o_1	0	2	2
o_2	1	1	3	o_2	1	1	1
o_3	1	2	2	o_3	2	2	1
o_4	2	2	1	o_4	2	1	2

We compute $\sigma_1^x(w) = \frac{1}{4}2 + \frac{1}{4}0 + \frac{1}{2}2 = 1.5$, and similarly $\sigma_2^x(w) = 2$, $\sigma_3^x(w) = 1.75$, and $\sigma_4^x(w) = 1.5$. The ranking by the first agent is therefore $o_2 \succ^x o_3 \succ^x o_1 \sim^x o_4$. Hence this complete preorder from x contributes to the global assessment with the Borda numbers $B_x(o_1) = B_x(o_4) = 0 - 2 = -2$, $B_x(o_2) = 3 - 0 = 3$ and $B_x(o_3) = 2 - 1 = 1$.

The second assessment gives us the figures $\sigma_1^y(w) = \frac{1}{4}0 + \frac{1}{4}2 + \frac{1}{2}2 = 1.5$, and similarly $\sigma_2^y(w) = 1$, $\sigma_3^y(w) = 1.5$, and $\sigma_4^y(w) = 1.75$. The second agent ranks $o_4 \succ^y o_1 \sim^y o_3 \succ^y o_2$. Hence the corresponding \succsim^y contributes to the global assessment with the Borda numbers $B_y(o_1) = B_y(o_3) = 1 - 1 = 0$, $B_y(o_2) = 0 - 3 = -3$ and $B_y(o_4) = 3 - 0 = 3$.

We can now merge the opinions of the experts to obtain the Borda numbers of the options:
 $B(o_1) = B_x(o_1) + B_y(o_1) = -2 + 0 = -2$,

$$\begin{aligned}
B(o_2) &= B_x(o_2) + B_y(o_2) = 3 - 3 = 0, \\
B(o_3) &= B_x(o_3) + B_y(o_3) = 1 + 0 = 1, \\
B(o_4) &= B_x(o_4) + B_y(o_4) = -2 + 3 = 1.
\end{aligned}$$

The recommendation is that either o_3 or o_4 are optimal solutions, and o_1 is the worst option.

4 Conclusions and future work

As an alternative to the *merge-then-decide* approach to N -soft set based multi-agent decisions Alcantud et al. [5], here we propose a *decide-then-merge* strategy for the same purpose. A comparison of both approaches, from normative and practical positions, is a research goal for further investigation.

If we adhere to the *decide-then-merge* strategy for N -soft set based multi-agent decisions, we can still vary either the first step (decide) or the second (merge) or both. Already [9] suggested an alternative decision criterion for N -soft sets which means an alternative approach to the first step. As to the second step –the aggregation of ordinal information–, social choice theory has produced an array of different methodologies like the positional voting rules (plurality or Black’s voting rules). The impact of the choice of these items in the final decision should be investigated accordingly.

References

- [1] Akram, M., Adeel, A., Alcantud, J.C.R., Fuzzy N -soft sets: A novel model with applications *Journal of Intelligent & Fuzzy Systems*, 35(4):4757–4771, 2018.
- [2] Akram, M., Adeel, A., Alcantud, J.C.R., Hesitant fuzzy N -soft sets: A new model with applications in decision-making *Journal of Intelligent & Fuzzy Systems*, 36(6):6113–6127, 2019.
- [3] Alcantud, J.C.R., Soft open bases and a novel construction of soft topologies from bases for topologies *Mathematics*, 8(5): 672, 2020.
- [4] Alcantud, J.C.R., Feng, F., Yager, R.R., An N -soft set approach to rough sets *IEEE Transactions on Fuzzy Systems*, forthcoming.
- [5] Alcantud, J.C.R., Santos-García, G., Akram, M., OWA aggregation operators and multi-agent decisions with N -soft sets. Mimeo, submitted, 2020.
- [6] Ali, G., Akram, M., Decision-making method based on fuzzy N -soft expert sets *Arabian Journal for Science and Engineering*, forthcoming. <https://doi.org/10.1007/s13369-020-04733-x>.
- [7] Çağman, N., Enginoğlu, S., Soft set theory and uni-int decision making *European Journal of Operational Research* 207(2): 848–855, 2010.
- [8] Chen, Y., Liu, J., Chen, Z., Zhang, Y., Group decision-making method based on generalized vague N -soft sets 2020 Chinese Control And Decision Conference (CCDC), Hefei, China, 2020, pp. 4010-4015. <https://doi.org/10.1109/CCDC49329.2020.9164602>.

- [9] Fatimah, F., Rosadi, D., Hakim, R.F., Alcantud, J.C.R., *N*-soft sets and their decision making algorithms *Soft Computing* 22(12):3829–3842, 2018.
- [10] Gärdenfors, P., Positionalist voting functions *Theory and Decision* 4:1–24, 1973.
- [11] Kamacı, H., Petchimuthu, S., Bipolar *N*-soft set theory with applications *Soft Computing*, forthcoming. <https://doi.org/10.1007/s00500-020-04968-8>.
- [12] Liao, H., Wu, X., Mi, X., Herrera, F., An integrated method for cognitive complex multiple experts multiple criteria decision making based on ELECTRE III with weighted Borda rule *Omega*, 93:102052, 2020.
- [13] Riaz, M., Cagman, N., Zareef, I., Aslam, M., *N*-soft topology and its applications to multi-criteria group decision making *Journal of Intelligent & Fuzzy Systems*, 36(6):6521–6536, 2019.
- [14] Shabir, M., Naz, M., On soft topological spaces *Computers & Mathematics with Applications* 61(7): 1786–1799, 2011.
- [15] Wu, X., Liao, H., Xu, Z., Hafezalkotob, A., Herrera, F., Probabilistic linguistic MULTI-MOORA: a multi-criteria decision making method based on the probabilistic linguistic expectation function and the improved Borda rule *IEEE Transactions on Fuzzy Systems*, 26(6):3688–3702, 2018.

Deep Learning AI-based solution for vineyard real-time health monitoring

Ana Sancho^{b1}, Eliseo Gómez^{b2}, Albert Pérez^{b3} and Julián Santos^{b4}

(b) Institute of Multidisciplinary Mathematics,
Universitat Politècnica de València.

1 Introduction

The spread of transboundary plant pests and diseases has increased dramatically in recent years. Globalization, trade and climate change, as well as reduced resilience in production systems due to decades of agricultural intensification, have all played a part [1]. The Food and Agriculture Organization of United Nations (FAO) estimates that each year between 20 to 40 percent of global crop production is lost due to pests and diseases, having an estimated global economic cost of around €200 Billion per year [2].

In all cases, early detection is a key element in avoiding loss of yield or even the entire crop, because it enables to take preventive measures, as decreasing the inoculum density, applying phytosanitary products or controlling the vector [3]. Generally, when symptoms are visible to the human eye the disease is already at an advanced stage, and the pathogen is probably distributed along a larger planting area.

Nowadays, most producers carry out the inspection of diseases in their crops through visual inspection, leading to the problem of subjectivity and detection at an advanced stage of the sickness. However, different tests can be carried out for the early detection of diseases whether within direct or indirect methods, despite these methods have different kind of limitations like its lack of accuracy, high time-consuming or expensive procedures. For these reasons, our goal was to develop a solution with quick execution, at a low cost, with rapid results and detecting diseases in an asymptomatic state, allowing them to substantially improve the risks management of their crops.

¹e-mail: ansanbru@upvnet.upv.es

²e-mail: elgomi@cam.upv.es

³e-mail: alpegan@etsii.upv.es

⁴e-mail: jusanve@cam.upv.es

2 Method

To achieve this goal, the purposed methodology is divided in following steps:

- i) Instrumentation: First, a drone with a five-band multispectral camera flies over the analysed terrain.
- ii) Software: It can be differentiated five stages:
 - An ortho-rectification of the hyperspectral images is performed to correct the displacement due to the terrain by means of Digital Elevation Models (DEM). In addition, the radiation values captured by the camera are also corrected. In addition, Similarly, atmospheric correction filters out environmental interference that may influence the capture process, resulting in appropriate irradiation of plantations, using the SMARTS model. Once corrected, the irradiation values captured by the cameras have been transformed to reflectance also by the SMARTS model.
 - The next step is to identify and discretize the tree units using an algorithm based on the binarization of the image by different colour filters and different thresholds. The aim is to divide the digital images into multiple regions that identify pure vineyard crowns to extract the characteristics of each object, in order to calculate the thermal and spectral parameters of all the pixels that make up each crown.

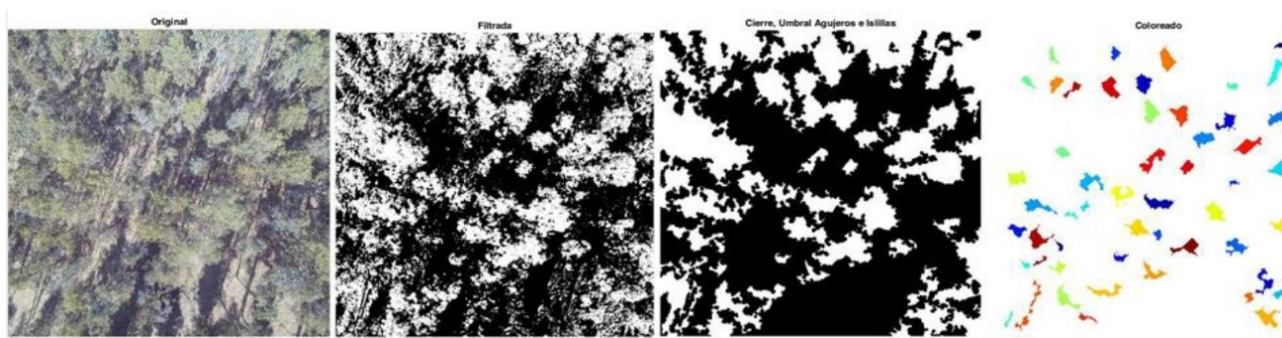


Figure 1: Identification and discretization of tree units.

- The spectral parameters are then calculated using a calculation algorithm that includes all the formulas belonging to the selected parameters:

Structural indices	
Normalized Difference Vegetation Index	$N D V I = (R 800 - R 670) / (R 800 + R 670)$
Renormalized Difference Vegetation Index	$R D V I = (R 800 - R 670) / (R 800 + R 670)$
Enhanced Vegetation Index	$E V I = 2.5 \cdot (R 800 - R 670) / (R 800 + 6 \cdot R 670 - 7.5 \cdot R 400 + 1)$
Optimized Soil-Adjusted Vegetation Index	$O S A V I = ((1 + 0.16) \cdot (R 800 - R 670) / (R 800 + R 670 + 0.16))$
Triangular Vegetation Index	$T V I = 0.5 \cdot [120 \cdot (R 750 - R 550) - 200 \cdot (R 670 - R 550)]$

Modified Triangular Vegetation Index	$M T V I = 1.2 \cdot [1.2 \cdot (R 800 - R 550) - 2.5 \cdot (R 670 - R 550)]$
Modified Simple Ratio	$M S R = R 800 / R 670 - 1 (R 800 / R 670) 0.5 + 1$
Xanthophyll indices	
Photochemical Reflectance Index (570)	$P R I 570 = (R 570 - R 531) / (R 570 + R 531)$
Chlorophyll a+b indices	
Vogelmann	$V O G 1 = R 740 / R 720$
Gitelson &Merzlyak indices	$G M 1 = R 750 / R 550$
Pigment Specific Simple Ratio Chlorophyll b	$P S S R b = R 800 / R 650$
Transformed Chlorophyll Absorption in Reflectance Index	$T C A R I = 3 \cdot [(R 700 - R 670) - 0.2 \cdot (R 700 - R 550) \cdot (R 700 / R 670)]$
Transformed Chlorophyll Absorption in Reflectance Index/ Optimized Soil- Adjusted Vegetation Index	$T C A R I / O S A V I = 3 \cdot [(R 700 - R 670) - 0.2 \cdot (R 700 - R 550) \cdot (R 700 / R 670) ((1 + 0.16) \cdot (R 800 - R 670) / (R 800 + R 670 + 0.16))]$
R/G/B indices	
Redness index	$R = R 700 / R 670$
Blue/green indices	$B G I 1 = R 400 / R 550$
Lichtenhaler index	$L I C 3 = R 440 / R 740$
Carotenoid indices	
Pigment Specific Simple Ratio Carotenoids	: NDVI
R515/R570	$R 515 / R 570$
R515/R670	$R 515 / R 670$
Fluorescence	
FLD	$F L D 3 (747; 762; 780)$
Plant disease index	
Healthy index	$H I = R 534 - R 698 R 534 + R 698 - 1 2 \cdot R 704$

Table 1: Spectral parameters

- A Back Propagation Neural Network (BPNN) is carried out to assign health status, disease, and degree of advancement.
- iii)* Calibration of the neuronal network: It is calibrated in different vineyards suffering from one of the target diseases at a degree of advancement. The network's training algorithms are of the deep learning type, feeding their precision as the system is used.
- iv)* Health status map of the crop: Lastly, based on the discretization algorithms and tree-units spatial location (registered by drone's GPS), in sum with algorithm for calculating spectral variables and classification of health status, a map is generated by which producers can overview their plantations. Users will also be able to access a dashboard with statistical information on the historical crop-health data, report on treatment of diseases, and recommendations for managing crops, among other functions.

3 Results and discussion

After the development of the method, flight tests were carried out in several tree units, close to the Polytechnic University of Valencia, verifying and validating the operation of the drone and the algorithms mentioned.

Once the flight of the drone and the algorithms developed have been validated, different field tests were carried out, which were basically divided into two stages: Firstly, the effectiveness of the algorithm for tree-units identification and individualization was checked out. Secondly, the system was tested in several vineyards already infected with different diseases to evaluate the spectral and thermal data analysis, as well as the accuracy in relation to the disease identification.

Following the above demonstration, the validation of the algorithmic package including data collection and processing, identification of the tree units, extraction of spectral characteristics and marking of health statuses were carried out. In order to assess the software performance, the neural network was previously trained in a real operation environment by using the Back-Propagation Method. When the NN was trained and calibrated with real data, the team proceeded to search vineyards of similar characteristics with the aim to validate the trained diseases.

4 Conclusions and future work

In this paper, a non-intrusive method for vineyard health monitoring has been defined. In addition, powerful algorithms as neural network has been implemented to identify the disease in the vineyard as well as its degree of progression. Conclusions obtained are mentioned as follows:

- The hyperspectral camera allows us registering the key spectral signals for the disease identification. Region of 400-1300 nm is captured, bear in mind plants express its health condition mainly through visible range (400–700 nm) combined with near infrared range (700–1300 nm).
- Diagnosis of the health status of a tree-crop plantation can be made rapidly (approximately 1.5 minutes per hectare), accurately (98% of successes), at a low cost (average of €50/Ha annually) and getting the results in real time.

References

- [1] “Food and Agriculture organization of United Nations (FAO). Plant pests and diseases”. (2017). Retrieved from fao.org/emergencies/emergency-types/plant-pests-and-diseases/en/.
- [2] “Food and Agriculture organization of United Nations (FAO). New standards to curb the global spread of plant pests and diseases”. (2019). Retrieved from www.fao.org/news/story/en/item/1187738/icode/.
- [3] “CABI International. Invasive Species Compendium”. (2019). Retrieved from www.cabi.org/isc/.

New system for the automatic counting of vehicles in roundabouts and intersections

Teresa Real^{b1}, Rubén Sancho^{b2}, Guillém Alandí^{b3} and Fernando López^{b4}

(b) Escuela Técnica Superior de Ingeniería del Diseño,
Universitat Politècnica de València,
(i) Institute of Multidisciplinary Mathematics,
Universitat Politècnica de València.

1 Introduction

Traffic management is increasingly important due to the high density of vehicles on the road network, together with the increase in the loads transported and the increase of the circulation speeds.

These factors lead to congestion problems on all types of road infrastructure, both urban and interurban, which, due to their high impact on society, have been quantified economically. In this sense, the annual cost of traffic congestion in Spain is estimated at approximately 5,500 million euros, with per capita expenditure reaching 1,000 euros per year.

In this sense, for a correct traffic management, it is very useful to have detailed and real-time information on origin-destination matrices, that is, matrices that show how many vehicles come from each specific origin (O) and go to each destination (D) determined, so that the managing body of the circulation is able to make the best decisions as quickly as possible.

Traditionally, the recording of data to carry out these origin-destination matrices has been done by manual counts on the site. However, they are only recommended for short periods, not exceeding 24 hours, as their high cost makes their use for longer periods unjustifiable. An alternative to this system, which allows to obtain origin-destination matrices at intersections continuously would be the license plate recognition systems. These systems have certain technical drawbacks as they require the installation of cameras at height that can be affected by inclement weather, traffic congestion, day/night transition light, contrast vehicle/road, among other causes; its elevated probability of failure makes it an unreliable system.

For this reason, a system has been proposed that is capable of, using the analysis of the records provided by a network of sensors (accelerometers and magnetometers), classifying the type of vehicle that passes through an intersection and at the same time generating origin-destination matrices in real time. Therefore, a tool is provided for the optimal and precise

¹e-mail: tereaher@upv.es

²e-mail: rusanmc@etsii.upv.es

³e-mail: guialma3@etsii.upv.es

⁴e-mail: ferlola@etsia.upv.es

management of traffic, which will make it possible to avoid traffic jams in a high percentage and, in any case, quickly reduce them, knowing the mobility patterns of the vehicles at any given time.

2 Methodology

As mentioned above, the design of a system capable of automatically and accurately generating origin-destination data at intersections was proposed. Therefore, this section tries to explain the methodology used by the system.

- i.* **Data logging.** This phase is carried out by means of a system of wireless nodes, which includes 5 magnetometers and 6 accelerometers embedded in the pavement. The system is capable of recording the vibration data generated on the pavement surface and the magnetic impression of all the vehicles circulating on it.
- ii.* **Data processing.** This phase includes the algorithm necessary for the processing of the data. Two algorithms are used for this:
 - **Vehicle classification algorithm.** Firstly, this “classification algorithm” is composed of a system for calculating speed through the signal emitted by the magnetometers, an axle detection algorithm with the information provided by the accelerometers and with the results of these two algorithms a third algorithm has been developed to classify the detected vehicle. A diagram of the process is shown in the Figure 1.

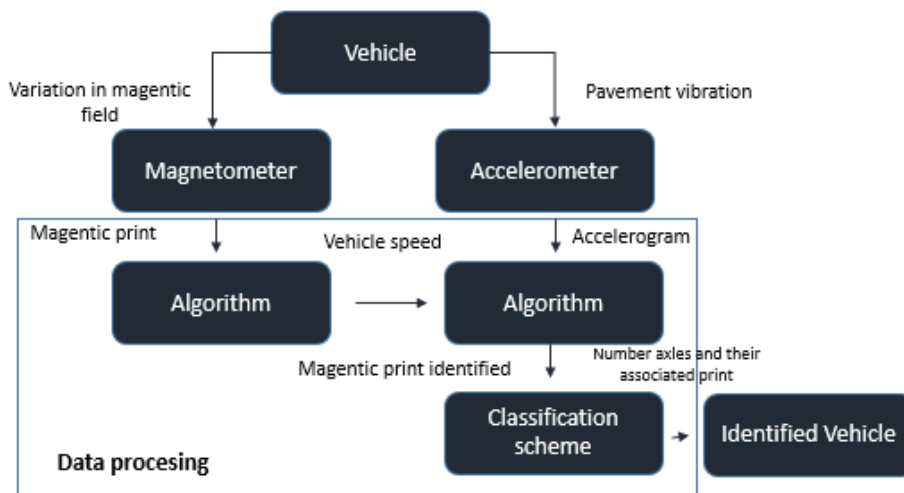


Figure 1: General classification vehicle algorithm. Sources: [1]

- **Re-identification algorithm.** Secondly, the re-identification algorithm whose correct operation is essential for the system to have an adequate performance. This second algorithm starts with the filtering of the signal received by the magnetometers. Once the signal is filtered, it is necessary to identify when a vehicle is started and stopped in order to extract its magnetic print. Once the print is extracted it will

be compared with the prints of other stations in order to identify the entry and exit point of the same vehicle. In order to make the comparison more reliable and robust, several magnetometers have been placed in the same station with the aim of having several samples of the same print. Obviously it has been necessary to establish a system of comparison of tracks, this has been done through cross-correlations. A diagram of the process is shown in the Figure 2.

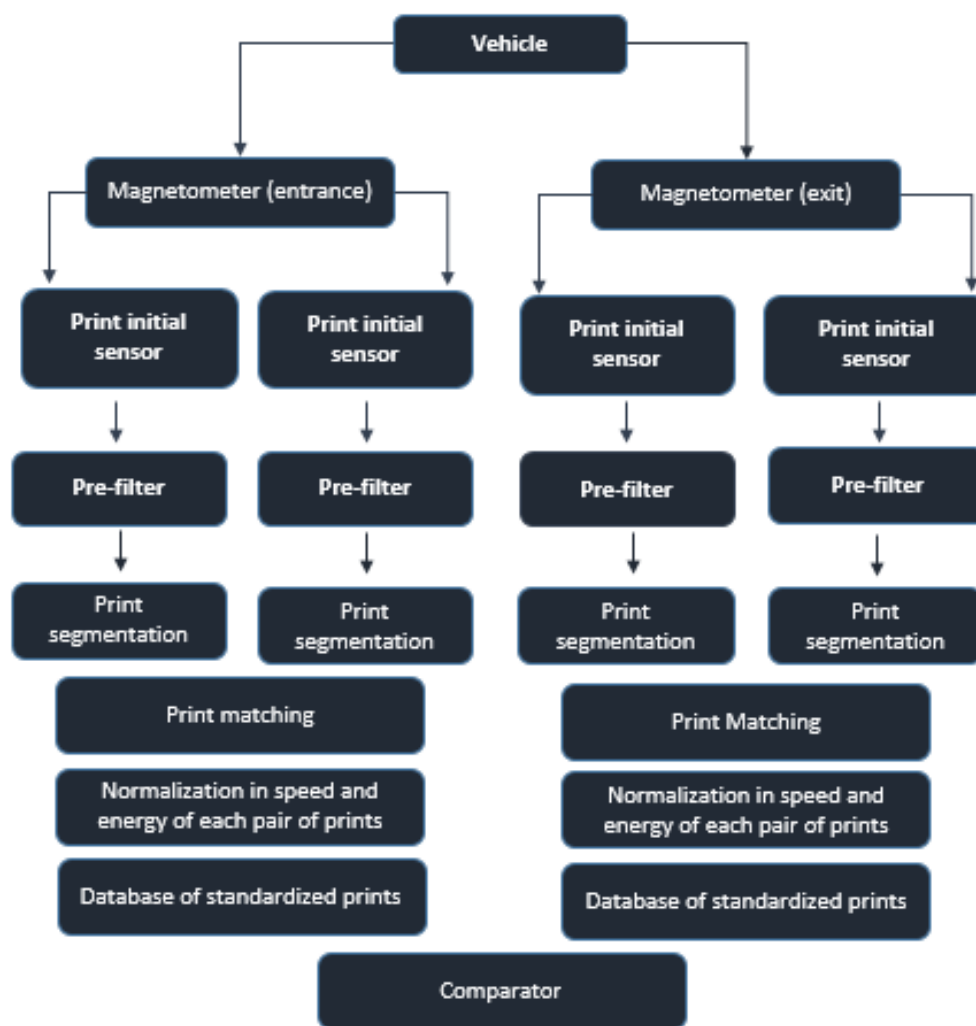


Figure 2: Re-identification algorithm. Sources: [2]

The complex methodology exposed has been checked and verified in controlled conditions, so we will try to explain the results and conclusions obtained.

3 Results and discussion

To verify the correct operation of the algorithm, it is necessary to subject it to different tests.

First, the tests were carried out under controlled conditions. In them, registers were executed using both types of sensors (accelerometer and magnetometer) which allowed, on the one hand,

to adjust and validate the performance of the algorithms described, and on the other hand, to define the exact number of sensors required and their adequate arrangement.

Once this point was reached, tests were carried out in a real environment, where very promising results were obtained from the use of the system both at intersections and roundabouts, with a very low error rate.

4 Conclusions and future work

Based on the previous works, the following conclusions are obtained:

- Useful and minimally invasive tool for traffic management.
- System capable of generating origin-destination matrices automatically and continuously.
- Economic, simple and easy system to install at roundabouts and intersections.

References

- [1] W. Ma, D. Xing, A. McKee, R. Bajwa, C. Flores, B. Fuller and P. Varaiya, A Wireless accelerometer-based automatic vehicle classification prototype system, *Intelligent Transportation Systems*, 104 – 111, 2013.
- [2] M. Ndoye, V. Totten, J. Krogmeier and D. Bullock, Sensing and signal processing for vehicle reidentification and travel time estimation, *Intelligent Transportation Systems*, 119 – 131, 2011.

A System Dynamics model to predict the impact of COVID-19 in Spain

M.T. Sanz ^{b1}, A. Caselles ^b, J. C. Micó[#] and C. Soler^{##}

(b) Departament de Didàctica de la Matemàtica,
Universitat de València, Av. dels Tarongers, 4, 46022 València, Spain,

(b) IASCYS member, Departament de Matemàtica Aplicada,
Universitat de València (retired), Dr. Moliner 50, 46100 Burjassot, Spain,

(#)Institut Universitari de Matemàtica Multidisciplinar,
Universitat Politècnica de València, Camí de Vera s/n, 46022 València, Spain,

(##)Institut Valencià de Cultura,
Generalitat Valenciana, Polígon Accés Ademús s/n, 46100 Burjassot, Spain.

1 Introduction

On 21 January 2020, the World Health Organization published its first report about the situation of the world with the Novel Coronavirus (2019-nCoV), a new human infectious disease. A total number of confirmed cases in that day was 282 and this disease was only present in China, Japan, Republic of Korea and Thailand. Nowadays, this organization has published its 94 report and it reflects that COVID-19 is around the world (Figure 1), the actual cases number is 2544792 and there are 175694 deaths.

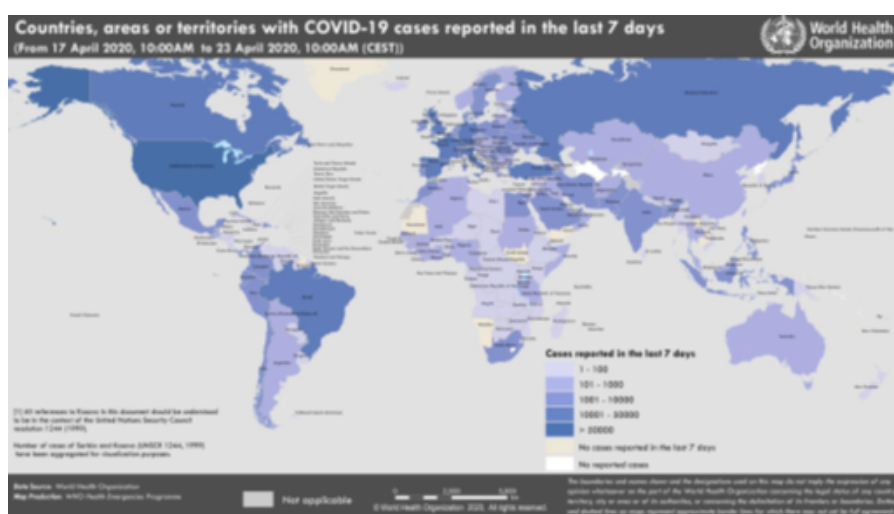


Figure 1: Cases of COVID-19 on 23 April 2020. Obtained from <https://www.who.int>

¹e-mail: m.teresa.sanz@uv.es

The scientific community concentrates its efforts on obtaining predictive models that can be an instrument to help governments to establish sanitary and social measures [1] or to identify cases as fast as possible [2]. In Spain, the Spanish Mathematics Committee calls on mathematicians and statisticians to participate in the construction of a meta-predictor to provide the authorities with information on the short-term behaviour of important variables in the spread of the COVID-19. The method uses the predictions from different models or algorithms that are provided by the participating researchers (<https://covid19.citic.udc.es/>), and build optimized combinations of these, disaggregated by Autonomous Communities. Thus, in order to help our Government in this fight, the DinSisCovid19 group is created, the members of which are the authors of this paper.

2 The model

The model presented in this research is an extension of the simplest model of the epidemic outbreak evolution, the SIR [3]. According to this model, the population can be divided into three different groups: a) susceptible (S), individuals without immunity to the infectious agent but they can be infected if exposed to the infectious agent; b) infected (I), individuals who are infected at any given time and can transmit the infection to susceptible population; and c) recovered (R), individuals who are immune to infection, and consequently the transmission does not affect when they are in contact with other individuals. This model provides a coupled system of three differential equations for the cited variables.

$$\frac{dS(t)}{dt} = -\beta \cdot S(t) \cdot I(t), \quad (1)$$

$$\frac{dI(t)}{dt} = \beta \cdot S(t) \cdot I(t) - \gamma \cdot I(t), \quad (2)$$

$$\frac{dN(t)}{dt} = \gamma \cdot I(t). \quad (3)$$

Being β the transmission rate, γ the recovery rate and $1/\gamma$ the average recovery period of the epidemic. These equations have been generalized in this paper in order to increase their predictive power. First, the population of the territory, $N(t)$, is considered. It is calculated as the initial population minus the deaths flow (4),

$$\frac{dR(t)}{dt} = -kf \cdot \left(\frac{E(t)}{\tau f} + S(t) \cdot E(t) \cdot \frac{ka}{\tau a} + S(t) \cdot R(t) \cdot \frac{kb}{\tau b} \right), \quad (4)$$

where, kf is the deaths rate of the sick population ($E(t)$); τf is the sick population deaths delay; and $S(t) \cdot E(t) \cdot ka/\tau a + S(t) \cdot R(t) \cdot kb/\tau b$, refers to those infected at each time step, i.e., the infection flow. The latter expression is used to calculate the infected population $I(t)$ that is modified in (2) through (5).

$$\frac{dI(t)}{dt} = S(t) \cdot \left(E(t) \cdot \frac{ka}{\tau a} + R(t) \cdot \frac{kb}{\tau b} \right). \quad (5)$$

The infected population come not only from the sick population but also from the recovered population ($R(t)$), and both interact with the susceptible population ($S(t)$) through the ratio of interaction rate and its corresponding delay, $ka/\tau a$ y $kb/\tau b$, respectively. Regarding the susceptible population, (1) is transformed into (6). In (1), a fixed initial susceptible population is changed through the infection flow. In the present model, we start from total population that is becoming susceptible due to the susceptibility rate (kq). It is calculated as the new susceptible population, $kq \cdot N(t)$, minus the infection flow.

$$\frac{dS(t)}{dt} = kq \cdot N(t) - S(t) \cdot \left(E(t) \cdot \frac{ka}{\tau a} + R(t) \cdot \frac{kb}{\tau b} \right). \quad (6)$$

Regarding the recovered population, equation (2) becomes (7). It is defined as the recovered rate, kr , multiplied by the sum of the infection flow and the sick population affected by the recovered population delay (τr).

$$\frac{dR(t)}{dt} = kr \cdot \left(S(t) \cdot E(t) \cdot \frac{ka}{\tau a} + S(t) \cdot R(t) \cdot \frac{kb}{\tau b} + \frac{E(t)}{\tau r} \right). \quad (7)$$

The deaths flow allows calculating the total deaths of the system (8).

$$\frac{dD(t)}{dt} = kf \cdot \left(S(t) \cdot E(t) \cdot \frac{ka}{\tau a} + S(t) \cdot R(t) \cdot \frac{kb}{\tau b} + \frac{E(t)}{\tau f} \right). \quad (8)$$

Finally, the sick population is calculated through the infected flow minus deaths and recovered flow.

$$\begin{aligned} \frac{dE(t)}{dt} = & \left(S(t) \cdot E(t) \cdot \frac{ka}{\tau a} + S(t) \cdot R(t) \cdot \frac{kb}{\tau b} \right) - \\ & kf \cdot \left(S(t) \cdot E(t) \cdot \frac{ka}{\tau a} + S(t) \cdot R(t) \cdot \frac{kb}{\tau b} + \frac{E(t)}{\tau f} \right) - \\ & kr \cdot \left(S(t) \cdot E(t) \cdot \frac{ka}{\tau a} + S(t) \cdot R(t) \cdot \frac{kb}{\tau b} + \frac{E(t)}{\tau r} \right). \end{aligned} \quad (9)$$

It should be noted that two additional variables are added to the model: hospitalized (H) and ICU (U), both are included by the collaboration that our research group carries out with the Spanish Mathematics Committee (CEMAT).

$$\frac{dH(t)}{dt} = kh \cdot \left(S(t) \cdot E(t) \cdot \frac{ka}{\tau a} + S(t) \cdot R(t) \cdot \frac{kb}{\tau b} + \frac{E(t)}{\tau h} \right), \quad (10)$$

$$\frac{dU(t)}{dt} = ku \cdot \left(S(t) \cdot E(t) \cdot \frac{ka}{\tau a} + S(t) \cdot R(t) \cdot \frac{kb}{\tau b} + \frac{E(t)}{\tau u} \right). \quad (11)$$

Where kh is the hospitalization rate of the sick population and ku is the ICU rate of the hospitalized population. Moreover, τh and τu represent the delay of the flow of both variables with respect to the sick and hospitalized population, respectively.

3 Results and discussion

For the calibration of the model, the genetic algorithm (hereinafter GA) implemented in Sigem [1] is used. With this tool, rates and delays are variables that the model calculates from an assumed initial data defined on the chromosome. The genetic algorithm is provided with a minimum and maximum oscillation of these variables, as well as a percentage that corresponds to the corresponding search window. In addition, the sum of the absolute values of the differences between the infected, deceased, recovered, hospitalized and admitted to the ICU calculated by the model and the actual trend of each variable is defined as an objective variable to be minimized by the GA. The aforementioned real trend is temporarily fitted through Gaussian combinations.

These adjustments are the ones that allow extrapolations of the variables contained in the chromosome to be able to make future predictions. The real data are obtained from <https://covid19.isciii.es/> and the time period here studied corresponds to the one from January 31 to April 22, 2020.

Figure 2 shows the validation of the model's deterministic formulation through the fitting to reality degree of infected, deceased, recovered, hospitalized, admitted to the ICU and sick population. The results show a great reliability of the model, being the determination coefficients higher than 0.99, a good graphic overlap between real and simulated data, and a good relative error, that in all cases, is less than 5%.

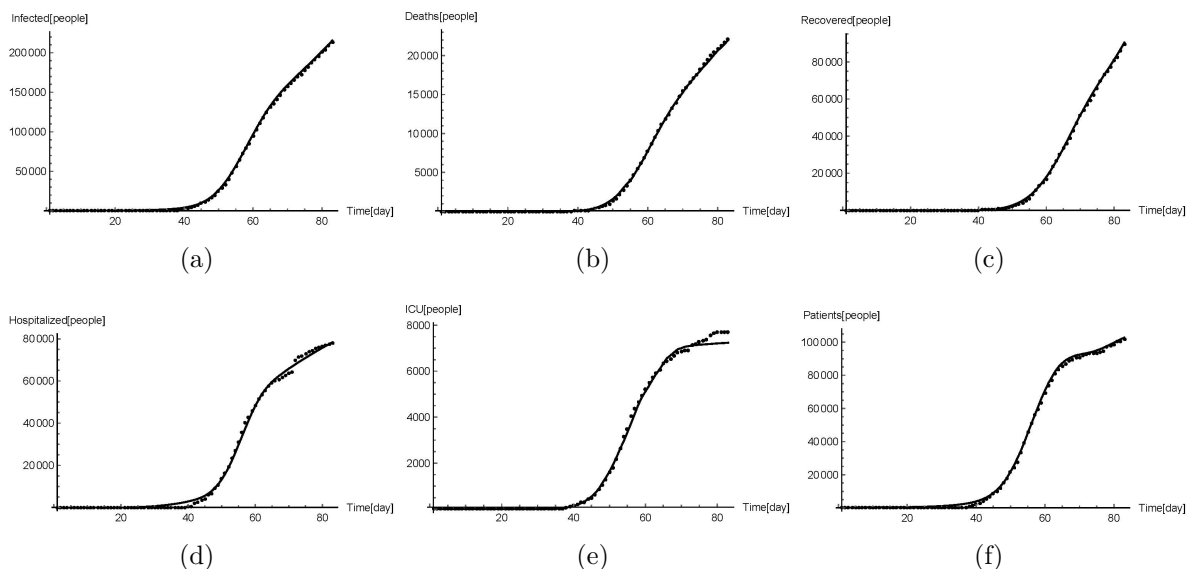


Figure 2: Validation of the model's deterministic formulation in the period from January 31 to April 22, 2020. a) Infected population. $R^2= 0.999877$; b) Deceased population. $R^2= 0.999779$; c) Recovered population. $R^2= 0.999709$; d) Hospitalized population. $R^2= 0.998582$; e) ICU population. $R^2= 0.998089$; f) Sick population. $R^2= 0.99972$. Real data: dots. GA simulated data: line.

The application of the model has been the prediction of the infected flow, deceased flow, recovered flow, hospitalized flow, admitted to the ICU flow, as well as the sickening flow in the period from April 23 to May 14, 2020. For this, the chromosome variables are extrapolated

into the mentioned period, and they become input variables of the model designed for this work.

Figure 3 presents past and future evolution of the first five previously mentioned variables. It can be seen that by the measure of confinement introduced by the Government, the infection flow has been reduced. However, with the application of massive tests to asymptomatic people, a slight rise in the number of registered cases is expected.

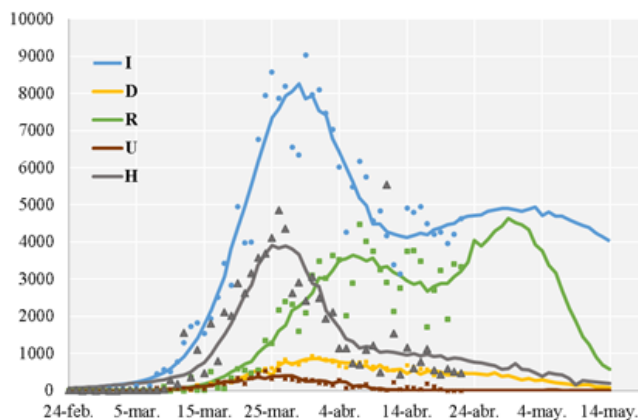


Figure 3: Prediction in a trend scenario in the period April 23 to May 14, 2020. Real data: points. Simulated data: line.

Regarding the sicking flow (Figure 4), it can be seen that for May 14 the trend continues growing, being observed this increase since April 20, that is the date when the relaxation of the containment measures for certain production sectors in the territory took place. In addition, we want to emphasize that the slope of the forecasted curve is the same as the one that occurred in the last period from March 11 to 31, approximately.

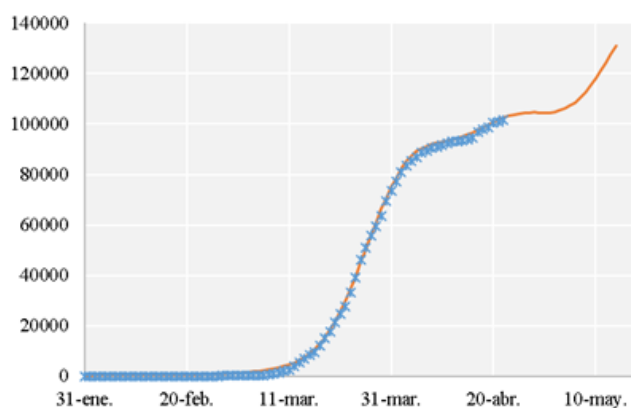


Figure 4: Prediction in a trend scenario of the sicking flow in the period from April 23 to May 14, 2020. Real data: blue blades. Simulated data: orange line.

4 Conclusions and future work

In this report we have analyzed the epidemic data made available to the scientific community by the Gobierno de España (<https://covid19.isciii.es/>) and referred to the 31/01/2020 –

23/04/2020 period. Our results suggest that the containment measures taken by the authorities have reduced the spread of COVID-19 among people in Spain. But the introduction of new rapid tests together with the PCR tests that were carried out from the beginning of the epidemic, have led to an increase in detected cases since April 14. This fact does not indicate an increase in new cases, but rather reflects the actual viral reality that our country had. Likewise, the de-escalation process accelerated by the fear to economic collapse from April 20 also causes an increase in cases. The future work on this model is challenging. On the one hand, the present model will be compared with models already published by the scientific community. On the other hand, its application to different countries of the world must be done, so that its validity be ratified. Regarding the improvement of the model, the construction of the corresponding stochastic model formulation will allow giving predictions with a confidence interval. Likewise, the definition of the same by using cohorts and sexes could enable us to evaluate the different kinds of population and to develop specific measures in both directions. Finally, a possible study of the past evolution of the parameters included in the chromosome (detected in the calibration process) could teach something about how to influence the future evolution of the pandemic in Spain.

References

- [1] Fanelli, D., Piazza, F., Analysis and forecast of COVID-19 spreading in China, Italy and France *Chaos, Solitons & Fractals*, Volume(134):1–5, 2020.
- [2] Rao, A., Vazquez, J., Identification of COVID-19 Can be Quicker through Artificial Intelligence framework using a Mobile Phone-Based Survey in the Populations when Cities/Towns Are Under Quarantine *Infection Control & Hospital Epidemiology*, Volume(41):1–18, 2020.
- [3] Kermack, W., McKendrick, A. G., Walker, G., A contribution to the mathematical theory of epidemics *Proceedings of the Royal Society*, Volume(A115):700–721, 1927.
- [4] Caselles, A., SIGEM: a realistic models generator expert system. In Trappl (Ed.) *Cybernetics and Systems '88* (pp. 101-108) Dordrecht, Kluwer Academic Publishers, 1988.

An epidemic grid model to address the spread of Covid-19. The case of Valencian Community (Spain)

M.T Signes Pont^{b1}, J.J. Cortés Plana^b, H. Mora Mora^b and C. Bordehore Fontanet^d #

(b)Department of Computer Science and Technology, University of Alicante,
Ctra. San Vicente s/n 03080 Alicante, Spain,

(d) Department of Ecology, University of Alicante,
Ctra. San Vicente s/n 03080 Alicante, Spain.

1 Introduction

Since December 2019, the world is facing the most serious pandemic since the Spanish flu of 1918. After starting in China, the coronavirus epidemic reaches Europe (Italy) in late January 2020. Shortly thereafter, in february, the first positives appear in the Canary Islands (Spain). After the number of affected cases outside China has multiplied by 13 in two weeks and the number of affected countries has tripled in this period, the World Health Organization (WHO) declares the pandemic on March 11, 2020. We are therefore in a health emergency, fighting against an unknown virus, learning on the go, without having enough perspective (we do not know whether patients can be reinfected after healing or not, or whether asymptomatic patients can infect or not), and without the necessary data to study the disease in an accurate way (the counts are difficult to register, because testing capacity, differing public health protocols and political meddling may have distorted coronavirus death and infected counts around the world). A lot of research has been carried out since the first days of the pandemic. Some works aim to determine the basic reproduction number of Covid-19 following different approaches. Reference [1] uses the exponential growth model method. Their result for R_0 in Wuhan ranges from 2.24 to 3.58, and is significantly larger than 1. In [2], the authors also aim to determine R_0 but they use the Susceptible-Exposed-Infected-Recovered (SEIR) model. They demonstrate the early transmission ability of Covid-19, close to or slightly higher than SARS -1. In their opinion, this outbreak is a controllable disease with moderate to high transmissibility. Other approaches aim to estimate the size of the epidemic. Reference [3] deals with data for cities on the basis of the number of cases exported from Wuhan. In Reference [4], the authors develop a Susceptible-Unquarantined-Infected, Quarantined-Infected, Confirmed-Infected (SUQC) model to characterize the dynamics of Covid-19 and explicitly parameterize the intervention effects of control measures. In Spain, many research teams also present different approaches. MUNQU (Modelling Uncertainty Quantification group) at the Politechnic University of Valencia has presented an epidemic model in order to provide a daily prediction of the expansion of Covid-19 which is available at <https://covid19.webs.upv.es/>. The model

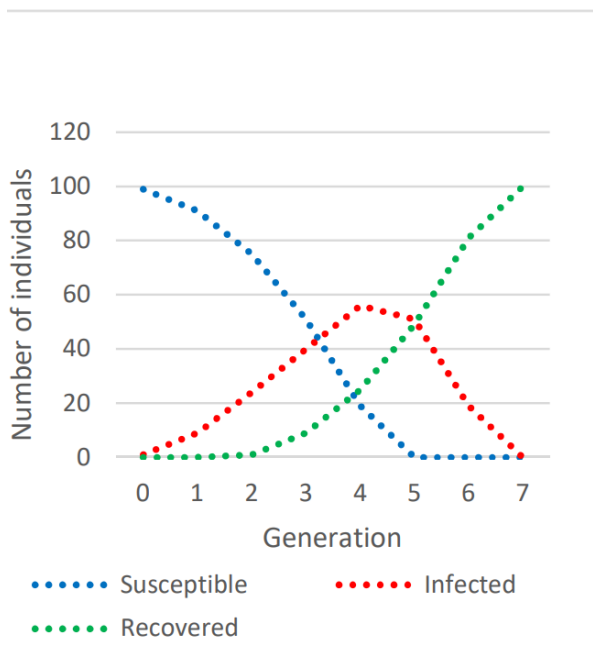
¹e-mail: teresa@dtic.ua.es

bases on a variant of Susceptible-Infected-Recovered (SIR) paradigm, with 9 compartments: Susceptible- Quarantine- Latent - Infected- Hospitalized- ICU (intensive care unit)- Hospitalized post ICU-Recovered-Dead. The system is solved by a set of differential ordinary equations (ODE) [5]. A group of Galician researchers (University of Santiago de Compostela) and northern Portugal (University of Aveiro) use an SEIR model that has been used successfully in the past to analyze diseases such as ebola or zika. They propose a new compartment P (super-propagators) which have higher infection power than other people. The authors forecast the infected peak between the 20 and 35th days after the first known infection. In this model, environmental and cultural parameters such as geographic dispersion, climate and seasonal times, age and customs are considered, in reference to the cultures that have a social treatment with more physical proximity, as it is the case of Spain, or more distant as in the case of Asian countries. At the R. Margaleff Institute of Research (University of Alicante), Dr. C. Bordehore leads a multidisciplinary research team which studies the spread of Covid-19. He follows an open SEIR model which can include different realistic scenarios to provide an estimate of the impact of each parameter on the spread. The model is currently in an update phase that aims to define R_0 with more accuracy [6]. To guide the planning of the use of health resources in order to improve the fight against Covid-19, we present an epidemic Susceptible-Infected (or Asymptomatic)-Recovered (or Dead), SIR model. The basic framework is implemented by a grid in which an “infected” cell (value = 1) contaminates its susceptible neighbors (value = 0). Various types of neighborhood are proposed (4-neighbors, 8-neighbors, and chess horse jump), along with a local binary update rule, which defines the result of the interaction between neighbors in terms of contagion. A more accurate approach assumes the disease spreads in quite different ways depending on environmental, sectorial or even cultural circumstances, in addition to the virus and patients ones so, our model associates a grid to each characteristic and the weighted impact of all them builds the realistic scenarios of the spread. This provides flexibility and adaptability when a territorial analysis (cities/ countryside) or sectorial analysis (elderly population/ population in nursing homes/health personnel) is needed to help designing dedicated action protocols and, therefore, more effective policies. The protocols applied are those that manage to bend the curves and ensure that the available resources are sufficient when they are needed. Thus, within the chain, “adaptive” modeling can be a crucial issue.

2 Results and discussion

Our model has already been analyzed in previous works and compared with the continuous models solved by ordinary differential equations (ODE), coming to find the homologous parameters between both approaches [7-10]. Thus, it has been possible to prove that the combination neighborhood-update rule is responsible for the rate of expansion and recovering of the illness. The delays (between Susceptible and Infected, Infected and Recovered) may have a crucial impact on both the peak of Infected and the recovery rate, which are much more attenuated in the case of Von Neumann neighbourhood than for other neighborhoods. This theoretical model has been successfully tested in the case of the spread of plant pests [11, 14] or the dissemination of information through mobile social networks [10, 13, 14]. In the case of Covid-19 we consider the impact on the spread of the disease of environmental parameters, such as climatic factors, habitat, communication network, cultural practices, and personal health state (age, previous pathologies) as shown in Figures 1, 2 and 3. The impact can be low, medium or high and this will be reflected by the value of the delays: Low means the values of the delay depend weakly on

this characteristic so, only one value is assigned to the corresponding delay; Medium: the values of the delay depend on this characteristic, so, we assign (arbitrarily) two values to the corresponding delay and finally, High: the values of the delay depend strongly on this characteristic so, we assign (arbitrarily) three values to the corresponding delay, see Figure 4. The delays are estimated in generations, that is a generic measure that can be tuned (hours, days, ...) to meet the particularities of the studied disease. Despite we are not yet able to compare the estimated recovery time for Covid-19 with the actual one at this moment, our preliminary results provide a trend that seems to meet the data available in Valencian government databases.



	3	3	3	3	3	3	3		
	3	2	2	2	2	2	3		
	3	2	1	1	1	2	3		
	3	2	1	0	1	2	3		
	3	2	1	1	1	2	3		
	3	2	2	2	2	2	3		
	3	3	3	3	3	3	3		

Spread schedule at generation n° 3 (out of 7)

Susceptible: 51
 Infected: 40
 Recovered: 9 (generations n° 0 and 1)

Figure 1. The basic SIR model ($\Delta_{RS-I} = 1$ generation, $\Delta_{I-R} = 2$ generations (generic time unit))

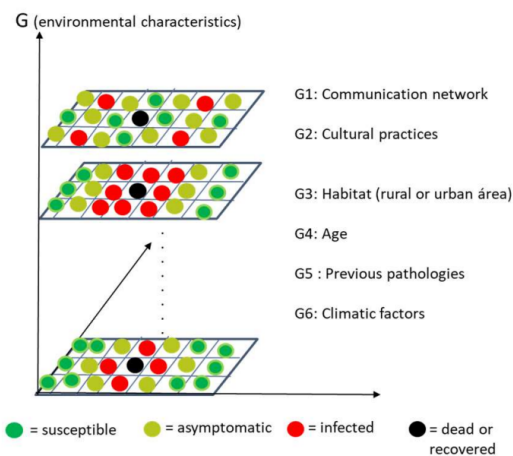


Figure 2. The multi-grid implementation

G (environmental characteristics)	Delays	
	$\Delta_{S-I/A}$ Susceptible - Infected (or Asymptomatic)	$\Delta_{I/A-R/D}$ Infected (or Asymptomatic) - Recovered (or Dead)
G1- Communication network	High (III)	Low (I)
G2- Cultural practices	High (III)	Low (I)
G3- Habitat	Medium (II)	Low (I)
G4- Age	Low (I)	High (III)
G5- Previous pathologies	Low (I)	High (III)
G6- Climatic factors	Medium (III)	Low (I)

Figure 3. Relative impact of the environmental characteristics

3 Conclusions and future work

The advantages of this discrete model are the ability to include both behavioral variability at the cell level (by modifying the neighborhood and/or the update rule and/or the delays) and modularity (by easy scaling the number of grids). This provides a wide range of possibilities to deal with realistic scenarios. The relevance of this project is enormous in the fight against the Covid-19 virus. In these weeks, it has become clear that the main drawbacks of the outbreak management came from the pressure in the ICUs and the hospitals that were on the verge of collapse. It is evident that a health system with a higher endowment has infinitely more possibilities of success than a weaker one. But, regardless of conditions on which science has little to do, and sticking to the purely scientific-research field, it seems that forecasting the evolution of pandemic leaves some room for maneuver. The management of the pandemic with the modification of its parameters can be an alternative way to avoid the overflow of the sanitary structures. In this sense, the knowledge of environmental, cultural, population, and organizational characteristics that surround the pandemic is an enormous addition to the more traditional modeling that considers only the parameters of the disease.

References

- [1] Preliminary estimation of the basic reproduction number of novel coronavirus (2019-nCoV) in China, from 2019 to 2020: A data-driven analysis in the early phase of the outbreak, Zhao, Shi and Lin, Qianyin and Ran, Jinjun and Musa, Salihu S and Yang, Guangpu and Wang, Weiming and Lou, Yijun and Gao, Daozhou and Yang, Lin and He, Daihai and others, *International journal of infectious diseases*, Volume(92):214–217, Elsevier,2020.
- [2] Preliminary prediction of the basic reproduction number of the Wuhan novel coronavirus 2019-nCoV, Zhou, Tao and Liu, Quanhui and Yang, Zimo and Liao, Jingyi and Yang, Kexin and Bai, Wei and Lu, Xin and Zhang, Wei, *Journal of Evidence-Based Medicine*, Volume(13-1):3–7, Wiley Online Library, 2020.
- [3] Nowcasting and forecasting the potential domestic and international spread of the 2019-nCoV outbreak originating in Wuhan, China: a modelling study, Wu, Joseph T and Leung, Kathy and Leung, Gabriel M, *The Lancet*, Volume(395-10225):689–697, Elsevier, 2020.
- [4] Modeling the epidemic dynamics and control of COVID-19 outbreak in China, Zhao, Shilei and Chen, Hua, *Quantitative Biology*:1–9, Springer, 2020.
- [5] Modelo para el estudio de la dinámica de transmisión del SARS-COV-2 y la enfermedad del COVID19. *Descripción técnica. Instituto Universitario de Matemática Multidisciplinar, Universitat Politècnica de Valencia, 46022, <https://covid19.webs.upv.es/>*, 2020.
- [6] Understanding COVID-19 spreading through simulation modeling and scenarios comparison: preliminary results.,Bordehore, Cesar and Navarro, Miriam and Herrador, Zaida and Fonfria, Eva S,*medRxiv*, Cold Spring Harbor Laboratory Press, 2020.
- [7] The susceptible-infectious model of disease expansion analyzed under the scope of connectivity and neighbor rules. Pont, Maria Teresa Signes and Mora, Higinio Mora and Cortés,

Antonio, *Proceedings of the conference, computer science & information technology, CSITA (CS & IT)*, Volume=(7):1–10, 2017.

- [8] A discrete approach of the Susceptible-Infectious-Susceptible (SIS) model of disease expansion, Pont, Maria Teresa Signes and Mora, Higinio Mora and Castillo, Antonio Cortés, *International Journal of Computers*, Volume(2), International Association of Research and Science, 2017.
- [9] The Susceptible-Infectious-Recovered (SIR) model of disease expansion: a new approach, Pont, Maria Teresa Signes and Mora, Higinio Mora and Castillo, Antonio Cortés, *jornadas.imm.upv.es*, 2017.
- [10] Modelización de la propagación de información a través de las redes informáticas, Antonio Cortés Castillo, Director: Dra. María Teresa Signes Pont, 2020
- [11] A multigrid approximation to the expansion of *Xylella Fastidiosa* in almond trees, Signes Pont, María Teresa and Ramirez-Martinez, Devis Eduard and García-Chamizo, Juan Manuel and Mora, Higinio and others, WSEAS, 2019.
- [12] Computational model to approach the spread of plant pests, Signes et al., *7th Business Systems Laboratory International Symposium: Challenges for sustainable development in the digital era. Alicante*, January 2020.
- [13] A grid model to address the behaviour of the nodes in the dissemination of information, Signes-Pont, María Teresa and Mora, Higinio and Cortés-Castillo, Antonio and Mollá-Sirvent, Rafael, *Kybernetes*, Emerald Publishing Limited, 2019.
- [14] A framework to address the impact of people's behavior in the dissemination of information through mobile social networks, María Teresa Signes-Pont, Antonio Cortés-Castillo, Higinio Mora-Mora, Rafael Mollá-Sirvent, *Business Systems Laboratory International Symposium, Pavia (Italia)*, 2019.

The Relativistic Harmonic Oscillator in a Uniform Gravitational Field

Michael M. Tung*

Instituto de Matemática Multidisciplinar
Universitat Politècnica de València,
Camino de Vera, s/n, 46022 Valencia, Spain.

1 Introduction

The harmonic oscillator or mechanical spring, implementing Hooke's Law, is one of the standard textbook examples for introducing the student to Newtonian mechanics. Its treatment is simplest [1], notwithstanding additional difficulties when velocity-dependent forces are added. Remarkably, the relativistic counterpart of an oscillator or a pendulum—which approximates to a harmonic oscillator for small amplitudes—stationed within some supplementary force field has so far been dealt with only scarcely [2–5].

In the present work, the Euler-Lagrange formalism is used to derive the equations of motion for a harmonic oscillator in the framework of special relativity [6]. For this configuration, considerable complications occur since the oscillator will be suspended in a uniform gravitational field. Although we are able to derive the corresponding relativistic gravitational potential (for a rigorous general definition of this potential see [2]), the final results for the motion become intangible for analytic evaluation.

By employing numerical integration in the final step and presenting some illustrative examples, we will be able to simulate the dynamics of this model and explore some significant characteristics of the system.

2 Discussion and Results

Robert Hooke (1635–1703) first pointed out that the mathematical description for small oscillations of a body with mass $m_0 > 0$ attached to an elastic spring with position $x = x(t)$ takes the form: $\ddot{x} = -kx$. The positive constant $k > 0$ depends on the elastic properties of the spring in question. This mechanical system is termed “harmonic oscillator.” Then, in Lagrangian mechanics, the deterministic equations of motion result from the following principle of least action

$$\delta \int dt \left[\frac{1}{2} m_0 \dot{x}^2 - \frac{1}{2} k x^2 - m_0 g x \right] = 0 \quad (1)$$

*e-mail: mtung@imm.upv.es

by varying over all possible paths $x = x(t)$ and keeping the end points fixed. Eq. (1) includes the gravitational potential $V_g(x) = m_0 g x$, since we will consider the mechanical system to be stationed within a uniform gravitational field determined by the gravitational constant $g > 0$. Finally, the Euler-Lagrange equations readily produce a simple linear second-order differential equation whose general solution is

$$x(t) = C_1 \cos\left(\sqrt{\frac{k}{m_0}} t\right) + C_2 \sin\left(\sqrt{\frac{k}{m_0}} t\right) - \frac{m_0 g}{k}. \quad (2)$$

However, this classical result does not contemplate strong gravitational fields with $g \gg 1$ and when velocities \dot{x} get closer to the speed of light $c > 0$. Thus, Eq. (2) will utterly fail in giving a faithful description of the physical effects in the relativistic domain.

In order to generalize to a correct description in the relativistic domain, the best starting point is to modify the principle of least action in Eq. (1). Therefore, we postulate

$$\delta \int dt \left[-m_0 c^2 \sqrt{1 - \frac{\dot{x}^2}{c^2}} - \frac{1}{2} k x^2 - V_g \right] = 0, \quad (3)$$

where the rest mass m_0 is divided by the usual relativistic factor $\gamma = 1/\sqrt{1 - \dot{x}^2/c^2}$ to include rest mass and kinetic energy. The spring potential is unaltered, and the relativistic gravitational potential V_g , however, is hitherto undetermined. Complications for identifying V_g arise since in relativity the mass ($m = \gamma m_0$) itself is a dynamical property and gravitates itself, meaning that as the body oscillates on the spring, its kinetic energy fluctuates which continuously modifies its own gravitating mass. By using the relativistic ansatz [2]

$$V_g(x) = \int dx m g = m_0 g \int \frac{dx}{\sqrt{1 - \frac{\dot{x}^2}{c^2}}}, \quad (4)$$

and also using energy conservation, we obtain the full analytical solution for $V_g(x)$. The arbitrary integration constant in Eq. (4) is chosen such that $V_g(0) = 0$. The post-Newtonian expansion up to first order in g/c^2 is

$$V_g(x) = m_0 g x - \frac{1}{6} k \left(\frac{g}{c^2}\right) x^3 + \mathcal{O}\left(\frac{g}{c^2}\right)^2. \quad (5)$$

So in first approximation the odd powers indicate a symmetric result, more precisely rotational symmetry with respect to rotations of 180° about the origin. Yet this symmetry is broken in the relativistic domain.

Figure 1 gives the full relativistic result for V_g in a strong gravitational field. Here, to achieve $g/c^2 = 1$ (measured in physical units m^{-1}), all parameters are set to unity, except for the spring constant which we chose to be $k = 2$ (measured in physical units kg/s^2). We also provide the gradient, V'_g , for any position $x \in [-1, 1]$. Note that the gravitational force, $F_g(x) = -V'_g(x)$, will flip sign at

$$x_0 = \frac{c^2}{g} \left[W_0 \left(\frac{\frac{m_0 g^2}{k c^2} - 1}{e} \right) + 1 \right], \quad (6)$$

where W_0 is the principal branch of Lambert's W function [7, §4.13]. In Figure 1, it is $x_0 \approx 0.77$, and thus all estimates for $x > x_0$ are unphysical. Nevertheless, for the initial conditions we will assume

$$x(0) = 0 \quad \text{and} \quad \dot{x}(0) = 0, \quad (7)$$

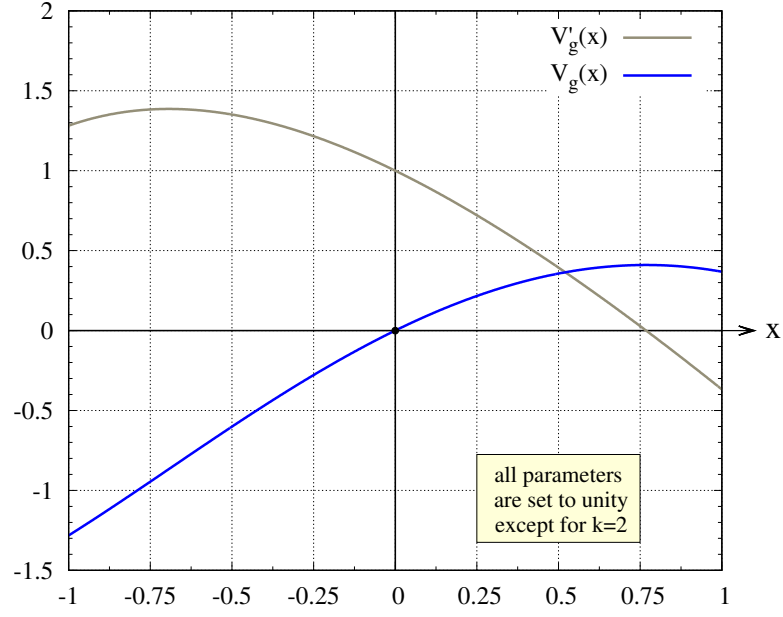


Figure 1: The relativistic gravitational potential, $V_g(x)$, for an oscillating body posted in a strong uniform gravitational field. For the graphical representation we use $m_0 = 1 \text{ kg}$, $g = 1 \text{ kg m/s}^2$, and $k = 2 \text{ kg/s}^2$. Further, the speed of light is normalized to $c = 1 \text{ m/s}$. The gradient, $V'_g(x)$, is also displayed.

such that the body will move only on the negative axis, $x \leq 0$, and thus safely be in the physical region.

Applying the action principle, Eq. (3), with the fully analytic relativistic result of $V_g(x)$ yields after a lengthy but straightforward calculation the Euler-Lagrange equation which govern the physical system at hand:

$$\alpha(x)\ddot{x} + \beta(x)g = 0, \quad (8)$$

where

$$\begin{cases} \alpha(x) = \left(1 - \frac{\frac{1}{2}kx^2 + V_g(x)}{m_0c^2}\right)^3, \\ \beta(x) = \frac{\frac{1}{2}k\left(\frac{2c^2}{g} - x\right)x + m_0c^2 - V_g(x)}{m_0c^2}. \end{cases} \quad (9)$$

Note that the dimensionless functions $\alpha(x)$ and $\beta(x)$ contain $V_g(x)$ and necessarily satisfy the physical conditions $\alpha(0) = \beta(0) = 1$. Additionally, the physical relativistic domain given by energy conservation and $1 \leq \gamma$ provides the constraint

$$V_g(x) \leq -\frac{1}{2}kx^2. \quad (10)$$

The post-Newtonian expansion of Eq. (8) up to first order in g/c^2 is

$$m_0\ddot{x} + m_0g + kx + \left(2m_0gx + 4kx^2 + \frac{3k^2}{2m_0g}x^3\right)\frac{g}{c^2} = 0, \quad (11)$$

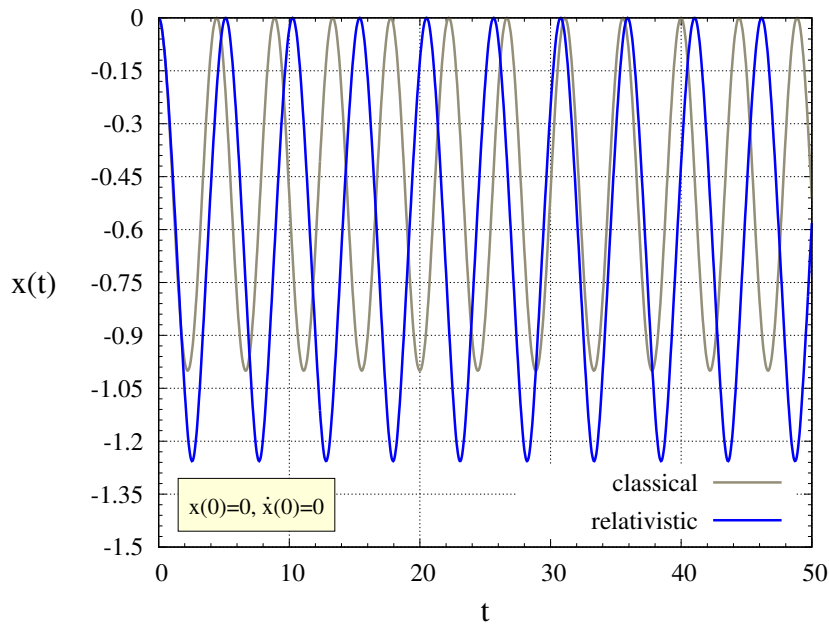


Figure 2: The relativistic harmonic oscillator compared to the classical model, both suspended in a uniform gravitational field, either using the simple classical solution, *viz.* Eq. (2), or the relativistic estimates resulting by numerical integration of Eqs. (8)–(9). The gravitational field is strong with $g/c^2 \sim 1$, choosing again all parameters unity, except for $k = 2 \text{ kg/s}^2$, see Figure 1. The two initial conditions are $x(0) = \dot{x}(0) = 0$, see Eq. (7).

and analytical integration already will yield a rather convoluted list of elliptic integrals. Hence, for the full result—including all higher orders—numerical integration is the most appropriate, if not the only possible, open pathway.

For the actual numerical integration of Eqs. (8)–(9), we decided to implement the code in Julia due to its efficiency and high performance [8]. Figure 2 displays the classical and relativistic estimates, again for all parameters set equal to unity, except for the spring constant with $k = 2$. Using the Julia library `DifferentialEquations.jl` [9], the algorithm is based on first-order interpolation with at least stepsize $\Delta t = 0.05$ and a relative tolerance of 10^{-8} in the adaptive timestepping. In Figure 2, the difference between classical and relativistic predictions is pronounced—not only in amplitude but also in phase. The relativistic results always give higher corrections for the amplitude and a positive phase shift.

Figure 3 more clearly illustrates the difference between relativistic and classical predictions, $\Delta x(t)$, over an extended time interval $t \in [0, 100]$. Obviously, these corrections are periodic. As may be anticipated before from the two curves shown in Figure 2, the relativistic corrections are easily recognized to propagate with a positive phase while significantly modulating the amplitude of the classical model.

3 Conclusions and future work

The present work fills an outstanding gap in the existing research literature. In 2017, the most recent publication [5] in this area of research focusses on relativistic extensions for the motion

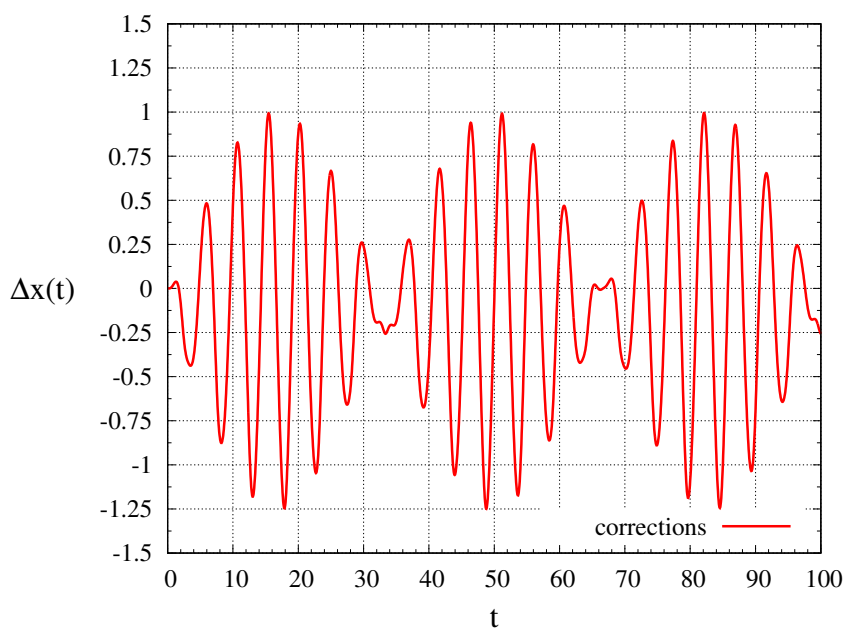


Figure 3: The relativistic corrections $\Delta x(t)$ for the classical harmonic oscillator in a strong uniform gravitational field, corresponding to the physical configuration of Figure 2, but for the larger time interval $t \in [0, 100]$. These periodic corrections are significant and modulate in both, amplitude and phase.

of the harmonic oscillator from the view of the oscillating body, but without including any gravitational effects.

Here, we have derived and studied the relativistic corrections for a body oscillating in alignment with a uniform gravitational field, having gravitational constant $g > 0$. If gravity is strong, meaning $g/c^2 \sim 1$, these contributions become substantial and cannot be neglected. Remarkably, we have seen that the relativistic corrections take the shape of pronounced periodic wave packets. It remains to be investigated if these wave packets possibly resemble Bloch waves.

Further future work will concentrate on a more detailed study of the phasespace in question and other extensions of the model which may incorporate friction.

Acknowledgements

This work has been supported by the Spanish *Ministerio de Economía y Competitividad*, the European Regional Development Fund (ERDF) under grant TIN2017-89314-P, and the *Programa de Apoyo a la Investigación y Desarrollo 2018* (PAID-06-18) of the Universitat Politècnica de València under grant SP20180016.

References

- [1] Goldstein, H., Poole, C., Safko, J., *Classical Mechanics*, Boston, Addison Wesley, 2001.

- [2] Goldstein, H. F., Bender, C. M. Relativistic brachistochrone, *J. Math. Phys.*, 27(2):507–511, 1986.
- [3] Erkal, C., The simple pendulum: a relativistic revisit, *Eur. J. Phys.*, 21:377–384, 2000.
- [4] Torres, P. J., Periodic oscillations of the relativistic pendulum with friction, *Phys. Lett. A*, 372:6386–6387, 2008.
- [5] de la Fuente, D., Torres, P. J., A new relativistic extension of the harmonic oscillator satisfying an isochronicity principle, *Qual. Theory Dyn. Syst.*, 34(3):579–589, 2017.
- [6] Christodoulides, C., *The Special Theory of Relativity: Foundations, Theory, Verification, Applications*, New York, Springer, 2016.
- [7] Olver, F. J. W., *et al.*, eds., NIST Digital Library of Mathematical Functions, Release 1.0.27 of 2020-06-15, Section 4.13: Lambert W -Function, <https://dlmf.nist.gov/4.13>.
- [8] Bezanson, J., Edelman, A., Karpinski, S., Shah, V. B., Julia: A fresh approach to numerical computing, *SIAM Review*, 59(1):65–98, 2017.
- [9] Rackauckas, C., Nie, Q., DifferentialEquations.jl—A performant and feature-rich ecosystem for solving differential equations in Julia, *J. Open Res. Softw.*, 5(1):15, 2017.

A disruptive technology that enables low cost real-time monitoring of road pavement condition by any ordinary vehicle circulating on the road, and automatically designs plans for predictive maintenance

Francisco José Veá^{b1}, Adrián Zornoza^{‡2}, Juan Ramón Sánchez^{‡3} and Ismael Muñoz^{‡4}

(b) Ministry of Public Works,
Government of Chile,

(‡) Institute of Multidisciplinary Mathematics,
Universitat Politècnica de València.

1 Introduction

Special attention should be paid to current pavement state of a certain road, since it is directly related with circulation costs (fuel cost and vehicle maintenance) and with driving safety and comfort. Usually pavement state is measured by its roughness. Erosion and defect appearance on pavement increases its roughness.

Pavement roughness is defined as the quantity of irregularities in pavement surface that adversely affect vehicle ride quality and vehicle delay costs, fuel consumption and maintenance costs. Today, roughness is typically quantified using different indexes, such as, present serviceability rating (PSR), Mean Panel Rating (MPR), Profile Index (PI), Ride Number (RN) and Root Mean Square Vertical Acceleration (RMSVA), being International Roughness Index (IRI) the most prevalent.

For that, in this paper, a predictive maintenance software is developed. It is capable of processing and analysing all the inertial road-vehicle interaction to obtain IRI parameters, roughness data and longitudinal evenness; capable of locating and evaluating pavement defects; and capable of determining pavement maintenance plans automatically.

2 Method

In this section, it is explained the methodology for the development of the predictive maintenance software, that is composed of the next algorithms:

¹e-mail: alex.union@mop.gov.cl

²e-mail: adzorar@cam.upv.es

³e-mail: juasanv6@etsii.upv.es

⁴e-mail: ismael.munoz@innovating4m.es

- Algorithm for obtaining the roughness profile (IRI) of a road in real time (*i*).
- Algorithm for detecting specific defects such as cracks and their qualification (*ii*).
- Algorithm for predicting the evolution of IRI over time (*iii*).
- Algorithm for maintenance plan (*iv*).

First, the main feature is IRI estimation (*i*). IRI is obtained from position and acceleration data. Accelerometers are installed on sprung and un-sprung masses of the vehicle. Position is obtained from OBD interface (or GPS sensor) and it references the results to the road section. The algorithm is based on Quarter-Car model, obtaining first the profile and then IRI. Quarter Car Model simulates half of a vehicle axle, that is, interaction between wheel (and its damping system) and road surface [1]. First step is vehicle's masses differentiation: sprung mass (M_s) and unsprung mass (M_u).

On the other hand, displacement, L , is calculated by integrating vehicle speed, v , and GPS position. With elevation variations and displacement, IRI is defined as the sum of measured distances, in module over the horizontal, for the distance considered. That is, IRI is cumulative vertical movement of vehicle's driver's seat over a given distance.

$$IRI = \frac{1}{L} \int_0^{\frac{L}{v}} |\dot{Z}_s - \dot{Z}_u| dt$$

Another feature is road defects and imperfections location and classification. For that, two algorithms based on Wavelet Transform (WT) have been developed using unsprung mass acceleration (*ii*). For defect identification, an algorithm based on the Scale Space Filter (SSF) is developed. SSF filter achieves greater signal noise elimination by multiplying Wavelet coefficients from different adjacent levels.

Also for defect identification, based on the study carried out in [2], Daubechey family of functions, specifically db2 wavelet, is proposed as the best mother function. Developed algorithm follows a process to obtain new filtered wavelet coefficients. These coefficients are used to identify sudden changes in acceleration due to potholes or bumps presence over the road. With new coefficients obtained from detection defect algorithm, anomalous points can be determined using a threshold and a window size previously defined.

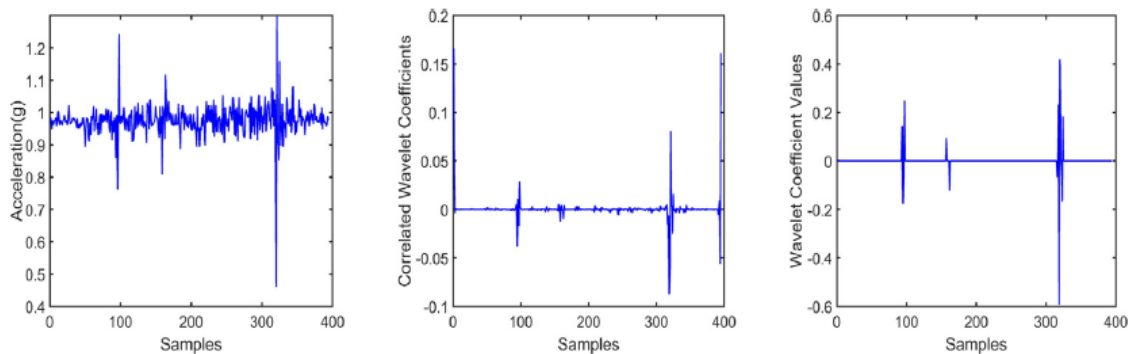


Figure 1: Original accelerometer signal (left) and correlated wavelet coefficient $\Omega_2(1, k)$ and $W_{new}(j, k)$ (right). Source: [2].

In a different sense, maintenance plans consist of classifying road sets according to their current pavement condition. In addition, a prediction of its evolution is also obtained (*iii*). There are numerous empirical mathematical models [3], to predict IRI evolution on a pavement. These models are based on road type characterization: asphalt kind, climate and flow, road traffic type, etc. Other studies [4], make a comparison between mathematical models and artificial neural networks based also on pavement characterization. Neural network-based models have better results than empirical models. On the other hand, there are also studies [5] that are not based on pathway type characterization, hear previous IRI evolution has considered. That is, it is able to predict future IRI values by only taking past IRI values. To obtain both models advantages, for our software an artificial neural network based on both methods has been implemented.

Finally, maintenance Operation Library has been created (*iv*). In this library maintenance operation required for each possible pavement state and costs approximation are collected. In this way, through the developed library and predicting pavement state evolution, maintenance plans can be proposed to ensure best driving conditions, minimizing their costs. Based on repair and maintenance techniques depending on defect classification and their severity, [6], a library has been developed with the best possible treatment to be performed. The system is able to detect the type of pavement distress that occurred.

For the validation of the system, different scenarios have been defined. A testing plan has been defined according to different algorithms that make up the software to have the necessary data for each one validation. For IRI validation, 23 routes have been defined through which the system was driven. For all routes, IRI value was calculated with our system and with a commercial class I system.

For validation of defects identification and classification, it is necessary to carry out a visual inspection of routes. Here, defects identification and classification were done manually. Visual inspection results were compared with our results. Visual camera was installed in the vehicle to facilitate manual identification. Camera focus was wheel track where the system had been installed.

IRI prediction validation was carried out in two ways:

- Historical IRI measurements were considered in 3 routes.
- Monthly measurements were carried out using our system on 5 routes.

Finally, for maintenance plan validation, some route operative maintenance plan results were evaluated by technicians specialized in the matter.

3 Results and discussion

In this section, there are exposed the results of the validation of the different algorithms.

First, after comparing IRI curves obtained using our system and commercial system, it was possible to validate correct algorithm working (*i*), getting a clear correlation between two systems.

The comparison between number of defects obtained visually and those obtained using the algorithm (*ii*) had a degree of accuracy greater than 80%.

Finally, maintenance plan (*iv*) has been evaluated by a specialized technician, giving its approval as one of the best solutions for each of the proposed problems, with a completely agree validation of 80% and an acceptable validation of 12%.

4 Conclusions and future work

This paper develops final version of predictive maintenance software that contains different algorithm functions: obtaining the roughness profile (IRI) of a road in real time, detection of specific defects such as cracks and their qualification, prediction of the temporal IRI evolution and preparation of maintenance plan.

With the predictive maintenance software we achieved a high accuracy (with IRI calculation algorithm and defects detection algorithm) and a new system capabilities regarding other existing solutions (with algorithm to predict IRI's evolution and a large library which relates each maintenance operation with each type and severity of pavement defect). All results have been validated with a large elaborated plan of test on different scenarios.

References

- [1] Eshkabilov, Sulaymon. Measuring and Assessing Road Profile by Employing Accelerometers and IRI Assessment Tools. *Journal of Traffic and Transportation Engineering*. 3. 10.11648/j.ajtte.20180302.12. (2018).
- [2] H.Bello-Salau, A.M. Aibinu, A.J. Onumanyi, J.J. Dukiya, H. Ohize. New road anomaly detection and characterization algorithm for autonomous vehicles. *Applied Computing and Informatics*. (2018).
- [3] H. Pérez-Acebo, A. Linares-Unamunzaga, E.Rojí and H. Gonzalo-Orden. IRI Performance Models for Flexible Pavements in Two-Lane Roads until First Maintenance and/or Rehabilitation Work.
- [4] Abouelsaad, Ahmed & El-Badwy, Sherif & Ibrahim, Murad. International Roughness Index Predictive Model for Rigid Pavements based on LTPP Data. (2019).
- [5] Georgiou, Panos & Plati, Christina & Loizos, Andreas. Soft Computing Models to Predict Pavement Roughness: A Comparative Study. *Advances in Civil Engineering*. 1-8. 10.1155/2018/5939806. (2018).
- [6] W. James Wilde . Cost-Effective Pavement Preservation Solutions for the Real World. Center for Transportation Research and Implementation Minnesota State University, Mankato. September 2014.